Reliable and Safe Motion Control of Unmanned Vehicles

Zhixiang Liu

A Thesis

in

The Department

of

Mechanical and Industrial Engineering

Presented in Partial Fulfillment of the Requirements

for the Degree of

Doctor of Philosophy (Mechanical Engineering) at

Concordia University

Montréal, Québec, Canada

October 2016

CONCORDIA UNIVERSITY

SCHOOL OF GRADUATE STUDIES

This is to certify that the thesis prepared

By: **Zhixiang Liu**

Entitled: **Reliable and Safe Motion Control of Unmanned Vehicles**

and submitted in partial fulfillment of the requirements for the degree of

Doctor of Philosophy (Mechanical Engineering)

complies with the regulations of this University and meets the accepted standards with respect to originality and quality.

Signed by the Final Examining Committee:

_____ Chair
Dr. Tarek Zayed

_____ External Examiner
Dr. Jason Gu

_____ External to Program
Dr. Amir Aghdam

_____ Examiner
Dr. Henry Hong

_____ Examiner
Dr. Subhash Rakheja

_____ Thesis Supervisor
Dr. Youmin Zhang

Approved by   _____
                Chair of Department or Graduate Program Director

_____   _____
                        Dean of Faculty

Abstract

Reliable and Safe Motion Control of Unmanned Vehicles

Zhixiang Liu, Ph.D.

Concordia University, 2016

Unmanned vehicles (UVs) are playing an increasingly significant role in modern daily life. In the past decades, numerous commercial, scientific, and military communities across the world are developing fully autonomous UVs for a variety of applications, such as environmental monitoring and surveillance, post-disaster search and rescue, border patrol, natural resources exploration, and experimental platforms for new technologies verification. The excessive opportunities and threats that come along with these diverse applications have created a niche demand for UVs to extend their capabilities to perform more sophisticated and hazardous missions with greater autonomy, lower costs of development and operation, improved personnel safety and security, extended operational range (reliability) and precision, as well as increased flexibility in sophisticated environments including so-called dirty, dull, harsh, and dangerous missions.

In order to successfully and effectively execute missions and meet their corresponding performance criteria and overcome these ever-increasing challenges, greater autonomy together with more advanced reliable and safe motion control systems are required to offer the critical technologies for ensuring intelligent, safe, reliable, and efficient control of UVs in the presence of disturbances, actuator saturation, and even actuator faults, especially for practical applications.

This thesis concentrates on the development of different reliable and safe motion control algorithms/strategies applicable to UVs, in particular, unmanned aerial vehicles (UAVs) and unmanned surface vehicles (USVs). A number of contributions pertaining to the fault detection and diagnosis

(FDD), fault-tolerant control (FTC), disturbance estimation and compensation, and actuator saturation avoidance have been made in this thesis. In addition to the control problems, this thesis also presents several guidance-related contributions, including adaptive observer-based line-of-sight (LOS) guidance law, time-varying lookahead distance scheme, piecewise path switching criterion for guiding a single UV, as well as a proportional-integral (PI) type of leader-follower formation guidance strategy for a group of UVs.

Acknowledgments

much from them.

Finally, I would like to thank my family, my parents, my wife and my lovely daughter, for their love, understanding, consistent support, and countless sacrifices, which have played an indispensable role in my life. It can never be enough for me to thank them.

List of Publications

Journal Papers

(1) Zhixiang Liu, Youmin Zhang, Xiang Yu, & Chi Yuan (2016). Unmanned surface vehicles: An overview of developments and challenges. *Annual Reviews in Control*, 41: 71-93. DOI:10.1016/j.arcontrol.2016.04.018.

(2) Zhixiang Liu, Chi Yuan, Youmin Zhang, & Jun Luo (2015). A learning-based fault tolerant tracking control of an unmanned quadrotor helicopter. *Journal of Intelligent and Robotic Systems*, pp. 1-18. DOI: 10.1007/s10846-015-0293-0.

(3) Zhixiang Liu, Chi Yuan, Xiang Yu, & Youmin Zhang (2016). Leader-follower formation control of unmanned aerial vehicles in the presence of obstacles and actuator faults. *Unmanned Systems*, 4(4), 2016 (To appear).

(4) Zhixiang Liu, Chi Yuan, & Youmin Zhang (2016). Active fault-tolerant control of unmanned quadrotor helicopter using linear parameter varying technique. *Journal of Intelligent and Robotic Systems* (Submitted).

(5) Zhixiang Liu, Chi Yuan, & Youmin Zhang (2016). Reliable and safe line-of-sight path following control of unmanned surface vehicle. *IEEE Transactions on Control Systems Technology* (Submitted).

(6) Zhixiang Liu, Chi Yuan, & Youmin Zhang (2016). Adaptive fault-tolerant tracking control of an unmanned quadrotor helicopter considering actuator dynamics. *International Journal*

vii

of Robust and Nonlinear Control (To be submitted).

(7) Zhixiang Liu, Chi Yuan, Xiang Yu, & Youmin Zhang (2016). Active disturbance compensating tracking control of unmanned surface vehicle subjecting to actuator saturation and steering constraints. *Journal of The Franklin Institute* (To be submitted).

(8) Chi Yuan, Youmin Zhang, & Zhixiang Liu (2015). A survey on computer vision based technologies for automatic forest fire detection using UAVs and remote sensing techniques. *Canadian Journal of Forest Research*, 45(7): 783-792. DOI: 10.1139/cjfr-2014-0347.

(9) Xiang Yu, Zhixiang Liu, & Youmin Zhang (2016). Fault-tolerant formation control of multiple UAVs in the presence of actuator faults. *International Journal of Robust and Nonlinear Control*, 26(12): 2668-2685. DOI: 10.1002/rnc.3467.

(10) Xiang Yu, Youmin Zhang, & Zhixiang Liu (2016). Fault-tolerant control design with explicit consideration of reconfiguration transients. *Journal of Guidance, Control, and Dynamics*, 39(3): 556-563. DOI: 10.2514/1.G001414.

(11) Xiang Yu, Zhixiang Liu, & Youmin Zhang (2016). Fault-tolerant flight control with finite-time adaptation under actuator stuck failures. *IEEE Transactions on Control Systems Technology* (on-line published on 23 September 2016; DOI: 10.1109/TCST.2016.2603072).

(12) Chi Yuan, Zhixiang Liu, & Youmin Zhang (2016). Forest fire detection in aerial images for firefighting using optical remote sensing techniques and unmanned aerial vehicles. *Journal of Intelligent and Robotic Systems* (Submitted).

Conference Papers

(1) Zhixiang Liu, Chi Yuan, & Youmin Zhang (2016). Adaptive fault-tolerant control of unmanned quadrotor helicopter using linear parameter varying control technique. *The International Conference on Unmanned Aircraft Systems (ICUAS 2016)*, June 7-10, 2016, Arlington, VA, USA.

(2) Zhixiang Liu, Chi Yuan, & Youmin Zhang (2016). Linear parameter varying control of unmanned quadrotor helicopter with mass variation and battery drainage. *The IEEE Chinese Guidance, Navigation and Control Conference (CGNCC 2016)*, August 12-14, 2016, Nanjing, Jiangsu, China.

(3) Zhixiang Liu, Chi Yuan, & Youmin Zhang (2016). A hybrid collision avoidance method for unmanned surface vehicle considering international maritime regulation. *The International Conference on Intelligent Unmanned Systems (ICIUS 2016)*, August 23-25, 2016, Xi'an, Shaanxi, China.

(4) Zhixiang Liu, Xiang Yu, Youmin Zhang, Chi Yuan, & Jun Luo (2015). Active disturbance compensating tracking control of an unmanned quadrotor helicopter. *The ASME 2015 International Design Engineering Technical Conferences & Computers and Information in Engineering Conference (IDETC/CIE 2015)*, August 2-5, 2015, Boston, Massachusetts, USA.

(5) Zhixiang Liu, Xiang Yu, Chi Yuan, & Youmin Zhang (2015). Leader-follower formation control of unmanned aerial vehicles with fault tolerant and collision avoidance capabilities. *The International Conference on Unmanned Aircraft Systems (ICUAS 2015)*, June 9-12, 2015, Denver, Colorado, USA.

(6) Zhixiang Liu, Youmin Zhang, Chi Yuan, & Jun Luo (2015). An adaptive linear parameter varying fault tolerant control scheme for unmanned surface vehicle steering control. *The 34th Chinese Control Conference and SICE Annual Conference (CCC&SICE 2015)*, July 28 - 30, 2015, Hangzhou, Jiangsu, China.

(7) Zhixiang Liu, Chi Yuan, & Youmin Zhang (2015). Linear parameter varying adaptive control of an unmanned surface vehicle. *The 10th IFAC Conference on Manoeuvring and Control of Marine Craft (MCMC 2015)*, August 22-26, 2015, Copenhagen, Denmark.

(8) Zhixiang Liu, Youmin Zhang, & Chi Yuan (2015). Active fault tolerant control of an unmanned surface vehicle. *The 15th International Conference on Control, Automation and Systems (ICCAS 2015)*, October 13-16, 2015, Busan, Korea.

(9) Zhixiang Liu, Youmin Zhang, & Chi Yuan (2015). A survey of recent developments and challenges on unmanned surface vehicles. *The 2015 Unmanned Systems Canada Annual Conference*, November 3-5, 2015, Halifax, Canada.

(10) Zhixiang Liu, Chi Yuan, Youmin Zhang, & Jun Luo (2014). A learning-based fuzzy LQR control scheme for height control of an unmanned quadrotor helicopter. *The International Conference on Unmanned Aircraft Systems (ICUAS 2014)*, May 27-30, 2014, Orlando, FL, USA.

(11) Zhixiang Liu, Xiang Yu, Youmin Zhang, Chi Yuan, & Jun Luo (2014). Straight line following active disturbances attenuation control of an unmanned surface vehicle. *The International Conference on Intelligent Unmanned Systems (ICIUS 2014)*, September 29 - October 1, 2014, Montreal, Quebec, Canada.

(12) Chi Yuan, Zhixiang Liu, & Youmin Zhang (2016). Vison-based forest fire detection in aerial images for firefighting using UAVs. *The International Conference on Unmanned Aircraft Systems (ICUAS 2016)*, June 7-10, 2016, Arlington, VA, USA.

(13) Chi Yuan, Khaled A. Ghamry, Zhixiang Liu, & Youmin Zhang (2016). Unmanned aerial vehicle based forest fire monitoring and detection using image processing technique. *The IEEE Chinese Guidance, Navigation and Control Conference (CGNCC 2016)*, August 12-14, 2016, Nanjing, Jiangsu, China.

(14) Yiqun Dong, Zhixiang Liu, Bin Yu, & Youmin Zhang (2015). Application of model predictive control to position and height limitation of a quadrotor unmanned aerial vehicle. *The ASME 2015 International Design Engineering Technical Conferences & Computers and Information in Engineering Conference (IDETC/CIE 2015)*, August 2-5, 2015, Boston, Massachusetts, USA.

(15) Chi Yuan, Zhixiang Liu, & Youmin Zhang (2015). UAVs based forest fire detection and tracking using image processing techniques. *The International Conference on Unmanned Aircraft Systems (ICUAS 2015)*, June 9-12, 2015, Denver, Colorado, USA.

(16) Youmin Zhang, Didier Theilliol, Xiang Yu, Chi Yuan, & Zhixiang Liu (2015). New development and applications on sense & avoid, fault-tolerant & cooperative control of unmanned systems (Pre-conference Workshop Presentation). *The International Conference on Unmanned Aircraft Systems (ICUAS 2015)*, June 9-12, 2015, Denver, Colorado, USA.

(17) Chi Yuan, Youmin Zhang, & Zhixiang Liu (2014). Automatic vision-based forest fire detection technologies for unmanned aerial vehicles: A review. *The International Conference on Intelligent Unmanned Systems (ICIUS 2014)*, September 29 - October 1, 2014, Montreal, Quebec, Canada.

Contents

List of Figures

List of Tables

Nomenclature and Acronyms

Nomenclature

A	State transition matrix
A_m	State transition matrix of reference model
B	Control input matrix
B_m	Control input matrix of reference model
C	Output matrix
C_m	Output matrix of reference model
D	Distance between the centre of mass and the control point
x	Position along the X coordinate of earth reference frame
y	Position along the Y coordinate of earth reference frame
v	Forward velocity
$x(t)$	State vector of a system
$y(t)$	Output vector of a system
$u(t)$	Control inputs
ω	Angular velocity of heading angle
d_f^d	Desired distance with respect to forward direction
d_l^d	Desired distance with respect to lateral direction
e_f	Forward distance error between the actual and desired values
e_l	Lateral distance error between the actual and desired values
α	Angle of attack

β	Sideslip angle
θ	Pitch angle
ϕ	Roll angle
ψ	Yaw angle
p	Roll rate
q	Pitch rate
r	Yaw rate
δ_e	Elevator deflection
δ_t	Throttle deflection
δ_a	Aileron deflection
δ_r	Rudder deflection
m	Mass of unmanned vehicle
χ_g	Unmanned vehicle's CG along the X coordinate of body-fixed frame
e	Cross-track error
ψ_e	Heading error
ψ_{SF}	Heading angle of virtual vessel
κ	Curvature of the desired path
$u_z(t)$	Total lift force
$u_\theta(t)$	Applied torque in θ direction
$u_\phi(t)$	Applied torque in ϕ direction
$u_\psi(t)$	Applied torque in ψ direction
$K_n(n = 1, ..., 6)$	Drag coefficients
$u_i(i = 1, ..., 4)$	Thrust of each rotor
L	Centre distance between the gravity of UQH and each propeller
C_m	Thrust-to-moment scaling factor
g	Acceleration of gravity
I_x	Moment of inertia along x direction

I_y	Moment of inertia along y direction
I_z	Moment of inertia along z direction
ω_m	Actuator bandwidth
K_m	A positive gain
$u_{ci}(i = 1, ..., 4)$	Pulse width modulation signals distributed to each rotor
$\boldsymbol{M}$	System inertia matrix (including added mass)
$\boldsymbol{M}_{RB}$	Rigid-body system inertia matrix
$\boldsymbol{M}_A$	Added mass
$\boldsymbol{C}(\boldsymbol{\nu})$	Coriolis and centripetal matrix (including added mass)
$\boldsymbol{C}_{RB}(\boldsymbol{\nu})$	Rigid-body Coriolis and centripetal matrix
$\boldsymbol{C}_A(\boldsymbol{\nu})$	Hydrodynamic Coriolis and centripetal matrix
$\boldsymbol{D}$	Linear damping matrix
$\boldsymbol{D}(\boldsymbol{\nu})$	Hydrodynamic damping matrix
$\boldsymbol{D}_n(\boldsymbol{\nu})$	Nonlinear damping matrix
$\boldsymbol{g}(\boldsymbol{\eta})$	Restoring forces and moments
$\boldsymbol{\tau}$	Control inputs acting on unmanned vehicle
$\boldsymbol{\tau}_u$	Control inputs (forces) in surge direction
$\boldsymbol{\tau}_v$	Control inputs (forces) in sway direction
$\boldsymbol{\tau}_r$	Control inputs (moments) in yaw direction
$\boldsymbol{\tau}_E$	Environmental disturbances (winds, waves and currents)
$Y_E O_E X_E$	The earth-fixed frame
$Y_B O_B X_B$	The ship body-fixed frame
$Y_{SF} O_{SF} X_{SF}$	The Serret-Frenet frame
X_{SF}	Tangent direction of the desired path at the origin of frame $\{Y_{SF}O_{SF}X_{SF}\}$
Y_{SF}	Normal direction of the desired path at the origin of frame $\{Y_{SF}O_{SF}X_{SF}\}$
X_B	Tangent direction of the desired path at the origin of frame $\{Y_B O_B X_B\}$
Y_B	Normal direction of the desired path at the origin of frame $\{Y_B O_B X_B\}$

Acronyms

AC   Adaptive Control

AFTC   Active Fault-Tolerant Control

AFTCS   Active Fault-Tolerant Control System

BRL   Bounded Real Lemma

CB   Center of Buoyancy

CG   Center of Gravity

DOFs   Degrees of Freedom

EKF   Extended Kalman Filter

FDD   Fault Detection and Diagnosis

FDI   Fault Detection and Isolation

FLC   Fuzzy Logic Control

FTC   Fault-Tolerant Control

FTFC   Fault-Tolerant Formation Control

FTTC   Fault-Tolerant Tracking Control

GNC   Guidance, Navigation, and Control

GPSs   Global Positioning Systems

GNSS   Global Navigation Satellite System

IFAC   International Federation of Automatic Control

IMUs   Inertial Measurement Units

LMI   Linear Matrix Inequality

LOS   Line-of-Sight

LPV   Linear Parameter Varying

LQ   Linear Quadratic

LQR   Linear Quadratic Regulator

MPC   Model Predictive Control

MRAC   Model Reference Adaptive Control

PFTCS	Passive Fault-Tolerant Control Systems
PI	Proportional-Integral
PID	Proportional-Integral-Derivative
PWM	Pulse Width Modulation
RC	Robust Control
SF	Serret-Frenet
SFST	State Feedback for State Tracking
SMC	Sliding Model Control
TI-ADCTC	Time-Invariant Adaptive Disturbance Compensating Tracking Controller
TV-ADCTC	Time-Varying Adaptive Disturbance Compensating Tracking Controller
UAVs	Unmanned Aerial Vehicles
UGVs	Unmanned Ground Vehicles
UQH	Unmanned Quadrotor Helicopter
USCs	Unmanned Space-Crafts
USGES	Uniform Semi-Global Exponential Stability
USVs	Unmanned Surface Vehicles
UUVs	Unmanned Underwater Vehicles
UVs	Unmanned Vehicles

Chapter 1

Introduction

1.1 Background

1.1.1 Unmanned Vehicles

Unmanned vehicles (UVs) including unmanned aerial vehicles (UAVs), unmanned ground vehicles (UGVs), unmanned surface vehicles (USVs), unmanned space-crafts (USCs), and unmanned underwater vehicles (UUVs). They possess self-governing characteristics and are capable of performing assigned missions without human intervention.

In the past decades, numerous commercial entities, universities, research institutes, and military around the world have widely employed UVs in their applications [1, 3]. These applications cover a variety of specific fields, such as environmental monitoring and surveillance [4, 5], platforms for testing and validating the newly developed algorithms [6, 7], post-disaster search and rescue [8], cooperative and formation control [9, 10], goods delivery and in-flight refueling [11–13], as well as various military missions [14].

However, the current development of UVs is still in the early stage. Most existing UVs are confined to experimental platforms, comprised primarily of relatively small-scale UVs with limited autonomy, endurance, payloads, power outputs, as well as remote operation requirements. UVs remain scarce in commercial markets as well, and the majority of industrial-level vehicles are still
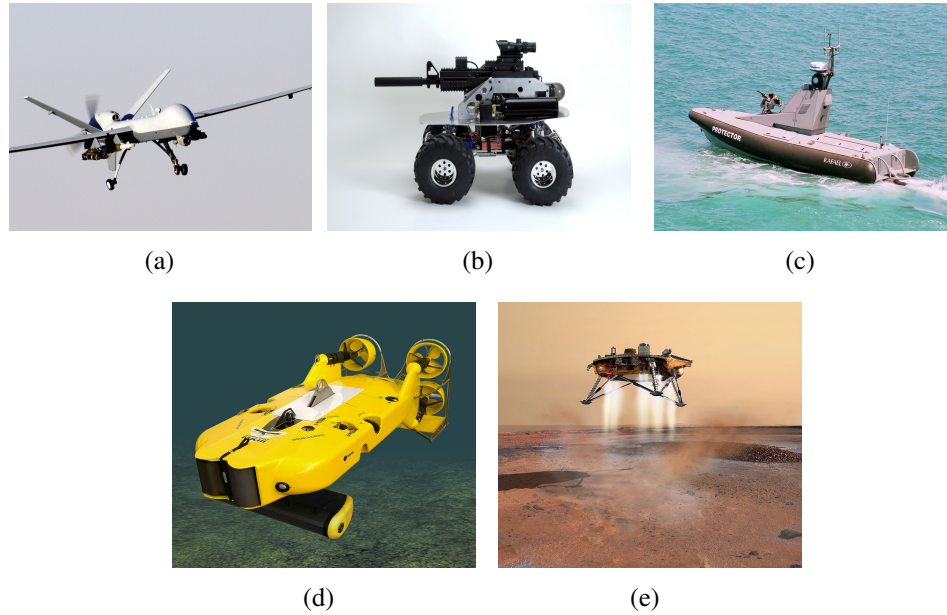
Figure 1.1: Several types of UVs, UAV (a), UGV (b), USV (c), UUV (d), USC (e).

used within military and research fields.

1.1.2 State-of-the-Art Unmanned Vehicles

1.1.2.1 Elements of Unmanned Vehicles

Depending on practical applications, UVs may come into a variety of appearances and functionalities. However, the following basic elements that must be included in every UVs (taking the USV for example here, as seen in Fig. 1.2):

(1) *Hull and auxiliary structural elements*: The hulls of UVs are normally designed corresponding to the specific applications of UVs, revealing some basic design issues and trends in their development, such as greater endurance and payload capacity, convenient mounting and loading capabilities, easy to be manufactured or modified from manned vehicles, enhanced system stability, and decreased risk of crash.

(2) *Propulsion and power system*: Translational and rotational motion control of most existing UVs are provided by actuators, which are producers of forces and moments from the
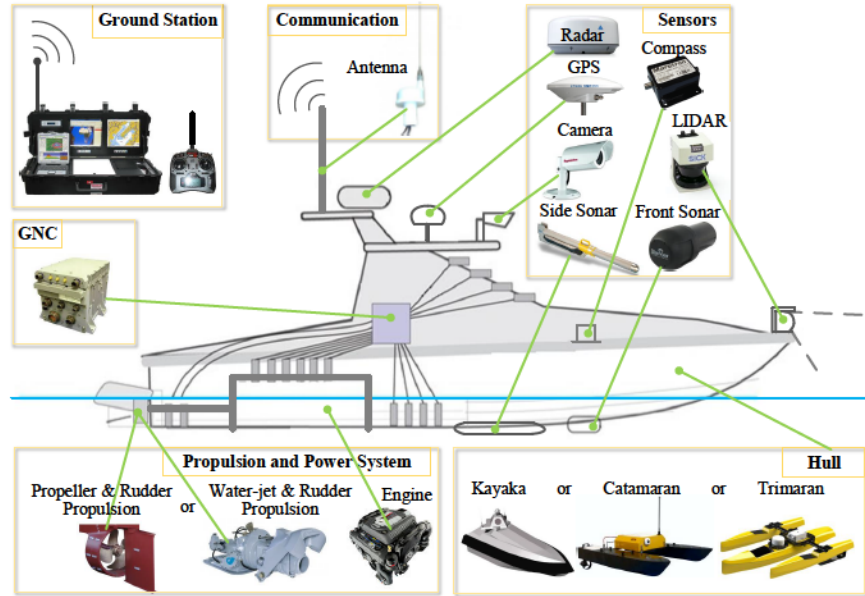
Figure 1.2: Fundamental architecture of a typical USV [1].

corresponding commands of controller.

(3) *Guidance, navigation, and control (GNC) systems*: As the most vital component of a UV, GNC modules generally consist of onboard computers and software, which together are responsible for managing the entire UV system.

(4) *Communication systems*: Communication systems include not only wireless communication with ground control stations and other vehicles to perform cooperative control, but also onboard wired/wireless communication with a variety of sensors, actuators, and other equipment. The reliability of communication systems is thereby of paramount importance.

(5) *Data collection equipment*: Together with the above-mentioned components, inertial measurement units (IMUs) and global positioning systems (GPSs) as the basic sensors are typically used in combination with the system to guarantee the UV remains in good operating condition, and to improve its performance. Besides, cameras, radar, sonar, as well as other kinds of sensors are optionally adopted, depending on the specific task at hand, such as monitoring and operating UVs under all different conditions (i.e. cabin temperature and humidity, electronic equipment health, fuel consumption, etc.) [15].

3
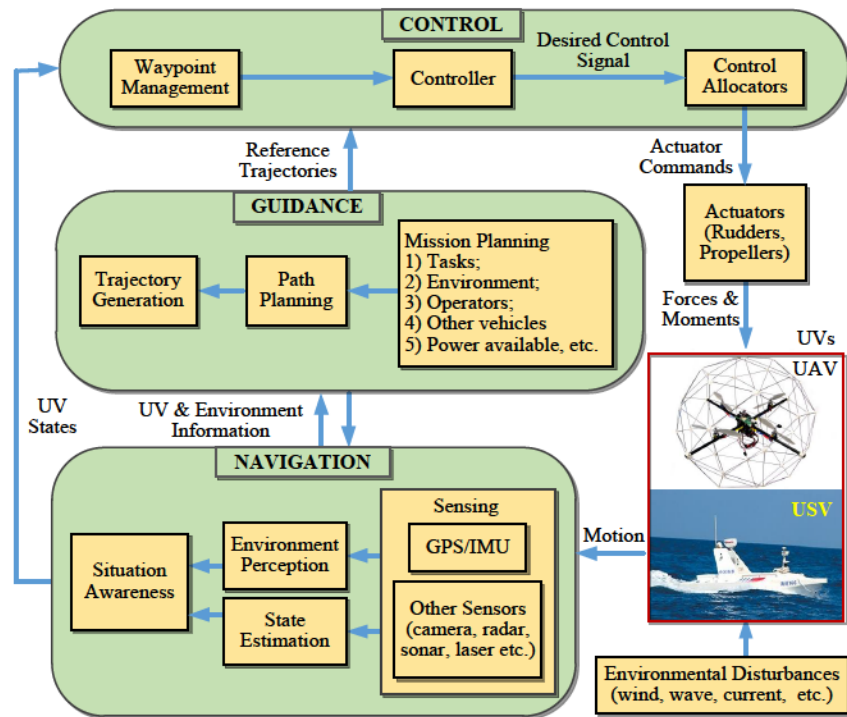
Figure 1.3: General structure of UVs guidance, navigation, and control systems [1].

(6) *Ground station*: Ground station also plays an important role in UVs' GNC systems, which can be located in a fixed facility or a mobile vehicle. In general, missions are assigned to UVs via wireless communication systems. The real-time status of UVs and their onboard equipments are all monitored by the ground station, while for remotely operated UVs, control commands are also sent from ground station.

1.1.2.2 Relationships among Guidance, Navigation and Control Subsystems

As indicated in Fig. 1.3, the fundamental elements for autonomously operating UVs generally constitute *guidance, navigation*, and *control* subsystems. These subsystems work in interaction with each other, to the point where imperfections in one subsystem may degrade the performance of the whole system.

(1) *Guidance system* is responsible for generating and updating feasible and optimal trajectory commands to the control system according to the information provided by the navigation system, assigned missions, vehicle capability, and environmental conditions.
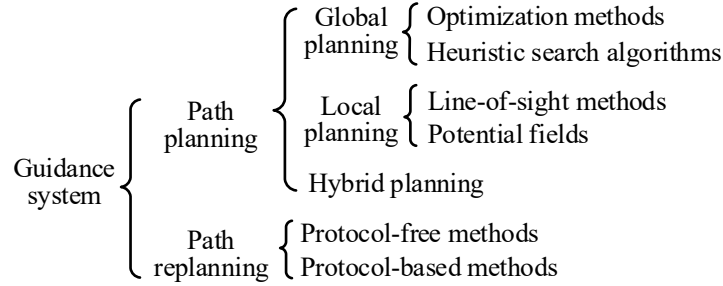
Figure 1.4: Classification of UV guidance systems [1].
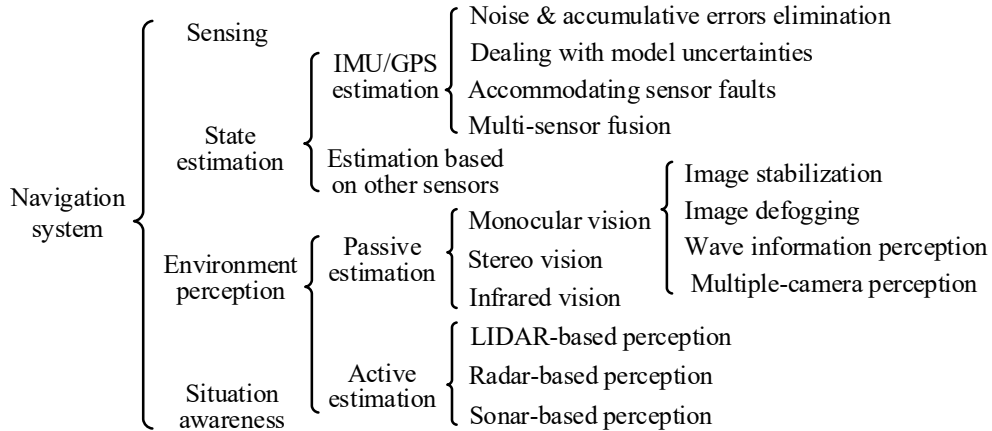
Figure 1.5: Classification of UV navigation systems [1].

(2) *Navigation system* concentrates on identifying the UVs' current and future states (such as position, orientation, velocity, and acceleration), and its surrounding environment based on the past and current states of the UV as well as environmental information (such as the ocean currents and wind speed) obtained from its onboard sensors.

(3) *Control system* focuses on determining the proper control forces and moments to be generated in conjunction with instruction provided by the guidance and navigation systems, while at the same time satisfying desired control objectives.

In order to provide readers a better understanding of the current work on GNC system of UVs, Figs. 1.4, 1.5, and 1.6 have summarized the overviews of the existing research in UVs' *guidance*, *navigation*, and *control* subsystems, respectively.

Control system
- Control objectives
  - Set-point regulation
  - Trajectory tracking
  - Path following
  - Path maneuvering
- Practical problems
  - Disturbance
    - Current
    - Wave
    - Wind
  - Uncertainty
    - Unmodelled dynamics
    - Parameter uncertainty
  - Underactuation
  - Constraints
    - Actuator
    - State/Output
  - Faults
    - Actuator malfunctions
    - Sensor faults
    - Communication faults
  - Validation
    - Simulation
    - Experiments

Figure 1.6: Classification of UV control systems [1].

1.2 Problem Formulation

The deployment of UVs is generally in cluttered, sophisticated, and even hostile environment [16], and subject to environmental disturbances, sideslip effects, actuator faults, collisions, etc. More specifically, the motion of UVs is affected by not only environmental disturbances (winds, waves, and currents) and steering motion caused sideslip effects, but also actuator faults due to numerous factors, such as propeller and rudder damage and deformation, gear and transmission system wear and deformation, shaft deformation, and lower power supply [17–19]. These negative impacts may seriously degrade the overall system performance and even lead to catastrophic consequences (collision or crash). The development of reliable and safe motion control systems of UVs is thereby of critical importance.

1.2.1 Actuator Faults, Failures, and Malfunctions

Although the system faults and failures have been explicitly studied and widely distributed over various technological areas including industrial and academic communities and much effort

has also been dedicated to their standardization, the terminology use is still not unique. According to the international federation of automatic control (IFAC)-Technical Committee SAFEPROCESS and related literatures, the following terminologies are defined and used in this thesis [20].

- *Fault*: A fault means an unpermitted deviation of the system's characteristic features from the acceptable and normally healthy condition.

- *Failure*: A failure indicates that an interruption occurs in system and it permanently loses its ability to perform a desired function under specific operating conditions.

- *Malfunction*: A malfunction is an intermittent and irregular execution of a system's required function.

Obviously, the failure is more severe than the fault. For example, in the occurrence of fault, the actuator may operate with slower response and reduced effectiveness but still be practicable. However, a failure in actuator means total loss of its control effectiveness, additional actuators are then required to compensate the associated adverse impact.

1.2.2 Fault-Tolerant Control

Some specific applications, such as fire fighting, special military missions, tasks in extreme weather conditions or natural disasters or cluttered mountainous regions, and particular military missions, may bring UVs into sophisticated and hazardous environments. Furthermore, as a kind of consumable hardware, numerous UVs' low development cost may decrease their reliability and safety as well. These situations may seriously threaten the reliability and safety of UVs. Taking UAVs as example, according to a Washington Post's investigation, in USA, more than 400 military UAVs have crashed since 2001, while commercial UAV failure events are expected to be far more than that experienced in the military [21]. These crashes have seriously affected the safety of homes, farms, airports, and forests, and resulted in tremendous loss of property. A great majority of these accidents, however, is reported to be actuator faults/failures caused.

As a vital element of UVs operation, actuators may fail to operate due to a variety of malfunctions, such as wear and tear of the gear, motor failure, mechanical deformation, control surface damage, and battery drainage. The presence of actuator faults/failures increases reliability and safety demands of UVs which are beyond what the traditional control methods can offer, meanwhile the faulty actuators may deteriorate the system performance and even cause catastrophic results (crash). In addition, slow compensation of actuator faults may likewise bring UVs into a hazardous situation. The primacy among these challenges is thereby how to design a fault-tolerant control (FTC) law [22] for UVs in the event of actuators, sensors and system components faults/failures. Fortunately, recent years, the growing demand for the reliability and safety in engineering systems can provide significant references to the FTC design for UVs [3, 20, 23–29].

In a fault-tolerant control system (FTCS), the achievable and acceptable system performance mainly depends on the availability of redundancy and capability of actuators in the control system as well as the design methodologies adopted in the synthesis of fault-tolerant controllers. Their predominant objectives are to preserve the stability of the overall system and to maintain a satisfactory level of performance in the presence of system component malfunctions. Current FTCSs are generally classified into two categories, namely, active and passive FTCSs [22, 30]. A commonality in both approaches is the utilization of system redundancies, while their primary difference is how the redundancy is used.

The design philosophy of active FTCS is to adapt to system component malfunctions (including actuators, sensors, and system itself) by reconfiguring the controller according to the real-time detected faults information from a fault detection and diagnosis (FDD) mechanism. A typical active FTCS consists of a FDD scheme, a reconfigurable controller, and a control reconfiguration mechanism. On the other hand, in a passive FTCS design, a list of potential faults is assumed to be a *priori* known at the design stage and controller is designed by considering the possible faults during the design stage. This indicates that no additional fault compensating actions are needed by the existing control system in response to the event of faults. Neither the FDD scheme nor control reconfiguration mechanism is required in passive FTCSs..

Since neither fault detection and diagnosis (FDD) schemes nor controller reconfiguration mechanisms are required in passive FTC approach, the fault-tolerant property is achieved primarily attributes to the controller's robustness to a wide operation range of a specific system. A fuzzy proportional-integral-derivative (PID) based FTC method is developed in [31] for compensating the loss of control effectiveness in all motors and a single motor, respectively. [32] introduces an augmented sliding mode control (SMC) approach to further enhance the robustness of traditional SMC and make it capable of dealing with both fault-free and faulty systems. This proposed method is experimentally validated with loss of 15% control effectiveness in one single actuator of the unmanned quadrotor helicopter (UQH). In [33], a learning-based FTC scheme is developed with online self-tuning of control gains capabilities, this is expected to ensure an acceptable performance of UQH in either the absence or presence of actuator faults. In [34], employing its adaptive and self-tuning capabilities to system parameters variations, the model reference adaptive control (MRAC) method is used for tolerating the actuator failure of UQH. Another interesting application is conducted in [35], the robust feedback linearization control approach is developed for the stabilization of UQH along the vertical axis, sacrificing the controllability of the yaw state when one of the actuators' control effectiveness is totally lost.

In terms of the active FTC approach, based on the estimates of actuator faults from FDD module, it actively responds to system components failures via reconfiguring control actions so that the stability and acceptable performance of the entire system can be guaranteed; and much previous work has been carried out as well. In [36], feedback linearization techniques are adopted in the double-layer FTC architecture with inner and outer loops, while the fault information is supposed to be available from a fault detection and isolation (FDI) module. [37] presents a FTC method with a fault recovery mechanism employing an adaptive feedback linearization methodology. A parameter estimation algorithm is also introduced to estimate the loss of control effectiveness fault. A FTC methodology combining an integral action with the conventional SMC is proposed in [32] to effectively compensate the adverse effects of actuator faults. In [34, 38], the gain-scheduled (GS)

technique is utilized to parametrize the PID parameters as functions of the GS variable including a group of control gains calculated in offline for both normal and faulty situations, an online switching among different PID gains is then conducted based on the result of FDD, but no FDD mechanism design is addressed in these papers. As an alternative and promising FTC approach, the control allocation (CA) technique is adopted in [39], and the partial loss of control effectiveness in actuators is considered. Recently, [40] presents a FTC design approach using the linear parameter varying (LPV) control technique. Moreover, model predictive control (MPC) technique is likewise adopted to appropriately compensate the side effects of actuator faults, where the fault parameters are obtained employing a moving horizon estimator (MHE) [41].

1.2.3 Actuator Saturation

In addition to FTC, as another critical and practical issue, actuator dynamics such as amplitude and rate constraints and time delays should be also taken into consideration in the control strategy design in order to prevent actuator saturation and unacceptable system performance degradation. Particularly in the case of actuator faults compensation, increasing control efforts demands may cause the remaining healthy actuators to work beyond their normal duty, and eventually lead to the violation of their amplitude/rate limits and system uncontrollability. Furthermore, actuator dynamics cannot be prompt enough to be negligible in practice, aggressive actuator actions may cause excessive wear and tear of actuators, actuator saturation, and even the probability of further damage. As reported in the existing literatures, two types of techniques are adopted in the FTC scheme design with integration of actuator limits. One type is to consider actuator dynamics at the design stage of the FTC strategy preventing actuators from exceeding their limits [42, 43]; while the other one suggests a system command adjustment mechanism for actuator saturation prevention with an acceptable performance degradation [44–47].

1.2.4 Environmental Disturbances

Applications employing UVs are inevitably influenced by environmental disturbances, such as winds, waves, and currents, while the small-scale UVs in particular are more sensitive to environmental disturbances owing to their low inertia and small size. Disturbances produce a pressure variation on the hull surface, which in turn induce forces and moments. An accurate description of environmental disturbances is not only significant in UVs simulators that are developed for human operators, but also critical for improving the performance of UVs' GNC systems.

One of the most significant challenges in path following of USV is to accurately reject the time-varying environmental disturbances. For example, the failure of disturbance rejection may deteriorate system performance or even lead to catastrophic accidents. Especially, in the application of environmental monitoring and seabed exploration, it is challenging to steer USV to follow the desired path within an acceptable bound of cross-track errors. Therefore, it is significant to take into account of the time-varying disturbances attenuation in USV's controller design.

In view of path following of UVs under environmental disturbances, great efforts have been devoted. Adaptive control is used for straight line following in [48], but only the constant ocean current is considered. In addition, a backstepping control scheme that forces a USV to follow a reference path under disturbances is reported in [49]. In [50], a nonlinear robust adaptive control strategy is designed to steer an underactuated ship to follow a planned path in the presence of environmental disturbances. Lyapunov's direct, backstepping, and parameter projection methods are employed in the controller design procedure. It is worth mentioning that, in [51], path following of a USV is achieved using the state feedback linearization.

With respect to the time-varying disturbances, some control strategies have been proposed accordingly. In [52], unknown time-varying environmental disturbances are accounted for trajectory tracking control of a USV. An observer is constructed to provide the estimation of unknown disturbances, and a backstepping controller is developed to track the desired path. Backstepping and Lyapunov synthesis methods are utilized to reject time-varying disturbances during the course of trajectory tracking in [53]. In [54], a linear algebra approach originated from a robotic system is

applied for a USV to follow a desirable path under the time-varying disturbances. In [55], a controller named as disturbance compensating model predictive control (DC-MPC) is presented with consideration of environmental disturbances and system constraints. The time-invariant disturbances are estimated by an observer and compensated by solving a low-dimensional optimization problem, whereas it may not be appropriate in the presence of time-varying disturbances. Moreover, the identical limits for the nominal, additional, and their incorporated (the ultimate control input) control inputs may cause the additional compensating mechanism becomes infeasible when the nominal control input saturates. Unfortunately, to the best of the author's knowledge, the constraints of system states and actuators are not considered in most of the open literatures of USVs. Furthermore, most of the existing controllers with fixed control gains are often robust to large variations in the system or external disturbances by sacrificing their control performance, while others can only guarantee the control performance under small scale disturbances.

1.2.5 Reliability and Safety of Unmanned Vehicles

Reliability and safety play a vital role in the overall functioning of elements, components, and systems. Reliability is the ability of a system to perform an assigned mission with a satisfactory performance under distinct environmental conditions, within an acceptable range, and during a specific period of time. Whereas safety is defined as the capability of a system not to threaten the normal functionality of persons, facilities and environment in vicinity.

However, an improvement of system safety may somewhat cause a deterioration of the system reliability if, for instance, the increase of components number. In order to guarantee the satisfactory performance of system and the successful implementation of assigned missions, several approaches presented in this thesis exactly deal with the reliability and safety issues of UVs.

1.2.6 Path Following Schemes

Due to the high dependence on the reference model and sophisticated control laws of the trajectory tracking methods, researchers in control community have studied the path following problem,

which is proved to be quite suitable for practical implementation. Currently, two types of path following approaches are well designed and commonly implemented in practice, namely the Serret-Frenet (SF) frame based path following method and line-of-sight (LOS) path following method.

1.2.6.1 Serret-Frenet Frame Based Path Following

As a commonly adopted path following strategy for UVs, SF frame based path following scheme is defined as projecting the position of an actual vehicle onto the desired geometrical path, effectively guaranteeing that an imagined and virtual target vehicle exists on the closest position of the path to the real UV during the entire mission [56]. The associated kinematics of UV, which are the path tangential frame at the exact point of projection, are yielded with respect to the SF frame. Then, the path following problem is solved by employing the SF error dynamics.

Numerous relative research works have been conducted. In [57], a fourth-order ship model is used in SF frame for developing a control strategy to track both a straight line and a circle in the presence of constant ocean current. To properly compensate the cross-track and heading errors, two different control methods are studied, namely the back-stepping control approach which relies on a feedback dominance scheme [58] and the model predictive control (MPC) approach with a disturbance compensating mechanism [55]. An alternative way of treating SF frame based path following problem is proposed in [59], the mathematical model of the ship is first written in the SF frame. A nonlinear controller is then synthesised by employing the Lyapunov's direct method and backstepping technique. [60] introduces a Lyapunov-based guidance law which can make the path following error coordinates converge to zero. Moreover, the SF frame based path following problems are also well studied in [61–63].

1.2.6.2 Line-of-Sight Path Following

Another popular and effective way to follow the predefined path independent of temporal constraint (path following application [64]) is to implement a lookahead distance based LOS guidance rule [65], mimicking the actions of experienced helmsman. Based on the geometry of UVs, this

13

guidance system generates a reference trajectory for the heading angles, which are then fed into the control system to follow. Numerous applications using LOS guidance are carried out [66–68], the uniform semi-global exponential stability (USGES) of LOS guidance law is also proved in [69]. Despite they are effective and easy-to-use, the classical proportional LOS guidance methods still own the drawbacks of being susceptible to environmental disturbances, since they are designed assuming that there are no external disturbances acting on vehicles.

But in reality, there normally exist ocean currents that are caused by the gravity, Coriolis force, wind friction, water density variation, heat exchange at the sea surface, as well as salinity changes. The adverse effects of currents along with the USV's turning induced lateral acceleration can result in the so-called sideslip angle, which may cause the USV exhibits large cross-track errors during either curved or straight line path following applications [70]. However, this disadvantage may not be perfectly overcome by solely developing an effective heading angle tracking controller, since the negative impacts primarily originate from the heading reference generator. The solution suggested in the existing literatures is to include an integral term in the LOS guidance law. This new guidance law is then referred to as a proportional-integral (PI) type of LOS guidance law (the relative applications can be found in [71–74]). These LOS guidance laws, to some extent, are effective to the sideslip angle compensating with a specific range. Recently, an adaptive LOS guidance law [70,75] capable of further improving the performance of sideslip angle compensating with extended range is proposed, whereas the sideslip angle is required online.

The most straightforward and effective way of measuring the sideslip angle is usually deemed to use onboard sensors including optical correlation sensors, accelerometers, and global navigation satellite system (GNSS). But the optical correlation sensors are usually pricey, while the accelerometer measurements and GNSS tend to be noisy and cause large accumulated errors during long-term operations due to their bias. Although the information of ocean currents is crucial for estimating sideslip angle and improving path following performance, it is often difficult, expensive, and time-consuming to measure ocean currents from a moving USV. Furthermore, as a powerful equipment to acquire the estimations of current velocities, electromagnetic current meters and

14

acoustic Doppler current profilers are nowadays widely installed on ships [76, 77], whereas space constraints of USV also limit the number and size of onboard equipments [74].

In order to tackle the abovementioned problems, observer-based sideslip angle estimation approaches are then extensively studied in the literature [78–80]. Later on, sideslip angle estimation and compensating are both considered in [70, 75] to adjust the desired heading angles before feeding them to the control system so that the control system can follow the anticipated trajectory with significantly reduced path deviation.

1.3   Ojectives of This Thesis

This thesis aims to design and develop reliable and safe motion control schemes with application to unmanned vehicles at both individual unmanned vehicle and a group of unmanned vehicles levels. Particularly, this thesis is organized based on the following research objectives:

- Designing and developing effective path following methodologies that can counteract the adverse effects from sideslip angle and environmental disturbances, while successfully operate the unmanned vehicles to follow the desired path.

- Designing and developing a passive fault-tolerant control method without an explicit model.

- Designing and developing fault detection and diagnosis schemes and active fault-tolerant control approaches based on accurate system models for improving the reliability of unmanned vehicles.

- Designing and developing an effective time-varying control strategy for the operation of unmanned vehicles under different working conditions.

- Designing and developing a formation control scheme for the operation of a group of unmanned vehicles simultaneously considering actuator faults, actuator saturation, and collision avoidance in order to enhance the reliability and safety of the entire formation.

To sum up, the conducted research works in this thesis are primarily expected to synthesize advanced levels of path following, disturbance estimation and compensation, fault detection and diagnosis, fault-tolerant control, actuator saturation prevention, and collision avoidance capabilities in unmanned vehicles, these in turn can guarantee the satisfactory, reliable, and safe performance at both individual and multiple unmanned vehicles levels. Finally, the proposed schemes and strategies are verified by a series of simulations on well-known unmanned vehicles models and experimental tests in the presence of environmental disturbances, different realistic fault scenarios, actuator saturation, and obstacles.

1.4 Contributions of This Thesis

The main contribution of this thesis can be categorized into the following four major aspects:

(1) *Reliable and safe path following*

(a) Design of an adaptive sideslip angle estimating and compensating based LOS path following scheme for USV.

(b) Design of a SF frame based path following method for USV with consideration of environmental disturbances and actuator dynamics.

(2) *Reliable and safe control of single unmanned vehicle*

(a) Desgin of a learning-based fault-tolerant tracking control (FTTC) approach for the unmanned quadrotor helicopter under disturbances, uncertainties, and actuator faults.

(b) Design of an adaptive fault estimation and FTTC law for unmanned quadrotor helicopter, while considering actuator dynamics.

(c) Design of a PI type of adaptive FTTC law for USV.

(d) Design of a linear parameter varying (LPV) based parameter estimation law and a LPV-based FTC law for the operation of USV with actuator faults and payload variations.

16

(3) *Reliable and safe formation control multiple unmanned vehicles*

    (a) Design of a PI type of leader-follower formation control scheme for a group of UAVs.

    (b) Simultaneous consideration of FTC, actuator saturation, and collision avoidance in the UAVs formation control.

(4) *USV experimental platform development*

    (a) Development and system integration of USV and control system.

    (b) System identification of USV's actuators.

1.5 Organization of This Thesis

The rest of this thesis is organized as follows:

- Chapter 2 provides an overview of some preliminary knowledges used in the thesis.

- Chapter 3 addresses the problem of reliable and safe path following of UVs. Two types of path following schemes are studied, namely the SF frame based path following method and LOS path following method. In the SF frame based path following method, both environmental disturbances and actuator saturation are considered. Whereas inertia and currents caused sideslip angle is detailedly studied in the LOS path following scheme design.

- Chapter 4 introduces the issues of reliable and safe control of UVs. Several FTC approaches are designed, from passive FTC method to active FTC method. A learning-based fault-tolerant tracking controller is devised for learning and compensating the negative effects of actuator faults. Then, an adaptive FTTC method is proposed considering actuator saturation. For the variations of UVs' working conditions, a LPV control technique is also employed for estimating the amplitude of actuator faults and mitigating their side effects.

- Chapter 5 illustrates the formation control of multiple UAVs. A leader-follower formation control methodology is designed, and FTC and collision avoidance problems are simultaneously taken into account as well.

- Chapter 6 presents conclusions of the conducted research works and important findings, and summarizes several predominant ideas for the future developments of the thesis's outcomes.

Chapter 2

Preliminaries

2.1 Modelling of Unmanned Vehicles

In this thesis, two types of unmanned vehicles are mainly studied; one is unmanned aerial vehicle (UAV), the other one is unmanned surface vehicle (USV). Their corresponding motion models and associated guidance, navigation, and control (GNC) issues are discussed in the subsequent sections of this chapter.

2.1.1 Unmanned Surface Vehicle

Roughly two-thirds of the earth is covered by oceans [1], but comparatively little of these areas have been thoroughly explored. Climate change, environmental abnormalities, personnel requirements, and national security issues have all led to a strong demand from commercial, scientific, and military communities for the development of innovative unmanned surface vehicles (USVs), also known as autonomous surface vehicles (ASVs) or autonomous surface crafts (ASCs). Despite this, only semi-autonomous USVs have normally been used rather than fully-autonomous USVs, owing to numerous challenges facing by the latter, such as limited autonomy due to the challenges in automated and reliable GNC functions for all different operating conditions in face of sophisticated and hazardous environments, and sensor, actuator and communication failures. Further

development of fully-autonomous USVs is required in order to minimize both the needs for human control and the safe and reliable operation of USVs [81].

USVs can be defined as unmanned vehicles which perform tasks in a variety of cluttered environments without any human intervention, and essentially exhibit highly nonlinear dynamics [82]. Further development of USVs are expected to produce tremendous benefits, such as lower development and operation costs, improved personnel safety and security, extended operational range (reliability) and precision, greater autonomy, as well as increased flexibility in sophisticated environments, including so-called dirty, dull, harsh, and dangerous missions [15, 82].

With the aid of more effective, compact, commercially available and affordable navigation equipment, including global positioning systems (GPSs) and inertial measurement units (IMUs), as well as more powerful and reliable wireless communication systems, greater opportunities have been provided for USVs and their applications than ever before. USVs can be developed for a wide range of potential applications (as listed in Table 2.1) in a cost-effective way.

Table 2.1: Potential applications of USVs [1]

Types	Specific Applications
Scientific research	Bathymetric survey [15]; ocean biological phenomena, and migration and changes in major ecosystems [83]; ocean activities research; multi-vehicle cooperation (cooperative work among aerial, ground, water surface or underwater vehicles) [84, 85]; as experimental platforms for the purpose of testing hull designs, communication and sensor equipments, propulsion and operating systems, as well as control schemes [82].
Environmental missions	Environmental monitoring, samplings, and assessment [86]; disaster (like tsunami, hurricane, eruption of submarine volcano) aided prediction and management, and emergency response [87]; pollution measurements and clean-up.
Ocean resource	Oil, gas and mine explorations [15]; offshore platform/pipeline construction and maintenance [88].
exploration Military uses	Port, harbor, and coastal surveillance, reconnaissance and patrolling [89–91]; search and rescue [15, 87]; anti-terrorism/force protection [81]; mine countermeasures; remote weapons platform [92]; target drone boats [15].
Other applications	Transportation [93]; mobile communication relays [94]; refueling platform for USVs, unmanned aerial vehicles (UAVs), unmanned underwater vehicles (UUVs), and other manned vehicles.

USVs are always in competition with other manned or unmanned systems in terms of some specific applications [95]. Table 2.2 provides a brief comparison of these systems, and the following advantages of USVs can be identified: 1) USVs can perform longer and more hazardous missions than manned vehicles; 2) Maintenance costs are lower and personnel safety is far greater since no
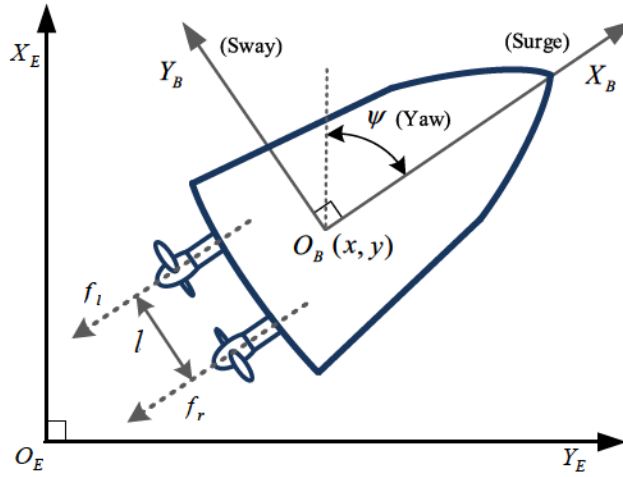
Figure 2.1: Illustration of USV moving in the horizontal plane.

crew is onboard; 3) The low weight and compact dimensions of USVs give them enhanced maneuverability and deployability in shallow waters (riverine and coastal areas) where larger craft cannot operate effectively; 4) USVs also have greater potential payload capacity and are able to perform deeper water depth monitoring and sampling compared to other aircraft/UAVs and spacecraft.

Table 2.2: Performance comparison of USVs and other vehicles [1]

● Clear advantage of USVs   ◐ Near parity   ○ Clear disadvantage of USVs

Attributes	UUVs	Float Platforms	Satellites	Manned Ships	UAVs	Manned Aircrafts
Endurance	●	○	○	◐	●	●
Payload capacity	●	◐	●	◐	●	◐
Cost	◐	○	●	◐	●	◐
Maneuverability	●	●	●	●	○	●
Deployability	●	●	●	●	○	●
Water depth measurement	○	◐	●	◐	●	◐
Autonomy requirement	◐	●	●	●	◐	●

2.1.1.1 Kinematics of Unmanned Surface Vehicle

A system model that describes its dynamics is essential to the controller design. The kinematics and kinetics of USV are addressed in the following. With respect to USV control, there is no

Table 2.3: Nomenclature of USV parameters

Symbols	Explanation
M	System inertia matrix (including added mass)
M_{RB}	Rigid-body system inertia matrix
M_A	Added mass
$C(\nu)$	Coriolis and centripetal matrix (including added mass)
$C_{RB}(\nu)$	Rigid-body Coriolis and centripetal matrix
$C_A(\nu)$	Hydrodynamic Coriolis and centripetal matrix
D	Linear damping matrix
$D(\nu)$	Hydrodynamic damping matrix
$D_n(\nu)$	Nonlinear damping matrix
$g(\eta)$	Restoring forces and moments due to gravitation/buoyancy
τ	Control inputs acting on USV $\tau = [\tau_u, \tau_v, \tau_r]^T$ is for fully-actuated USV, while $\tau = [\tau_u, 0, \tau_r]^T$ is for underactuated USV
τ_u	Control inputs (forces) in surge direction
τ_v	Control inputs (forces) in sway direction
τ_r	Control inputs (moments) in yaw direction
τ_E	Environmental disturbances (winds, waves and currents)
m	Mass of USV
I_z	USV inertia about the Z axis of body-fixed frame
χ_g	USV CG along the X coordinate of body-fixed frame

requirement for the consideration of either passenger comfort or cargo stability. Its primary purpose is merely to ensure the USV follows the desired path as accurately as possible. Based on this characteristic, the general six-DOF model can be reduced to only consider the position and orientation of USV, a standard three degrees of freedom (DOF) model is often employed to describe the planar motion of USV (shown in Fig. 2.1). This model only involves the motion of surge, sway, and yaw velocities v_x, v_y, and r, while the dynamics related to heave, roll, and pitch velocities v_z, p, and q are normally neglected.

The typical USV's kinematics model [96] in planar motion and without the presence of disturbances can then be expressed as:

$$
\begin{bmatrix} \dot{x} \\ \dot{y} \\ \dot{\psi} \end{bmatrix} = \begin{bmatrix} \cos\psi & -\sin\psi & 0 \\ \sin\psi & \cos\psi & 0 \\ 0 & 0 & 1 \end{bmatrix} \begin{bmatrix} v_x \\ v_y \\ r \end{bmatrix}, \tag{1}
$$

where (x, y) denotes the earth-fixed position of the center of mass of USV.

2.1.1.2 Kinetics of Unmanned Surface Vehicle

In addition to kinematics, USV's kinetics, which are the analysis of forces acting on the motion of USV, have also been extensively studied. The reason for this is their crucial importance for advanced controller design [97], as well as the fact that kinematics model on their own are not sufficient for USV motion modeling, particularly when USVs exhibit significant sideslip angle. For a more comprehensive history of USV dynamic model development, readers are encouraged to refer to [65, 96, 98]. The following model is the most widely used kinetics model in the ship motion control research community:

$$M\dot{\nu} + C(\nu)\nu + D(\nu)\nu + g(\eta) = \tau + \tau_E, \tag{2}$$

where the physical meanings of symbols in (2) are all outlined in Table 2.3, while the representation of each symbol is introduced as belows:

$$M = M_{RB} + M_A = \begin{bmatrix} m_{11} & 0 & 0 \\ 0 & m_{22} & m_{23} \\ 0 & m_{32} & m_{33} \end{bmatrix},$$

$$M_{RB} = \begin{bmatrix} m & 0 & 0 \\ 0 & m & m\chi_g \\ 0 & m\chi_g & I_z \end{bmatrix}, M_A = \begin{bmatrix} -X_{\dot{u}} & 0 & 0 \\ 0 & -Y_{\dot{v}} & -Y_{\dot{r}} \\ 0 & -N_{\dot{v}} & -N_{\dot{r}} \end{bmatrix},$$

$$D(\nu) = D + D_n(\nu) = \begin{bmatrix} d_{11}(u) & 0 & 0 \\ 0 & d_{22}(v,r) & d_{23}(v,r) \\ 0 & d_{32}(v,r) & d_{33}(v,r) \end{bmatrix}, D = \begin{bmatrix} -X_u & 0 & 0 \\ 0 & -Y_v & -Y_r \\ 0 & -N_v & -N_r \end{bmatrix},$$

$$D_n(\nu) = \begin{bmatrix} -X_{u|u|}|u| & 0 & 0 \\ 0 & -Y_{v|v|}|v| - Y_{r|v|}|r| & -Y_{|v|r}|v| - Y_{|r|r}|r| \\ 0 & -N_{v|v|}|v| - N_{r|v|}|r| & -N_{|v|r}|v| - N_{|r|r}|r| \end{bmatrix},$$

23

$$C(\nu) = C_{RB}(\nu) + C_A(\nu) = \begin{bmatrix} 0 & 0 & -m_{22}v - \frac{1}{2}(m_{23} + m_{32})r \\ 0 & 0 & m_{11}u \\ m_{22}v + \frac{1}{2}(m_{23} + m_{32})r & -m_{11}u & 0 \end{bmatrix},$$

$$C_A(\nu) = -\begin{bmatrix} 0 & 0 & -Y_{\dot{v}}v - \frac{1}{2}(Y_{\dot{r}} + N_{\dot{v}})r \\ 0 & 0 & X_{\dot{u}}u \\ Y_{\dot{v}}v + \frac{1}{2}(Y_{\dot{r}} + N_{\dot{v}})r & -X_{\dot{u}}u & 0 \end{bmatrix},$$

$$C_{RB}(\nu) = \begin{bmatrix} 0 & 0 & -m(\chi_g r + v) \\ 0 & 0 & mu \\ m(\chi_g r + v) & -mu & 0 \end{bmatrix}.$$

Other hydrodynamic coefficients (such as X_u, Y_v, Y_r, N_v, and N_r) can be referred to [97, 98]. $\eta = [x, y, \psi]^T$ denotes the vector of position and orientation with coordinates in the earth-fixed reference frame, $\nu = [v_x, v_y, r]^T$ denotes the vector of linear and angular velocity with coordinates in the body-fixed reference frame, $\eta = [x, \ y, \ \psi]^T$, $\nu = [u, \ v, \ r]^T$, and $\tau = [\tau_u, \ 0, \ \tau_r]^T$ with τ_u and τ_r being the surge force generated by the propeller, and yaw moment provided by the rudder, and $\tau_E = [\tau_{uE} \ \tau_{vE} \ \tau_{rE}]^T$ with τ_{uE}, τ_{vE} and τ_{rE} being the environmental disturbances (induced by waves, wind, and currents) respectively acting on the surge, sway, and yaw axes.

In order to better facilitate the control design, existing research assumes that:

(1) USVs are moving in a horizontal plane in the ideal fluid;

(2) USV masses are uniformly distributed;

(3) the body-fixed coordinate axis coincides with the center of gravity (CG);

(4) both the CG and the center of buoyancy (CB) point vertically along the Z-axis;

(5) USVs own the port-starboard symmetry; and

(6) surge and sway-yaw dynamics are essentially decoupled.

Based on these assumptions, a widely used dynamic model of USV can be obtained [98]:

$$\dot{v}_x = \frac{m_{22}}{m_{11}}v_y r - \frac{d_{11}}{m_{11}}v_x + \frac{1}{m_{11}}(\tau_u + \tau_{uE})$$

$$\dot{v}_y = -\frac{m_{11}}{m_{22}}v_x r - \frac{d_{22}}{m_{22}}(v_y + \tau_{vE}) \tag{3}$$

$$\dot{r} = \frac{m_{11} - m_{22}}{m_{33}}v_x v_y - \frac{d_{33}}{m_{33}}r + \frac{1}{m_{33}}(\tau_r + \tau_{rE}),$$

where the terms m_{11}, m_{22}, and m_{33} denote the ship inertia and added mass effects, while the parameters d_{11}, d_{22}, and d_{33} represent the hydrodynamic damping forces.
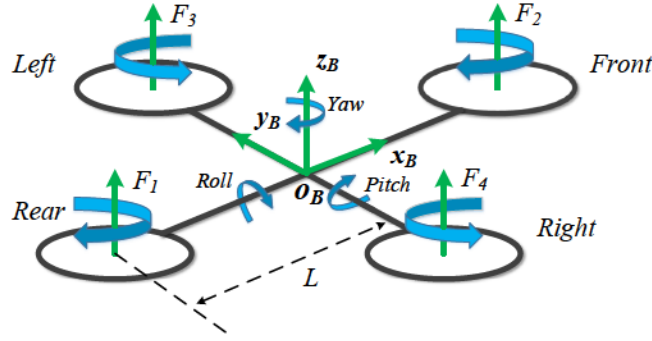
Figure 2.2: Illustration of a typical unmanned quadrotor helicopter.

2.1.2   Unmanned Aerial Vehicle

As illustrated in Fig. 2.2, the thrusts (u_1, u_2, u_3, u_4) are generated by four individual motor-driven propellers which are configured at the front, rear, left, and right corners, respectively. The front and rear motors spin clockwise, while the right and left motors spin counter-clockwise. The generated thrusts are always pointing upward in the z_B−direction. Therefore,

(1) the vertical translation can be achieved by straightforwardly assigning identical amount of control signal to each motor; and

(2) the horizontal translation requires the unmanned quadrotor helicopter (UQH) to roll or pitch in advance, so that a forward or lateral movement can then be produced.

25

Moreover, the roll and pitch rotations can be achieved by distributing a different amount of control signals to the opposite motors, which force the UQH to tilt towards the slowest motor [33].

2.1.2.1 Nonlinear Model of Unmanned Aerial Vehicle

A widely employed nonlinear UQH model [33] with respect to the earth-fixed coordinate system can be defined as:

$$
\begin{aligned}
\ddot{x} &= \frac{(sin\psi sin\phi + cos\psi sin\theta cos\phi)u_z - K_1\dot{x}}{m} \\
\ddot{y} &= \frac{(sin\psi sin\theta cos\phi - cos\psi sin\phi)u_z - K_2\dot{y}}{m} \\
\ddot{z} &= \frac{(cos\theta cos\phi)u_z - K_3\dot{z}}{m} - g \\
\ddot{\phi} &= \frac{u_\phi - K_4\dot{\phi}}{I_x} \\
\ddot{\theta} &= \frac{u_\theta - K_5\dot{\theta}}{I_y} \\
\ddot{\psi} &= \frac{u_\psi - K_6\dot{\psi}}{I_z}.
\end{aligned}
\tag{4}
$$

The relationship between accelerations and lifts/torques can be expressed as:

$$
\begin{bmatrix} u_z \\ u_\theta \\ u_\phi \\ u_\psi \end{bmatrix} = \begin{bmatrix} 1 & 1 & 1 & 1 \\ L & -L & 0 & 0 \\ 0 & 0 & L & -L \\ C & C & -C & -C \end{bmatrix} \begin{bmatrix} F_1 \\ F_2 \\ F_3 \\ F_4 \end{bmatrix}.
\tag{5}
$$

2.1.2.2 Linearization of Unmanned Aerial Vehicle Model

Assumption 1 *The UQH is assumed to move in near-hovering flight condition, this implies that 1) $u_z \approx mg$ along the vertical direction; 2) pitch and roll angles are so small that $sin\phi \approx \phi$ and $sin\theta \approx \theta$; In addition, there is no operation for yaw motion ($\psi = 0$) during the entire flight period.*

Based on *Assumption 1*, a linearized model of (4) can be obtained:

$$\ddot{x} = \theta g$$
$$\ddot{y} = -\phi g$$
$$\ddot{z} = u_z/m - g$$
$$I_x\ddot{\phi} = u_\phi(t) \tag{6}$$
$$I_y\ddot{\theta} = u_\theta(t)$$
$$I_z\ddot{\psi} = u_\psi.$$

2.1.2.3 Actuator Dynamics

For a typical UQH, the produced thrust F_i of the ith rotor is related to its corresponding pulse width modulation (PWM) input u_i^{pwm} with the following first-order linear transfer function:

$$F_i = K_m\frac{\omega_m}{s + \omega_m}u_i^{pwm}. \tag{7}$$

In the existing research [33, 34], in order to facilitate the linear controller design, the actuator model is usually simplified as $K_m\frac{\omega_m}{s+\omega_m} \approx K_m$. However, in practice, actuator dynamics are not sufficiently fast to be omitted. The overall system performance may be significantly deteriorated when actuator dynamics are not considered in the controller design procedure. It is worth noting that K_m and ω_m are theoretically assumed to be identical for the four motors; whereas this may not be the case in practice, which can cause model uncertainties entering into the control system.

From (7), the derivative of F_i can be derived as follows:

$$F_{ri} = \dot{F}_i = K_m\omega_m u_i^{pwm} - \omega_m F_i, \tag{8}$$

where F_{ri} denotes the thrust variation rate of the ith rotor.

To meet the physical constraints of each actuator in practice, F_i and F_{ri} are then limited within

their corresponding safe operating region:

$$F_i \in [-\Phi_{di}, \Phi_{di}],$$

$$F_{ri} \in [-\Phi_{ri}, \Phi_{ri}],$$

(9)

where Φ_{di} and Φ_{ri} represent the limits of F_i and F_{ri}, respectively, $i \in [1, ..., 4]$.

Table 2.4: Nomenclature (earth-fixed coordinate system)

Symbols	Explanation
x, y, z	Coordinates of UQH at center of mass
θ	Pitch angle
ϕ	Roll angle
ψ	Yaw angle
$u_z(t)$	Total lift force
$u_\theta(t)$	The applied torque in θ direction
$u_\phi(t)$	The applied torque in ϕ direction
$u_\psi(t)$	The applied torque in ψ direction
K_n $(n = 1, 2, ..., 6)$	Drag coefficients
$u_i(t)$ $(i = 1, 2, 3, 4)$	Thrust of each rotor
L	Center distance between the gravity of UQH and each propeller
C_m	Thrust-to-moment scaling factor
g	Acceleration of gravity
m	UQH mass
I_x	Moment of inertia along x direction
I_y	Moment of inertia along y direction
I_z	Moment of inertia along z direction
ω_m	Actuator bandwidth
K_m	A positive gain
$u_{ci}(t)$ $(i = 1, 2, 3, 4)$	PWM signals distributed to each rotor

Similarly, it is possible to formulate the operating constraints for multiple actuators:

$$F \in [-\Phi_d, \Phi_d],$$

$$F_r = K_m \omega_m u^{pwm} - \omega_m F, \ F_r \in [-\Phi_r, \Phi_r],$$

(10)

where $F_r = [F_{r1}, F_{r2}, F_{r3}, F_{r4}]^T$, $\Phi_d = [\Phi_{d1}, \Phi_{d2}, \Phi_{d3}, \Phi_{d4}]^T$, and $\Phi_r = [\Phi_{r1}, \Phi_{r2}, \Phi_{r3}, \Phi_{r4}]^T$.

The definition of the above-mentioned symbols are all summarized in Table 2.4.

2.2 Actuator Faults Formulation

To formulate the FTC problem, A faulty actuator model can be formulated as. Writing the faulty control input as follows:

$$u_f(t) = (I_m - L_f)u(t), \tag{11}$$

where $u_f(t) = [u_{f1}(t), u_{f2}(t), u_{f3}(t), u_{f4}(t)]^T$ and $L_f = diag\{l_{f1}, l_{f2}, l_{f3}, l_{f4}\}$ denote the faulty control input and loss of control effectiveness ratio. $I_m \in \Re^{m \times m}$ is an identity matrix. $u_{fi}(t)$ is the control input of the ith faulty actuator, $0 \leq l_{fi} \leq 1$ is the partial loss of control effectiveness. $l_{fi} = 0$ indicates the ith actuator is healthy, while $l_{fi} = 1$ means a total failure of the ith actuator.

2.3 Environmental Disturbances Formulation

Waves and currents are regarded as the dominant factors of influencing USV performance [99].

2.3.1 Waves

According to [98], the wave $w(s)$ can be described as:

$$w(s) = \frac{K_\omega s}{s^2 + 2\zeta\omega_0 s + \omega_0^2} h(s), \tag{12}$$

where $h(s)$ is Gaussian white noise, ω_0, ζ and K_ω are the model frequency, damping coefficient and gain constant, respectively.

2.3.2 Currents

As stated in [98], the two-dimensional current is composed of the direction of the current γ_c and the average speed of current $V_c(t)$. The average velocity of current can be simulated by using the

first-order Gauss-Markov process $\frac{dV_c(t)}{dt} + \mu_0 V_c(t) = \omega(t)$, where constant $\mu_0 \geqslant 0$ and $h(s)$ is a zero mean Gaussian white noise sequence. The boundary of $V_c(t)$ is denoted as $V_{min} \leqslant V_c(t) \leqslant V_{max}$.

Therefore, the body-fixed kinematic equations can be expressed as:

$$u_c = V_c(t)cos(\gamma_c - \psi)$$
$$v_c = V_c(t)sin(\gamma_c - \psi). \tag{13}$$

2.4 Path Following Schemes

Two types of path following methods are studied in this research, one is LOS path following, while the other one is SF frame based path following.
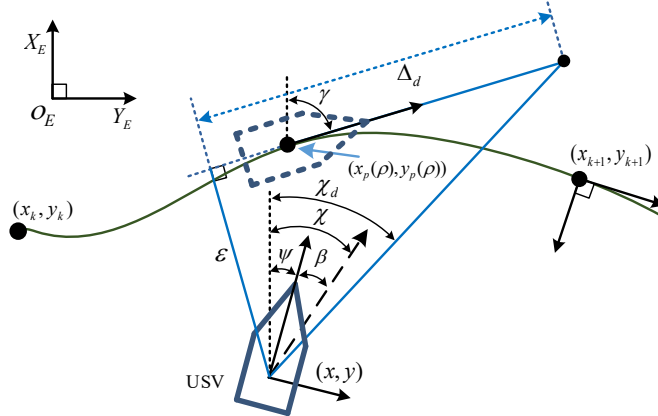
Figure 2.3: Schematic diagram of the LOS guidance geometry.

2.4.1 Line-of-Sight Path Following

As illustrated in Fig. 2.3, a two-dimensional (2D) continuous $\mathcal{C}^1$ parametrized path $(x_p(\rho), y_p(\rho))$ is considered in this study, where ρ represents the path variable, is assumed to go through a set of successive waypoints (x_k, y_k) for $k = 1, ..., N$. And for arbitrary path point $(x_p(\rho), y_p(\rho))$, the path-tangential angle $\gamma(\rho)$ is calculated by:

$$\gamma(\rho) = \arctan(y'_p(\rho), x'_p(\rho)), \tag{14}$$

30

where $x_p'(\rho) = \partial x_p / \partial \rho$ and $y_p'(\rho) = \partial y_p / \partial \rho$. It is worth noting that $\gamma = \arctan(y_{k+1} - y_k, x_{k+1} - x_k)$ is constant when the desired path is a straight line between the waypoints, while $\gamma(\rho)$ varies according to (14) when the desired path is a parametrized curve.

For the USV locates at (x, y), the cross-track error, which is defined as the orthogonal distance to the path tangential reference frame, can be computed by:

$$\varepsilon = -(x - x_p(\rho)) \sin(\gamma(\rho)) + (y - y_p(\rho)) \cos(\gamma(\rho)). \tag{15}$$

The path-normal line can then be obtained as:

$$y - y_p(\rho) = -\frac{1}{\tan(\gamma(\rho))}(x - x_p(\rho)). \tag{16}$$

Differentiating (15) with respect to time gives:

$$\dot{\varepsilon} = -(\dot{x} - \dot{x}_p(\rho)) \sin(\gamma) + (\dot{y} - \dot{y}_p(\rho)) \cos(\gamma) - [(x - x_p(\rho)) \cos(\gamma) + (y - y_p(\rho)) \sin(\gamma)]\dot{\gamma}. \tag{17}$$

According to (14) and (16), one can obtain:

$$
\begin{aligned}
\dot{x}_p(\rho) \sin(\gamma) - \dot{y}_p(\rho) \cos(\gamma) &= 0, \\
(x - x_p(\rho)) \cos(\gamma) + (y - y_p(\rho)) \sin(\gamma) &= 0.
\end{aligned}
\tag{18}
$$

Based on (18), the combination of (1) and (17) generates:

$$
\begin{aligned}
\dot{\varepsilon} &= -\dot{x} \sin(\gamma) + \dot{y} \cos(\gamma) \\
&= -(v_x \cos\psi - v_y \sin\psi) \sin(\gamma) + (v_x \sin\psi + v_y \cos\psi) \cos(\gamma).
\end{aligned}
\tag{19}
$$

Writing into *amplitude-phase form*, (19) becomes:

$$\dot{\varepsilon} = U \sin(\chi - \gamma), \tag{20}$$

31

where $U = \sqrt{v_x^2 + v_y^2}$, the course angle $\chi = \psi + \beta$, and $\beta = \mathrm{atan2}(v_y, v_x)$ denotes the sideslip angle caused by the drift forces (winds, waves, and currents) and USV's steering operation during the path following procedure.

Assumption 2 *It assumes that the sideslip angle β is constant and so small that $\dot{\beta} = 0$ during path following, and it also implies that $\sin(\beta) \approx \beta$ and $\cos(\beta) \approx 1$.*

This assumption is reasonable when the USV is under normal operation, and only a few degrees of sideslip is also observed in this case [75]. Furthermore, the sideslip angle varies much slower than the control bandwidth, these variations can thereby be properly tracked by the adaptation law. However, the path following performance of USV to some extent can be affected, although the sideslip angle is relatively small (typically $\beta < 5 \deg$). A significant deviation from the anticipated path may eventually be induced if no proper compensation action to the sideslip angle is conducted.

Making use of the kinematic property, $\sin(A_k + B_k) = \sin(A_k)\cos(B_k) + \cos(A_k)\sin(B_k)$, then (20) becomes:

$$\dot{\varepsilon} = U \sin(\psi - \gamma) \cos\beta + U \cos(\psi - \gamma) \sin(\beta). \tag{21}$$

Based on Assumption 2, (21) reduces to:

$$\dot{\varepsilon} = U \sin(\psi - \gamma) + U \cos(\psi - \gamma)\beta. \tag{22}$$

2.4.2 Serret-Frenet Frame Based Path Following

Serret-Frenet frame (illustrated in Fig. 2.4) is often adopted to obtain the error dynamics as:

$$\dot{\psi}_e = \dot{\psi} - \dot{\psi}_{SF} = \frac{\kappa}{1 - e\kappa}(v_x sin\psi_e - v_y cos\psi_e) + r, \tag{23}$$

$$\dot{e} = v_x sin\psi_e + v_y cos\psi_e, \tag{24}$$

where the symbols in (23) and (24) as well as Fig. 2.4 are illustrated in Table 2.5.

Table 2.5: Nomenclature of USV parameters

Symbols	Explanation
$\{Y_E O_E X_E\}$	The earth-fixed frame
$\{Y_B O_B X_B\}$	The ship body-fixed frame
$\{Y_{SF} O_{SF} X_{SF}\}$	The Serret-Frenet frame
e	The cross-track error
ψ_e	The heading error
ψ_{SF}	The heading angle of virtual vessel
κ	The curvature of the desired path
X_{SF}	Tangent direction at the origin of $\{Y_{SF} O_{SF} X_{SF}\}$
Y_{SF}	Normal direction at the origin of $\{Y_{SF} O_{SF} X_{SF}\}$
X_B	Tangent direction at the origin of $\{Y_B O_B X_B\}$
Y_B	Normal direction at the origin of $\{Y_B O_B X_B\}$
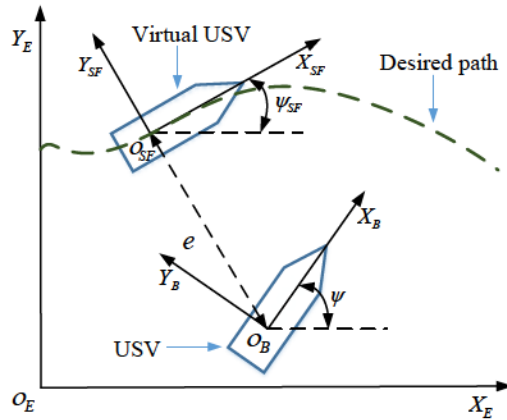
Figure 2.4: The variables and coordinates for Serret-Frenet frame based path following.

The general principle of Serret-Frenet frame based path following can be represented by forcing e and ψ_e to converge to zero, while keeping a specific rudder angle to neutralize the environmental disturbances. Additionally, when a USV follows a straight line path, κ tends to be zero.

Chapter 3

Reliable and Safe Path Following of Unmanned Vehicles

This chapter studies the topics of path following of USV. In the application of path following, USV is required to follow a user-defined path by independently tracking an expected forward speed profile and steering its orientation. Comparing with trajectory tracking, a smoother path and lower probability of actuator saturation can be achieved due to the fact that spatial constraints are given priority over the temporal constraints in the path following tasks. Two types of general path following methods are studied in the subsequence, namely the adaptive LOS path following approach and Serret-Frenet frame based path following approach.

3.1   Adaptive Line-of-Sight Path Following
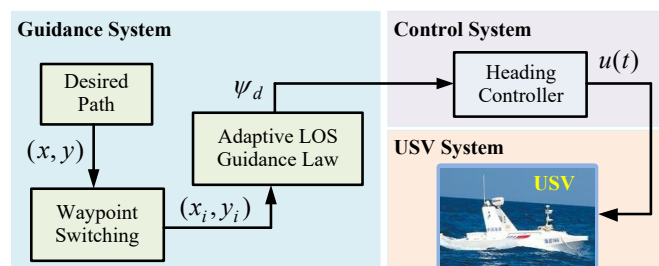
Figure 3.1: Overall structure of the proposed method.
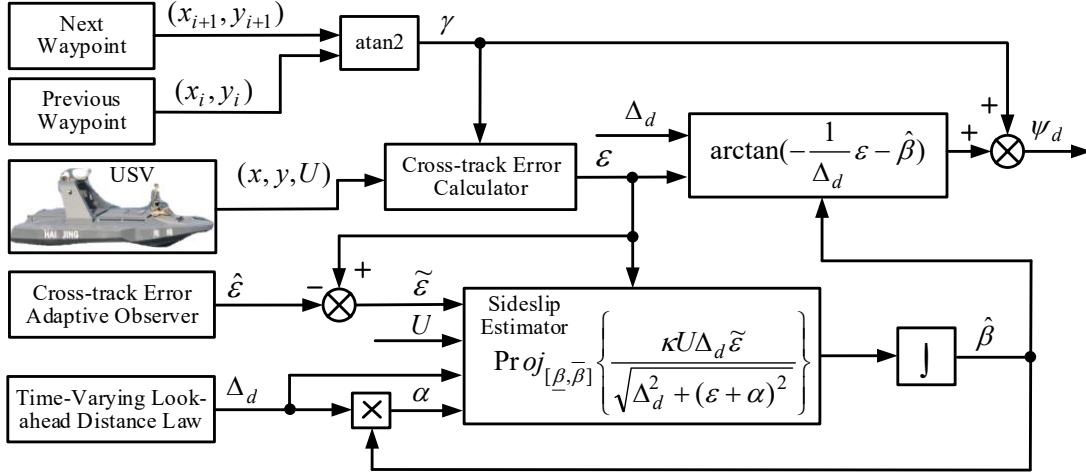
Figure 3.2: Block diagram of the proposed adaptive LOS path-following method.

3.1.1 Adaptive Observer Based Line-of-Sight Guidance Law Design

As a basic and essential component for USV system, a feasible and effective guidance system is critical for continuously generating and updating smooth and feasible path commands to the control system to properly accomplish tasks. The LOS guidance laws for path following are usually adopted at a kinematic level in order to produce a desired heading angle ψ_d (as shown in Fig. 3.1) to the USV heading control system. Then, the control system steers the USV to track the desired heading angle such that $\psi = \psi_d$. More detailed design procedure can refer to the following subsections along with Fig. 3.2.

Although GPSs are widely adopted for measuring the course over ground of ground and aerial vehicles, it is common to obtain the yaw angle using a compass in practical applications. It is thereby of great interest to estimate β so that ε can be exponentially regulated to zero and the desired path can be accurately followed.

To design a feasible desired heading angle ψ_d, the following relationship is chosen:

$$\psi_d = \gamma + \arctan\left(-\frac{1}{\Delta_d}(\varepsilon + \alpha)\right), \tag{25}$$

where γ and ε are assumed to be known and online measurable, respectively. $0 < \Delta_{dmin} \le \Delta_d \le \Delta_{dmax}$ denotes the user defined lookahead distance, while α is the control input to be designed.

35

Before proceeding to the next procedure, the following formulae are established:

$$\begin{cases} \sin\left(\arctan(-\dfrac{1}{\Delta_d}(\varepsilon + \alpha))\right) = -\dfrac{\varepsilon + \alpha}{\sqrt{\Delta_d^2 + (\varepsilon + \alpha)^2}} \\ \cos\left(\arctan(-\dfrac{1}{\Delta_d}(\varepsilon + \alpha))\right) = \dfrac{\Delta_d}{\sqrt{\Delta_d^2 + (\varepsilon + \alpha)^2}} \end{cases}. \tag{26}$$

Based on (26), then (22) becomes:

$$\dot{\varepsilon} = -\frac{U(\varepsilon + \alpha)}{\sqrt{\Delta_d^2 + (\varepsilon + \alpha)^2}} + \frac{U\Delta_d}{\sqrt{\Delta_d^2 + (\varepsilon + \alpha)^2}}\beta. \tag{27}$$

To estimate β, the following nonlinear adaptive observer is constructed:

$$\dot{\hat{\varepsilon}} = -\frac{U(\hat{\varepsilon} + \alpha)}{\Omega} + \frac{U\Delta_d\hat{\beta}}{\Omega} + K_o(\varepsilon - \hat{\varepsilon}), \tag{28}$$

where $\hat{\varepsilon}$ and $\hat{\beta}$ are the estimates of ε and β, $\Omega = \sqrt{\Delta_d^2 + (\varepsilon + \alpha)^2}$, and observer gain $K_o > 0$.

Define $\tilde{\varepsilon} = \varepsilon - \hat{\varepsilon}$, the difference of (27) and (28) then gives:

$$\dot{\tilde{\varepsilon}} = -\frac{U\tilde{\varepsilon}}{\Omega} + \frac{U\Delta_d\tilde{\beta}}{\Omega} - K_o\tilde{\varepsilon}, \tag{29}$$

where the parameter estimation error $\tilde{\beta} = \beta - \hat{\beta}$.

Theorem 1 *If Assumption 1 holds and the heading controller successfully tracks the desired heading angle, the sideslip angle $\hat{\beta}$ can then be determined by the following adaptive estimation law:*

$$\begin{aligned} \dot{\hat{\beta}} &= Proj_{[\underline{\beta},\overline{\beta}]}\left\{\frac{\kappa U\Delta_d\tilde{\varepsilon}}{\sqrt{\Delta_d^2 + (\varepsilon + \alpha)^2}}\right\} \\ &= \begin{cases} 0 & \text{if } \hat{\beta} = \underline{\beta}, \dfrac{\kappa U\Delta_d\tilde{\varepsilon}}{\sqrt{\Delta_d^2 + (\varepsilon + \alpha)^2}} < 0 \\ & \text{or } \hat{\beta} = \overline{\beta}, \dfrac{\kappa U\Delta_d\tilde{\varepsilon}}{\sqrt{\Delta_d^2 + (\varepsilon + \alpha)^2}} \geq 0, \\ \dfrac{\kappa U\Delta_d\tilde{\varepsilon}}{\sqrt{\Delta_d^2 + (\varepsilon + \alpha)^2}} & \text{otherwise,} \end{cases} \end{aligned} \tag{30}$$

where $\kappa > 0$ is the adaptation gain, $\underline{\beta}$ and $\overline{\beta}$ denote the lower and upper bounds of β, $0 < U_{min} \leq U \leq U_{max}$. The projection operator $Proj\{\cdot\}$ [100] is adopted for projecting the estimates $\dot{\hat{\beta}}$ to the acceptable sideslip interval $[\underline{\beta}, \overline{\beta}]$.

Proof of Theorem 1: Choosing the Lyapunov function candidate as follows:

$$V_1 = \frac{1}{2}\tilde{\varepsilon}^2 + \frac{1}{2\kappa}\tilde{\beta}^2 > 0. \tag{31}$$

According to (29), the derivation of (31) with respect to time gives:

$$\dot{V}_1 = \tilde{\varepsilon}\dot{\tilde{\varepsilon}} + \frac{1}{\kappa}\tilde{\beta}\dot{\tilde{\beta}} = -\frac{U}{\Omega}\tilde{\varepsilon}^2 - K_o\tilde{\varepsilon}^2 + \frac{\tilde{\beta}\dot{\tilde{\beta}}}{\kappa} + \frac{U\Delta_d\tilde{\beta}}{\Omega}\tilde{\varepsilon}^2. \tag{32}$$

Recalling *Assumption 1*, it follows that $\dot{\tilde{\beta}} = -\dot{\hat{\beta}}$, substituting (30) into (32), this derives that:

$$\dot{V}_1 = -\frac{U}{\Omega}\tilde{\varepsilon}^2 - K_o\tilde{\varepsilon}^2 \leq 0. \tag{33}$$

Finally, the global convergence of *Theorem 1* can be proven applying *Barbălat's lemma* [101].

Corollary 1 *Assume the control objective of path following is to achieve* $\lim_{\hat{\beta} \to \beta} \varepsilon = 0$. *Making use of the nonlinear adaptive observer (29) and Theorem 1 together, then the virtual control input* $\alpha = \Delta_d\hat{\beta}$ *is chosen to asymptotically cancel the sideslip angle* β *in (27), so that the following desired heading angle can ultimately be obtained:*

$$\psi_d = \gamma + \arctan\left(-\frac{1}{\Delta_d}\varepsilon - \hat{\beta}\right). \tag{34}$$

3.1.2 Time-Varying Lookahead Distance Scheme Design

As illustrated in [74], a smaller Δ_d can cause a more rapid steering action with comparison of a larger Δ_d. A fixed lookahead distance Δ_d can be well designed for rapidly decreasing the croostrack error, while an unexpected oscillatory behavior around the desired path may be induced. Therefore, in order to achieve the faster cross-track error reduction and to avoid the undesired oscillation around the path, the lookahead distance Δ_d is further designed to be time-varying in this study, which is constructed as below:

$$\Delta_d(v_x, \varepsilon) = \Delta_\Delta \times exp^{-(K_{\varepsilon 1}\varepsilon^2 + K_{\varepsilon 2}\dot{\varepsilon}^2)} + \Delta_{min}, \tag{35}$$

where $K_{\varepsilon 1}$ and $K_{\varepsilon 2}$ are the design parameters, $\Delta_\Delta = \Delta_{max} - \Delta_{min}$, and Δ_{max} and Δ_{min} denote the maximum and minimum boundaries of the automatically adjustable lookahead distance Δ_d.

The design concept of (35) can be intuitively interpreted by the following two situations:

(1) a more aggressive action is usually needed to minimize the cross-track error in a fast manner when the USV is far away from the expected path. This performance can be achieved by assigning a small value of Δ_d;

(2) a more gentle behavior is required to avoid the undesired overshoot when the USV is approaching the desired path. A large value allocated to Δ_d is intended to realize the anticipated objective. A little different from [74] is that $\dot{\varepsilon}$ is also considered in the calculation of Δ_d in this study. It is meaningful to take into account of this additional term, because the variation rate of cross-track error, to some extent, can affect the USV path following behavior as well.

To investigate the effects of the time-varying lookahead disturbance to the stability of guidance system, (33) is rewritten as:

$$\dot{V}_1 = -\frac{U}{\sqrt{\Delta_{max}^2 + (\varepsilon + \alpha)^2}}\tilde{\varepsilon}^2 - K_o\tilde{\varepsilon}^2 \leq 0. \tag{36}$$

As can be seen from (36), the stability region of the guidance system is subject to Δ_{max}. More specifically, a larger Δ_{max} can result in a more limited system stability region, while a smaller Δ_{max} can lead to a less limited system stability region.

3.1.3 Piecewise Path Switching Criteria Design

In the implementation of path following, the desired path is normally divided into n straight-line segments connected by $n + 1$ waypoints, then a waypoint switching strategy should be employed for the switch between these segments as they are traversed. In the existing literature [65], a most intuitive method is suggested, which is to assign a so-called circle of acceptance to each waypoint. Alternatively, this research presents a perhaps more practical switching criterion solely involves the along-track distance R_k. The studied switching criteria indeed preserves advantages of the circle of acceptance strategy, while contributes to the elimination of certain deviations from reference path caused by the circle of acceptance and reduction of the probability of failing to reach the next waypoint. Moreover, there is no need for USV to enter the next waypoint enclosing circle for a switch to occur [82]. The proposed switching rule [102] is to project the motion of USV to the reference path, and to calculate its corresponding position along the reference path, which is established as follows:

$$R_B - R_k \leq R_s, \tag{37}$$

where R_A is the distance between the previous waypoint and USV's current position, R_B denotes the distance between two neighbouring waypoints along the desired path, and R_s represents the switching distance determining the occurrence of moving to the next piece of path.

As shown in Fig. 3.3, the distance between the USV and desired path is defined as the length of the normal line between them. The normal line is perpendicular to the path and passes through the USV. The along-track distance R_k can be obtained in the following way:
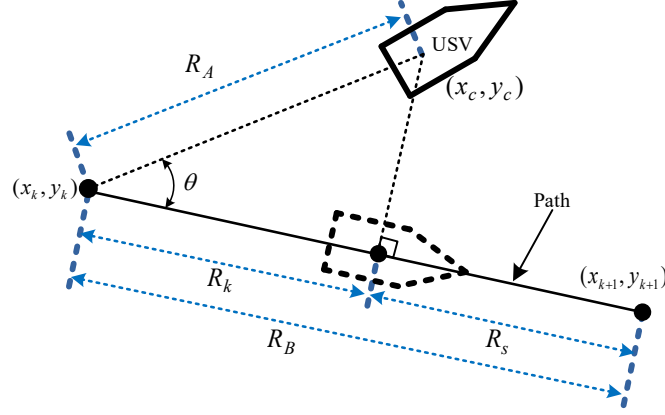
Figure 3.3: Illustration of waypoint switching criteria.

(1) first, the angle θ between the distances of $\overrightarrow{R}_A$ and $\overrightarrow{R}_B$ can be calculated as follows:

$$\theta = \arccos[(\overrightarrow{R}_A \cdot \overrightarrow{R}_B)/(||\overrightarrow{R}_A|| \cdot ||\overrightarrow{R}_B||)], \tag{38}$$

where $\overrightarrow{R}_A = (x_c - x_k, y_c - y_k)$ and $\overrightarrow{R}_B = (x_{k+1} - x_k, y_{k+1} - y_k)$, $\overrightarrow{R}_A \cdot \overrightarrow{R}_B = (x_c - x_k) \cdot (x_{k+1} - x_k) + (y_c - y_k) \cdot (y_{k+1} - y_k)$;

(2) then R_k is achievable using the following formula:

$$R_k = R_A \cos \theta; \tag{39}$$

(3) based on the waypoint switching law (37) and obtained along-track distance R_k, it is possible to determine the waypoint switching action.

3.1.4 Simulation Results

In order to generate a smooth and practical path connecting the desired waypoints $WP1 = (40, 24)$, $WP2 = (30, 90)$, $WP3 = (80, 100)$ and $WP4 = (80, 170)$, while avoiding wiggles and zigzags of USV, in this study, these waypoints are interpolated using the cubic Hermite spline algorithm [74]. The USV starts at position $(0, 0)$ with $0\ deg$ initial heading angle, travelling with a

40
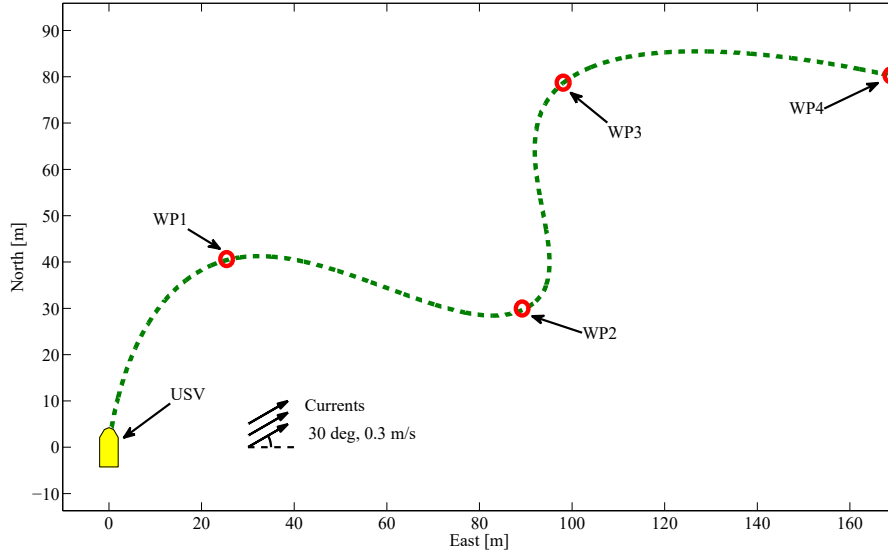
Figure 3.4: The desired path.

constant forward speed ($1.5\ m/s$). The resulting path is then shown in Fig. 3.4. A first-order filter is also utilized before feeding the yaw rate commands to the control system since the generated path is not continuous on its second derivative. The proposed method is simulated on a nonlinear model (parameters are selected as in Table 3.1) identified from a real USV.

Table 3.1: The system parameters used in the simulation

Parameter	Value	Unit
m_{11}	1.956	-
m_{22}	2.405	-
m_{33}	0.403	-
d_{11}	2.436	-
d_{22}	12.992	-
d_{33}	0.0564	-
l	0.07	m

3.1.4.1 Scenarios Description

The following two scenarios have been considered:

(1) *Scenario 1*: to demonstrate the effectiveness of the proposed adaptive integral LOS path following method comparing with a classical one. A current disturbance with constant speed

of $0.3\ m/s$ and direction of $30\ deg$ is imposed. The adaptive observer and adaptation gains are assigned the values of $K_o = 100$ and $\kappa = 2.1$, respectively.

(2) *Scenario 2*: to verify the function of the proposed time-varying lookahead distance mechanism. This mechanism is applied in the proposed method ($\Delta_{max} = 6\ m$ and $\Delta_{min} = 2\ m$), while a constant lookahead distance ($\Delta = 4\ m$) is considered in the compared algorithm.
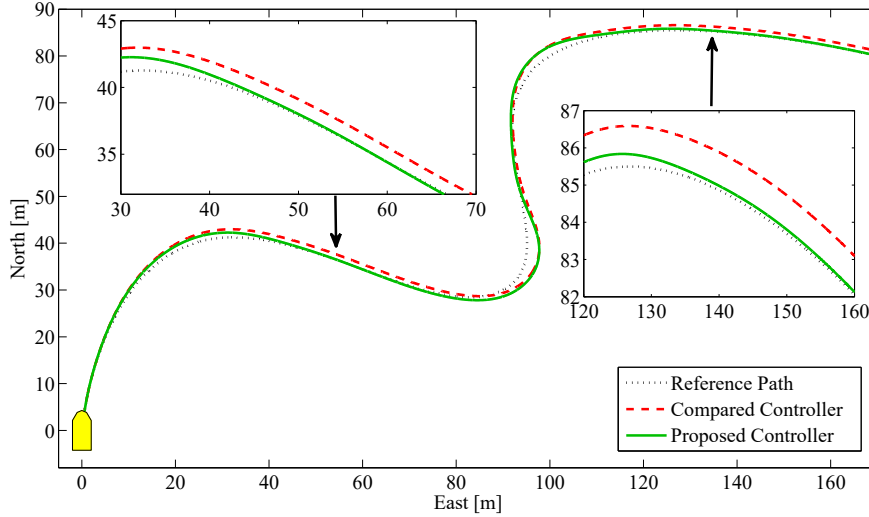
Figure 3.5: Performance comparison of path following.
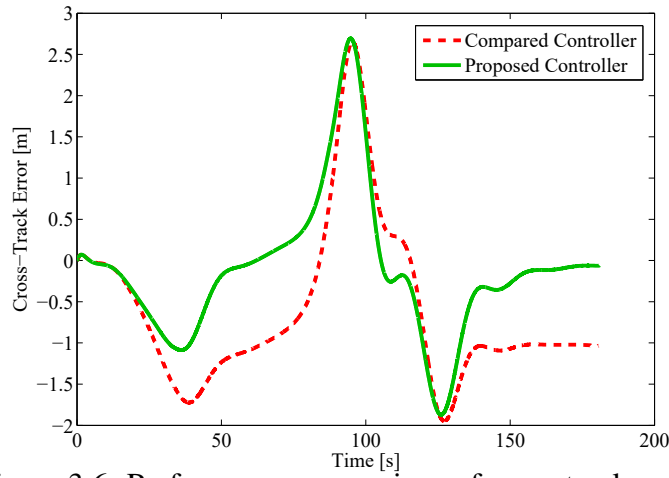
Figure 3.6: Performance comparison of cross-track errors.

3.1.4.2 Results of Scenario 1 and Evaluation

The current disturbance with constant speed of $0.3\ m/s$ and direction of $30\ deg$ is injected in all case studies. The design parameters for the time-varying lookahead distances are chosen as
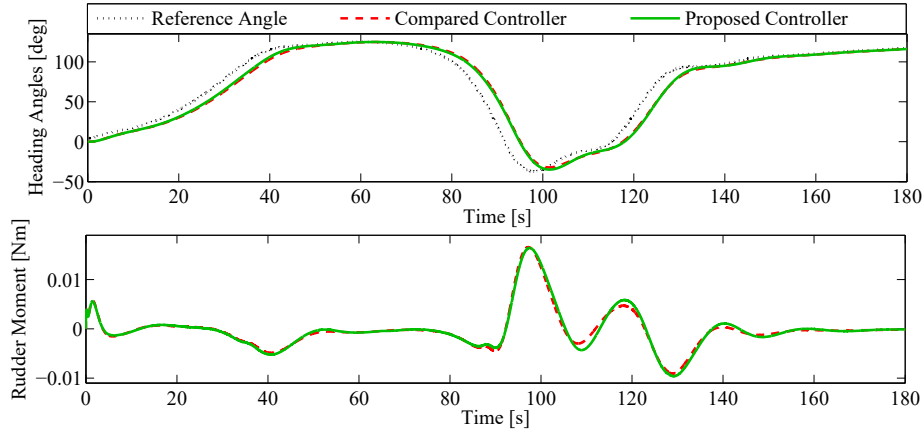
Figure 3.7: Performance of heading angle tracking and rudder operation.

$K_{\varepsilon 1} = 4$ and $K_{\varepsilon 2} = 1$. The adaptive fault estimation gains $k_{Pi} = 250000$ and $k_{Di} = 2.75$ are selected as the same for all case studies.
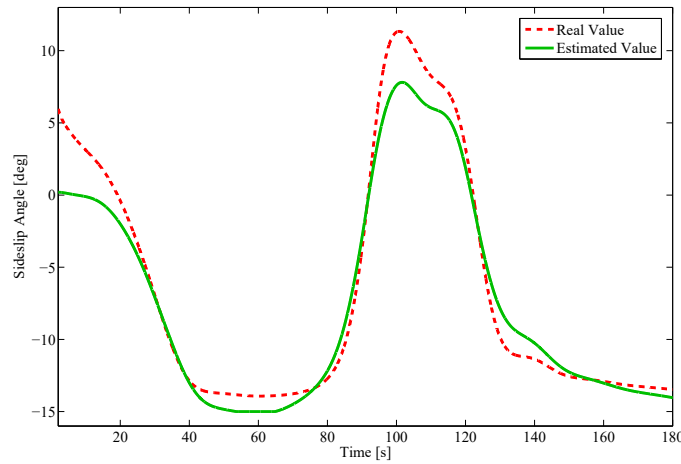
Figure 3.8: The estimation of sideslip angle.

Fig. 3.5 displays that the desired path is well followed under the supervision of the proposed adaptive LOS law comparing with the classical LOS method without the adaptive scheme. More clearly shown in Fig. 3.6, the cross-track error is significantly eliminated by the proposed guidance law. Its good performance is mainly due to the introduction of an integral term into the LOS law design based on the estimates of sideslip angles. From Fig. 3.7, the USV operated by the proposed guidance law tracks the desired heading angle faster than that of the compared method.

This also explains the reason of the cross-track error reduction induced by the proposed controller. Furthermore, it can be observed from Fig. 3.8 that sideslip angles caused by the imposed

current and USV turning action are well estimated using the proposed adaptive estimation law.
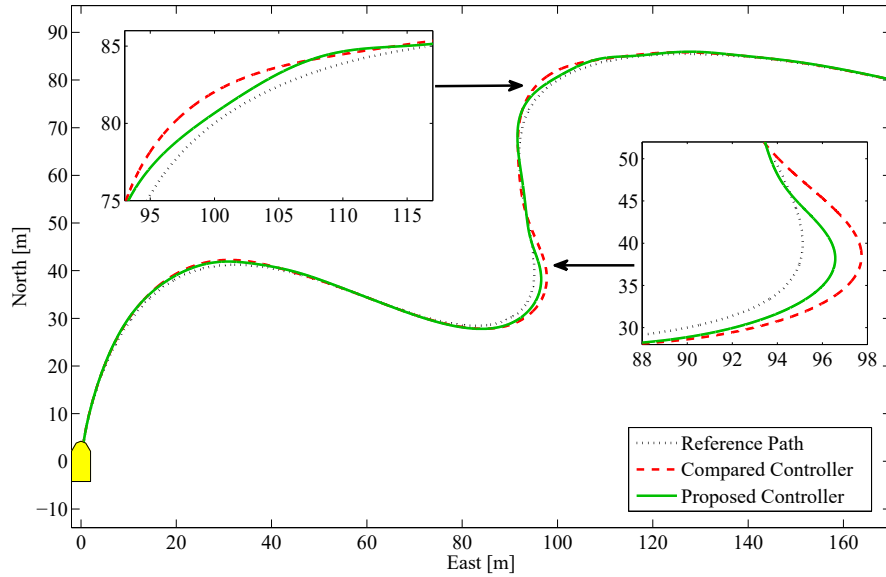
Figure 3.9: Performance comparison of path following.
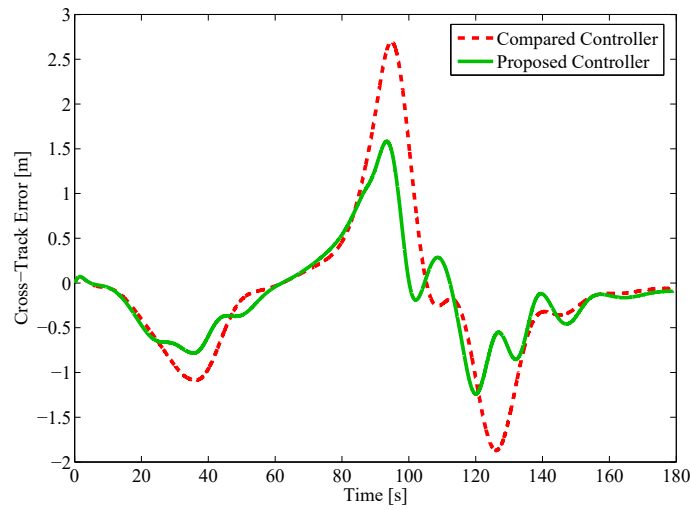
Figure 3.10: Performance comparison of cross-track errors.

3.1.4.3 Results of Scenario 2 and Evaluation

Fig. 3.9 shows that the LOS path following method with variable lookahead distance outperforms that with constant lookahead distance. This variant lookahead distance contributes to a fast convergence speed to the desired path when the USV is far away from the path, while a gentle action when the USV is moving close to the path. More specifically, from Fig. 3.10, the time-varying

lookahead distance method induces smaller cross-track error than the constant lookahead distance approach does, especially in each turning corner.

The variation of the lookahead distance during the operation is shown in Fig. 3.11. As it is expected, the lookahead distance is close to its maximum value when the USV approaches to the desired path, while it tends to be its minimum value when the USV departs away from the path. This mechanism accordingly improves the performance of heading angle tracking, which can significantly reduce the path deviation during the path following course.
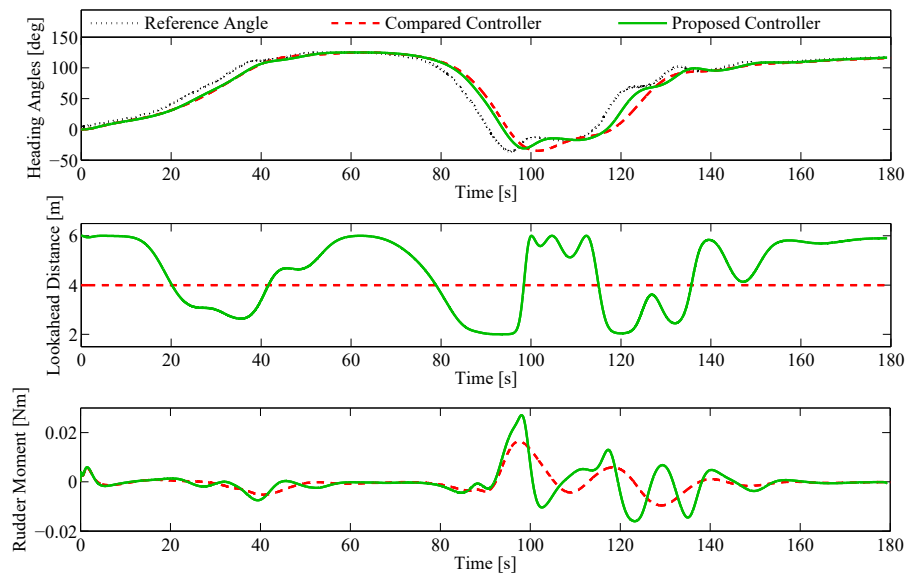
Figure 3.11: Performance of heading angle, lookahead distance, and rudder.

3.1.5 Field Test Results

The effectiveness of the proposed adaptive LOS path following method is further verified on a real-size USV (see Fig. 3.12) developed by our collaborator, a research group in Shanghai University. This USV, which is of $6.5m$ in length, $2.8m$ in width, and 3 ton in weight, is equipped with a group of sensors for providing required information to guidance and control systems as well as an onboard computer for executing command. There are two modes for the operation of USV, one is manual remote control of USV by operator, while the other one is that the USV autonomously carries out the predefined missions. In the autonomous mode (which is used for testing the proposed methods in this research), the desired trajectory (starts at the start waypoint, travels through WP1,

WP2 and WP3 in sequence, and finally stops at WP1) from the operator can be first planned in the graphic user interface, and then assigned to the USV via the wireless network to execution.
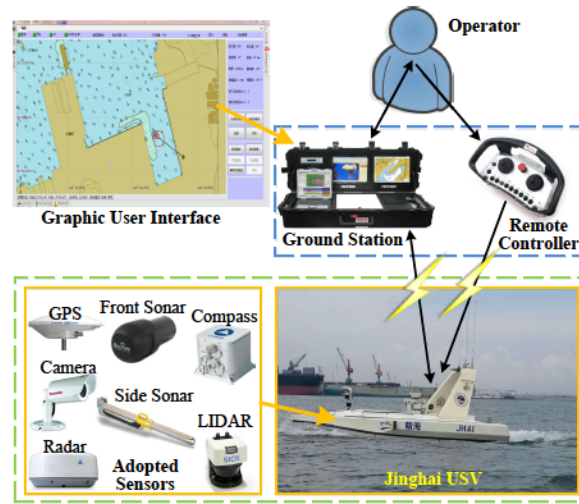
Figure 3.12: The employed "Jinghai" USV system.

From Fig. 3.13, the USV can follow the planned path with a satisfactory performance, using the proposed path following method. Although the second and third waypoints are not reached accurately, which is reasonable due to the physical limitation of the USV for satisfying such sharp turning maneuvering motions with the designed waypoints. In order to avoid steep steering in the real world application, a waypoint selecting mechanism is designed. This mechanism partially drops the trajectory with sharp angles.

Fig. 3.14 shows the result of cross-track error which is critical for the evaluation of path following performance. Larger value of cross-track error means poorer path following performance,
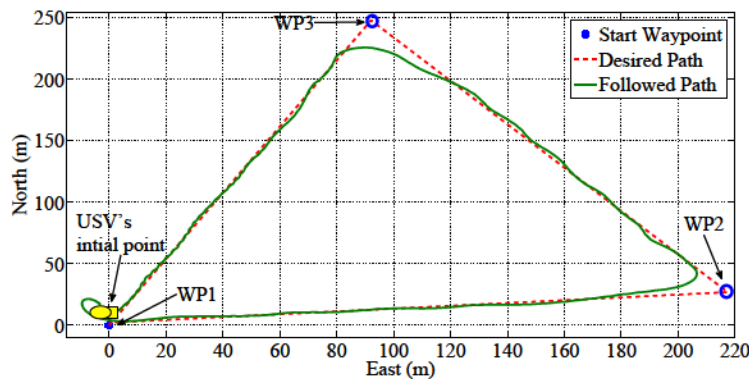
Figure 3.13: The performance of path following.
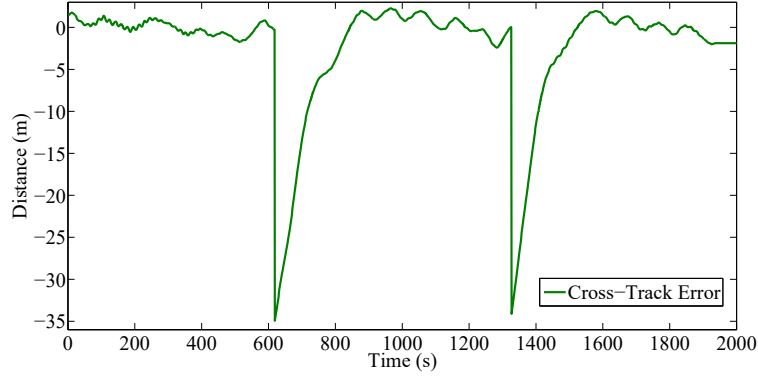
Figure 3.14: Results of cross-track error.
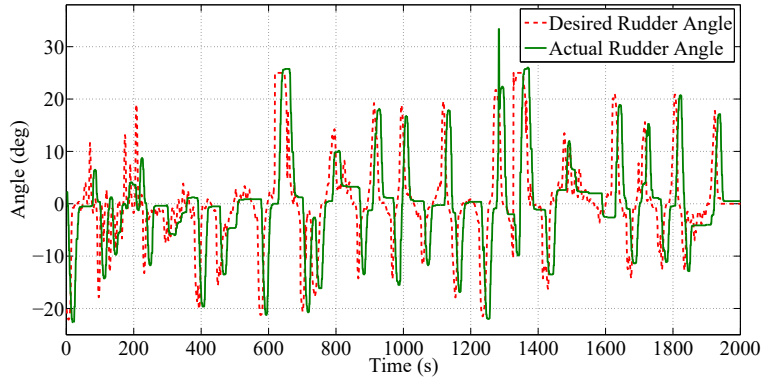
Figure 3.15: The performance of rudder operation.

while smaller value of cross-track error indicates better path following performance. It is worth-mentioning that there are two large cross-track errors during the entire period of path following, one happens at around 600th second, the other one occurs at around 1320th second. Actually, this phenomenon corresponds to the operation of two sharp waypoints selection procedure, rather than the reduced performance of the proposed method.

As displayed in Fig. 3.15, the rudder can track the desired reference without violating the constraint of rudder deflection $[-30deg, 30deg]$.

3.2 Serret-Frenet Frame Based Path Following Subject to Environmental Disturbances and Actuator Saturation

In this section, the other path following approach with the capability of attenuating time-varying disturbances and subjecting to actuator saturation is proposed. The basic idea of this

approach is to combine the control inputs from an adaptive disturbance compensating mechanism and a normal controller, so that the negative effects of environmental disturbances can be effectively eliminated, and the desirable performance can be guaranteed as well. Likewise, yaw rate constraint, the limits of rudder deflection and its rate are all taken into consideration at the control design stage. The controller's design procedure can be described as follows: 1) first, a state feedback tracking controller is selected as the normal controller for the operation of USV in the calm water. This is meaningful because USVs normally operate in this kind of environment most of the time; 2) then, a disturbance estimator is designed to detect the disturbance and estimate its amplitude, while a retrofit adaptive disturbance compensating mechanism is developed to compensate the adverse impacts of disturbance; 3) finally, the normal and adaptive disturbance compensating control inputs are synthesized to operate the USV along the desired path.

3.2.1 USV Modelling under Environmental Disturbances

Assumption 3 *The path to be followed is a straight/way-point path, so that the curvature κ in (24) can be treated as zero. The sway velocity is so small that it is negligible (this derives $v_y = 0$). The USV moves with a constant surge speed, which means $\dot{v}_x = 0$.*

Based on *Assumption 3*, Eqs. (3), (23) and (24) can be combined and further simplified, the simplified model including the dynamics of USV and path following error can then be obtained as:

$$
\begin{aligned}
\dot{e} &= v_x \psi_e \\
\dot{\psi}_e &= r \\
\dot{v}_y &= a_{11} v_y + a_{12} r + b_1 \tau_{vE} \\
\dot{r} &= a_{21} v_y + a_{22} r + b_2 \theta + b_3 \tau_{rE},
\end{aligned}
\tag{40}
$$

where $a_{11} = -\frac{d_{22}}{m_{22}}$, $a_{12} = -\frac{m_{11}}{m_{22}} u$, $a_{21} = \frac{m_{11} - m_{22}}{m_{33}} u$, $a_{22} = -\frac{d_{33}}{m_{33}}$, $b_1 = -\frac{d_{22}}{m_{22}}$, b_2, and $b_3 = \frac{1}{m_{33}}$. b_2 is the proportional scale between τ_r and rudder angle θ.

Considering environmental disturbances, (40) can be written into the state-space form as:

$$
\begin{cases}
\dot{x}(t) = Ax(t) + Bu(t) + Gw(t) \\
y(t) = Cx(t),
\end{cases}
\tag{41}
$$

where $u(t) = \theta \in \Re^m$, $x(t) = \begin{bmatrix} e & \psi_e & r & v_y \end{bmatrix}^T \in \Re^n$, $y(t) \in \Re^p$, and $w(t) = \begin{bmatrix} \tau_{rE} & \tau_{vE} \end{bmatrix}^T \in \Re^r \in [\underline{w}, \overline{w}]$ denote the control input, state, output, and bounded external disturbance, respectively.

$$
A = \begin{bmatrix} 0 & v_x & 0 & 0 \\ 0 & 0 & 1 & 0 \\ 0 & 0 & a_{21} & a_{22} \\ 0 & 0 & a_{11} & a_{12} \end{bmatrix}, B = \begin{bmatrix} 0 & 0 & b_2 & 0 \end{bmatrix}^T, C = \begin{bmatrix} 1 & 0 & 0 & 0 \\ 0 & 1 & 0 & 0 \\ 0 & 0 & 1 & 0 \\ 0 & 0 & 0 & 1 \end{bmatrix}, \text{ and } G = \begin{bmatrix} 0 & 0 & b_3 & 0 \\ 0 & 0 & 0 & b_1 \end{bmatrix}^T.
$$

3.2.2 Constraints of USV Actuators and System States

3.2.2.1 USV Actuator Model and Constraints

The actuator, which converts the control signal into the physical action, plays a critical role in the control system of USV. As shown in Fig. 3.16, position (a) is the actuator's initial position when the telemotor and floating lever are at rest. Once the control input u_{oi} is generated to operate the actuator, the port valve is then commanded to open. Consequently, the hydraulic oil can be pumped into the steering cylinder. Therefore, the piston of steering cylinder is moved by the pressure of hydraulic oil, this leads the floating lever to go upwards to position (c), and the actuator is driven to the desired position u_i. Similarly, once the starboard valve is ordered to open, the floating lever will be pushed downwards to position (b), and the actuator is driven to the expected position.

Normally, mechanical actuators are subject to their physical limitations. When these limitations are exceeded, the closed-loop system may become destabilized [103], even cause secondary damages to actuators [104] leading to a serious consequence (crash). In practice, the frequent actuator action is common in extreme weather conditions since the compensation of high frequency disturbances is required. However, continual actuator operation may inevitably lead to the oscillations,
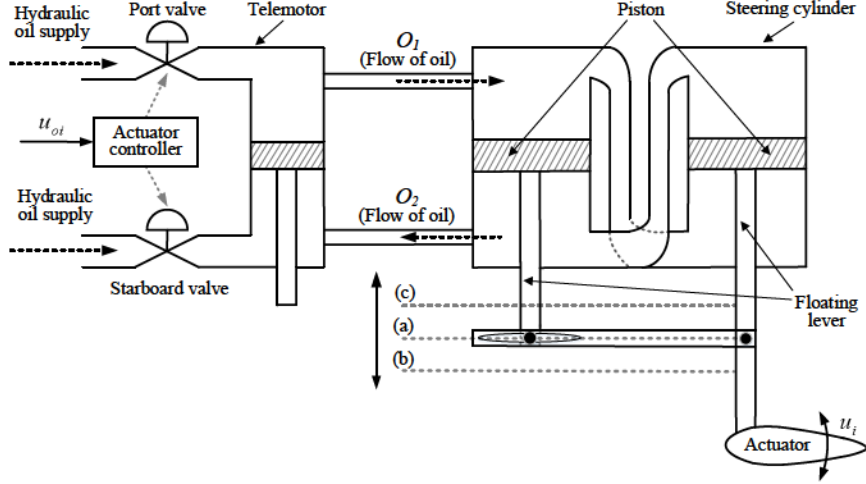
Figure 3.16: Simplified diagram of a two-stage hydraulic mechanical actuator.

unwanted impacts, and wear and tear of the steering system [98].

Drawing lessons from [98], a commonly used simplified dynamic relationship between the ith actuator output $u_i(s)$ and ith control input $u_{oi}(s)$ can be represented as:

$$\frac{u_i(s)}{u_{oi}(s)} = \frac{b_i}{s + a_i}, \tag{42}$$

where a_i and b_i denote the model parameters of ith actuator, $i \in [1, ..., m]$.

Based on (42), the rate of $u_i(t)$ can be denoted as follows:

$$u_{ri}(t) = bu_{oi}(t) - au_i(t), \tag{43}$$

where $u_{ri}(t)$ is the deflection rate of $u_i(t)$, and physical limits on the actuator's internal variables can be defined as $\phi_{d(i)}$ and $\phi_{r(i)}$ for displacement and rate, respectively. Thus, the ith actuator variables are constrained within the following safe operating region:

$$-\phi_{d(i)} \leq u_i(t) \leq \phi_{d(i)},$$
$$-\phi_{r(i)} \leq u_{ri}(t) = b_i u_{oi}(t) - a_i u_i(t) \leq \phi_{r(i)}, \tag{44}$$

With respect to multiple actuators, the actuator amplitude and rate limits can be represented by $\phi_d = [\phi_{d(1)}, ..., \phi_{d(m)}]^T$ and $\phi_r = [\phi_{r(1)}, ..., \phi_{r(m)}]^T$. Diagonal matrices $W_1 = diag\{a_1, ..., a_m\}$ and

50

$W_2 = diag\{b_1, ..., b_m\}$, the operating constraints on multiple actuators can be shown as:

$$-\phi_d \leq u(t) \leq \phi_d,$$

$$-\phi_r \leq u_r(t) = W_2 u_c(t) - W_1 u(t) \leq \phi_r,$$

(45)

where $u(t) = [u_1(t), ..., u_m(t)]^T$ and $u_r(t) = [u_{r1}(t), ..., u_{rm}(t)]^T$.

3.2.2.2 Safety Margin

Although actuators have their extreme operating ranges due to the existence of power capacity, they are usually constrained within their corresponding operating regions. The difference between the physical limit and desired operating limit is named as safety margin $\Delta\phi_{di}$ for the ith actuator, as shown in Fig. 3.17.
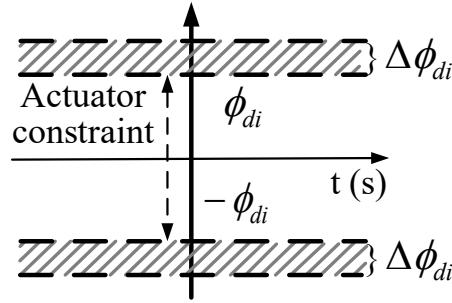
Figure 3.17: Illustration of the safety margin.

In this thesis, since the system's ultimate control input is synthesized by a normal and an additional control inputs, the idea of *safety margin* is employed for ensuring the availability of additional control input when the normal controller violates its constraint.

As shown in Fig. 3.17, the normal control input is under the ith actuator constraint $[-\phi_{di}, \phi_{di}]$. Then, both the ith additional control input and ultimate control input are set to be limited within $[-\phi_{di} - \Delta\phi_{di}, \phi_{di} + \Delta\phi_{di}]$, which is the sum of the ith actuator constraint and its *safety margin*. Therefore, even though the nominal controller saturates, the effectiveness of additional control input can be guaranteed, because it is still constrained in $[-\Delta\phi_{di}, \Delta\phi_{di}]$. This design technique is of significant importance in practical implementation.

3.2.2.3 State Constraints

In addition to actuator saturation, for the case of USV turning, extremely abrupt turns and undesirable motion may even capsize it due to the existence of inertia. Thus, preventing the yaw rate from reaching its limit cannot be neglected in practice as well.

The limit of the jth state (yaw rate is considered) is assumed to be $\phi_{s(j)}$, and the jth state is constrained within the following safety boundary:

$$-\phi_{s(j)} \leq x_j(t) \leq \phi_{s(j)}, \ j \in [1,...,n]. \tag{46}$$

For multiple state constraints, they can be denoted as $\phi_s = [\phi_{r(1)}, ..., \phi_{r(n)}]^T$. Hence, the operating constraints on multiple states can be expressed as:

$$-\phi_s \leq x(t) \leq \phi_s, \tag{47}$$

where $x(t) = [x_1(t), ..., x_n(t)]^T$.

3.2.3 Normal Controller Design

It is well known that the steady state error can be effectively eliminated by the integral action [105], the corresponding augmented state-space description of (41) can then be defined as:

$$\begin{cases} \dot{x}_a(t) = A_a x_a(t) + B_a u(t) + G_a w_a(t) \\ y_a(t) = C_a x_a(t), \end{cases} \tag{48}$$

where $x_a(t) = \left[(\int_0^t \epsilon(\tau)d\tau)^T, \ x^T(t)\right]^T$ and $y_a(t) = \left[(\int_0^t \epsilon(\tau)d\tau)^T, \ y^T(t)\right]^T$ are the augmented state vector and output vector, $\epsilon(t) = y_{ref}^T(t) - y^T(t)$ denotes the error between reference signal and output, $w_a(t) = \left[\omega^T(t), \ y_{ref}^T(t)\right]^T$ includes bounded external disturbance vector $\omega^T(t)$ and

reference input signal $y_{ref}^T(t)$. In addition, $A_a = \begin{bmatrix} 0 & -C \\ 0 & A \end{bmatrix} \in \Re^{(l+n)\times(l+n)}$, $B_a = \begin{bmatrix} 0 \\ B \end{bmatrix} \in$

$\Re^{(l+n)\times m}$, $C_a = \begin{bmatrix} I & 0 \\ 0 & C \end{bmatrix} \in \Re^{(l+p)\times(l+n)}$ and $G_a = \begin{bmatrix} 0 & I \\ G & 0 \end{bmatrix} \in \Re^{(l+n)\times(l+r)}$.

Incorporating the constraints of actuators (45) and states (47) into the augmented system (48)
[106], one can then obtain the following representations:

$$
\begin{cases}
\dot{\bar{x}}_a(t) = \bar{A}_a \bar{x}_a(t) + \bar{B}_a u(t) + \bar{G}_a w_a(t) \\
\bar{y}_a(t) = \bar{C}_a \bar{x}_a(t),
\end{cases}
\tag{49}
$$

where $\bar{x}_a(t) = [x_a(t), u(t)]^T \in \Re^{(l+n+2m)}$, $\bar{A}_a = \begin{bmatrix} A_a & B_a \\ 0 & W_1 \end{bmatrix} \in \Re^{(l+n+2m)\times(l+n+2m)}$, $\bar{B}_a =$

$[0, W_2]^T \in \Re^{(l+n+2m)\times m}$, $\bar{G}_a = [G_a, 0]^T \in \Re^{(l+n+2m)\times l}$, and $\bar{C}_a = [I_{q+n}, 0] \in \Re^{(l+n)\times(l+p+2m)}$.

Assumption 4 *The states of USV are available at every time instant, these variables are assumed to be measurable or observable.*

Based on *Assumption 4*, the controller with closed-loop state feedback and the integral term of tracking error can be formed by:

$$
u(t) = K \bar{x}_a(t) = K_e \int_0^t \epsilon(\tau) d\tau + K_x \bar{x}_a(t),
\tag{50}
$$

where $K = [K_e \ K_x] \in \Re^{(l+n+2m)\times(l+n+2m)}$.

As a result, integrating the augmented system (49) with the closed-loop state feedback control law (50), the closed-loop control system can be written as follows:

$$
\dot{\bar{x}}_a(t) = (\bar{A}_a + \bar{B}_a K \bar{C}_a)\bar{x}_a(t) + \bar{G}_a w_a(t).
\tag{51}
$$

The control law $u(t) = K \bar{C}_a \bar{x}_a(t)$ can be used as the output feedback control for the augmented system (49). For the sake of decreasing the difficulties of implementation, the displacements and

rates of actuators are not involved in feedback signals.

The design objectives thereby include:

- The closed-loop system is stable during normal operation, and the output $y(t)$ follows the reference signal $y_{ref}(t)$ without steady-state error, namely:

$$\lim_{t \to \infty} \epsilon(t) = 0. \tag{52}$$

The controller minimizes the following upper bound of linear-quadratic (LQ) cost function:

$$J = \int_0^t (\bar{x}_a^T(\tau) Q \bar{x}_a(\tau) + u^T(\tau) R u(\tau)) d\tau, \tag{53}$$

where $Q \in \Re^{l+n}$ and $R \in \Re^{l+m}$ are symmetric positive-semidefinite and positive definite weighting matrices, respectively.

- The USV is intended to follow the desired path in the event of external time-varying disturbances, when the closed-loop system is still stabilized and the required output $y(t)$ asymptotically tracks the reference signal $y_{ref}(t)$ with no steady-state error.

- The rudder and yaw rate obey their corresponding safe regions.

Theorem 2 *Consider the closed-loop system given in (51). For a known positive constant γ, if there exist positive symmetric matrices $X = \begin{bmatrix} X_{11} & 0 \\ X_{21} & X_{22} \end{bmatrix} \in \Re^{(l+n+2m) \times (l+n+2m)}$, $X_{11} = X_{11}^T$, and $Z = Z^T > 0 \in \Re^{(l+n+2m) \times (l+n+2m)}$, matrices $Y = [Y_1, 0] \in \Re^{n \times (l+n+2m)}$ lead to the following LMIs (54), (55), (56) and (57) hold, where the symbol $*$ represents a symmetric entry. Then system (51) can be stabilized by the controller $u(t) = K \bar{x}_a(t)$, where $K = [K_e, K_x] = Y_1^*(X_{11}^*)^{-1}$, and Y_1^* and X_{11}^* are the optimal solutions of Y_1 and X_{11}, and simultaneously meet the design requirements $u(t) \in [-\phi_d, \phi_d]$, $u_r(t) \in [-\phi_r, \phi_r]$, and $\bar{x}_a(t) \in [-\phi_s, \phi_s]$:*

54

$$
\begin{bmatrix}
\bar{A}_a X + \bar{B}_a Y + (\bar{A}_a X + \bar{B}_a Y)^T & \bar{G}_a & Y^T R^{1/2} & XQ^{1/2} \\
* & -\gamma I & 0 & 0 \\
* & * & -I & 0 \\
* & * & * & -I
\end{bmatrix} < 0, \tag{54}
$$

$$
\begin{bmatrix}
Z & * \\
I_{(l+n+i)}WX & \phi_d^2/r_{max}^2
\end{bmatrix} > 0, \ i = 1, ..., m, \tag{55}
$$

$$
\begin{bmatrix}
Z & * \\
-[0, W_{1(i)}]WX + W_{1(ii)}Y_{1(i)} & \phi_r^2/r_{max}^2
\end{bmatrix} > 0, \ i = 1, ..., m, \tag{56}
$$

$$
\begin{bmatrix}
Z & * \\
I_{(l+j)}WX & \phi_s^2/r_{max}^2
\end{bmatrix} > 0, \ i = 1, ..., n, \tag{57}
$$

where Y^* and X^* stand for the optimal results of LMIs (54), (55), (56) and (57). γ is related to the H_∞ norm of $T_{zw_a}(s)$ from the bounded external disturbance to the performance output [18], and $P = P^T$. $W = [\bar{C}_a^T(\bar{C}_a\bar{C}_a^T)^{-1}, \bar{C}_a^\perp]$, $\bar{C}_a^\perp$ represents the orthogonal basis for the null space of $\bar{C}_a$. $W_{1(i)}$ and $Y_{1(i)}$ denote the ith rows of matrices W_1 and Y_1. $I_{(l+n+i)}$ and $I_{(l+j)}$ respectively stand for the $(l + n + i)$th and $(l + j)$th row of identical matrix I. In addition, the upper bound of cost performance index (53) can be represented as:

$$
J \leqslant \gamma^2 \int_0^t w_a^T(\tau)w_a(\tau)d\tau + \bar{x}_a^T(0)X^{-1}\bar{x}_a(0). \tag{58}
$$

Proof of Theorem 2: Based on *Lemma 1* in [105], its sufficient condition can be rewritten by synthesizing the USV control system with the performance constraints of LQ and closed-loop H_∞ norm as:

$$
(\bar{A}_a + \bar{B}_a K)^T P + P(\bar{A}_a + \bar{B}_a K) + K^T RK + Q + (\frac{1}{\gamma^2})P\bar{G}_a\bar{G}_a^T P < 0. \tag{59}
$$

According to the *Reciprocal Projection Lemma* in [107], apply the Schur complement [108] and let $P = X^{-1}$, (59) can be rewritten as (60).

$$
\begin{bmatrix} Q + (\frac{1}{\gamma^2})P\bar{G}_a\bar{G}_a^T P + K^T R K + P - (Y + Y^T) & (\bar{A}_a + \bar{B}_a K)^T P + Y^T \\ P(\bar{A}_a + \bar{B}_a K) + Y & -P \end{bmatrix}
$$
$$
= \begin{bmatrix} \bar{A}_a X + \bar{B}_a Y + (\bar{A}_a X + \bar{B}_a Y)^T & \bar{G}_a & Y^T R^{1/2} & X Q^{1/2} \\ * & -\gamma^2 I & 0 & 0 \\ * & * & -I & 0 \\ * & * & * & -I \end{bmatrix} < 0. \tag{60}
$$

Furthermore, substituting $u(t) = K\bar{x}_a(t)$ in (50), and $P = X^{-1}$ into the performance index (53), (61) can be obtained which is exactly the same as inequality (58).

$$
J = \int_0^t \bar{x}_a^T(\tau)(Q + K^T R K)\bar{x}_a(\tau)d\tau < -\int_0^t \bar{x}_a^T(\tau)[(\bar{A}_a + \bar{B}_a K)^T P + P(\bar{A}_a + \bar{B}_a K)
$$
$$
+ \frac{1}{\gamma^2}P\bar{G}_a\bar{G}_a^T P]\bar{x}_a(\tau)d\tau \leqslant -\int_0^t d(\bar{x}_a^T(\tau)P\bar{x}_a(\tau) + \gamma^2 \int_0^t w_a^T(\tau)w_a(\tau)d\tau \tag{61}
$$
$$
\leqslant \gamma^2 \int_0^t w_a^T(\tau)w_a(\tau)d\tau + \bar{x}_a^T(0)X^{-1}\bar{x}_a(0).
$$

The inequality (55) is used to limit the actual angle of ith actuator within the safe operating region $\phi_{d(i)}$. Employing Schur's complement, (55) equals to

$$
P = X^{-1} \geq I_{l+n+i}^T \frac{r_{max}^2}{\phi_{d(i)}^2} I_{l+n+i}
$$
$$
\Rightarrow \phi_{d(i)}^2 \geq X^{\frac{1}{2}} I_{l+n+i}^T I_{l+n+i} X^{\frac{1}{2}} r_{max}^2 \geq \alpha_{max}(X^{\frac{1}{2}} I_{l+n+i}^T I_{l+n+i} X^{\frac{1}{2}} r_{max}^2)
$$
$$
\geq max_{|\bar{x}_{aa}(t)| \geq r_{max}^2} ||I_{l+n+i} X^{\frac{1}{2}} \bar{x}_{aa}(t)||^2 \geq \max_{|X^{-\frac{1}{2}}\bar{x}_a(t)| \geq r_{max}^2} ||I_{l+n+i}\bar{x}_a(t)||^2
$$
$$
\geq \max_{\bar{x}_a \in \Omega} ||I_{l+n+i}\bar{x}_a(t)||^2 \geq (I_{l+n+i}\bar{x}_a(t))^2 = u_{(i)}^2(t),
$$

where $\alpha_{max}(\cdot)$ denotes the maximal eigenvalue and $i = 1, ..., m$.

Inequality (56) guarantees that the actual rate of ith actuator within the desired operating

boundary $\phi_{r(i)}$. Utilizing Schur's complement, (56) can be equivalent to

$$Z = (WX)^T P(WX) \geq (-W_{1(i)}WX + W_{1(ii)}Y_{1(i)})^T \frac{r_{max}^2}{\phi_{rate(i)}^2}(-W_{1(i)}WX + W_{1(ii)}Y_{1(i)})$$

$$\Rightarrow \phi_{r(i)}^2 \geq X^{\frac{1}{2}}(WX)^{-T}(-W_{1(i)}WX + W_{1(ii)}Y_{1(i)})^T(-W_{1(i)}WX + W_{1(ii)}Y_{1(i)})(WX)^{-1}r_{max}^2$$

$$\geq \alpha_{max}(X^{\frac{1}{2}}(-W_{1(i)} + W_{1(ii)}Y_{1(i)}(WX)^{-T})^T(-W_{1(i)} + W_{1(ii)}Y_{1(i)}(WX)^{-1})X^{\frac{1}{2}}r_{max}^2)$$

$$\geq \max_{|\bar{x}_{aa}(t)| \geq r_{max}^2} ||(-W_{1(i)} + W_{1(ii)}K\bar{C}_a)X^{\frac{1}{2}}\bar{x}_{aa}(t)||^2$$

$$\geq \max_{|X^{-\frac{1}{2}}\bar{x}_a(t)| \geq r_{max}^2} ||(-W_{1(i)} + W_{1(ii)}K\bar{C}_a)\bar{x}_a(t)||^2$$

$$\geq (-W_{1(i)}u(t) + W_{1(ii)}K\bar{C}_a\bar{x}_a(t))^2 = u_{r(i)}^2(t).$$

Inequality (57) is exploited to constrain the actual jth state of controlled system within the expected operating limit $\phi_{s(j)}$. Using Schur's complement, (57) equals to

$$P = X^{-1} \geq I_{l+j}^T \frac{r_{max}^2}{\phi_{s(j)}^2}I_{l+j}$$

$$\Rightarrow \phi_{s(j)}^2 \geq X^{\frac{1}{2}}I_{l+j}^T I_{l+j}X^{\frac{1}{2}}r_{max}^2 \geq \alpha_{max}(X^{\frac{1}{2}}I_{l+j}^T I_{l+j}X^{\frac{1}{2}}r_{max}^2)$$

$$\geq \max_{|\bar{x}_{aa}(t)| \geq r_{max}^2} ||I_{l+j}X^{\frac{1}{2}}\bar{x}_{aa}(t)||^2 \geq \max_{|X^{-\frac{1}{2}}\bar{x}_a(t)| \geq r_{max}^2} ||I_{l+j}\bar{x}_a(t)||^2$$

$$\geq \max_{\bar{x}_a \in \Omega} ||I_{l+j}\bar{x}_a(t)||^2 \geq (I_{l+j}\bar{x}_a(t))^2 = \bar{x}_{a(j)}^2(t).$$

Therefore, the problem can be solved if conditions (54), (55), (56), and (57) are simultaneously satisfied with $K = Y_1(X_{11})^{-1}$. In addition, the closed-loop system can be stabilized under the actuator constraints of $u(t) \in [-\phi_d, \phi_d]$, $u_r(t) \in [-\phi_r, \phi_r]$, and state constraints of $\bar{x}_a(t) \in [-\phi_s, \phi_s]$.

Remark 1 *Using LMI Toolbox in Matlab [108], the upper bound of performance index (58) can be minimized by solving the optimization problem:* $\min Trace(Z)$ *subject to (55), (56), and (57). Conditions (55), (56) and (57) guarantee that the amplitude and rate of actuators, and states are limited within their safe regions. The normal controller can be synthesized by $K = Y_1^*(X_{11}^*)^{-1}$.*

3.2.4 Active Disturbance Compensating Tracking Controller Design

The mathematical representation of the ultimate control input $u_c(t)$ can be written as follows:

$$u_c(t) = u(t) + u_{ad}(t), \tag{62}$$

where $u_{ad}(t)$ and $u(t)$ are the added and normal control inputs, respectively.
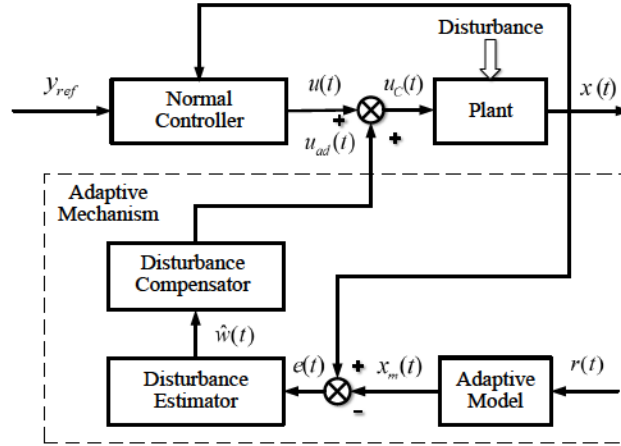
Figure 3.18: Schematic diagram of proposed control approach.

As shown in Fig. 3.18, the general idea of (62) can be illustrated as follows:

(1) first, the USV is operated by the normal controller in calm water;

(2) in the event of disturbance, a disturbance estimator is activated and estimate the amplitude of disturbance according to an adaptive estimation law;

(3) based on the estimated value, a disturbance compensator generates the appropriate control input $u_{ad}(t)$ to be combined with the normal control $u(t)$ for compensating disturbances.

3.2.4.1 Time-Invariant Disturbance Detection and Estimation

In order to effectively estimate the disturbances, an adaptive observer is constructed as:

$$\dot{\hat{x}}_a(t) = \bar{A}_a \hat{x}_a(t) + \bar{B}_a u(t) + \bar{G}_a \hat{w}_a(t) + L(\hat{x}_a - \bar{x}_a), \tag{63}$$

where $\hat{x}(t)$ and $\hat{w}(t)$ denote the estimated values of the state and external disturbances, respectively. L is the observer gain matrix, which is selected to make $A_L = (\bar{A}_a + L)$ Hurwitz.

The state error $e(t) = \hat{x}_a(t) - \bar{x}_a(t)$ is obtained from (49) and (63), the derivative of the state error can then be denoted as:

$$\dot{e}(t) = \dot{\hat{x}}_a(t) - \dot{\bar{x}}_a(t) = A_L e + \bar{G}_a \tilde{w}_a(t), \tag{64}$$

where $\tilde{w}_a(t) = \hat{w}_a(t) - w_a(t)$ is estimated disturbance error and $\tilde{w}_a(t) = diag[\tilde{w}_{a1}(t)...\tilde{w}_{an}(t)]$.

Assumption 5 *The disturbance can be seen as constant in every neighbouring sampling time since the frequency of disturbance is relative low comparing with the fast sampling time of sensors.*

Then, the following result can be achieved based on *Assumption 5*:

$$\dot{\tilde{w}}_a(t) = \dot{\hat{w}}_a(t) - \dot{w}_a(t) = \dot{\hat{w}}_a(t). \tag{65}$$

Theorem 3 *There exist symmetric positive definite matrices P, $Q \in \Re^{(l+n+2m)\times(l+n+2m)}$, an observer gain $L \in \Re^{n\times(l+n+2m)}$, and a matrix $H \in \Re^{r\times(l+n+2m)}$, such that the following conditions hold:*

$$PA_L + A_L^T P = -Q, \ \ and \ \ \bar{G}_a^T P = H, \tag{66}$$

and $\dot{\hat{w}}_a(t)$ is determined by the following adaptive estimation law:

$$\dot{\hat{w}}_a(t) = Proj_{[\underline{w},\overline{w}]}\{-k\bar{G}_a^T Pe(t)\}$$
$$= \begin{cases} 0 & if \ \hat{w}_a(t) = \underline{w}, -k\bar{G}_a^T Pe(t) \leqslant 0 \\ & or \ \hat{w}_a(t) = \overline{w}, -k\bar{G}_a^T Pe(t) \geqslant 0, \\ -k\bar{G}_a^T Pe(t) & otherwise, \end{cases} \tag{67}$$

where $k > 0$ denotes the adaptive law gain, $Proj\{\cdot\}$ is the projection operator [100] employed for projecting the estimates $\hat{w}_a(t)$ to an acceptable interval $[\underline{w},\overline{w}]$.

Proof of Theorem 3: The Lyapunov candidate function can be chosen as follows:

$$V_{sf} = e^T(t)Pe(t) + \frac{\tilde{w}_a^T(t)\tilde{w}_a(t)}{k}. \tag{68}$$

Then, the derivative of V_{sf} is written as:

$$\dot{V}_{sf} = e^T(t)[PA_L + A_L P]e(t) + 2e^T(t)P\bar{G}_a\tilde{w}_a(t) + 2\frac{\dot{\tilde{w}}_a^T\tilde{w}_a}{k}. \tag{69}$$

If the following inequality is selected:

$$\dot{\hat{w}}_a = \dot{\tilde{w}}_a \leqslant -k\bar{G}_a^T Pe(t), \tag{70}$$

and (67) is chosen as the adaptive law. Thus, inequality (69) can be rewritten as:

$$\dot{V}_{sf} \leqslant e^T(t)[P(\bar{A}_a + \bar{B}_a F) + (\bar{A}_a + \bar{B}_a F)^T P]e(t). \tag{71}$$

If there is a symmetric positive definite matrix Q, such that the following equality holds:

$$P(\bar{A}_a + \bar{B}_a F) + (\bar{A}_a + \bar{B}_a F)^T P = -Q. \tag{72}$$

Substituting the above Eq. (72) into (71), it is derived that:

$$\dot{V}_{sf} = -e^T(t)Qe(t) < 0. \tag{73}$$

From (73), it follows that $V \in L^\infty$, and according to (68), it implies that $e(t) \in L^\infty$. So far, the augmented state error Eq. (64) is stabilized, moreover $e(t) \in L^2$ is implied by integrating both sides of (73) from 0 to ∞. Thus, the proof of *Theorem 3* is finished.

Remark 2 *Using the aforementioned approach, the disturbance can be estimated by:*

$$\hat{w}_a = -k\bar{G}_a^T P \int_{t_d}^{t} e(\tau)d\tau. \tag{74}$$

In essence, this approach only contains a pure integral term, it is difficult to deal with the time-varying disturbances. Thus, an additional correction procedure is needed.

3.2.4.2 Time-Varying Disturbance Estimation Correction

Generally, the environmental disturbances are time-varying. With respect to the USV control system design, a challenging issue is to avoid the 1st-order wave-induced time-varying disturbances [50]. In this thesis, a time-varying estimation method is developed, its basic idea is to combine an additional correction mechanism with the previously designed estimation law [109].

Theorem 4 *If disturbance $w_a(t)$ is time-varying, an enhanced disturbance estimation scheme is established as $\hat{w}_c(t) = \hat{w}_a(t) - L_0(t)e(t)$, where $\hat{w}_a(t) = L_0(t)e(t)$ denotes the approximated relationship between $e(t)$ and $\hat{w}_a(t)$, and $L_0(t)$ is achieved by integrating (75) on-line.*

$$\dot{L}_0(t) = -(L_0(t)A_L + L_0(t)\bar{G}_a L_0(t) + k\bar{G}_a^T P), \tag{75}$$

where $L_0(t)$ specifies the correction gain, and $A_L = \bar{A}_a - L$.

Proof of Theorem 4: Assuming that:

$$\hat{w}_a(t) = L_0(t)e(t). \tag{76}$$

In order to satisfy the condition that $\dot{V}_{sf} < 0$, Eq. (76) should be consistent with (67). The derivative of Eq. (76) can then be written as:

$$\dot{\hat{w}}_a(t) = \dot{L}_0(t)e(t) + L_0(t)\dot{e}(t) = \dot{L}_0(t)e(t) + L_0(t)(A_L e(t) + \bar{G}_a \tilde{w}_a(t)). \tag{77}$$

61

When disturbances present, substituting $\dot{\hat{w}}_a(t) = Proj_{[\underline{w},\overline{w}]}\{-k\bar{G}_a^T Pe(t)\} = -k\bar{G}_a^T Pe(t)$ and Eq. (76) into Eq. (77), the following matrix differential equation can be obtained:

$$\dot{L}_0(t) = -(L_0(t)A_L + L_0(t)\bar{G}_a L_0(t) + k\bar{G}_a^T P). \tag{78}$$

Hence, from Eq. (76), the time-varying disturbance estimation scheme is then achieved as $\hat{w}_c(t) = \hat{w}_a(t) - L_0(t)e(t)$. Proof of *Theorem 4* is completed.

Eventually, the time-varying disturbance estimation laws can be obtained:

$$\dot{\tilde{w}}_a(t) = \dot{\hat{w}}_a(t) = Proj_{[\underline{w},\overline{w}]}\{-k\bar{G}_a^T Pe(t)\}, \tag{79}$$

where $\hat{w}_c(t) = \hat{w}_a(t) - L_0(t)e(t)$.

3.2.4.3 Disturbance Compensating under State and Control Input Constraints

An appropriate disturbance compensating input $u_{ad}^*(t)$ can be calculated by:

$$\min_{u_{ad}(t)\in\Re^n} ||\bar{B}_a u_{ad}(t) + \bar{G}_a \hat{w}_c(t)||, \tag{80}$$

subject to

$$S\bar{B}_a u_{ad}(t) \leq -S\bar{A}_a e(t) - H_w, \tag{81}$$

$$Eu_{ad}(t) \leq T - Eu(t), \tag{82}$$

where state constraints are defined by S and F, and control input constraints are represented by matrices E and T, $H_w = max(S\bar{G}_a \hat{w}_c(t))$.

Remark 3 *Due to the fact that actuators cannot produce unlimited output to compensate the external disturbances, the actuator constraint (81) is employed to limit the boundary of actuators. In view of (82), when the normal control input exists, the constraint of additional control input is the*

result of overall control input constraint subtracts the normal control input.

As a result, considering Eqs. (62), (79), (80), and normal control input together, the ultimate control input can be achieved:

$$u_c(t) = u(t) + u_{ad}(t) = K\bar{x}_a(t) + u^*_{ad}(t). \tag{83}$$

Proposition 1 *If the control law (83) is applied to the closed-loop system (49), the control input constraint of normal controller is satisfied, and the optimization problems (80, 81, 82) are feasible, then the state and control input constraints $S\dot{\hat{x}}_a(t) \leq F$ and $Eu_c(t) \leq T$ can be guaranteed.*

Proof of Proposition 1: For the convenience of proving *Proposition 1*, the state and control input constraints for normal controller can be restated as:

$$Eu(t) \leq T - \Delta T, \tag{84}$$

$$S\dot{\bar{x}}_a(t) \leq F, \tag{85}$$

where ΔT is the *safety margin*.

Applying (83) and $e(t) = \hat{x}_a(t) - \bar{x}_a(t)$, the estimated state $\hat{x}_a(t)$ can be obtained:

$$\dot{\hat{x}}_a(t) = \dot{\bar{x}}_a(t) + \bar{A}_a e(t) + \bar{B}_a u_{ad}(t) + \bar{G}_a \hat{w}_c(t). \tag{86}$$

Assuming constraints (81) and (85) are satisfied, the following inequality can be obtained:

$$S\bar{B}_a u_{ad}(t) + S\dot{\bar{x}}_a(t) + S\bar{A}_a e(t) + H_w \leq F. \tag{87}$$

Thus, the following inequality can be achieved by pre-multiplying Eq. (86) by S:

$$S\dot{\hat{x}}_a(t) = S\bar{B}_a u_{ad}(t) + S\dot{\bar{x}}_a(t) + S\bar{A}_a e(t) + S\bar{G}_a \hat{w}_c(t), \tag{88}$$

furthermore, since $H_w = max(S\bar{G}_a \hat{w}_c(t))$, then

$$S\dot{\hat{x}}_a(t) \leq S\bar{B}_a u_{ad}(t) + S\dot{\tilde{x}}_a(t) + S\bar{A}_a e(t) + H_w \leq F. \tag{89}$$

When (82) is satisfied, pre-multiplying Eq. (83) by E, and incorporating (82) into Eq. (83):

$$Eu_c(t) = Eu(t) + Eu_{ad}(t) \leq Eu(t) + T - Eu(t) \leq T. \tag{90}$$

So far, the constraints of state $S\dot{\tilde{x}}_a(t) \leq F$ and control input $Eu_c(t) \leq T$ are both satisfied.

Remark 4 *$u_{ad}^*(t)$ is calculated by quadratic programming (QP) [110]. The computational load is not a concern since it is a low-dimension optimization problem.*

Remark 5 *In addition to compensating environmental disturbances, the proposed control method is intended to optimize the performance of the normal controller as well, it makes sense as it can also guarantee the optimal performance when USV works in the calm water.*

Table 3.2: System parameters used in the simulation

Parameter	Value
m_{11}	$25.8\ [kg]$
m_{22}	$33.8\ [kg]$
m_{33}	$2.76\ [kg]$
d_{11}	12
d_{22}	17
d_{33}	0.5
b_2	0.0028385
W_1	1
W_2	1

3.2.5 Simulation Results

The selected parameters for the nonlinear USV model [111] are listed in Table 3.2. The length of the selected USV is $1.2\ m$, and its mass is $17.5\ kg$. In this case study, a straight line path that is

along the trajectory of line $y = 2\ m$, starts from $x = 0\ m$ to $x = 20\ m$ is selected as the desired path. The surge speed is fixed at $u = 0.1\ m/s$. The initial position and orientation of the ship are chosen as $1.6\ m, 1\ m$ and $\psi = 90\ deg$, respectively. As listed in Table 3.3, the performance of five controllers are compared in the simulation.

Table 3.3: Illustration of controllers that are compared in the simulation

Name	Illustration
Controller-1	Normal controller with consideration of actuator and state constraints
Controller-2	TI-ADCTC with consideration of actuator and state constraints
Controller-3	TV-ADCTC with consideration of actuator and state constraints, which is the proposed controller
Controller-4	TV-ADCTC without consideration of actuator and state constraints
Controller-5	Normal controller without consideration of actuator and state constraints

Note: TI-ADCTC is the time-invariant adaptive disturbance compensating tracking controller, while TV-ADCTC is the time-varying adaptive disturbance compensating tracking controller.

The bound of rudder deflection is set to be $[-35\ deg,\ 35\ deg]$, the maximum rudder speed is constrained within $[-20\ deg/s,\ 20\ deg/s]$. To avoid abrupt turns, the yaw rate is limited in $[-20\ deg/s,\ 20\ deg/s]$. Furthermore, the *safety margin* is chosen as $\Delta T = [7\ deg,\ 7\ deg]^T$. Thus, the corresponding matrices E, F, S and T are given by:

$$E = \begin{bmatrix} 1 \\ -1 \end{bmatrix}, \quad F = \begin{bmatrix} 20 \\ 20 \end{bmatrix}, \quad S = \begin{bmatrix} 0 & 0 & 0 & 1 & 0 & 0 \\ 0 & 0 & 0 & -1 & 0 & 0 \end{bmatrix}, \quad \text{and } T = \begin{bmatrix} 35 \\ 35 \end{bmatrix}. \tag{91}$$

In this simulation, two kinds of disturbances are considered, namely first-order and second-order disturbances, mimicking the effects of waves and currents. The constant disturbance is selected as $-0.4\ m/s^2$, while the sinusoidal is represented as $0.4 sin(0.1t)\ m/s^2$. Both of them act on the lateral direction and vanish after a certain amount of time. In this case, the maximum deflection of disturbance is chosen as $H_w = [0.5\ m/s^2,\ -0.5\ m/s^2]^T$.
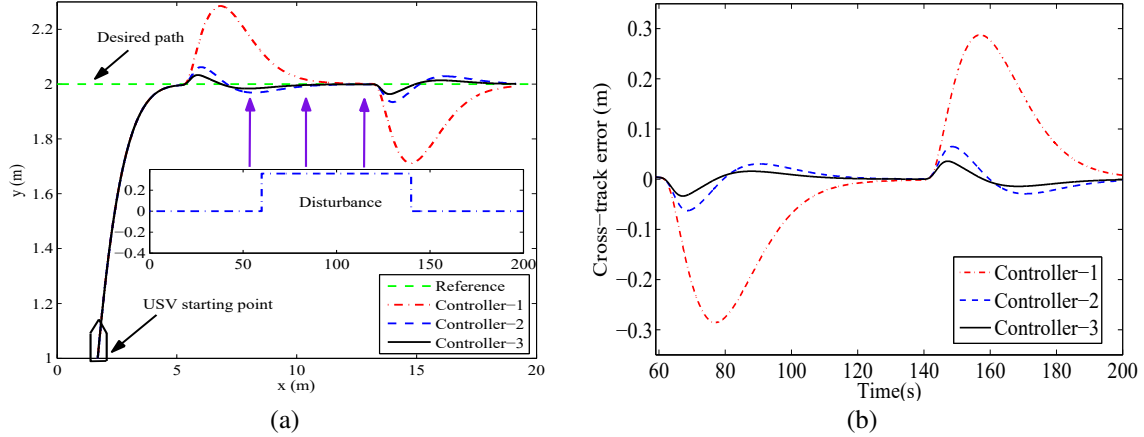
Figure 3.19: The comparison of path following performance.

3.2.5.1 Scenarios Description

To demonstrate the effectiveness of the proposed method, three scenarios are included:

(1) In *Scenario 1*, the constant disturbance, which occurs at 60th second and disappears at 140th second, is imposed in the system when USV is following a straight line path.

(2) In *Scenario 2*, the proposed approach is further validated under one set of sinusoidal disturbance, which is imposed at 60th second and lasts to the end of path following.

(3) In *Scenario 3*, to verify the effectiveness of the actuator saturation prevention mechanism of the proposed method, another constant disturbance with the amplitude of $0.5\ m/s^2$, which lasts from 60th to 140th second, is imposed into system as well.

3.2.5.2 Results of Scenario 1 and Evaluation

From Fig. 3.19(a), the performance achieved by the proposed Controller-3 is superior than that of the Controller-1 and Controller-2 in the presence of environmental disturbance.

More specifically, as shown in Fig. 3.19(b), 3.20(a) and Table 3.4, in the case of Controller-1, the maximal cross-track and heading errors are $0.28\ m$ and $23\ deg$, respectively. It is worthy to mention that the deviation can be gradually reduced due to the effect of tracking error integral action. In addition, around $0.065\ m$ of maximal cross-track error and $10\ deg$ of maximal

66

heading error are yielded by the disturbance under the operation of Controller-2. Comparing with Controller-1 and Controller-2, the errors of cross-track and heading angle are significantly eliminated by the Controller-3. The maximal cross-track and heading errors are within $0.03\ m$ and $7\ deg$, respectively. As illustrated in Fig. 3.20(b) and Table 3.4, although the yaw rate generated by three controllers are all within the limits of yaw rate, Controller-3 can compensate the external disturbance with the minimal yaw rate (about $4\ deg/s$).
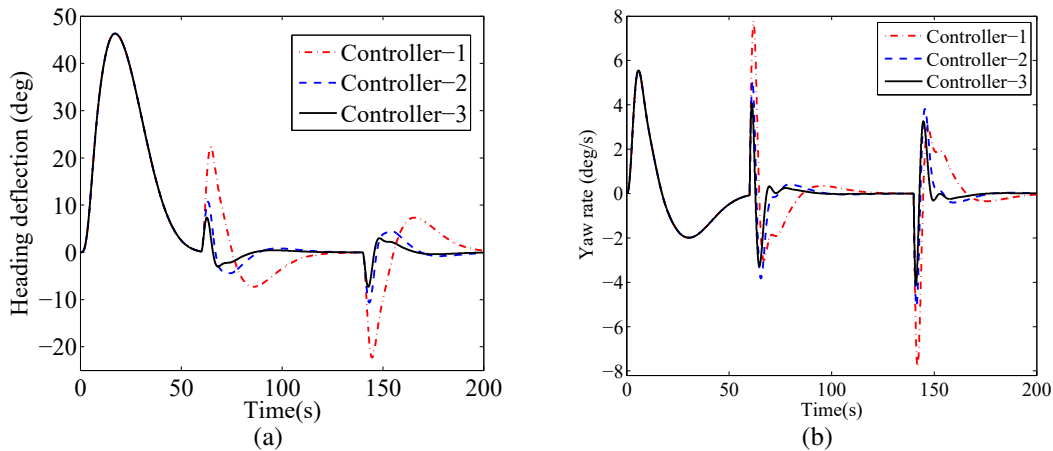
Figure 3.20: The responses of heading deflection and yaw rate.
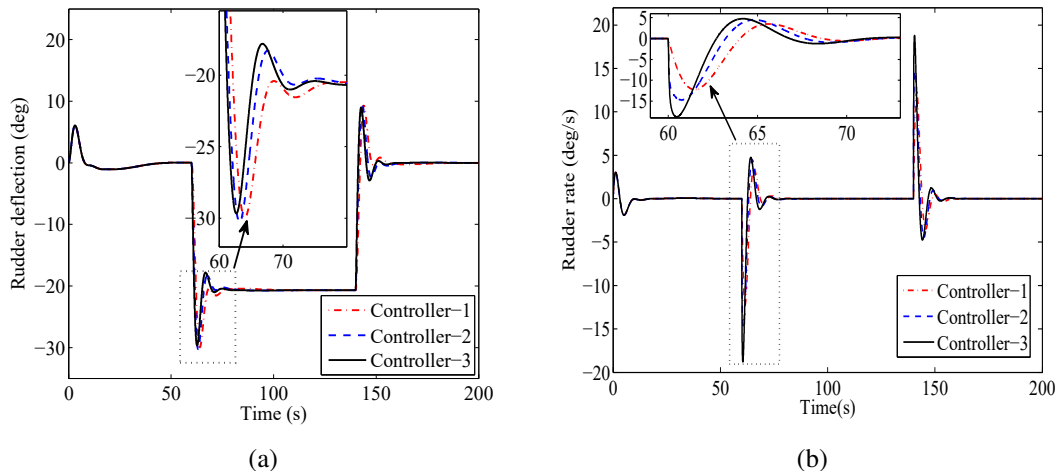
Figure 3.21: The responses of rudder deflection and rudder rate.

As can be observed in Fig. 3.21(a), Fig. 3.21(b) and Table 3.4, the control inputs of the three controllers are all under the limitations of USV's rudder. Moreover, Controller-3 is capable of

Table 3.4: Performance comparison of different control schemes

Performance Index	Controller-1	Controller-2	Controller-3
Maximal cross-track error	$0.28\ m$	$0.065\ m$	$0.03\ m$
Maximal heading error	$23\ deg$	$10\ deg$	$7\ deg$
Maximal yaw rate	$7.8\ deg/s$	$5.2\ deg/s$	$4\ deg/s$
Maximal rudder deflection	$-30.5\ deg$	$-30\ deg$	$-29.5\ deg$
Maximal rudder rate	$12\ deg/s$	$15\ deg/s$	$20\ deg/s$
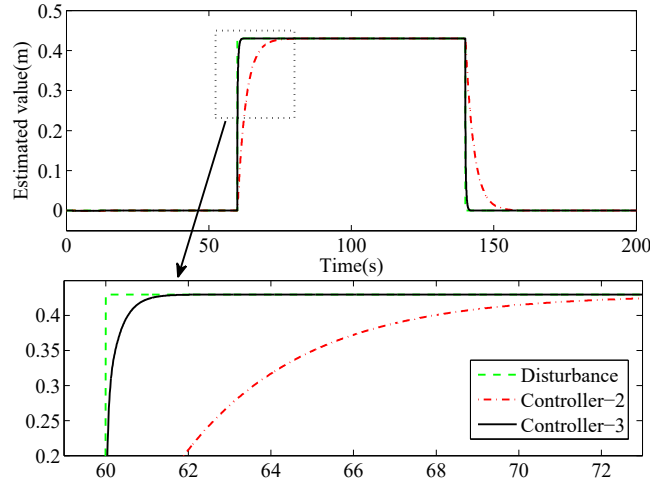
Figure 3.22: Sinusoid disturbance estimation performance.

operating the rudder promptly to accommodate the effects of disturbance.

As displayed in Fig. 3.22, the convergence speed of disturbance estimation error of Controller-3 is faster than that of Controller-2.

Table 3.5: Performance comparison of different control schemes

Performance Index	Controller-1	Controller-2	Controller-3
Maximal cross-track error	$0.3\ m$	$0.12\ m$	$0.05\ m$
Maximal heading error	$35\ deg$	$15\ deg$	$6\ deg$
Maximal yaw rate	$6.5\ deg/s$	$3.5\ deg/s$	$2.5\ deg/s$
Maximal rudder deflection	$24\ deg$	$22\ deg$	$21\ deg$
Maximal rudder rate	$4.8\ deg/s$	$6.7\ deg/s$	$9.9\ deg/s$

3.2.5.3 Results of Scenario 2 and Evaluation

In this scenario, the path following results of the compared three controllers are demonstrated in Fig. 3.23(a). With respect to path following, faster convergence and less oscillation are obtained by Controller-3 rather than other two controllers.
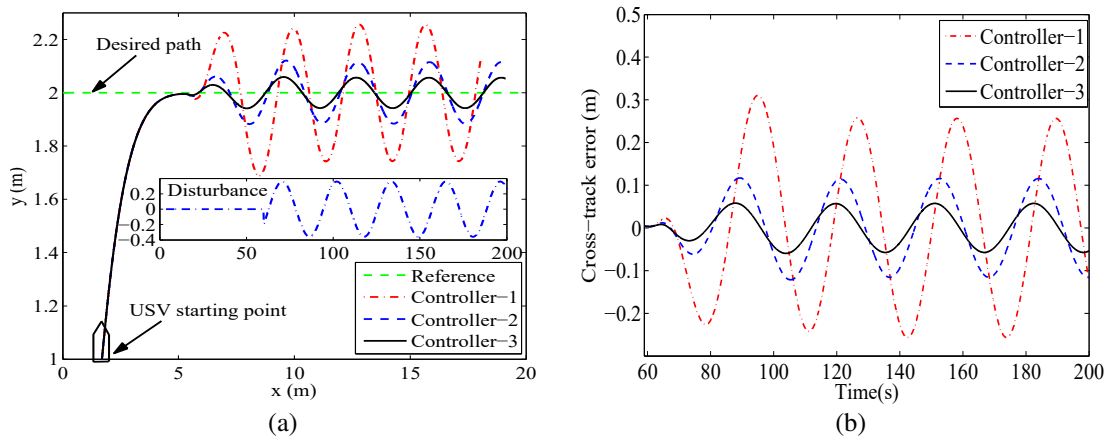
Figure 3.23: The comparison of path following performance.
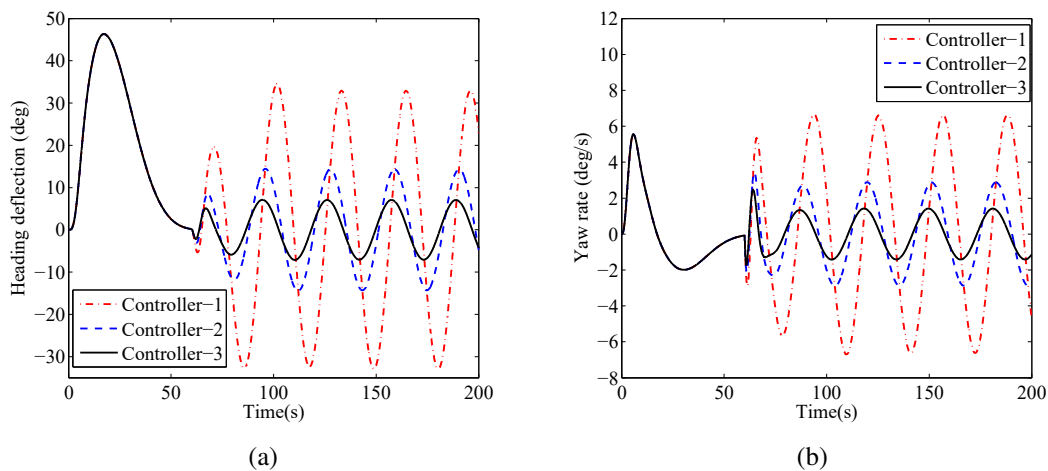
Figure 3.24: The responses of heading deflection and yaw rate.

As can be observed in Figs. 3.23(b), 3.24(a) and Table 3.5 that Controller-3 has a slight overshoot in both cross-track and heading errors ($0.05\ m$ and $6\ deg$) in the presence of disturbance. However, about $0.3\ m$ of cross-track error and $35\ deg$ of heading error are produced when Controller-1 is commissioned, and around $0.12\ m$ of cross-track error and $15\ deg$ of heading error are generated under the supervision of Controller-2. Fig. 3.24(b) shows that the yaw rate produced

69
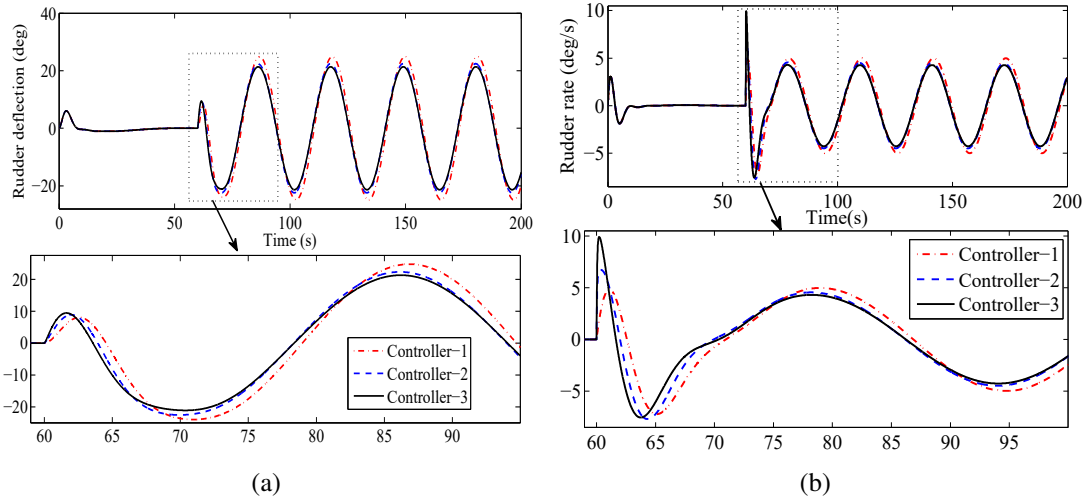
Figure 3.25: The responses of rudder deflection and rudder rate.

by these three controllers are all within the constraints of the yaw rate. However, Controller-3 can reject the external disturbance with minimal yaw rate, which can reduce the chance of capsizing.

As displayed in Fig. 3.25(a), Fig. 3.25(b) and Table 3.5, the rudder deflection and rate produced by three controllers are all within their constraints. However, more prompt rudder action is triggered by Controller-3, in other words, the USV's heading angle can be adjusted to compensate the environmental disturbance with less time delay. This leads to the smaller cross-track and heading angle errors, and superior performance of path following.

From Fig. 3.26, the disturbance is estimated by either Controller-2 or Controller-3, while it is evident that the proposed control scheme can improve the speed of disturbance estimation.

3.2.5.4   Results of Scenario 3 and Evaluation

The advantage of the proposed control strategy with consideration of actuator and state characteristics is verified by the performance comparisons of Controller-3, Controller-4, and Controller-5. As illustrated in Fig. 3.27(a) and Fig. 3.27(b), about $0.04\ m$ of maximal cross-track error is yielded by Controller-3 in the event of disturbance. However, the USV that is operated by either Controller-4 or Controller-5 cannot follow the desired path.

Fig. 3.28(a) and Fig. 3.28(b)) shows that nearly $8/deg$ of maximal heading error is generated by Controller-3. Meanwhile, yaw rate constraints are violated by both Controller-4 and Controller-5.

70
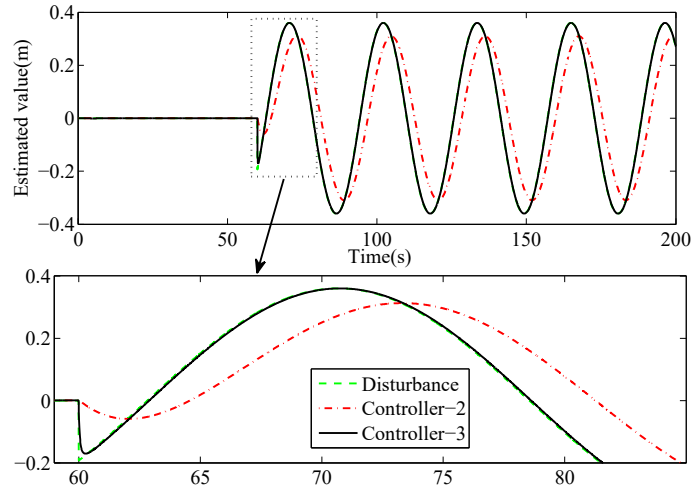
Figure 3.26: Sinusoid disturbance estimation performance.

(a)

(b)
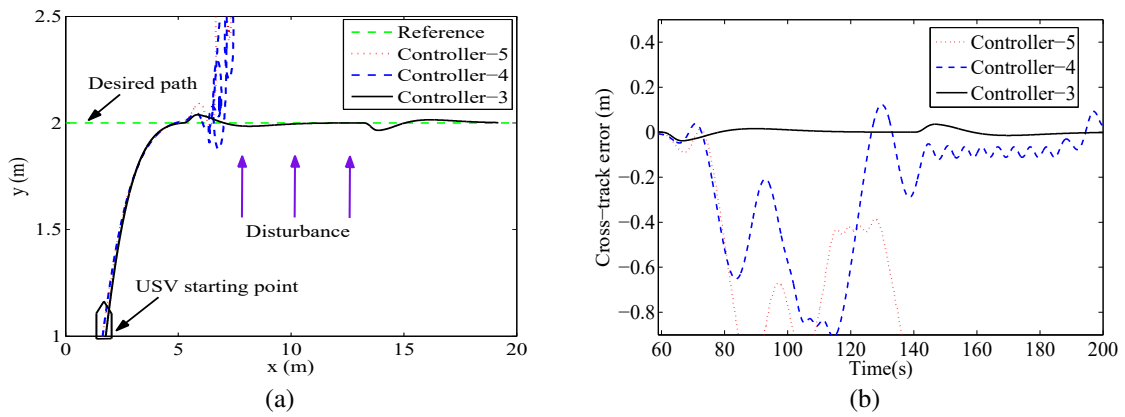
Figure 3.27: Performance comparison of path following.

From Fig. 3.29(a) and Fig. 3.29(b)), rudder deflection and rate are oscillatory in the case of Controller-4 and Controller-5, while the Controller-3 drives the rudder more smoothly. When the disturbance presents, Controller-3 can still perform without violating the constraints of actuator, whereas the actuators under the operation of the other two controllers are saturated. Therefore, Controller-3 enables the control signals to operate the rudder to react more gently than the other two controllers. This is of significant importance in practice because the excessive utilization of rudder is the primary cause of wear and tear. In addition, over-quick turning of USV may increase the possibility of capsizing.

(a)　　　　　　　　　　　　(b)
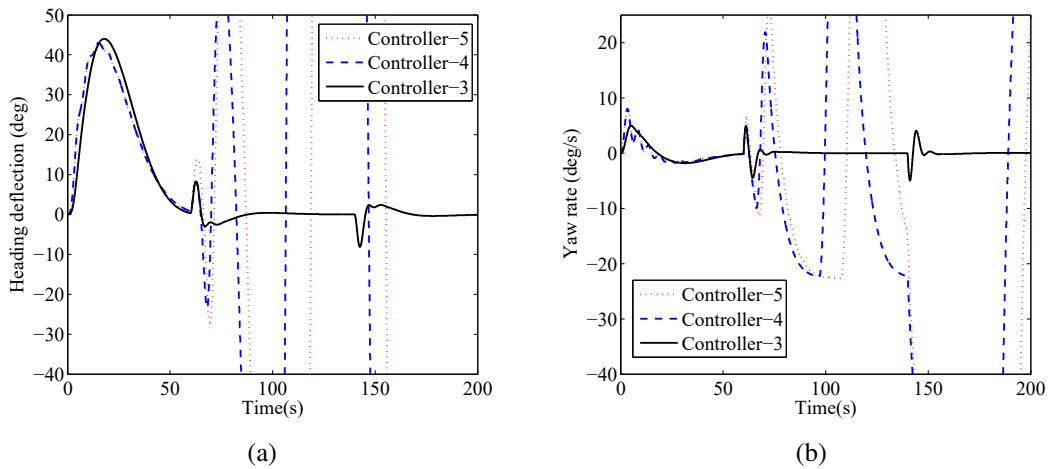
Figure 3.28: The responses of heading deflection and yaw rate.

(a)　　　　　　　　　　　　(b)
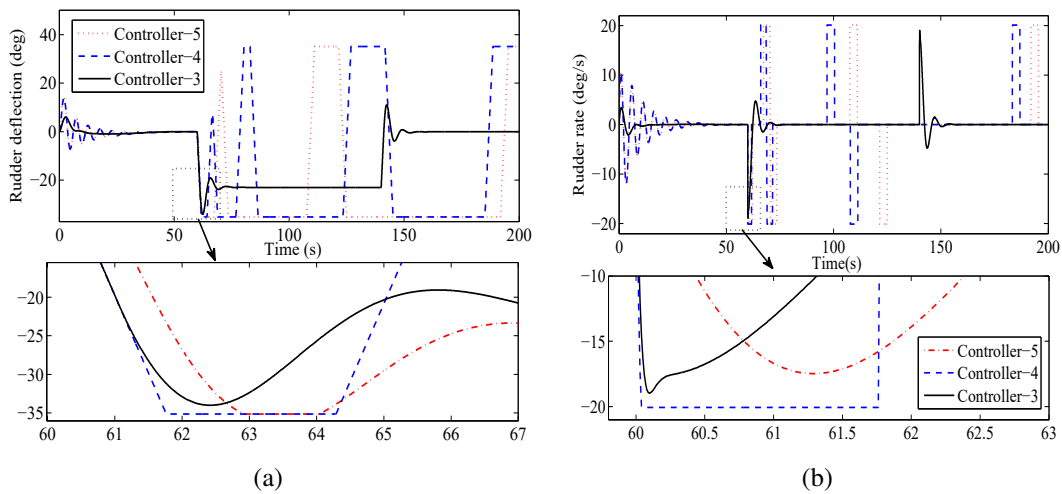
Figure 3.29: The responses of rudder deflection and rudder rate.

Chapter 4

Reliable and Safe Control of Unmanned Vehicles

In this chapter, the problems of reliable and safe control of UVs in the presence of actuator faults, saturation, and variations of working conditions are studied. Section 4.1 presents a new passive FTC strategy for the compensation of actuator faults of unmanned quadrotor helicopter (UQH); section 4.2, 4.3, and 4.4 introduce three different active FTC schemes mitigating the negative effects of actuator faults, while actuator dynamics are also considered in the controllers presented in section 4.2 and 4.3.

4.1 Learning-Based Fault-Tolerant Tracking Control of An Unmanned Aerial Vehicle

Motivated by the successful use of extended Kalman filter (EKF) to train fuzzy logic system in [112, 113], and the fuzzy logic control (FLC) to regulate the gains of linear quadratic regulator (LQR) [114] in [115], a novel learning-based fault-tolerant state-feedback tracking control approach with the capability of tolerating actuator faults is proposed for the control of an UQH, for the purpose of improving its reliability and safety. The basic idea behind this is to change

the shape of membership functions and rules of fuzzy system to generate an additional regulating control input, so that the imposed faults can be compensated and the control performance can be guaranteed accordingly.

4.1.1 State-Feedback Tracking Controller Design Procedure

The objective is to design a controller which meets the following requirements:

(1) before the occurrence of actuator faults, the reference signal $y_{ref}(t)$ can be tracked by the output $y(t)$ without steady-state error, which means $\lim_{t\to\infty} \epsilon(t) = 0$. Additionally, the upper bound of the following performance index can be minimized:

$$J = \int_0^t (x_a^T(\tau)Qx_a(\tau) + u^T(\tau)Ru(\tau))d\tau, \tag{92}$$

where $Q \in \Re^{l+n}$ and $R \in \Re^{l+m}$ are symmetric positive-semidefinite and positive definite weighting matrices, respectively;

(2) in the event of actuator faults, the closed-loop system can still be stabilized, and the desired tracking performance can be guaranteed as well.

Written into state-space form, system model (6) along with (5) can be expressed as follows:

$$\begin{cases} \dot{x}(t) = Ax(t) + Bu(t) + G\omega(t) \\ y(t) = Cx(t), \end{cases} \tag{93}$$

where $x(t) \in \Re^n$ is the state vector, $u(t) \in \Re^m$ denotes the control input, and $y(t) \in \Re^p$ represents the output of system, $\omega(t) = [g \ \omega_d(t)]^T$ includes acceleration of gravity g and bounded external disturbance $\omega_d(t) \in \Re^r$, $u(t) = [u_z, u_\theta, u_\phi, u_\psi]^T$, $x(t) = [x, \dot{x}, y, \dot{y}, z, \dot{z}, \theta, \dot{\theta}, \phi, \dot{\phi}, \psi, \dot{\psi}]^T$,

$$C = \begin{bmatrix} 1 & 0 & 0 & 0 & 0 & 0 & 0 & 0 & 0 & 0 & 0 & 0 \\ 0 & 0 & 1 & 0 & 0 & 0 & 0 & 0 & 0 & 0 & 0 & 0 \\ 0 & 0 & 0 & 0 & 1 & 0 & 0 & 0 & 0 & 0 & 0 & 0 \\ 0 & 0 & 0 & 0 & 0 & 0 & 1 & 0 & 0 & 0 & 0 & 0 \end{bmatrix}, G = \begin{bmatrix} 1 & 1 & 1 & 1 & 1 & 1 & 1 & 1 & 1 & 1 & 1 & 1 \\ 0 & 0 & 0 & 0 & -1 & 0 & 0 & 0 & 0 & 0 & 0 & 0 \end{bmatrix}^T, A =$$

$$
\begin{bmatrix}
0 & 1 & 0 & 0 & 0 & 0 & 0 & 0 & 0 & 0 & 0 & 0 \\
0 & 0 & 0 & 0 & 0 & 0 & g & 0 & 0 & 0 & 0 & 0 \\
0 & 0 & 0 & 1 & 0 & 0 & 0 & 0 & 0 & 0 & 0 & 0 \\
0 & 0 & 0 & 0 & 0 & 0 & 0 & 0 & -g & 0 & 0 & 0 \\
0 & 0 & 0 & 0 & 0 & 1 & 0 & 0 & 0 & 0 & 0 & 0 \\
0 & 0 & 0 & 0 & 0 & 0 & 0 & 0 & 0 & 0 & 0 & 0 \\
0 & 0 & 0 & 0 & 0 & 0 & 0 & 1 & 0 & 0 & 0 & 0 \\
0 & 0 & 0 & 0 & 0 & 0 & 0 & 0 & 0 & 0 & 0 & 0 \\
0 & 0 & 0 & 0 & 0 & 0 & 0 & 0 & 0 & 1 & 0 & 0 \\
0 & 0 & 0 & 0 & 0 & 0 & 0 & 0 & 0 & 0 & 0 & 0 \\
0 & 0 & 0 & 0 & 0 & 0 & 0 & 0 & 0 & 0 & 0 & 1 \\
0 & 0 & 0 & 0 & 0 & 0 & 0 & 0 & 0 & 0 & 0 & 0
\end{bmatrix}
, B =
\begin{bmatrix}
0 & 0 & 0 & 0 \\
0 & 0 & 0 & 0 \\
0 & 0 & 0 & 0 \\
0 & 0 & 0 & 0 \\
0 & 0 & 0 & 0 \\
K_m/m & K_m/m & K_m/m & K_m/m \\
0 & 0 & 0 & 0 \\
K_mL/I_x & -K_mL/I_x & 0 & 0 \\
0 & 0 & 0 & 0 \\
0 & 0 & K_mL/I_y & -K_mL/I_y \\
0 & 0 & 0 & 0 \\
K_mC/I_z & K_mC/I_z & -K_mC/I_z & -K_mC/I_z
\end{bmatrix}.
$$

An augmented system can be obtained by adding an integral term into controller design [105]:

$$
\begin{cases}
\dot{x}_a(t) = A_a x_a(t) + B_a u(t) + G_a w_a(t) \\
y_a(t) = C_a x_a(t),
\end{cases}
\tag{94}
$$

where $x_a(t) = \left[(\int_0^t \epsilon(\tau)d\tau)^T, \quad x^T(t) \right]^T$ and $y_a(t) = \left[(\int_0^t \epsilon(\tau)d\tau)^T, \quad y^T(t) \right]^T$ are the augmented state and output vectors, $w_a(t) = [\omega^T(t), y_{ref}^T(t)]^T$, $y_{ref}(t)$ is the reference signal, and $\epsilon(t) = y_{ref}(t) - y(t)$ denotes the error between $y_{ref}(t)$ and $y_a(t)$.

$$
A_a = \begin{bmatrix} 0 & -C \\ 0 & A \end{bmatrix} \in \Re^{(l+n)\times(l+n)}, B_a = \begin{bmatrix} 0 \\ B \end{bmatrix} \in \Re^{(l+n)\times m},
$$

$$
C_a = \begin{bmatrix} I & 0 \\ 0 & C \end{bmatrix} \in \Re^{(l+p)\times(l+n)}, G_a = \begin{bmatrix} 0 & I \\ G & 0 \end{bmatrix} \in \Re^{(l+n)\times(l+r)}.
$$

Assumption 6 *The states of the closed-loop system are assumed to be measurable or observable.*

Based on (94) and *Assumption 6*, the following state-feedback controller can be defined:

$$u(t) = Kx_a(t) = K_e \int_0^t \epsilon(\tau)d\tau + K_s x(t), \tag{95}$$

where $K = [K_e \ K_s] \in \Re^{m \times (l+n)}$.

The corresponding closed-loop system can be represented as:

$$\dot{x}_a(t) = (A_a + B_a K)x_a(t) + G_a w_a(t). \tag{96}$$

Theorem 5 *For a known positive constant γ, there exist positive symmetric matrices X and Z $\in \Re^{(m+l) \times (m+l)}$ as well as matrix $Y \in \Re^{n \times (m+l)}$, such that LMIs (98) and (99) hold. System (96) can be stabilized by the controller $u(t) = Kx_a(t)$, where $K = Y^*(X^*)^{-1}$, and Y^* and X^* are the optimal results of (98) and (99) [18]. While the upper bound of (92) can be obtained:*

$$J \leqslant \gamma^2 \int_0^t w_a^T(t)w_a(t)dt + x_a^T(0)Z^{-1}x_a(0). \tag{97}$$

$$\begin{bmatrix} A_a X + B_a Y + (A_a X + B_a Y)^T & G_a & Y^T R^{1/2} & XQ^{1/2} \\ * & -\gamma^2 I & 0 & 0 \\ * & * & -I & 0 \\ * & * & * & -I \end{bmatrix} < 0, \tag{98}$$

$$\begin{bmatrix} Z & I \\ I & X \end{bmatrix} > 0. \tag{99}$$

Proof of Theorem 5: Based on *Lemma 1* in [105], its sufficient condition can be rewritten by synthesizing the performance constraints of LQ and the closed-loop H_∞ norm as:

$$(A_a + B_a K)^T P + P(A_a + B_a K) + K^T RK + Q + (\frac{1}{\gamma^2})PG_a G_a^T P < 0. \tag{100}$$

Post- and pre-multiplying (98) by $P = X^{-1}$, and using the *Receprocal Projection Lemma* [107] and Schur complement [108], (100) can then be restated as:

$$
\begin{bmatrix} Q + (\frac{1}{\gamma^2})PG_aG_a^TP + K^TRK + P - (Y + Y^T) & (A_a + B_aK)^TP + Y^T \\ P(A_a + B_aK) + Y & -P \end{bmatrix}
$$
$$
= \begin{bmatrix} A_aX + B_aY + (A_aX + B_aY)^T & G_a & Y^TR^{1/2} & XQ^{1/2} \\ * & -\gamma^2 I & 0 & 0 \\ * & * & -I & 0 \\ * & * & * & -I \end{bmatrix} < 0. \tag{101}
$$

Furthermore, if conditions (98) and (99) are simultaneously satisfied with $K = YX^{-1}$, then substituting $u(t) = Kx_a(t)$ in Eq. (95), and $P = X^{-1}$ into the performance index (92), (102) can be obtained which is exactly the same as inequality (97). Therefore, the proof is completed.

$$
\begin{aligned}
J &= \int_0^t x_a^T(t)(Q + K^TRK)x_a(t)dt < - \int_0^t x_a^T(t)[(A_a + \\
&\quad B_aK)^TP + P(A_a + B_aK) + \frac{1}{\gamma^2}PG_aG_a^TP]x_a(t)dt \\
&= - \int_0^t [(\dot{x}_a(t) - G_aw_a(t))^TPx_a(t) + x_a^T(t)P(\dot{x}_a(t) - \\
&\quad G_aw_a(t)) + \frac{1}{\gamma^2}x_a^T(t)PG_aG_a^TPx_a(t)]dt \\
&\leqslant - \int_0^t d(x_a^T(t)Px_a(t) + \gamma^2 \int_0^t w_a^T(t)w_a(t)dt \\
&\leqslant x_a^T(0)Px_a(0) + \gamma^2 \int_0^t w_a^T(t)w_a(t)dt \\
&= \gamma^2 \int_0^t w_a^T(t)w_a(t)dt + x_a^T(0)Z^{-1}x_a(0).
\end{aligned} \tag{102}
$$

Remark 6 *The state-feedback tracking controller can be synthesized by $K = Y^*(X^*)^{-1}$. In addition, the upper bound of performance index (97) can be minimized by employing LMI functions [108], while solving the optimization problem:* $\min Trace(Z)$ *subject to (98) and (99) [105].*
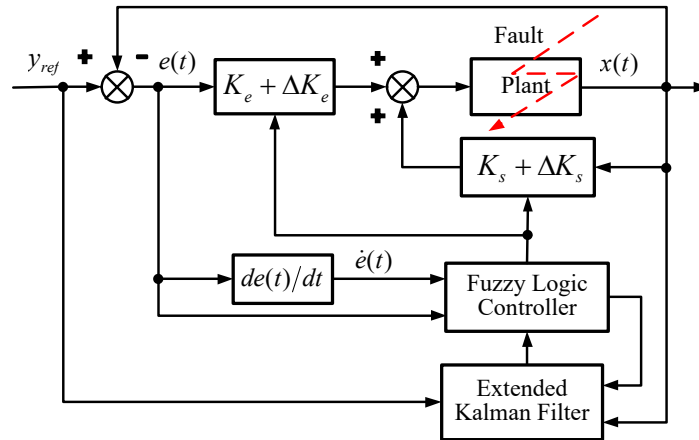
Figure 4.1: Illustration of learning-based fault-tolerant tracking control scheme.

4.1.2   Learning-Based Fault-Tolerant Tracking Controller Design Procedure

The performance of the aforementioned tracking control method with fixed feedback control gains may deteriorate when the UQH is exposed to actuator faults. A learning-based fault-tolerant tracking control approach is proposed in this study to counteract the negative effects of actuator faults and ensure the stabilization of the closed-loop system.

As addressed in Fig. 4.1, the primary concept of the proposed controller is to design a supervisory fuzzy controller which is capable of adjusting the parameters of tracking controller, such that the controller can achieve the desired performance even in the presence of actuator faults. The supervisory fuzzy controller includes an EKF and a FLC, which is synthesized as follows:

(1) an EKF is first designed based on the reference command and system states to provide additional tuning flexibility to FLC by reshaping its fuzzy membership functions and rules;

(2) then, the additional regulating gains can be generated according to the modified FLC controller and system states;

(3) eventually, the UQH can be properly operated by the reconfigured controller, incorporating the additional regulating gains into the tracking control gains.

It is worth mentioning that the idea behind this scheme is to combine the best features of the

78

online learning abilities of EKF, the capacities of FLC on dealing with sophisticated nonlinear systems with uncertainties, and those robust reference command tracking capabilities of the tracking controller. The detailed design procedure is introduced in the following subsections.

4.1.2.1 Fuzzy Logic Control

FLC is regarded as an excellent control approach that has been utilized in a variety of applications and comes along with real-time, nonlinearity and complex computation requirements [116].

The triangle membership function is used for each input and can be written as:

$$
f_{ij}(z_j) = \begin{cases} 1 + (z_j - c_{ij})/b_{ij}^- & if \ -b_{ij}^- \leq (z_j - c_{ij}) \leq 0, \\ 1 - (z_j - c_{ij})/b_{ij}^+ & if \ 0 \leq (z_j - c_{ij}) \leq b_{ij}^+, \\ 0 & otherwise, \end{cases} \tag{103}
$$

where i and j are the number of inputs and triangle membership functions, respectively. z_j denotes the jth input, c_{ij} represents the ith centroid, and b_{ij}^- and b_{ij}^+ are the lower half-width and upper half-width of the ith triangle membership function, respectively.

Furthermore, the max-min aggregation and centroid defuzzification approaches as one of the popularly applied defuzzification techniques have been borrowed to compute the outputs. It is assumed that there is only one output in this fuzzy system. Similar to input, the defuzzification rule for output can be obtained:

$$
m_j(y) = \begin{cases} 1 + (y - \gamma_j)/\beta_j^- & if \ -\beta_j^- \leq (y - \gamma_j) \leq 0, \\ 1 - (y - \gamma_j)/\beta_j^+ & if \ 0 \leq (y - \gamma_j) \leq \beta_j^+, \\ 0 & otherwise, \end{cases} \tag{104}
$$

where $m_j(y)$ is the jth fuzzy output, γ_j, y, β_j^-, and β_j^+ denote the modal point, crisp number, lower half-width, and upper half-width of the jth output rule, respectively.

Supposing that the jth rule is the result of $z_1 \in$ fuzzy set i and $z_2 \in$ fuzzy set k, then the activation level of the consequence of the jth rule can be denoted by w_j, which is illustrated as:

$$w_j = min[f_{i1}(z_1), f_{k2}(z_2)].$$ (105)

Thus, the corresponding fuzzy output can be expressed as:

$$\bar{m}_j(y) = w_j m_j(y),$$ (106)

and the whole fuzzy output $m(y)$ is proposed as:

$$m(y) = \sum_{j=1}^{M} \bar{m}_j(y).$$ (107)

Applying the centroid defuzzification method, the fuzzy output can be mapped to a crisp number $\hat{y}$ as follows:

$$\hat{y} = \frac{\sum_{j=1}^{M} \omega_j C_j S_j}{\sum_{j=1}^{M} \omega_j S_j},$$ (108)

where C_j and S_j are the centroid and area of the jth fuzzy membership function of output, respectively. Additionally, the centroid C_j is defined by:

$$C_j = \frac{\int y m_j(y) dy}{\int m_j(y) dy}.$$ (109)

4.1.2.2 Extended Kalman Filter

EKF has been widely applied in various engineering applications [117], which is employed in this study for training the aforementioned fuzzy systems on-line.

The stochastic variable x_i is assumed to be the system state at time t_i. In the succeeding stage,

the state can be replaced by a stochastic differential equation [118]:

$$\begin{cases} x_i & = f(x_{i-1}) + \omega_{i-1}, \\ d_i & = h(x_i) + \nu_i, \end{cases} \tag{110}$$

where ω_{i-1} and ν_i are the process and measurement noises, respectively. $f(\cdot)$ and $h(\cdot)$ represent the nonlinear vector functions of the states.

The desired estimate $\hat{x}_i$ can then be calculated by the following EKF recursive equations [118]:

$$\begin{cases} F_{i-1} & = \frac{\partial f(x)}{\partial x}\Big|_{x=\hat{x}_{i-1|i-1}}, \\ H_i & = \frac{\partial h(x)}{\partial x}\Big|_{x=\hat{x}_{i|i-1}}, \\ K_{ki} & = P_{i|i-1}H_i^T(R_i + H_i P_{i|i-1}H_i^T)^{-1}, \\ \hat{x}_{i|i} & = f(\hat{x}_{i-1|i-1}) + K_{ki}[d_i - h(\hat{x}_{i|i-1})], \\ P_{i|i} & = F_{i-1}(P_{i-1|i-1} - K_{ki}H_i P_{i-1|i-1})F_{i-1}^T + Q_{i-1}, \end{cases} \tag{111}$$

where d_i denotes the observation vector, K_{ki} is known as the Kalman gain, P_i represents the covariance matrix of state estimation error, and the estimated state $\hat{x}_{i|i}$ is the optimal solution which approaches the conditional mean value $E[x_i|(d_0, d_1, \ldots, d_i)]$.

4.1.2.3 Synthesis of Learning-Based Fault-Tolerant Tracking Controller

In order to synthesize the proposed controller, two critical design processes are further required: 1) the optimization of fuzzy membership functions and rules; and 2) the modification of state feedback tracking control gains.

Optimizing the fuzzy membership functions by EKF can be deemed as a weighted least-squares minimization problem. A two-input and one-output fuzzy system is selected in this study. The error "$e(t)$" and its derivative "$\dot{e}(t)$" are then chosen as the two inputs, while the regulating parameters are selected as the output. It is also assumed that there are n fuzzy sets for the first input, m fuzzy sets for the second input, and k fuzzy sets for the output.

Choosing a vector x that includes b_{ij}^-, b_{ij}^+, and c_{ij} of inputs in Eq. (103), and β_{ij}^-, β_{ij}^+, and γ_i of output in Eq. (104) as the state of the nonlinear system Eq. (110):

$$
\begin{aligned}
x = [&b_{11}^- \ b_{11}^+ \ c_{11} \ \ldots \ b_{n1}^- \ b_{n1}^+ \ c_{n1} \\
&b_{12}^- \ b_{12}^+ \ c_{12} \ \ldots \ b_{m2}^- \ b_{m2}^+ \ c_{m2} \\
&\beta_1^- \ \beta_1^+ \ \gamma_1 \ \ldots \ \beta_k^- \ \beta_k^+ \ \gamma_k]^T.
\end{aligned}
\tag{112}
$$

Then, applying the Kalman recursion in Eq. (111), where d_i represents the target output of the fuzzy system, $f(\cdot)$ denotes the identity mapping, $h(\hat{x}_i)$ is defined as the fuzzy system's actual output that gives the current membership function parameters, F_i is an identity matrix, and H_i is assigned to be the partial derivative of the fuzzy output with respect to the membership function parameters. Finally, the estimate $\hat{x}_i$ that includes the new fuzzy membership function parameters can be obtained after conducting Kalman recursion.

In addition, an on-line reconfigurable fuzzy controller is obtained based on the new fuzzy membership function parameters, which is capable of modifying the state feedback gain K to achieve the desirable control performance. The principle of the modification of state feedback control gains is defined as follows:

$$
\bar{K} = K + T\Delta K,
\tag{113}
$$

where $\bar{K} = \{\bar{K}_{e1}, ..., \bar{K}_{en}, \bar{K}_{s1}, ..., \bar{K}_{sn}\}^T$ denotes the ultimate state feedback gains. Moreover, $\Delta K = \{\Delta K_{e1}, ..., \Delta K_{en}, \Delta K_{s1}, ..., \Delta K_{sn}\}^T$ are the available regulation regions of $\bar{K}$, $\Delta K = K^{max} - K^{min}$, while $K^{max} = \{K_{e1}^{max}, ..., K_{en}^{max}, K_{s1}^{max}, ..., K_{sn}^{max}\}^T$ denotes the upper bound of $\bar{K}$, and $K^{min} = \{K_{e1}^{min}, ..., K_{en}^{min}, K_{s1}^{min}, ..., K_{sn}^{min}\}^T$ denotes the lower bound of $\bar{K}$. $T = \{T_{e1}, ..., T_{en}, T_{s1}, ..., T_{sn}\}^T$ includes the regulating parameters where $T_i \in [0, 1]$ ($i = 1, ..., 2n$).

Consequently, the modified state feedback tracking control gains $\bar{K}$ can be imported into the closed-loop control system to conduct the assigned tasks.

Table 4.1: The system parameters used in the simulation

Parameter	Value	Unit
ω_m	15	rad/s
K_m	120	N
m	1.4	kg
C	1	-
L	0.25	m
I_x	0.03	$kg \cdot m^2$
I_y	0.03	$kg \cdot m^2$
I_z	0.04	$kg \cdot m^2$

Table 4.2: The fuzzy rule base for the proposed controller

		$|e(t)|$				
		NL	NS	Z	PS	PL
	NL	Z	Z	Z	S	M
	NS	Z	Z	S	M	M
$|de(t)|$	Z	Z	S	M	M	M
	PS	S	S	M	B	B
	PL	M	M	M	B	B

4.1.3 Simulation Results

In this section, the effectiveness of the proposed control scheme is evaluated with comparison of the baseline tracking controller on a nonlinear UQH model (4). The performance evaluation is carried out in vertical, longitudinal, and lateral directions simultaneously. Table 4.1 shows the system parameters of the UQH that are used in the simulation.

As shown in Table 4.2, a fuzzy rule base with five membership functions for each of the two inputs and one output is defined. Where "NL" = "negative large", "NS" = "negative small", "Z" = "zero", "PS" = "positive small", and "PL" = "positive large" are selected as fuzzy values for the inputs, while "S" = "small", "M" = "medium", "B" = "big", and "Z" = "zero" are chosen as fuzzy values for output. Fig. 4.2 illustrates the initial membership functions of error, derivative of error for input, and output, respectively. For the control of vertical, longitudinal, and lateral directions, the error of each input is limited in $[-2, \ 2]$, the derivative of error of each input is constrained
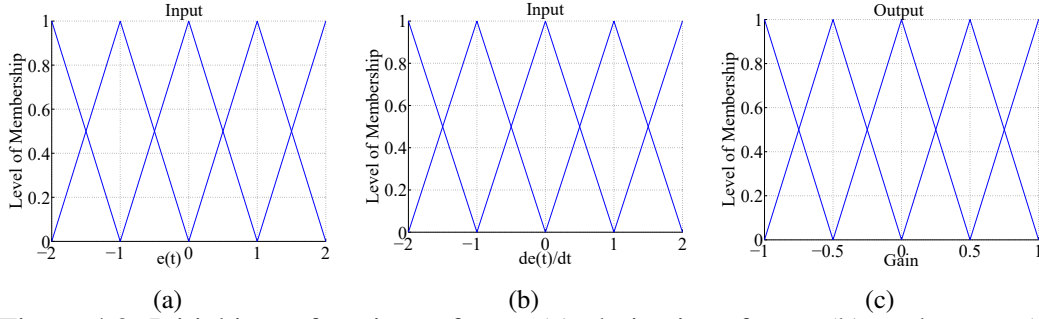
Figure 4.2: Initial input functions of error (a), derivative of error (b), and output (c).

within $[-2, \ 2]$, and fuzzy sets width of each output is restricted within $[-1, \ 1]$. The selected ranges of inputs and output are obtained from the absolute values of system error and its derivative through the scale factors chosen from the specification of the system performance. In terms of the selection of membership functions for partitioning the range of each input, the more membership functions are chosen, the more complex control system is to be and the more computation time are likewise required. Therefore, five triangle membership functions are utilized in this study based on the design experience obtained from our previous researches and the existing work on fuzzy logic control design for smoothly tuning the baseline state-feedback controller gains, while not much computation time effort is demanded for online applications.

It is worth noting that the fuzzy rule base is selected as the same for the control of vertical, longitudinal, and lateral directions. Meanwhile, the initial state feedback control gains are the same for the two controllers. The control inputs bounds of the two controllers are limited within $[0, \ 0.05]$.

4.1.3.1 Scenarios Description

To better evaluate the fault tolerant capability of the proposed control approach, the studied scenarios cover that:

(1) *Scenario 1*: In the first scenario, the comparison of the proposed approach and the baseline tracking control strategy is carried out under a loss of 25% control effectiveness in all motors, and the injected faults occur at 12th second. This kind of fault can result in a loss of altitude;

84

(2) *Scenario 2*: In this scenario, the proposed approach is further validated by comparing with the baseline tracking control method under a loss of 20% control effectiveness in two neighboring motors, and the fault happens at 12th second. This kind of fault may lead to a loss of altitude, and drifts in both lateral and longitudinal directions;

(3) *Scenario 3*: In order to make the simulation to be more realistic and further verify the stability of the unmanned quadrotor helicopter controlled by the proposed controller, it is supposed that all sensors are polluted by Gaussian white noise with zero mean. The sampling time and covariance of these random signals are 0.01 and 0.0001, respectively [119]. Besides, the proposed controller is also simulated in the same faulty system as Scenario 1.

4.1.3.2 Results of Scenario 1 and Evaluation

The performance of the selected two controllers in the vertical direction is illustrated in Fig. 4.3. Although both of the compared controllers can operate the quadrotor helicopter back to the desired height after a transient period, the performance achieved by the proposed controller is significantly superior than that of the baseline tracking controller after the occurrence of actuator faults. More specifically, around $0.9\ m$ of overshoot is generated by the baseline tracking controller, while the proposed controller successfully compensates the injected actuator faults at the expense of $0.15\ m$ overshoot.

Since the motion along either longitudinal or lateral direction can avoid influence from the actuator faults in this scenario, Fig. 4.4(a) and Fig. 4.4(b) show that almost the same good performances in longitudinal direction are achieved by both tracking controller and the proposed controller. Fig. 4.5(a) and Fig. 4.5(b) are the performances obtained in lateral direction, which illustrate the similar results as longitudinal direction.

As can be observed in Fig. 4.6, the control inputs of the compared two controllers are under actuator saturation. But the proposed controller is capable of achieving an faster actuator action than the tracking controller with the aid of control gain regulating mechanism. It can thereby properly adjust the thrust of motors to compensate the actuator faults with less time delay.
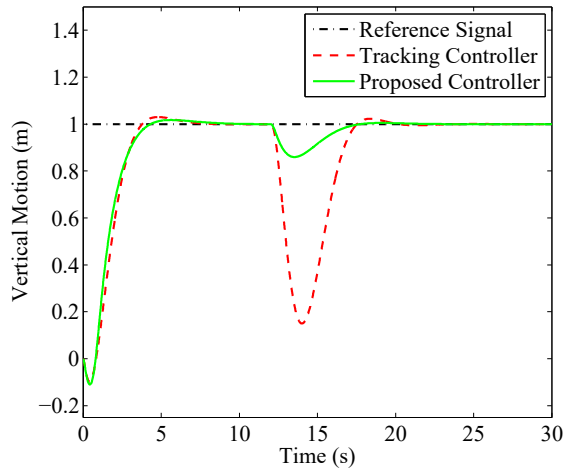
Figure 4.3: Performance comparison in the vertical direction.

(a)   (b)
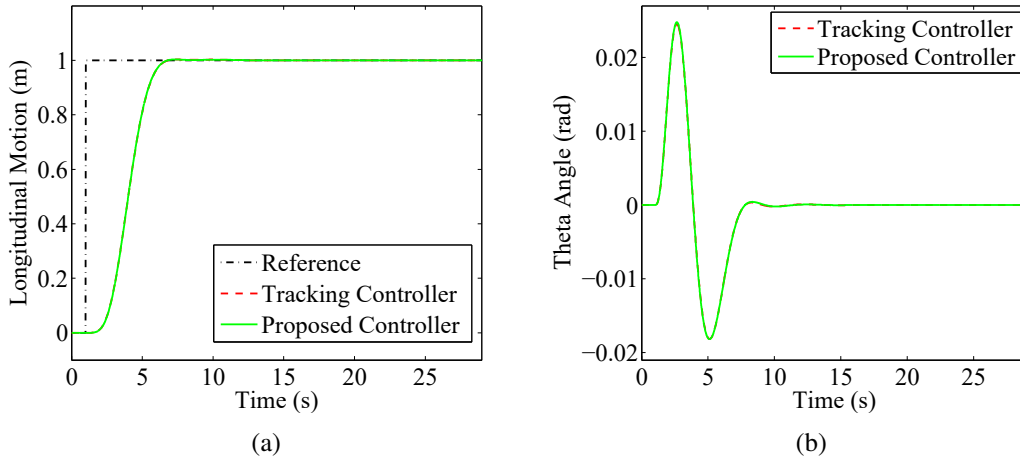
Figure 4.4: Performance comparison in longitudinal direction (a) and pitch angles (b).

In addition, the motion along the longitudinal and lateral directions are not affected by the injected faults in this scenario, hence only the membership functions of vertical direction control that are adjusted by EKF are shown in Fig. 4.7. A comparison with Fig. 4.2 displays that the changes in membership functions can be observed clearly.

4.1.3.3 Results of Scenario 2 and Evaluation

As shown in Fig. 4.8, this is the respective performance of two controllers in vertical direction in the presence of a loss of 20% control effectiveness. In this scenario, being controlled by the tracking controller, over $0.6m$ of overshoot is caused by the actuator faults. While the proposed
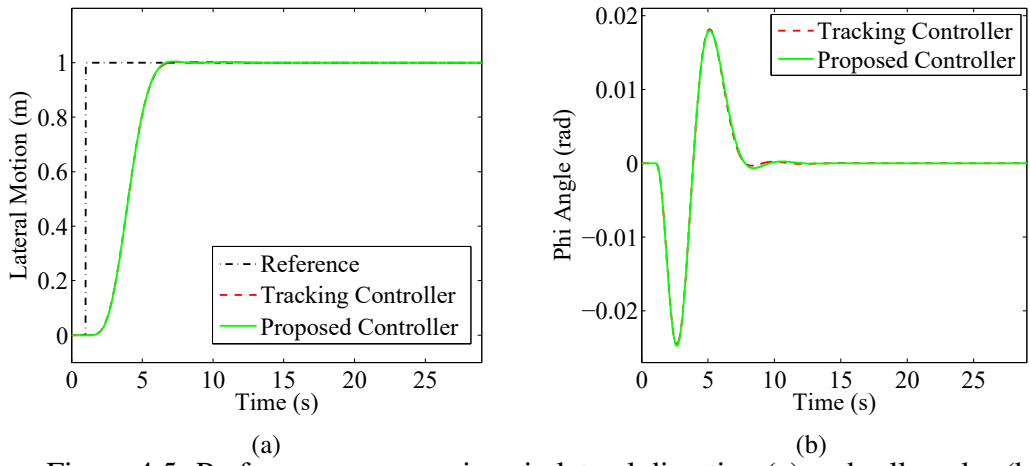
Figure 4.5: Performance comparison in lateral direction (a) and roll angles (b).
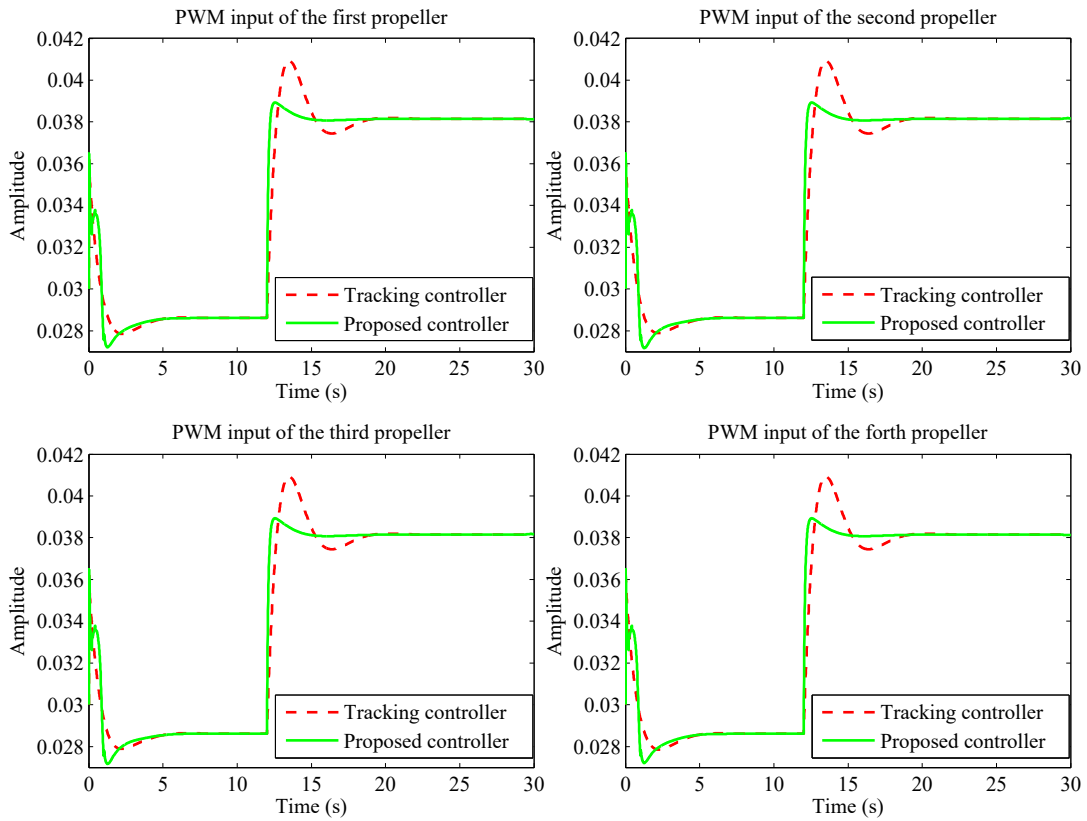
Figure 4.6: PWM input performance with faults in all actuators.
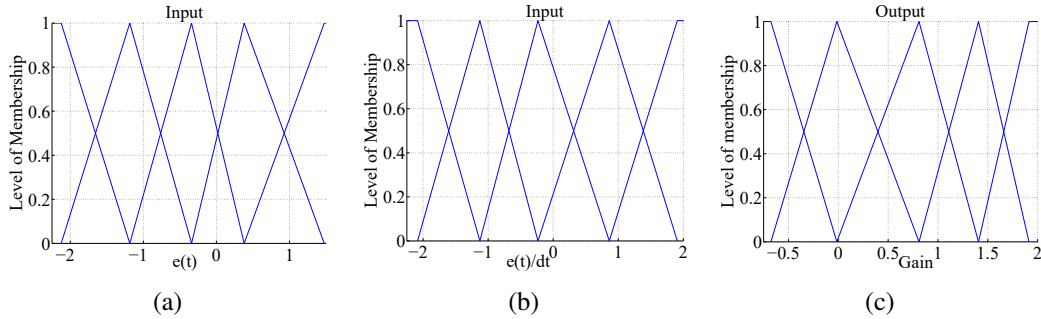
Figure 4.7: Adjusted input membership functions.
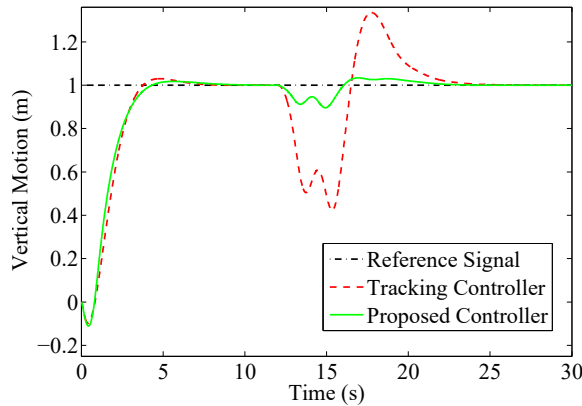
Figure 4.8: Performance comparison in the vertical direction.

controller can still maintain the stability of quadrotor helicopter at the expense of less than $0.1m$ of overshoot.

From Fig. 4.9(a) and Fig. 4.10(a), it can be observed that the proposed controller can steer the quadrotor helicopter to achieve faster angular action and smaller amplitude oscillation than the compared controller. As demonstrated in Fig. 4.9(b) and Fig. 4.10(b), the performance are significantly improved by the proposed controller with comparison of the tracking controller in both longitudinal and lateral directions.

Fig. 4.11 displays the corresponding PWM control signal inputs, the proposed controller can regulate the thrust of quadrotor more prompt and simultaneously obey the actuator limitation, comparing with the tracking controller.

Furthermore, Fig. 4.12, Fig. 4.13, and Fig. 4.14 show the membership functions of vertical, longitudinal, and vertical direction control, respectively. These memberships are distinctly adjusted with comparison of Fig. 4.2, which is optimized online for extending the operating conditions of
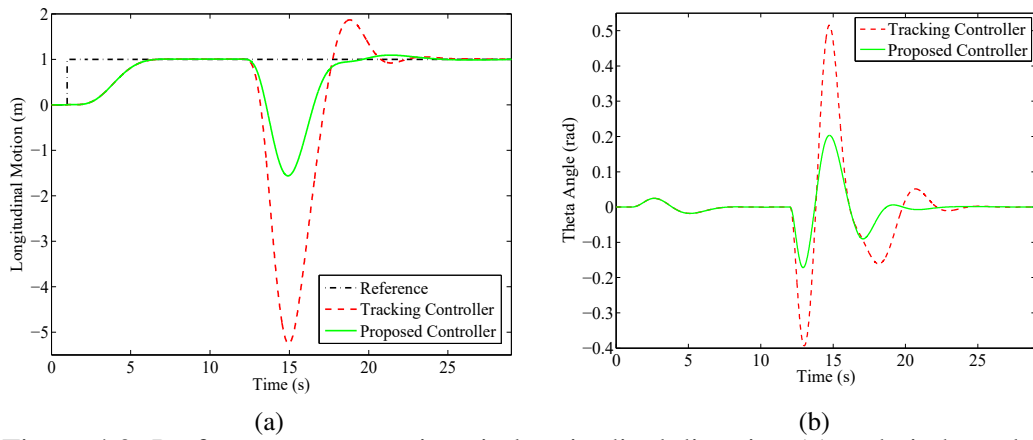
Figure 4.9: Performance comparison in longitudinal direction (a) and pitch angles (b).
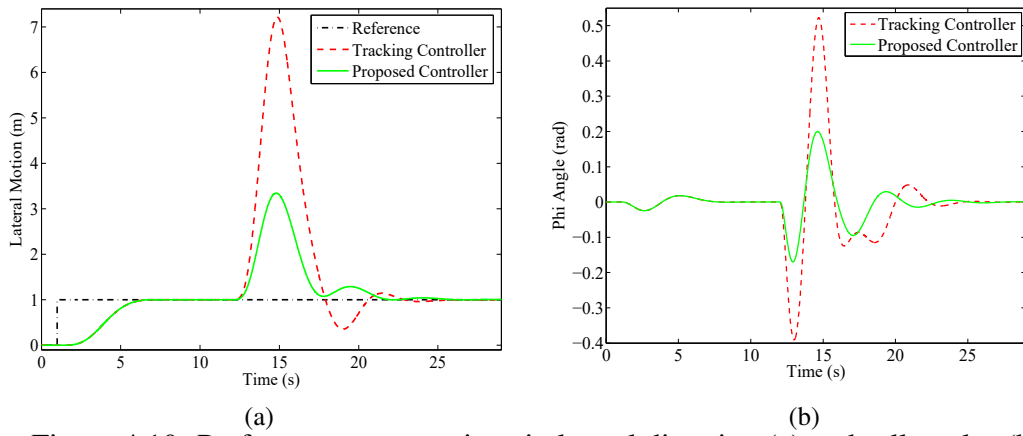
Figure 4.10: Performance comparison in lateral direction (a) and roll angles (b).
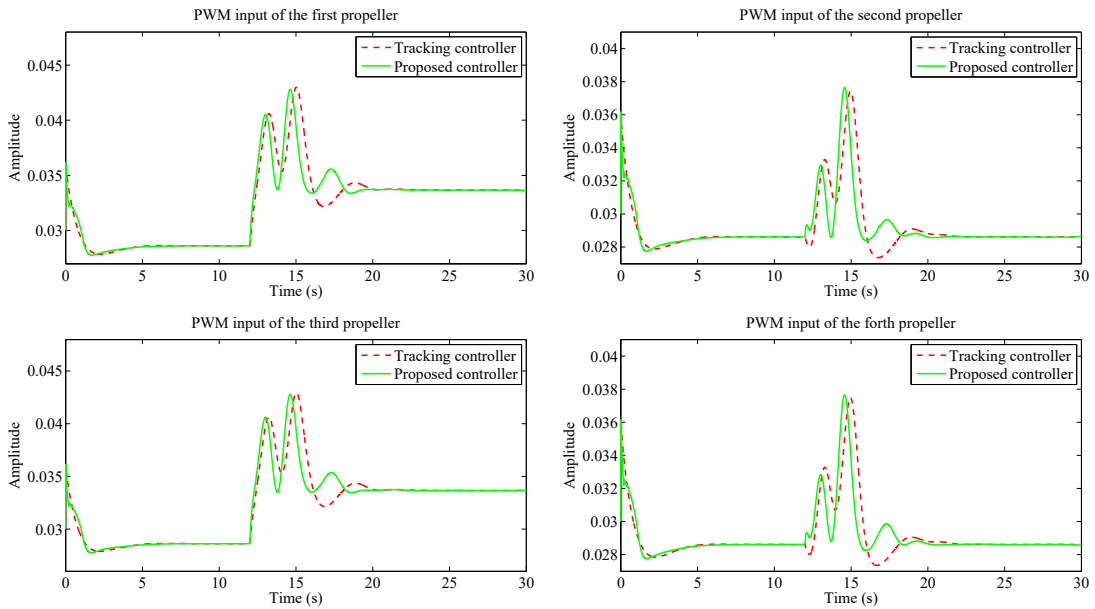
Figure 4.11: PWM input performance with faults in two neighboring propellers.

89
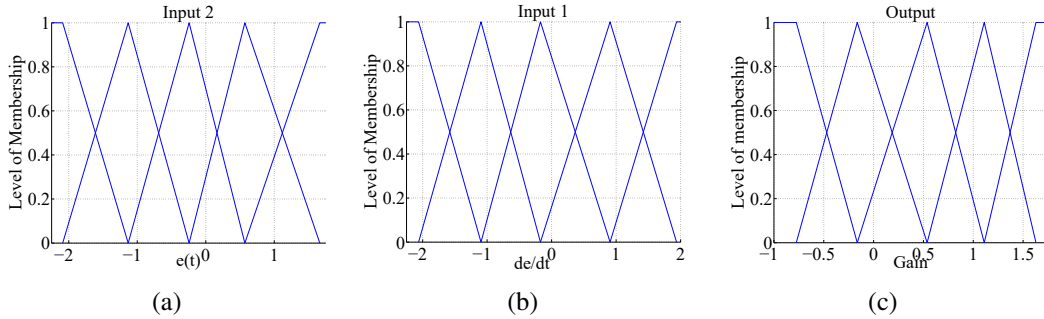
Figure 4.12: Adjusted input membership functions in vertical direction.
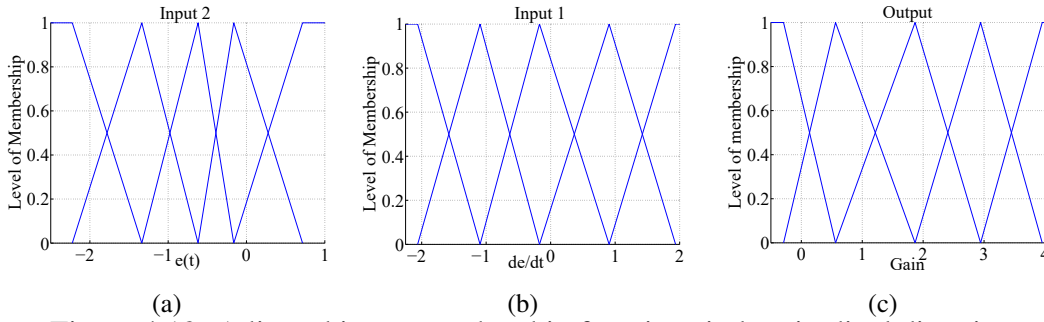
Figure 4.13: Adjusted input membership functions in longitudinal direction.

controller and also the reason behind good performance.

4.1.3.4 Results of Scenario 3 and Evaluation

From Fig. 4.15 and Fig. 4.16, the simulation results show that the proposed controller can still robustly stabilize the system and achieve the satisfactory tracking performance when the closed-loop system is subjected to both the actuator faults and measurement noises.
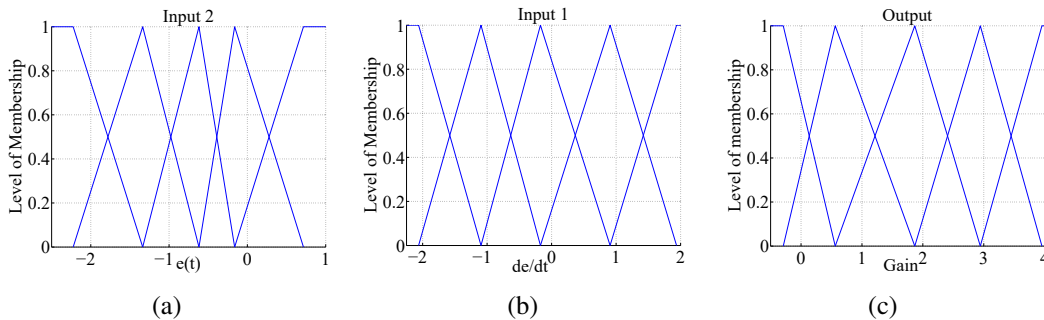
Figure 4.14: Adjusted input membership functions in lateral direction.
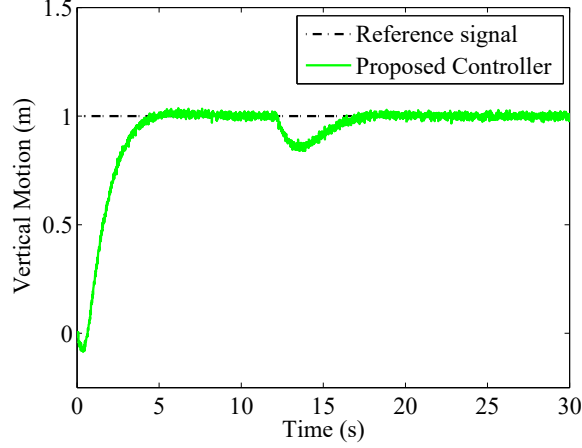
Figure 4.15: Quadrotor helicopter state response with sensor noise.

4.1.4 Experimental Validation on An Unmanned Surface Vehicle

In order to verify the effectiveness of the proposed method in practice and reduce the time and efforts to the implementation of algorithms in the field, an indoor experimental test platform has been established. The designed algorithm can be easily and conveniently applied on this system since it is Matlab/Simulink based, which enables the researcher can concentrate on the design of algorithms, rather than being distracted by other time-consuming problems, such as coding, communication, sensors data reading, and actuators control.

As shown in Fig. 4.17, the developed platform consists of a small container for the motion of USV, a group of 24 cameras based object localization system, a USV for algorithm validation, a ground station for mission assignment and displaying USV's states in real-time, a wireless communication module, and an onboard computer for executing the developed algorithm.

After establishing the experimental platform, system identification is critical for the controller design. In this study, only the dynamics of two motors are identified, while other dynamics of the USV are borrowed from an existing work in [120].

The moment T and propulsion force F are generated as follows:

$$\begin{cases} T = (F_L - F_R) * B/2 \\ F = F_L + F_R, \end{cases} \tag{114}$$

91
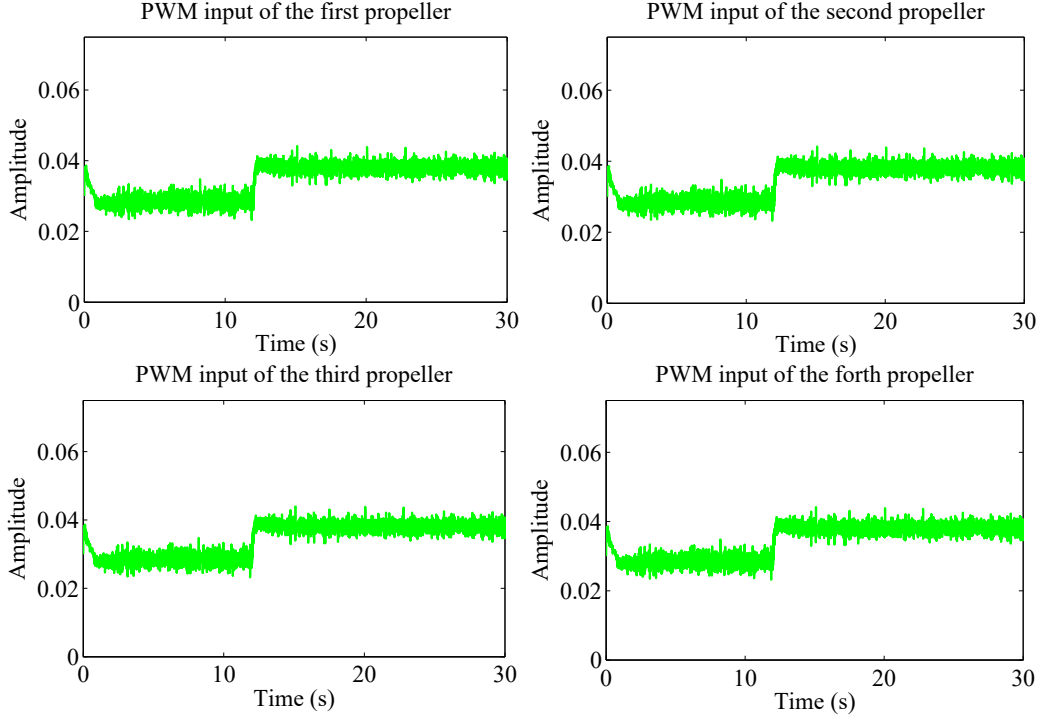
Figure 4.16: PWM input performance with noise.

where $B = 0.07$, F_L, and F_R are forces produced from left and right motors, respectively.

$$F_i = K_{pwm} * u_i^{pwm}, \tag{115}$$

where $i = L$ or R, and $K_{pwm} = 200$.

The range of the DC motor output V_m is limited between $V_{min} = 0\,V$ and $V_{max} = 7.6\,V$. PWM signals u_l and u_r are distributed to the left and right DC motors, respectively. Their operational ranges are accordingly constrained within the dead zone of $[0.074, 0.0876]$ and $[0.0734, 0.0851]$. And the dead zone is constrained in $[-0.3\,V,\ 0.2\,V]$. Due to the existence of dead zone, the initial PWM signal with the values of 0.074 and 0.0734 are thereby needed for the left and right motors, respectively. The control signal u_c generated from the controller is then added to this initial control signal for compensating the dead zone as the ultimate control input signal u_f:

$$u_f = u_c + u_i^{pwm}. \tag{116}$$
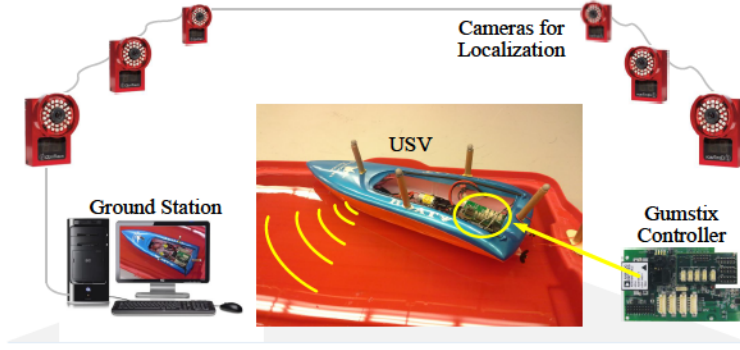
Figure 4.17: The developed experimental platform.
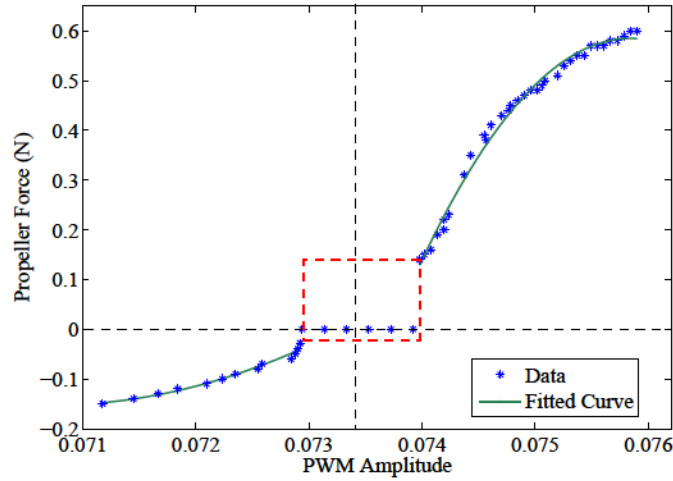
Figure 4.18: The relationship between the PWM signal and propeller force [2].

From Fig. 4.18, the relationship between the motor PWM input signal and propeller force can be established as a quadratic form [2] according to the measured data using the force gauge:

$$PWM_j = \begin{cases} 131100 f_j^2 + 19890 f_j - 753.7, & \text{if } f_j > 0, \\ 22660 f_j^2 - 3204 f_j + 113.1, & \text{if } f_j < 0, \end{cases} \tag{117}$$

where PWM_j is the PWM signal of motor, while f_i denotes the force from propeller.

From Fig. 4.19, the relationship between the PWM signal and its corresponding voltage of motor is obtained in a linear form as:

$$V_j = \begin{cases} 506.9 PWM_j - 37.27, & \text{if for the left motor,} \\ 513.7 PWM_j - 37.64, & \text{if for the right motor,} \end{cases} \tag{118}$$

93
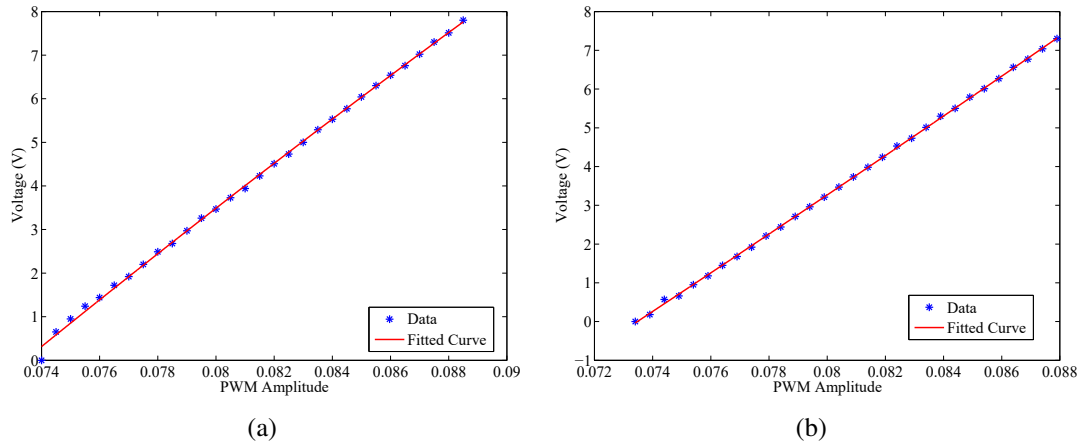
Figure 4.19: The relationship between left (a) and right (b) motor's voltage and PWM.
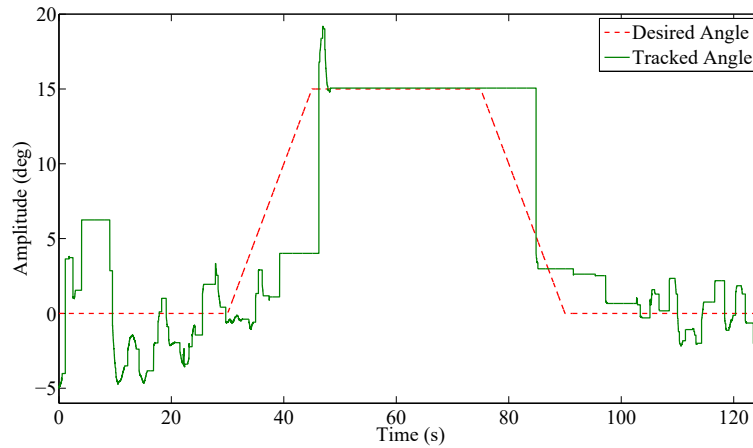
Figure 4.20: The performance of heading angle tracking.

where V_j is the motor input voltage.

The experimental test environment is set up as Fig. 4.17. The developed USV is operated in a container and a group of cameras is used for the localization and measuring the orientation of USV. The control inputs for balancing the USV are chosen as 0.075 and 0.0713 for left and right motors, respectively. The PWM input of right motor is set as a constant value of 0.0713.

As can be seen in Fig. 4.20, the desired heading angle is tracked by the developed USV, while the left motor performs without violating the actuator constraint (see Fig. 4.21).
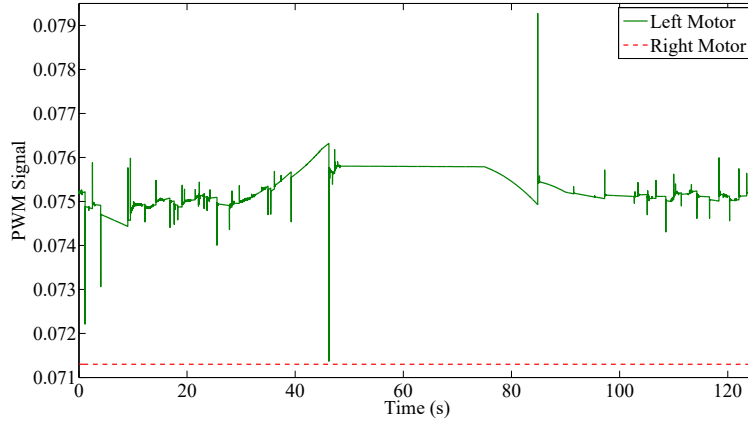
Figure 4.21: The PWM input signals of two motors.

4.2 Adaptive Fault-Tolerant Tracking Control of Unmanned Aerial Vehicle Considering Actuator Dynamics

In the event of actuator failure, the primary concern is to keep the system safe and stable, rather than performing as expected as that in the fault-free case. Motivated by the aforementioned factors in this chapter, the study in this section is intended to design an active FTC approach to mitigate the negative impacts of actuator faults, even external disturbances and unmodeled dynamics that are probably present, meanwhile subject to actuator dynamics and limits.

4.2.1 Preliminaries

4.2.1.1 Actuator Dynamics and Constraints

Written into state-space form, system model (6) along with (5) can be expressed as follows:

$$
\begin{cases}
\dot{x}(t) = Ax(t) + Bu(t) + Gg, \\
y(t) = Cx(t),
\end{cases}
\tag{119}
$$

where $x(t) = \begin{bmatrix} x, & \dot{x}, & y, & \dot{y}, & z & \dot{z}, & \phi, & \dot{\phi}, & \theta, & \dot{\theta}, & \psi, & \dot{\psi} \end{bmatrix}^T \in \Re^n$ is the system state vector,

$u(t) = \begin{bmatrix} F_1, & F_2, & F_3, & F_4 \end{bmatrix}^T \in \Re^m$ denotes the control input, and $y(t) \in \Re^p$ represents the system's output.

$$
A = \begin{bmatrix}
0 & 1 & 0 & 0 & 0 & 0 & 0 & 0 & 0 & 0 & 0 & 0 \\
0 & 0 & 0 & 0 & 0 & 0 & g & 0 & 0 & 0 & 0 & 0 \\
0 & 0 & 0 & 1 & 0 & 0 & 0 & 0 & 0 & 0 & 0 & 0 \\
0 & 0 & 0 & 0 & 0 & 0 & 0 & 0 & -g & 0 & 0 & 0 \\
0 & 0 & 0 & 0 & 0 & 1 & 0 & 0 & 0 & 0 & 0 & 0 \\
0 & 0 & 0 & 0 & 0 & 0 & 0 & 0 & 0 & 0 & 0 & 0 \\
0 & 0 & 0 & 0 & 0 & 0 & 0 & 1 & 0 & 0 & 0 & 0 \\
0 & 0 & 0 & 0 & 0 & 0 & 0 & 0 & 0 & 0 & 0 & 0 \\
0 & 0 & 0 & 0 & 0 & 0 & 0 & 0 & 0 & 1 & 0 & 0 \\
0 & 0 & 0 & 0 & 0 & 0 & 0 & 0 & 0 & 0 & 0 & 0 \\
0 & 0 & 0 & 0 & 0 & 0 & 0 & 0 & 0 & 0 & 0 & 1 \\
0 & 0 & 0 & 0 & 0 & 0 & 0 & 0 & 0 & 0 & 0 & 0
\end{bmatrix}, B = \begin{bmatrix}
0 & 0 & 0 & 0 \\
0 & 0 & 0 & 0 \\
0 & 0 & 0 & 0 \\
0 & 0 & 0 & 0 \\
0 & 0 & 0 & 0 \\
1/m & 1/m & 1/m & 1/m \\
0 & 0 & 0 & 0 \\
L/I_x & -L/I_x & 0 & 0 \\
0 & 0 & 0 & 0 \\
0 & 0 & L/I_y & -L/I_y \\
0 & 0 & 0 & 0 \\
C/I_z & C/I_z & -C/I_z & -C/I_z
\end{bmatrix},
$$

$$
C = \begin{bmatrix}
1 & 0 & 0 & 0 & 0 & 0 & 0 & 0 & 0 & 0 & 0 & 0 \\
0 & 0 & 1 & 0 & 0 & 0 & 0 & 0 & 0 & 0 & 0 & 0 \\
0 & 0 & 0 & 0 & 1 & 0 & 0 & 0 & 0 & 0 & 0 & 0 \\
0 & 0 & 0 & 0 & 0 & 0 & 1 & 0 & 0 & 0 & 0 & 0
\end{bmatrix}, G = \begin{bmatrix} 0 & 0 & 0 & 0 & 0 & -1 & 0 & 0 & 0 & 0 & 0 & 0 \end{bmatrix}^T.
$$

4.2.1.2 Actuator Faults Formulation

Combining with the faulty actuator model (11), (119) becomes:

$$
\begin{cases}
\dot{x}(t) = Ax(t) + Bu(t) + Gg + Ef(t), \\
y(t) = Cx(t),
\end{cases}
\tag{120}
$$

where $E = -B$ and $f(t) = L_f u(t)$.

Remark 7 *The actuator fault term $f(t)$ can include external disturbances and noises as well, this is reasonable since it is of primary concern to compensate total adverse effects of actuator faults,*

external disturbances, and noises, rather than distinguishing their negative impacts.

4.2.2 Adaptive Fault-Tolerant Tracking Control Design

In this section, the design procedure of a normal controller is first provided for UQH working without actuator failures. Next, the scheme of a retrofit adaptive FTTC is introduced against actuator faults. Finally, a reconfigurable control strategy constituting the normal and adaptive control laws are synthesized.

4.2.2.1 Normal Controller Design

A normal controller designed under a proportional and integral scheme is chosen to effectively eliminate the steady-state tracking error, the following augmented closed-loop state feedback control law can then be defined:

$$u(t) = Kx_a(t) = K_e \int_0^t \epsilon(\tau)d\tau + K_x x(t), \tag{121}$$

where $K = [K_e, K_x] \in \Re^{m \times (l+n)}$, $\epsilon(t) = y_{ref}(t) - y(t)$ denotes the error between the reference command $y_{ref}(t)$ and system output $y(t)$, and $x_a(t) = \left[(\int_0^t \epsilon(\tau)d\tau), \quad x(t) \right]^T$.

Accordingly, system (119) can be augmented as follows:

$$\begin{cases} \dot{x}_a(t) = A_a x_a(t) + B_a u(t) + G_a w(t), \\ y_a(t) = C_a x_a(t), \end{cases} \tag{122}$$

where $A_a = \begin{bmatrix} 0 & -S_x C \\ 0 & A \end{bmatrix} \in \Re^{(l+n)\times(l+n)}$, $B_a = [0 \ B]^T \in \Re^{(l+n)\times m}$, $C_a = \begin{bmatrix} I & 0 \\ 0 & C \end{bmatrix} \in \Re^{(l+p)\times(l+n)}$, $G_a = \begin{bmatrix} I & 0 \\ 0 & G \end{bmatrix} \in \Re^{(l+n)\times(l+r)}$, $S_x \in \Re^{q \times p}$ is designed to select system outputs for reference commands tracking, $w(t) = \left[y_{ref}(t), \quad g \right]^T$, and $y_a(t) = \left[(\int_0^t \epsilon(\tau)d\tau), \quad y(t) \right]^T$.

Considering (121) in (122), the augmented state feedback control system (122) becomes:

$$\begin{cases} \dot{x}_a(t) = (A_a + B_a K)x_a(t) + G_a w(t), \\ y_a(t) = C_a x_a(t), \end{cases} \tag{123}$$

As a result, the UQH with actuator faults can be expressed as:

$$\begin{cases} \dot{x}_a(t) = A_a x_a(t) + B_a u(t) + G_a w(t) + E_a f(t), \\ y_a(t) = C_a x_a(t), \end{cases} \tag{124}$$

where $E_a = [0, E]^T$ and UQH's control inputs are all constrained by (10).

Consider actuators dynamics (10), the augmented system (122) can be rewritten as:

$$\begin{cases} \dot{\bar{x}}_a(t) = \bar{A}_a \bar{x}_a(t) + \bar{B}_a u(t) + \bar{G}_a w(t), \\ \bar{y}_a(t) = \bar{C}_a \bar{x}_a(t), \end{cases} \tag{125}$$

where $\bar{x}_a(t) = [x_a(t), u^{pwm}]^T \in \Re^{(l+n+2m)}$, $\bar{y}_a(t) = \left[y(t)\ 0 \right]^T \in \Re^{p+2m+l}$, $\bar{A}_a = \begin{bmatrix} A_a & 0 \\ 0 & K_m \omega_m \end{bmatrix} \in \Re^{(l+n+2m)\times(l+n+2m)}$, $\bar{B}_a = [B_a\ -\omega_m]^T \in \Re^{(l+n+2m)\times m}$, $\bar{G}_a = [G_a\ 0]^T \in \Re^{(l+n+2m)\times l}$, and $\bar{C}_a = [I\ 0] \in \Re^{(l+n)\times(l+p+2m)}$.

The augmented faulty system (124) then becomes:

$$\begin{cases} \dot{\bar{x}}_a(t) = \bar{A}_a \bar{x}_a(t) + \bar{B}_a u(t) + \bar{G}_a w(t) + \bar{E}f(t), \\ \bar{y}_a(t) = \bar{C}_a \bar{x}_a(t), \end{cases} \tag{126}$$

where $\bar{E} = [E,\ 0]^T$.

Introduce the output feedback control $u(t) = K\bar{C}_a \bar{x}_a(t)$ into the closed-loop system (126), which can be expressed as:

$$\dot{\bar{x}}_a(t) = \bar{A}_a \bar{x}_a(t) + \bar{B}_a K \bar{C}_a \bar{x}_a(t) + \bar{G}_a w(t) + \bar{E}f(t). \tag{127}$$

Theorem 6 *For a known positive constant γ, if there exist positive symmetric matrices $X = X^T \in \Re^{(l+n+2m)\times(l+n+2m)}$ and $Z = Z^T > 0 \in \Re^{(l+n+2m)\times(l+n+2m)}$ and matrix $Y \in \Re^{n\times(l+n+2m)}$ that make the linear matrix inequalities (LMIs) (128), (129), and (130) hold, where the symbol $*$ is the symmetric entry. Then system (125) can be stabilized by the controller $u(t) = \bar{K}\bar{C}_a\bar{x}_a(t)$:*

$$
\begin{bmatrix}
\bar{A}_a X + \bar{B}_a Y + (\bar{A}_a X + \bar{B}_a Y)^T & \bar{G}_a & Y^T R^{1/2} & XQ^{1/2} \\
* & -\gamma^2 I & 0 & 0 \\
* & * & -I & 0 \\
* & * & * & -I
\end{bmatrix} < 0, \tag{128}
$$

$$
\begin{bmatrix}
Z & * \\
I_{(l+n+i)} W X & \Phi_d^2/r_{max}^2
\end{bmatrix} > 0, \; i = 1, ..., m, \tag{129}
$$

$$
\begin{bmatrix}
Z & * \\
-[0, W_{1(i)}] W X + W_{1(ii)} Y_{1(i)} & \Phi_r^2/r_{max}^2
\end{bmatrix} > 0, \; i = 1, ..., m. \tag{130}
$$

Here, γ is related to the H_∞ norm $T_{zw}(s)$ of transfer function ($\frac{||\bar{y}_a(t)||_2}{||w(t)||_2} < \gamma^2 I$) from $w(t)$ to the performance output [33]:

$$
\bar{y}_a(t) = [Q^{1/2}, 0]^T \bar{x}_a(t) + [0, R^{1/2}]^T u(t). \tag{131}
$$

In addition, $P = P^T = X^{-1}$, $W = [\bar{C}_a^T (\bar{C}_a \bar{C}_a^T)^{-1}, \bar{C}_a^\perp]$, and $\bar{C}_a^\perp$ represents the orthogonal basis for the null space of $\bar{C}_a$. $W_{1(i)}$ and $Y_{1(i)}$ denote the ith rows of matrices W_1 and Y_1, respectively. $Y = [Y_1, \; 0]$, $X = \begin{bmatrix} X_{11} & 0 \\ X_{21} & X_{22} \end{bmatrix}$ with $X_{11} = X_{11}^T$. $I_{(l+n+i)}$ and $I_{(l+j)}$ indicate the $(l + n + i)^{th}$ and $(l + j)^{th}$ row of identical matrix I, respectively. The reference command is assumed to be limited within a known bound $\Omega := \{y_{ref}(t)| \; y_{ref}^T(t)y_{ref}(t) \leq r_{max}^2, \forall t \geq 0\}$. Therefore, $K = Y_1^*(X_{11}^*)^{-1}$ can guarantee that the system (127) meets actuators constraints (10), and Y^* and X^* are the optimal solutions of Y and X.

Proof of Theorem 6: The following Lyapunov candidate is selected here:

$$V_1 = \bar{x}_a^T(t)P\bar{x}_a(t). \tag{132}$$

The derivative of V_1 along the trajectory of system (125) can be written as:

$$\begin{aligned}
\frac{dV_1(t)}{dt} =& \dot{\bar{x}}_a^T(t)P\bar{x}_a(t) + \bar{x}_a^T(t)P\dot{\bar{x}}_a(t) = \bar{x}_a^T(t)(\bar{A}_a + \bar{B}_a K)^T P\bar{x}_a(t) + w^T(t)\bar{G}_a^T P\bar{x}_a(t) \\
& + \bar{x}_a^T(t)P(\bar{A}_a + \bar{B}_a K)\bar{x}_a(t) + \bar{x}_a^T(t)P\bar{G}_a w(t).
\end{aligned} \tag{133}$$

In order to guarantee the system stability, it requires that $\dfrac{dV_1(t)}{dt} < 0$. Moreover, recalling the affine quadratic H_∞ condition $\frac{||\bar{y}_a(t)||_2}{||w(t)||_2} < \gamma^2 I$, then the following inequality can be obtained:

$$\begin{aligned}
& \frac{dV_1(t)}{dt} + \bar{y}_a^T(t)\bar{y}_a(t) - \gamma^2 w^T(t)w(t) \\
=& \bar{x}_a^T(t)(\bar{A}_a + \bar{B}_a K)^T P\bar{x}_a(t) + w^T(t)\bar{G}_a^T P\bar{x}_a(t) + \bar{x}_a^T(t)P(\bar{A}_a + \bar{B}_a K)\bar{x}_a(t) + \\
& \bar{x}_a^T(t)P\bar{G}_a w(t) + \bar{y}_a^T(t)\bar{y}_a(t) - \gamma^2 w^T(t)w(t) < 0.
\end{aligned} \tag{134}$$

From (131), one can easily derive that:

$$\bar{y}_a^T(t)\bar{y}_a(t) = \bar{x}_a^T(t)(K^T RK + Q)\bar{x}_a(t). \tag{135}$$

In addition, the following equality is obvious:

$$w^T(t)\bar{G}_a^T P\bar{x}_a(t) + \bar{x}_a^T(t)P\bar{G}_a w(t) \leqslant \gamma^2 w^T(t)w(t) + (\frac{1}{\gamma^2})\bar{x}_a^T(t)P\bar{G}_a\bar{G}_a^T P\bar{x}_a(t). \tag{136}$$

Eventually, substituting (135) and (136) into (134), the following inequality can be obtained:

$$(\bar{A}_a + \bar{B}_a K)^T P + P(\bar{A}_a + \bar{B}_a K) + K^T RK + Q + (\frac{1}{\gamma^2})P\bar{G}_a\bar{G}_a^T P < 0. \tag{137}$$

$$
\begin{bmatrix} Q + (\frac{1}{\gamma^2})P\bar{G}_a\bar{G}_a^T P + K^T R K + P - (Y + Y^T) & (\bar{A}_a + \bar{B}_a K)^T P + Y^T \\ P(\bar{A}_a + \bar{B}_a K) + Y & -P \end{bmatrix}
$$

$$
= \begin{bmatrix} \bar{A}_a X + \bar{B}_a Y + (\bar{A}_a X + \bar{B}_a Y)^T & \bar{G}_a & Y^T R^{1/2} & X Q^{1/2} \\ * & -\gamma^2 I & 0 & 0 \\ * & * & -I & 0 \\ * & * & * & -I \end{bmatrix} < 0. \tag{138}
$$

According to the *Reciprocal Projection Lemma* in [108], applying the Schur complement [107] and $P = X^{-1}$, (137) can be formulated into (138), which is the same as (128).

Eq. (129) ensures the ith actuator operating within the safety region $\Phi_{d(i)}$, which equals to

$$
P = X^{-1} \geq I_{l+n+i}^T \frac{r_{max}^2}{\Phi_{d(i)}^2} I_{l+n+i}
$$

$$
\Rightarrow \Phi_{d(i)}^2 \geq X^{\frac{1}{2}} I_{l+n+i}^T I_{l+n+i} X^{\frac{1}{2}} r_{max}^2 \geq \alpha_{max}(X^{\frac{1}{2}} I_{l+n+i}^T I_{l+n+i} X^{\frac{1}{2}} r_{max}^2)
$$

$$
\geq \max_{|\bar{x}_{aa}(t)| \geq r_{max}^2} ||I_{l+n+i} X^{\frac{1}{2}} \bar{x}_{aa}(t)||^2 \geq \max_{|X^{-\frac{1}{2}} \bar{x}_a(t)| \geq r_{max}^2} ||I_{l+n+i} \bar{x}_a(t)||^2
$$

$$
\geq \max_{\bar{x}_a \in \Omega} ||I_{l+n+i} \bar{x}_a(t)||^2
$$

$$
\Rightarrow \Phi_{d(i)}^2 \geq (I_{l+n+i} \bar{x}_a(t))^2 = u_{(i)}^2(t),
$$

where $\alpha_{max}(\cdot)$ denotes the maximal eigenvalue, $Z = (WX)^T P(WX)$, and $i = 1, ..., m$.

Eq. (130) guarantees the rate of the ith actuator operating within the desired boundary $\Phi_{r(i)}$. Utilizing the Schur's complement, (130) is equivalent to

$$
Z \geq (-W_{1(i)} WX + W_{1(ii)} Y_{1(i)})^T \frac{r_{max}^2}{\Phi_{r(i)}^2} (-W_{1(i)} WX + W_{1(ii)} Y_{1(i)})
$$

$$
\Rightarrow \Phi_{r(i)}^2 \geq X^{\frac{1}{2}} (WX)^{-T} (-W_{1(i)} WX + W_{1(ii)} Y_{1(i)})^T (-W_{1(i)} WX + W_{1(ii)} Y_{1(i)}) (WX)^{-1} r_{max}^2
$$

$$
\geq \alpha_{max}(X^{\frac{1}{2}} (-W_{1(i)} + W_{1(ii)} Y_{1(i)} (WX)^{-T})^T (-W_{1(i)} + W_{1(ii)} Y_{1(i)} (WX)^{-1}) X^{\frac{1}{2}} r_{max}^2)
$$

$$
\geq \max_{|\bar{x}_{aa}(t)| \geq r_{max}^2} ||(-W_{1(i)} + W_{1(ii)} K\bar{C}_a) X^{\frac{1}{2}} \bar{x}_{aa}(t)||^2
$$

$$
\geq \max_{|X^{-\frac{1}{2}} \bar{x}_a(t)| \geq r_{max}^2} ||(-W_{1(i)} + W_{1(ii)} K\bar{C}_a) \bar{x}_a(t)||^2
$$

$$
\Rightarrow \Phi_{r(i)}^2 \geq (-W_{1(i)} u(t) + W_{1(ii)} K\bar{C}_a \bar{x}_a(t))^2 = u_{r(i)}^2(t).
$$
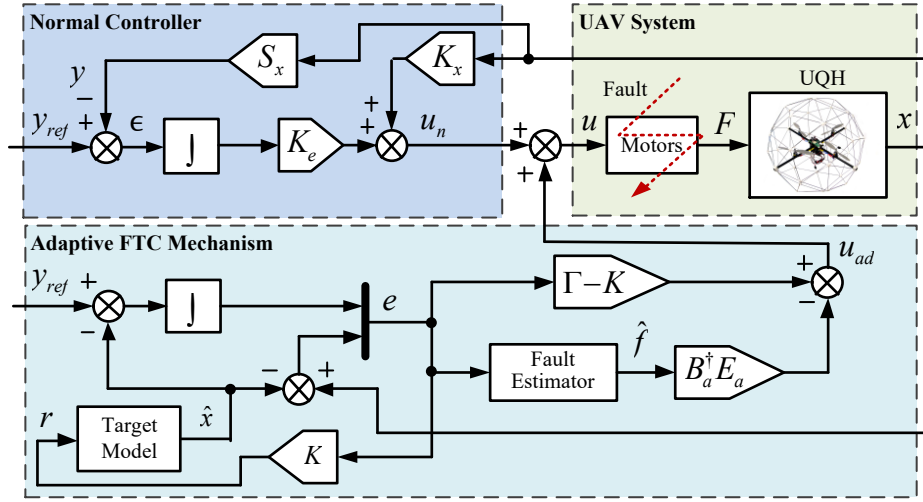
Figure 4.22: Schematic diagram of the proposed adaptive FTC scheme.

Therefore, the problem can be solved if conditions (128), (129), and (130) are simultaneously satisfied with $K = Y_1(X_{11})^{-1}$. In addition, the closed-loop system can be stabilized under the actuator constraints of $u(t) \in [-\Phi_d, \Phi_d]$, $u_r(t) \in [-\Phi_r, \Phi_r]$, and state constraints of $\bar{x}_a(t) \in [-\Phi_s, \Phi_s]$.

Remark 8 *The conditions (129) and (130) guarantee that the amplitude and rate of actuators are limited within their safe regions. The control effects can be adjusted by constraining the variable γ to meet the transient performance requirement.*

4.2.2.2 Adaptive Fault-Tolerant Controller Design

This predominant concept of the proposed adaptive FTC methodology can be illustrated in Fig. 4.22. The overall control system comprises a normal controller, a fault estimator, and a fault compensator. In the absence of actuator faults, the UQH is controlled by the normal controller. Once the actuator fails to operate, it is then detected by the fault estimator, its magnitude is also estimated using an adaptive law. Based on the estimated value, the fault compensator generates an additionally appropriate control input $u_{ad}(t)$ for tolerating the negative impact of actuator faults. Eventually, an adaptive FTC controller capable of counteracting actuator faults is synthesized by the additional control input $u_{ad}(t)$ and nominal one $u_n(t)$.

Written into mathematical representation, the ultimate control input becomes:

$$u(t) = u_n(t) + u_{ad}(t), \tag{139}$$

where $u_{ad}(t)$ is the additional control input, which is 0 with healthy actuators, while deviates from 0 with faulty actuators; $u_n(t)$ is from normal controller.

In order to obtain the magnitude of actuator faults online, a *target model* is first built:

$$\dot{\hat{x}}(t) = A\hat{x}(t) + Br(t) + Gg + E\hat{f}(t), \tag{140}$$

where $\hat{x}(t)$ and $\hat{f}(t)$ denote the estimation of states and actuator faults, respectively; the target control input $r(t) \in \Re^n$ is properly chosen to accomplish the control objective.

The augmentation form of (140) then offers:

$$\dot{\hat{x}}_a(t) = A_a\hat{x}_a(t) + B_a r(t) + G_a w(t) + E_a\hat{f}(t). \tag{141}$$

Define the system state error $e(t) = \hat{x}_a(t) - x_a(t)$ and the control input $u(t) = r(t) - \Gamma e(t)$, the error feedback gain Γ is introduced for stabilizing the augmented system (141), $E_a = [E_{a1}, ..., E_{am}]$. Then one can obtain the derivative of system state error as follows:

$$
\begin{aligned}
\dot{e}(t) &= \dot{\hat{x}}_a(t) - \dot{x}_a(t) \\
&= A_a e(t) + B_a(u(t) + \Gamma e(t)) + G_a(\hat{f}(t) - f(t)) \\
&= (A_a + B_a\Gamma)e + E_a\tilde{f}(t) \\
&= (A_a + B_a\Gamma)e + \sum_{i=1}^{n} E_{ai}\tilde{f}_i(t),
\end{aligned}
\tag{142}
$$

where $\tilde{f}(t) = \hat{f}(t) - f(t)$ is the estimation of disturbance errors and $\tilde{f}(t) = diag[\tilde{f}_1(t)...\tilde{f}_n(t)]$.

Theorem 7 *The augmented state error system (142) can be stabilized with the existence of positive symmetric matrix $X_2 \in \Re^{(m+l)\times(m+l)}$ and matrix $Y_2 \in \Re^{n\times(m+1)}$, meanwhile the following LMI*

(143) should hold:

$$A_a X_2 + B_a Y_2 + X_2 A_a^T + Y_2^T B_a^T < 0, \tag{143}$$

and $\dot{\hat{f}}(t)$ is determined by the following adaptive law:

$$\dot{\hat{f}}_i(t) = Proj_{[\underline{f}_i, \overline{f}_i]}\{-k_i e^T P E_{ai}\}$$

$$= \begin{cases} 0, & if \ \hat{f}_i(t) = \underline{f}_i, -k_i e^T P E_{ai} \leqslant 0 \ or \\ & \hat{f}_i(t) = \overline{f}_i, -k_i e^T P E_{ai} \geqslant 0, \\ -k_i e^T P E_{ai}, & otherwise, \end{cases} \tag{144}$$

where $k_i > 0$ denotes the adaptive law gain, $Proj\{\cdot\}$ is the projection operator projecting the estimates $\hat{f}_i(t)$ to the acceptable fault interval $[\underline{f}_i, \overline{f}_i]$.

Remark 9 *A feasible solution of X_2 and Y_2 can be calculated from (143) using LMI toolbox in Matlab. Then, the error feedback gain $\Gamma = Y_2 X_2^{-1}$ can be obtained [121].*

Proof of Theorem 7: Choosing the Lyapunov candidate function as follows:

$$V_2 = e^T(t) P e(t) + \sum_{i=1}^{n} \frac{\tilde{f}^2(t)}{k_i}. \tag{145}$$

The derivative of V_2 then gives:

$$\dot{V}_2 = e^T(t)[P(A_a + B_a\Gamma) + (A_a + B_a\Gamma)^T P]e(t) + 2\sum_{i=1}^{n} \tilde{f}_i e^T(t) P E_{ai} + 2\sum_{i=1}^{n} \frac{\tilde{f}_i \dot{\hat{f}}_i}{k_i}. \tag{146}$$

If the adaptive law (144) and the following LMI are selected, it follows that:

$$\frac{\tilde{f}_i \dot{\hat{f}}_i}{k_i} \leqslant -\tilde{f}_i e^T(t) P E_{ai}, \tag{147}$$

then, (146) can be rewritten as:

$$\dot{V}_2 \leqslant e^T(t)[P(A_a + B_a\Gamma) + (A_a + B_a\Gamma)^T P]e(t). \tag{148}$$

104

Choosing $\Gamma = Y_2 X_2^{-1}$ and $P = X_2^{-1}$, as well as (143) holds, one can obtain that:

$$P(A_a + B_a\Gamma) + (A_a + B_a\Gamma)^T P < 0. \tag{149}$$

Substituting (149) into (148), it gives:

$$\dot{V}_2 \leqslant -\beta||e(t)||^2 \leqslant 0, \tag{150}$$

where $\beta := -\max[P(A_a + B_a\Gamma) + (A_a + B_a\Gamma)^T P] > 0$.

So far, the augmented state error system (142) is stabilized and proof of *Theorem 7* is finished.

4.2.2.3 Control Schemes Synthesis

An appropriate control input $r(t) = K\hat{x}_a(t) - B_a^\dagger E_a \hat{f}(t)$ is devised in order to match the augmented target system (141) with the normal system (123), then (141) becomes:

$$\dot{\hat{x}}_a(t) = (A_a + B_a K)\hat{x}_a(t) + G_a w(t), \tag{151}$$

where $B_a^\dagger$ denotes the pseudo inverse of B_a.

Ultimately, the additional control effort compensating the undesired adverse effects of actuator faults can be derived:

$$\begin{aligned}
u(t) &= r(t) - \Gamma e(t) \\
&= K\hat{x}_a(t) - B_a^\dagger E_a \hat{f}(t) - \Gamma e(t) \\
&= u_n(t) + u_{ad}(t),
\end{aligned} \tag{152}$$

where $u_n(t) = Kx_a(t)$, and $u_{ad}(t) = (K - \Gamma)e(t) - B_a^\dagger E_a \hat{f}(t)$. The additional compensating control input $u_{ad}(t)$ varies from 0 in the event of actuator faults, while it remains 0 in the absence of actuator faults.

Remark 10 *The additional fault compensating control input $u_{ad}(t)$ comprises two terms $(K - \Gamma)e(t)$ and $-B_a^\dagger E_a \hat{f}(t)$. The first term, which activates once any residuals between the plant and*

adaptive model are generated, is designed for reducing the speed of fault induced performance deterioration with no fault information, so as to provide the FDD module with sufficient time to achieve more accurate diagnosis results and offer extra time for the control reconfiguration as well; the other term is triggered after the correct fault information is obtained from the FDD scheme.

4.2.3   Simulation and Experimental Results

The performance of the normal and proposed controllers are compared in the face of faulty actuators. The system parameters of the studied UQH are adopted from a real one, which are listed in Table 4.1. In order to better meet the practical conditions, the actuator saturation is considered in the system nonlinear model. The operation bound of PWM control input is restricted within $[0,\ 0.05]$ and its rate is limited under 0.05 per second for the simulation; while PWM control input is constrained in $[0.05,\ 0.1]$ and its rate is limited under 0.05 for the experiment.

4.2.3.1   Scenarios Description

Three scenarios are included in the method validation:

(1) *Scenario 1*: This scenario considers two actuator fault cases. First, there are partial loss of control effectiveness faults (60%) acting on all four motors which occurs at 30th second when the UQH is tracking a desired trajectory. Next, the performance comparison with partial loss of 50% control effectiveness in two neighbouring motors (rear and left motors) starting at 30th second is conducted.

(2) *Scenario 2*: In this scenario, the proposed control method considering actuator dynamics is further validated by comparing it with the normal control method without consideration of actuator dynamics. This performance comparison is conducted with partial loss of 30% control effectiveness imposed, which is solely acted on the rear motor starting at 20th second. To make the simulation to be more practical, it is important to show the proposed controller's
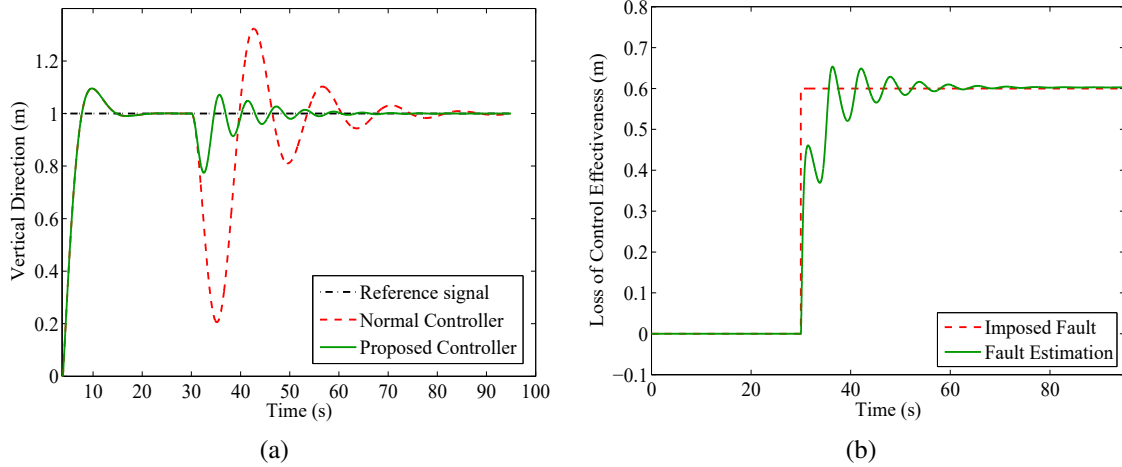
Figure 4.23: Performance comparison in vertical direction (a) and estimation result (b).

robust performance in the presence of external disturbances and noises. Accordingly, an environmental disturbance of $1\ N$ along vertical and $1\ N$ along longitudinal directions, which lasts from 40th second to 50th second, is injected into the system. Noises with variance of 0.0001 acting on all measurements are taken into account as well.

(3) *Scenario 3*: In order to further demonstrate the efficacy of the proposed FTC method in practice, experimental test is also carried out in an indoor experimental environment. Loss 25% of overall power of all motors is considered, mimicking the negative impact of battery drainage.

4.2.3.2   Results of Scenario 1 and Evaluation

Fig. 4.23(a) shows the performance achieved by the proposed controller is significantly superior than the normal controller when the UQH is exposed to actuator faults in all motors. Although the UQH can be steered to return to the intended altitude by both controllers, the performance of overshoot (80%) and settling time ($30s$) is not satisfactory in the case of normal controller. By contrast, the performance is significantly improved (with 20% of overshoot and $10s$ of settling time) by the proposed controller.

The estimated fault rate is displayed in Fig. 4.23(b). As can be observed in Fig. 4.24, the control inputs of both controllers are under actuator saturation, and the required PWM inputs to
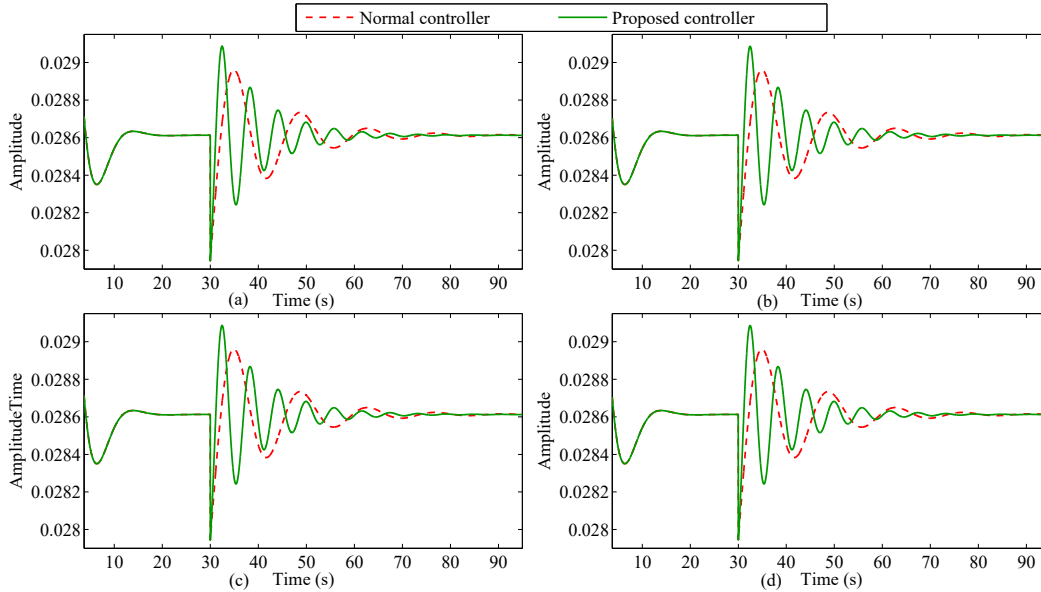
Figure 4.24: Performance of PWM control input signals.
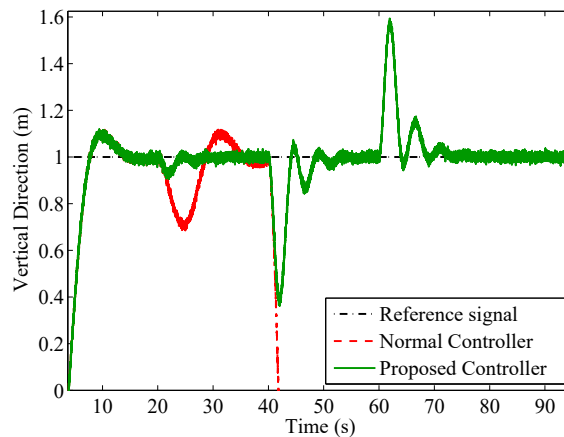
Figure 4.25: Performance comparison in the vertical direction.

compensate the effect of gravity and actuator faults is around 0.0286 (under the PWM deflection range $[0, 0.05]$). Moreover, it can also be seen from Fig. 4.24 that the better performance of the proposed controller is due to the more prompt control signal generation of the proposed controller than that of the normal controller.

4.2.3.3   Results of Scenario 2 and Evaluation

As can be seen the respective performance of two compared controllers in Fig. 4.25, although merely the amount of imposed actuator faults is not able to cause the UQH crash, eventually the normal controller cannot prevent this serious consequence in the event of both actuator faults
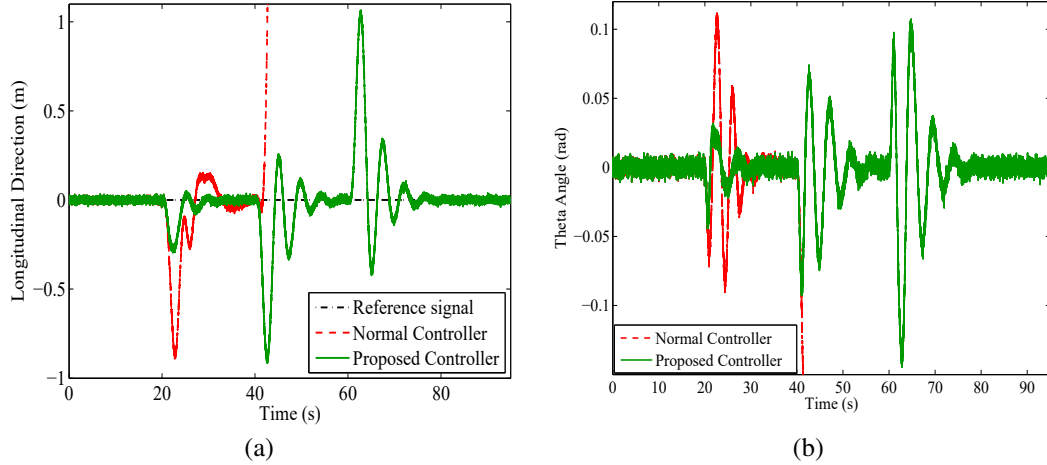
Figure 4.26: Performance comparison in longitudinal direction (a) and pitch angles (b).
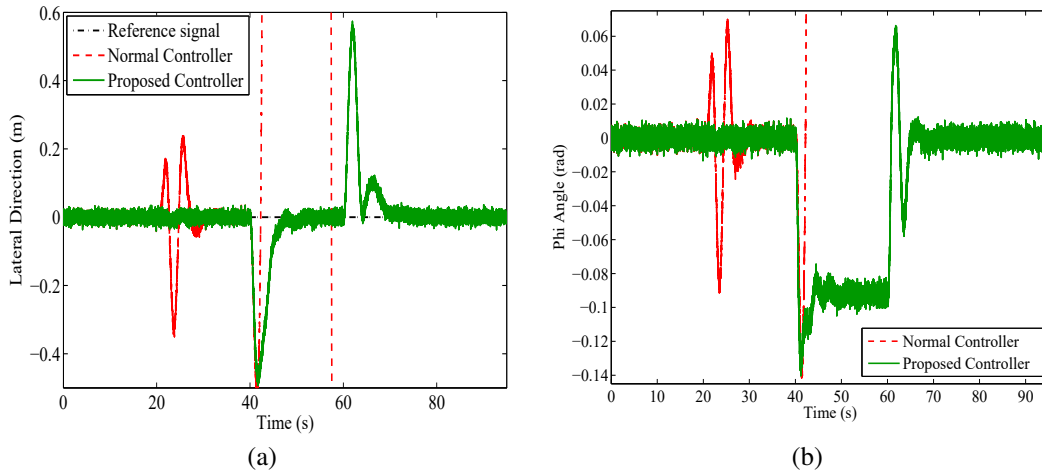
Figure 4.27: Performance comparison in lateral direction (a) and roll angles (b).

and external disturbances. While the proposed controller can eventually maintain the quadrotor's stability at the expense of 60% overshoot after the occurrence of disturbance.

It can be observed from Fig. 4.26(b) and 4.27(b), the normal controller cannot ensure Euler angles to track the reference signals. Eventually, as shown in Fig. 4.26(a) and 4.27(a), it cannot force the set-point tracking error to converge to zero quickly enough or even worse steer the quadrotor helicopter to the intended position within a stipulated time. On the contrary, within a graceful performance degradation, the proposed controller can still ensure stability of the quadrotor helicopter. This indicates the proposed controller has the capability to effectively reject large constant external disturbances comparing to the normal controller.

From Fig. 4.28, operated by the normal controller, the UQH's actuators are saturated when
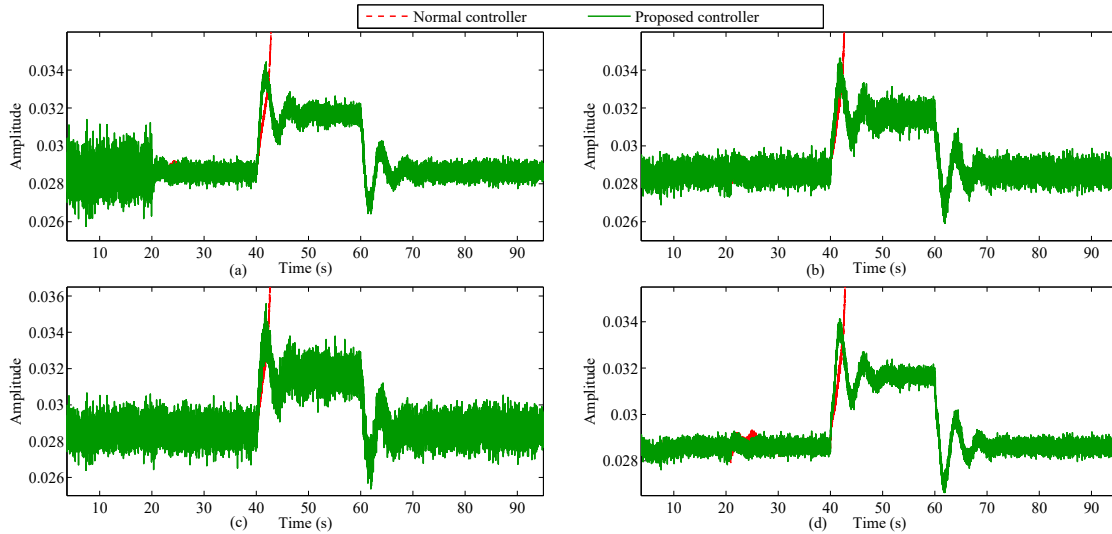
Figure 4.28: Performance of PWM control input signals.

it simultaneously encounters the actuator fault and external disturbances. This directly leads to the crash. However, by employing the proposed controller, the UQH can react effectively and its stability can also be guaranteed without violating actuator limits.

4.2.3.4 Results of Scenario 3 and Evaluation

Before the presence of actuator faults, the normal and proposed controllers (no fault compensating mechanism is activated) are similar, thereby the analogically good trajectory tracking performance can be observed in Fig. 4.29. After the occurrence of actuator faults, Fig. 4.29 shows a deviation from the expected path. One can see that the better tracking performance is achieved by the proposed controller comparing with the normal controller. The existence of fault compensating mechanism exactly explains the superior performance of the proposed controller.

To be more specific, from Fig. 4.30, $0.33\ m$ and $0.83\ m$ of height losses are induced under the supervision of the proposed and normal controllers, respectively. Furthermore, although no significant tracking errors are caused along the longitudinal direction (as shown in Fig. 4.32) when the UQH is operated by either the normal controller or proposed controller, the performance of the UQH along the lateral direction (as displayed in Fig. 4.31(a)) achieved by the normal controller (around $0.5\ m$) is worse than that of the proposed controller (around $0.17\ m$).
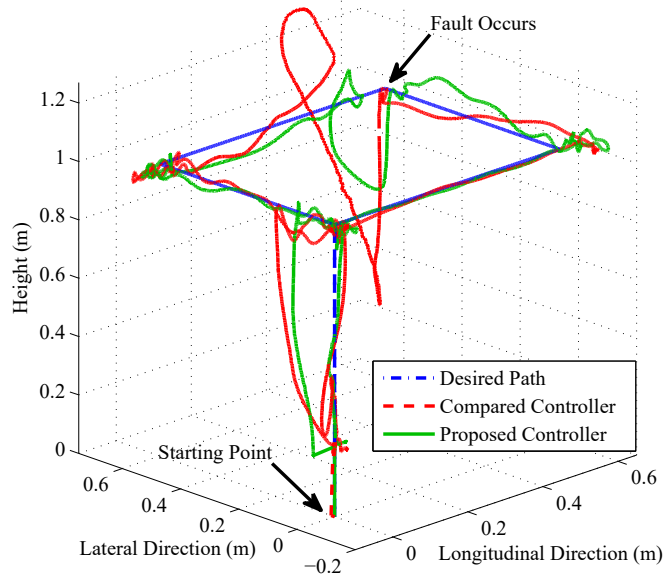
Figure 4.29: Performance comparison of normal and proposed controllers in 3D view.
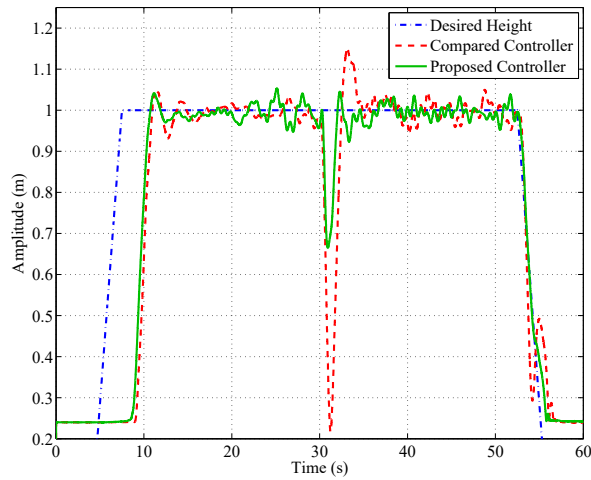
Figure 4.30: Performance comparison in the vertical direction.
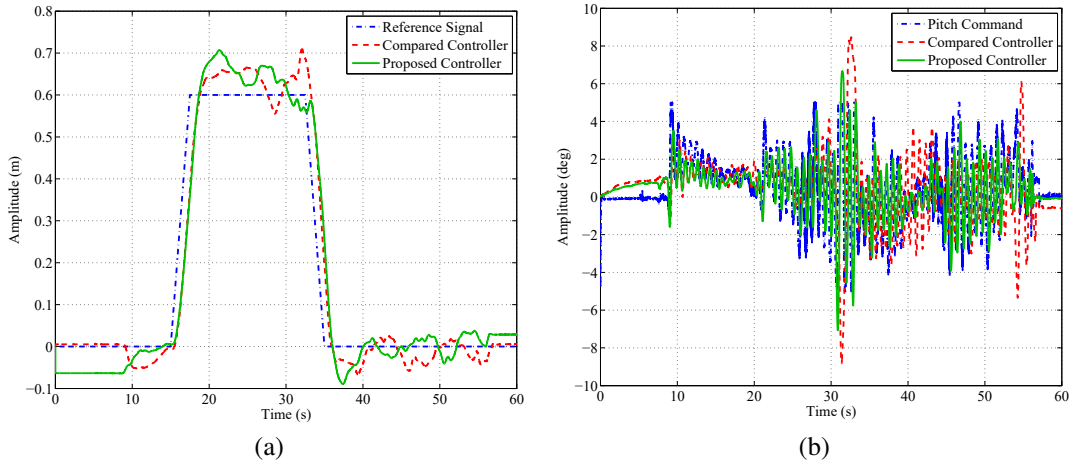
Figure 4.31: Performance comparison in longitudinal direction (a) and pitch angles (b).

111
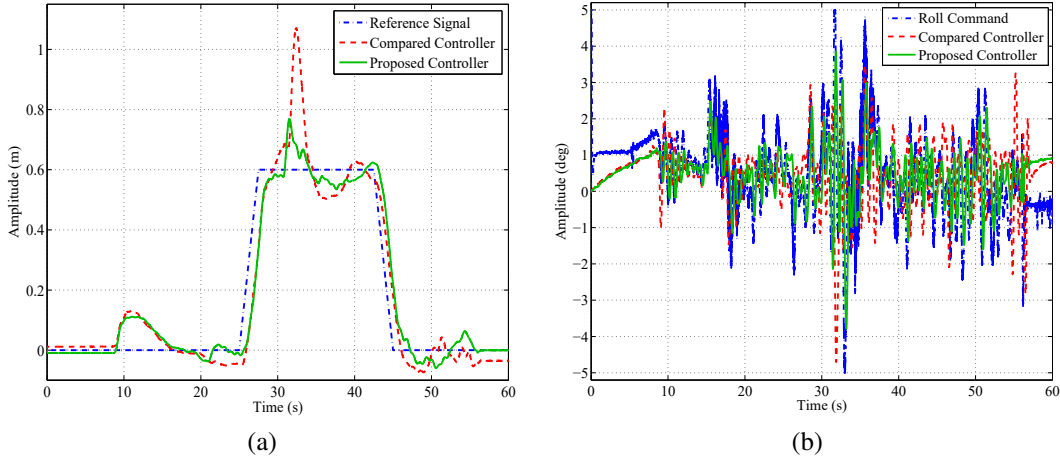
Figure 4.32: Performance comparison in lateral direction (a) and roll angles (b).

In addition, as can be seen in Fig. 4.33, more appropriate PWM inputs are generated by the proposed controller (by virtue of the consideration of actuator dynamics in the controller design) with comparison of the normal controller, while this correspondingly contributes to the less aggressive actions of the UQH manoeuvring by the proposed controller.

4.3 Adaptive Fault-Tolerant Tracking Control of Unmanned Surface Vehicle

In addition to the design of a reliable USV guidance system capable of compensating negative effects from environmental disturbances and turning motion (as stated in section 3.1), it is also of great importance to develop a FTC strategy to enhance the reliability and safety of USV control system and maintain an acceptable level of performance in the presence of system component malfunctions. As the connection between the control command and physical action, the actuator plays a vital role in USV control system. When actuators fail to operate as expected, the system performance degrades as well, even the stability of the overall system may be seriously threatened. These hazardous phenomena may further lead to two risks, the first risk implies that both rescue personnels and manned vessels are needed to fetch the USV with defect actuators; the other risk is to increase the collision probabilities and threats to other vessels and personnels in the vicinity of
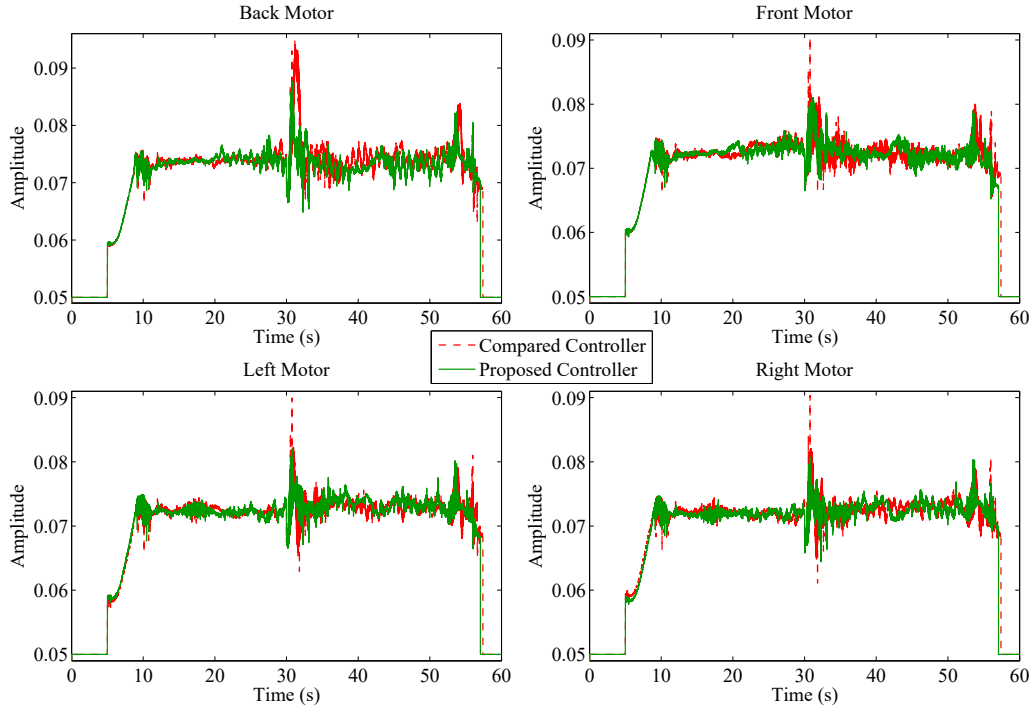
Figure 4.33: Performance comparison of PWM input signals.

the faulty USV.

The existing researches in the USV control community up to date, however, mainly involve the fault detection and diagnosis (FDD) of USV sensor and actuator failures, while limited number of papers devote to the FTC of USV problems. In terms of the FDD of USV sensor faults, a fuzzy logic adaptive federated Kalman filter (FLA-FKF) algorithm is developed in [122] in the event of sensor faults and measurement noises. In [123], an adaptive observer is proposed along with redundant sensors to detect sensor faults. A multiple model adaptive estimation (MMAE) technique is presented in [124] to detect and isolate the sensor faults. [125] introduces a federated Kalman filter (FKF) employing a fuzzy logic adaptive methodology for detecting and isolating different class of sensor faults. With respect to the FTC of USV, a reconfigurable control approach is adopted for the accommodation of ship propulsion faults in [126]. In [127], an unknown input observer based fault-tolerant control allocation technique is developed for the detection and isolation of actuator faults. [128] addresses a linear parameter varying control technique based FTC method considering the actuator fault as a time-varying term in the controller design. Furthermore, according to the existing work [74,75], the desired heading angle is normally assumed to be perfectly tracked by the
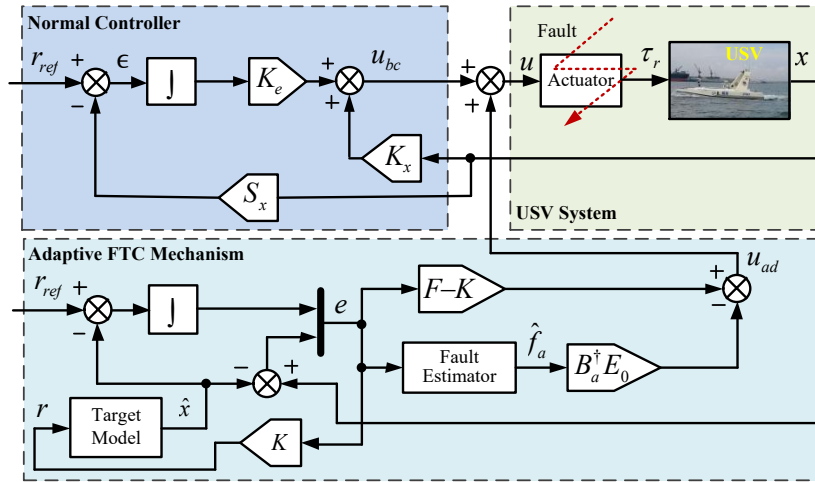
Figure 4.34: Block diagram of the proposed adaptive fault-tolerant tracking control scheme.

heading control system. In the practical situations, however, either environmental disturbances or actuator failures may seriously affect the performance of heading controller. The desired heading angle thereby may not be well tracked in these dangerous cases.

In the subsequence of this section, the design procedure of a normal tracking control method is first applied in the absence of actuator faults. Then, a retrofit adaptive fault estimation and compensating control scheme is introduced to counteract the actuator failure. Finally, a fault-tolerant tracking control strategy is constructed by synthesizing these two control laws.

4.3.1   Adaptive Fault-Tolerant Control Law Design

The primary idea behind the proposed FTC method is illustrated in Fig. 4.34, which is the combination of the aforementioned normal tracking control scheme and a fault estimation and compensating mechanism. Its design procedure can be generally introduced as follows:

(1) before encountering the actuator fault, the USV is controlled by the normal tracking controller to achieve the satisfactory performance;

(2) once the fault occurs, a fault estimator is activated and the amplitude of the fault is then estimated based on an indirect adaptive fault estimation law;

(3) after the fault estimation, a corresponding fault compensating control input is generated according to an actuator fault compensating control law; and

(4) eventually, an adaptive FTC input combining with the normal and fault compensating control inputs is synthesized so as to effectively counteract the adverse effect of actuator faults.

In the mathematical representation, the ultimate control input $u(t)$ can also be written as:

$$u(t) = u_{bc}(t) + u_{ad}(t), \tag{153}$$

where $u_{ad}(t)$ is the fault compensating control input, which is 0 in the normal case and deviates from 0 in the event of actuator fault, $u_{bc}(t)$ denotes the control input from the normal controller.

To further facilitate the controller design, as a widely adopted marine surface vehicles model, the USV model (3) has been reduced into the classic Nomoto model, which is employed in this research for modelling the yaw dynamics of USV:

$$\dot{\psi} = r$$
$$\dot{r} + \frac{d_{33}}{m_{33}}r = \frac{1}{m_{33}}\tau_r, \tag{154}$$

where τ_r is the yaw control moment, m_{33} and d_{33} denote the added mass effects and hydrodynamic damping, respectively [98].

In state-space representation, (154) can then be written into:

$$\dot{x}(t) = Ax(t) + Bu(t), \tag{155}$$

where $u(t) = \tau_r$ is the control input, $x(t) = [\psi, r]^T$ is the state vector, $A = \begin{bmatrix} 0 & 1 \\ 0 & -d_{33}/m_{33} \end{bmatrix}$, and $B = [0 \ 1/m_{33}]^T$.

Borrowing the idea of incorporation of state feedback control law with an integral action that is used in section 4.1, (155) can then be augmented as:

$$\dot{x}_a(t) = A_a x_a(t) + B_a u(t) + G_a r_{ref}(t), \tag{156}$$

where $A_a = \begin{bmatrix} 0 & -S_x \\ 0 & A \end{bmatrix} \in \Re^{(q+n)\times(q+n)}$, $B_a = [0 \ B]^T \in \Re^{(q+n)\times m}$, and $G_a = [I \ 0 \ 0]^T \in \Re^{(q+n)\times q}$.

Consider the closed-loop state feedback control with integration of the integral term of tracking error, the following controller can then be selected as the normal tracking control law:

$$u_{bc}(t) = K x_a(t) = K_e \int_0^t \epsilon(\tau)d\tau + K_x x(t), \tag{157}$$

where $K = [K_e \ K_x] \in \Re^{m\times(l+n)}$ which is designed using *Theorem 5* in section 4.1, $\epsilon(t) = r_{ref}(t) - S_x x(t)$ denotes the error between reference signal and state, $r_{ref}(t)$ is the reference signal, matrix $S_x \in \Re^{q\times p}$ determines the specific outputs for tracking the reference signals, and $x_a(t) = \begin{bmatrix} \int_0^t \epsilon(\tau)d\tau & x(t) \end{bmatrix}^T \in \Re^{(q+n)}$ is the augmented state vector.

Combine (156) and (157), the augmented closed-loop state feedback control system becomes:

$$\dot{x}_a(t) = (A_a + B_a K)x_a(t) + G_a r_{ref}(t). \tag{158}$$

Incorporate actuator fault (11) in the augmented system (156):

$$\dot{x}_a(t) = A_a x(t) + B_a u(t) + E_a f_a(t), \tag{159}$$

where $E_a = G_a + [0, \ E]^T = [I, \ E^T]^T$ and $f_a(t) = [r_{ref}(t), \ f(t)]^T$.

Consider a target model subjects to actuator faults, which has the following structure:

$$\dot{\hat{x}}(t) = A\hat{x}(t) + Br(t) + E\hat{f}(t), \tag{160}$$

116

where the target control input $r(t) \in \Re^n$ is properly determined so as to achieve the control objective. $\hat{x}(t)$ and $\hat{f}(t)$ denote the estimation of states and actuator faults, respectively.

The augmented form of the target model (160) becomes:

$$\dot{\hat{x}}_a(t) = A_a \hat{x}_a(t) + B_a r(t) + E_a \hat{f}_a(t), \tag{161}$$

where $\hat{x}_a = \left[\int_0^t \hat{\epsilon}(\tau)d\tau \quad \hat{x}(t) \right]^T$ and $f_a(t) = [r_{ref}(t), \ \hat{f}(t)]^T$.

Let the system state error $e(t) = x_a(t) - \hat{x}_a(t)$ and the control input $u(t) = r(t) + Fe(t)$, the derivative of the state error between (159) and (161) then gives:

$$\begin{aligned}
\dot{e}(t) &= \dot{x}_a(t) - \dot{\hat{x}}_a(t) \\
&= A_a e(t) + B_a(u(t) - r(t)) + E_a(f_a(t) - \hat{f}_a(t)) \\
&= (A_a + B_a F)e + E_a \tilde{f}_a(t),
\end{aligned} \tag{162}$$

where $\tilde{f}_a(t) = f_a(t) - \hat{f}_a(t)$ is the estimation of fault errors, $\tilde{f}_a(t) = [\tilde{f}_{a1}(t)...\tilde{f}_{an}(t)]^T$, and F is the error feedback gain which is designed for stabilizing the augmented system (161).

Writing $E_a = [E_{a1}...E_{an}]^T$, the following augmented system state errors can be obtained:

$$\dot{e}(t) = (A_a + B_a F)e + \sum_{i=1}^{n} E_{ai} \tilde{f}_{ai}(t). \tag{163}$$

Since the actuator fault can be regarded as constant within a relatively short period as compared with fast sampling time, then the following relationship is achievable:

$$\dot{\tilde{f}}_a(t) = \dot{f}_a(t) - \dot{\hat{f}}_a(t) = -\dot{\hat{f}}_a(t). \tag{164}$$

Theorem 8 *The augmented state error system (163) can be stabilized if there exist a positive symmetric matrix $X_a \in \Re^{(m+l)\times(m+l)}$ and matrix $Y_a \in \Re^{n\times(m+1)}$, while the linear matrix inequality (165) should hold:*

$$A_a X_a + B_a Y_a + X_a A_a^T + Y_a^T B_a^T < 0, \tag{165}$$

and $\dot{\hat{f}}_a(t)$ is determined by the following indirect adaptive law:

$$\dot{\hat{f}}_{ai}(t) = Proj_{[\underline{f}_i, \overline{f}_i]}\{k_{Pi}\Xi^T PE_{ai}\}$$

$$= \begin{cases} 0, & \text{if } \hat{f}_a(t) = \underline{f}_i, k_{Pi}\Xi^T PE_{ai} \leqslant 0 \\ & \text{or } \hat{f}_a(t) = \overline{f}_i, k_{Pi}\Xi^T PE_{ai} \geqslant 0, \\ k_{Pi}\Xi^T PE_{ai}, & \text{otherwise,} \end{cases} \tag{166}$$

where $\Xi = e(t) + k_{Di}\dot{e}(t)$, the adaptive law gain $k_{Pi} > 0$ and $k_{Di} > 0$, the positive symmetric matrix $P = X_a^{-1} > 0$, and $Proj\{\cdot\}$ denotes the projection operator [100] which is employed for projecting the estimates $\hat{f}_{ai}(t)$ to the acceptable fault interval $[\underline{f}_i, \overline{f}_i]$.

Proof of Theorem 8: Based on (163), the Lyapunov candidate function is chosen as:

$$V_2 = e^T(t)Pe(t) + \sum_{i=1}^{n} \frac{\tilde{f}_a^2(t)}{k_{Pi}}. \tag{167}$$

Deriving V_2 with respect to time and along the trajectory of the error (163), one can obtain:

$$\dot{V}_2 = e^T(t)[P(A_a + B_aF) + (A_a + B_aF)^T P]e(t) + 2\sum_{i=1}^{n} \tilde{f}_{ai}e^T(t)PE_{ai} + 2\sum_{i=1}^{n} \frac{\tilde{f}_{ai}\dot{\tilde{f}}_{ai}}{k_{Pi}}. \tag{168}$$

According to the adaptive law (166), one can obtain:

$$\frac{\tilde{f}_{ai}\dot{\tilde{f}}_{ai}}{k_{Pi}} = -\tilde{f}_{ai}[e(t) + k_{Di}\dot{e}(t)]^T PE_{ai}. \tag{169}$$

Substituting (169) into (168), it follows that:

$$\dot{V}_2 = e^T(t)[P(A_a + B_aF) + (A_a + B_aF)^T P]e(t) - 2\sum_{i=1}^{n} \frac{\tilde{f}_{ai}k_{Di}\dot{e}^T(t)PE_{ai}}{k_{Pi}}. \tag{170}$$

Setting V_2 as follows:

$$\dot{V}_2 = \dot{V}_{21} + \dot{V}_{22}, \tag{171}$$

118

where $\dot{V}_{21} = e^T(t)[P(A_a + B_aF) + (A_a + B_aF)^TP]e(t)$ and $\dot{V}_{22} = -2\sum_{i=1}^{n}\frac{\tilde{f}_{ai}k_{Di}\dot{e}^T(t)PE_{ai}}{k_{Pi}}$.

Let $F = Y_aX_a^{-1}$, $P = X_a^{-1}$, as well as (165) holds, the following inequality can be obtained:

$$\dot{V}_{21} = e^T(t)[P(A_a + B_aF) + (A_a + B_aF)^TP]e(t) < 0. \tag{172}$$

Next, substituting (163) into $\dot{V}_{22}$ gives:

$$\begin{aligned}
\dot{V}_{22} = & -2\sum_{i=1}^{n}\frac{\tilde{f}_{ai}k_{Di}[e^T(t)(A_a + B_aF)^T + (E_{ai}\tilde{f}_{ai})^T]PE_{ai}}{k_{Pi}} \\
\leq & -2\sum_{i=1}^{n}\frac{\tilde{f}_{ai}k_{Di}e^T(t)(A_a + B_aF)^TPE_{ai}}{k_{Pi}} - 2\sum_{i=1}^{n}\frac{\tilde{f}_{ai}^2k_{Di}E_{ai}^TPE_{ai}}{k_{Pi}}.
\end{aligned} \tag{173}$$

Employing the *Lemma 1* in [129], for a positive scalar μ and positive symmetric matrix P_0, one can obtain that:

$$\begin{aligned}
\dot{V}_{22} \leq & -2\sum_{i=1}^{n}\frac{\tilde{f}_{ai}k_{Di}e^T(t)A_{st}^TPE_{ai}}{k_{Pi}} - 2\sum_{i=1}^{n}\frac{\tilde{f}_{ai}^2k_{Di}E_{ai}^TPE_{ai}}{k_{Pi}} \\
\leq & \sum_{i=1}^{n}\frac{e^T(t)P_0e(t)}{\mu k_{Pi}} - 2\sum_{i=1}^{n}\frac{\tilde{f}_{ai}^2k_{Di}E_{ai}^TPE_{ai}}{k_{Pi}} + \mu\sum_{i=1}^{n}\frac{[\tilde{f}_{ai}k_{Di}A_{st}^TPE_{ai}]P_0^{-1}[\tilde{f}_{ai}k_{Di}A_{st}^TPE_{ai}]^T}{k_{Pi}} \\
\leq & \sum_{i=1}^{n}\frac{e^T(t)P_0e(t)}{\mu k_{Pi}} - 2\sum_{i=1}^{n}\frac{\tilde{f}_{ai}^2k_{Di}E_{ai}^TPE_{ai}}{k_{Pi}} \\
& + \mu\sum_{i=1}^{n}\frac{(\tilde{f}_{ai}k_{Di})^2}{k_{Pi}}\lambda_{max}\Big\{[A_{st}^TPE_{ai}]P_0^{-1}[A_{st}^TPE_{ai}]^T\Big\},
\end{aligned} \tag{174}$$

where $A_{st} = A_a + B_aF$.

Substituting (172) into (170) gives:

$$\dot{V}_2 = \dot{V}_{21} + \dot{V}_{22} \leq -(\delta_1 - \delta_2)||e(t)||^2 + \delta_3, \tag{175}$$

119

where

$$\delta_1 = -\max[PA_{st} + A_{st}^T P] > 0,$$

$$\delta_2 = \sum_{i=1}^{n} \frac{P_0}{\mu k_{Pi}} > 0,$$

$$\delta_3 = \mu \sum_{i=1}^{n} \frac{(\tilde{f}_{ai} k_{Di})^2}{k_{Pi}} \lambda_{max} \left\{ [A_{st}^T P E_{ai}] P_0^{-1} [A_{st}^T P E_{ai}]^T \right\} - 2 \sum_{i=1}^{n} \frac{\tilde{f}_{ai}^2 k_{Di} E_{ai}^T P E_{ai}}{k_{Pi}}.$$

Then, $\dot{V}_2 < 0$ for $(\delta_1 - \delta_2)||e(t)||^2 > \delta_3$, $\forall t \geq 0$, this implies that the errors $e(t)$ and $\tilde{f}_a$ are uniformly bounded and converge to a small set according to the Lyapunov stability theory [101], and the augmented state error (162) is also stabilized.

Remark 11 *A feasibility solution of X_a and Y_a is obtained by solving inequality (165) using Matlab LMI toolbox. The error feedback gain F can then be calculated by $F = Y_a X_a^{-1}$.*

Remark 12 *The adaptive fault estimation law (166) constitutes a proportional term with a derivative one, which can increase the rapidity of fault estimation comparing with the fault estimation law with solely the proportional term.*

4.3.2 Control Schemes Synthesis

In order to match the augmented target system model (161) with the fault-free system model (156), $r(t) = K\hat{x}_a(t) - B_a^\dagger E_0 \hat{f}(t)$ is chosen so that (161) becomes:

$$\dot{\hat{x}}_a(t) = A_a \hat{x}_a(t) + B_a K \hat{x}_a(t) + G_a r_{ref}(t), \tag{176}$$

where $E_0 = [0, \ E^T]^T$ and $B_a^\dagger$ is the pseudo inverse of B_a.

From *Theorem 8*, it implies that $\hat{x}_a(t) \in L^\infty$ and $r(t)$ are bounded. Moreover, $e(t) \in L^\infty$, the state vector $x_a(t)$ of augmented faulty model (159) is then bounded. Based on the augmented state error system (163), it follows that $\dot{e}(t)$ is bounded as well. Together with a fact that $e(t) \in$

$L^\infty \bigcap L^2$, it means that $lim_{t\to\infty}e(t) = 0$. As a result, the states encountering actuator faults can asymptotically track that of normal states and the final control goal is fulfilled [121].

The ultimate control effort compensating the negative impact of actuator faults is obtained:

$$
\begin{aligned}
u(t) &= r(t) + Fe(t) \\
&= K\hat{x}_a(t) - B_a^\dagger E_0 \hat{f}_a(t) + Fe(t) \\
&= u_{bc}(t) + u_{ad}(t),
\end{aligned}
\tag{177}
$$

where $u_{bc}(t) = Kx_a(t)$, and $u_{ad}(t) = (F - K)e(t) - B_a^\dagger E_0 \hat{f}_a(t)$. The additional control input $u_{ad}(t)$ will vary from 0 in the presence of actuator faults.

Remark 13 *In addition to counteracting the adverse effects of actuator faults, the proposed controller is capable of ensuring the satisfactory performance of normal controller as well. Actually, this property is of significance as the USV is operated under actuator failures most of the time.*

4.3.3 Simulation Results

The USV model and path to be followed, in this simulation, are selected as the same to the simulation of Section 3.1.

4.3.3.1 Scenarios Description

The following two scenarios have been considered:

(1) *Scenario 1*: A step fault with amplitude of $0.2\ Nm$, in this case, is injected in rudder control input. This fault begins at 20th second and disappears at 100th second. The performance of the normal and proposed controllers is compared.

(2) *Scenario 2*: To further validate the efficacy of the proposed controller, a time-varying actuator fault $(0.1 + 0.2sin(\pi/5)t)$ is introduced into rudder, lasting from 20th to 180th second.
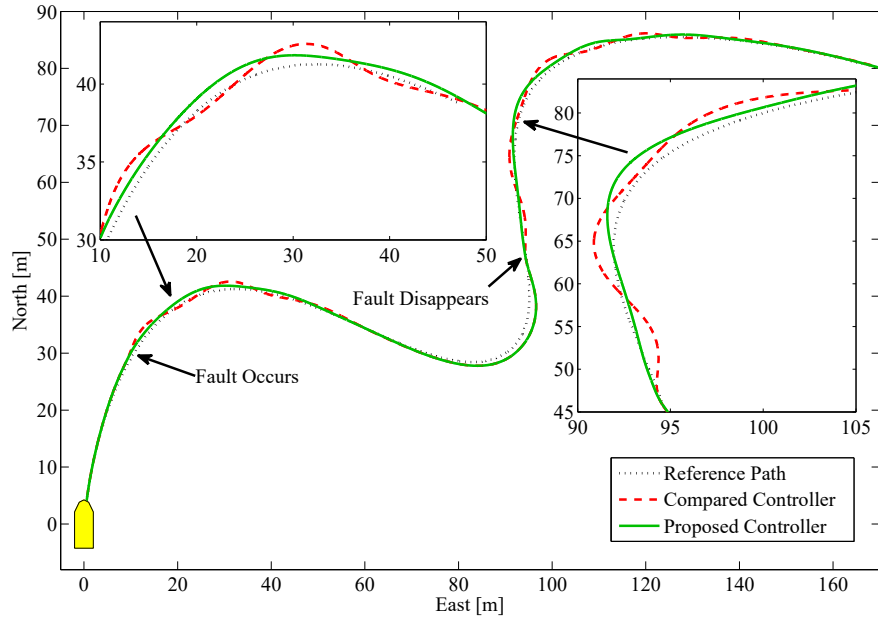
Figure 4.35: The performance comparison of path following.

4.3.3.2 Results of Scenario 1 and Evaluation

In Fig. 4.35, the path following performance of the normal and proposed controllers are compared. After either the occurrence or disappearance of actuator faults, the USV can smoothly follow the path under the supervision of the proposed adaptive FTC controller, while the transient oscillation is induced when the USV is operated by the normal controller.
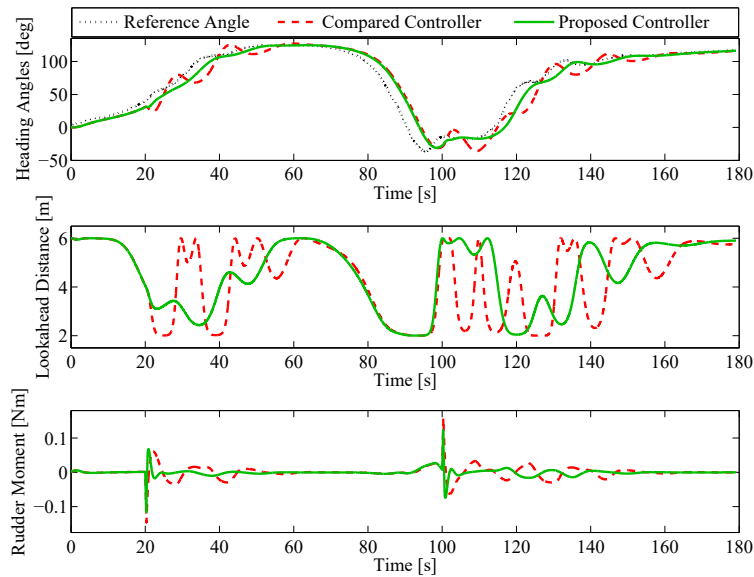
Figure 4.36: Performance of heading angle, lookahead distance, and rudder.
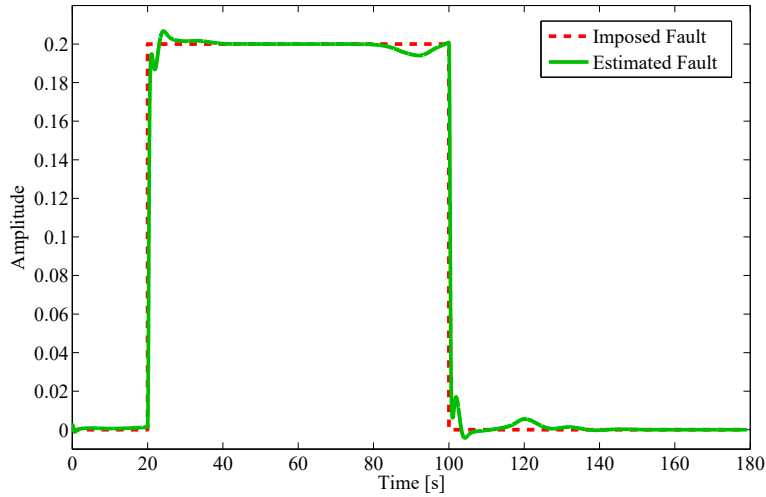
Figure 4.37: The estimation of actuator fault.
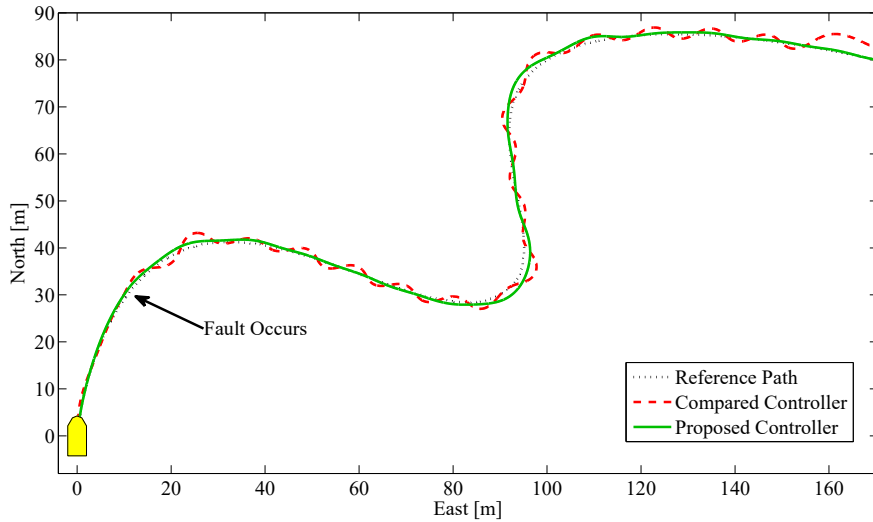
Figure 4.38: The performance comparison of path following.

Fig. 4.36 displays the time histories of heading angle tracking, lookahead distance, and rudder moment. It can be seen that a more prompt and proper rudder action is produced with the proposed controller comparing with normal controller. Accordingly, this results in a better heading angle tracking performance and less and smoother lookahead variation than that of the normal controller.

The fault estimation result is shown in Fig. 4.37, it clearly shows that the amplitude of the imposed actuator fault can be well and rapidly estimated.

123

4.3.3.3   Results of Scenario 2 and Evaluation

From Fig. 4.38, the added actuator fault seriously deteriorates the performance of the normal controller which makes the USV oscillates along the path, while the proposed controller capable of compensating the negative effects of fault maneuvers the USV to follow the desired path in a gentle and steady manner. This good results of the proposed controller is due to the rapid and appropriate rudder operation (see in Fig. 4.39), which likewise steers the USV to elegantly track the expected heading angle without causing obvious oscillation. Furthermore, compared with normal controller, the proposed controller induces less and smoother lookahead distance variation.
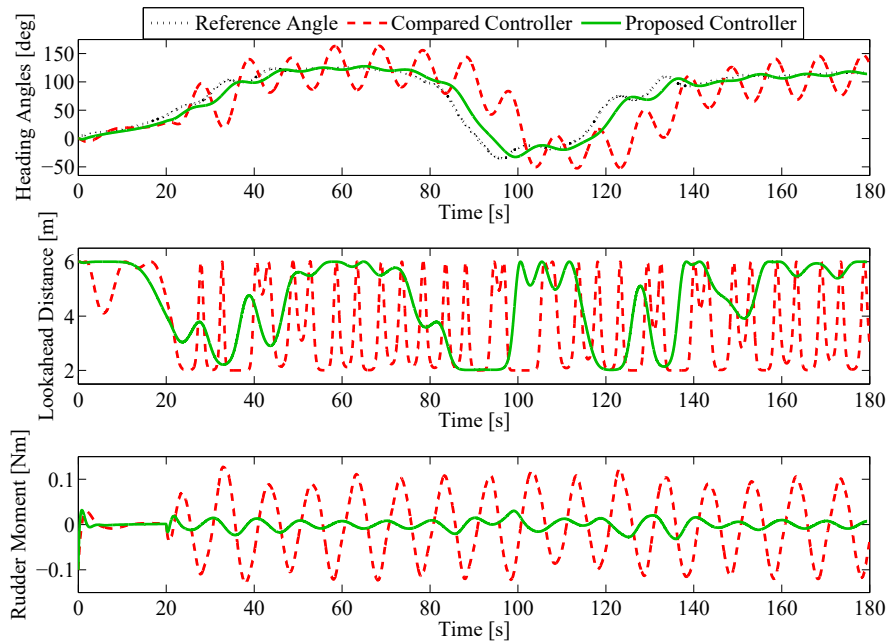
Figure 4.39: Performance of heading angle, lookahead distance, and rudder.

As displayed in Fig. 4.40, even the amplitude of the time-varying fault can be consistently estimated as well. This superior performance is because of the introduction of the derivative term in the fault estimation law which can guarantee a prompt convergence to the expected value.
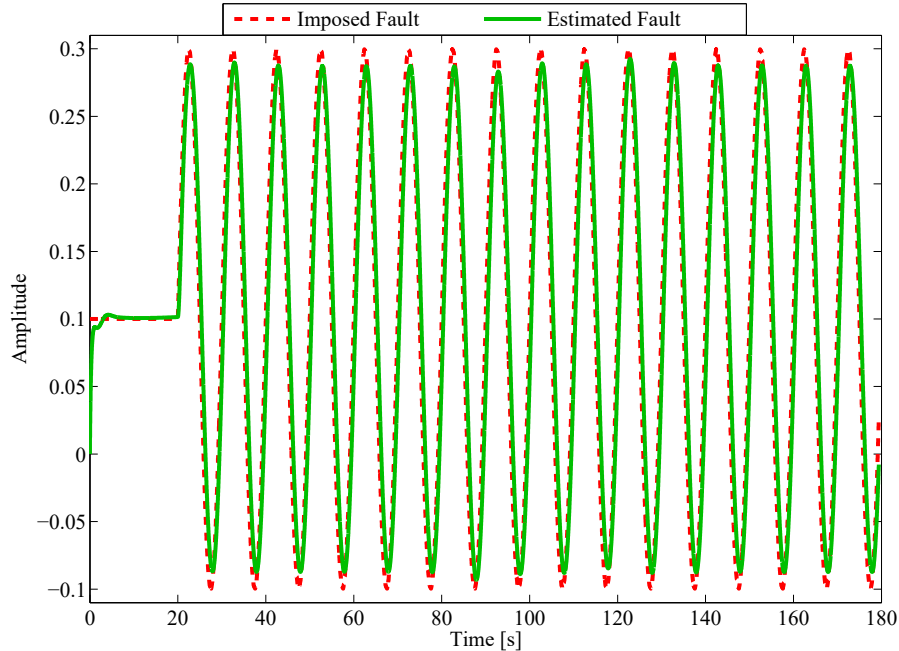
Figure 4.40: The estimation of actuator fault.

4.4 Linear Parameter Varying Control of Unmanned Surface Vehicle with Actuator Faults and Mass Variation

In real life situations, the mass of USV may suddenly and dramatically change due to payload deployment, aircraft taking-off and landing, as well as missile launching. It may also gradually alter over a period of time due to fuel consumption and water sampling. These factors can directly lead to the variation of system dynamics (inertia and Coriolis and centripetal effects), and may ultimately deteriorate the performance of USV controller that is designed on the basis of a static internal model. More seriously, it may likewise cause the frequent operation as well as wear and tear of actuators which can severely threaten the health of actuators (actuator faults), result in missions being aborted, and probably threaten the safety of other marine crafts and personnels in its proximity [130]. In order to cope with such issues and successfully accomplish assigned missions without significant performance degradation, the development of an efficient and effective gain-scheduling control methodology with adaptive dynamics updating capabilities is highly demanded. Unfortunately, the variation of mass, which is responsible for the significant deterioration

in terms of controller performance, is normally unknown in advance. The precise estimation of mass variation is thereby critical in real-time applications. However, little research to date involve in this topic, only a recent publication is found in [130], in which a model predictive control (MPC) combining with three parameter estimation algorithms (including gradient descent, least squares, and weighted least squares) is developed.

Most of the existing USVs control approaches are developed based on linear models or the linearization of nonlinear systems around a specific operating point. But for systems with a wide operating range, the linearized methods may fail to achieve satisfactory performance. Alternatively, the linear parameter varying (LPV) control [131] capable of effectively solving numerous nonlinear control problems has progressed steadily into a mature tool [132]. It has a significant advantage over the fixed-gain controllers since its feedback control gains can be scheduled along with the variation of dynamics, which contributes to less conservativeness of the controller as well. In industrial applications, LPV control method has been widely adopted to solve variety of practical problems due to its capability of guaranteeing system stability and performance over a wide range of operating conditions [133]. The idea of LPV is firstly appeared in [134] which is to analyse the interpolation and realization issues in the traditional gain-scheduling control approaches. In the successive development, many methodologies are gradually developed to contribute to the LPV control design including linear matrix inequality (LMI) [135], stable realizations [136], and set-invariance methods [137].

In order to overcome the challenges addressed above, this thesis investigates the design of an adaptive gain scheduling control method for USV tackling the sudden change in mass, while encountering actuator faults. This proposed controller includes the following components: 1) a LPV state feedback controller is designed to control USV under different operating conditions, these conditions include variations of overall mass and actuator faults, which are considered as the scheduling variables in the LPV controller design; 2) an adaptive parameter estimation mechanism and a finite-time adaptive fault estimation scheme are devised to provide the real-time information of mass and actuator faults variations during the maneuver of USV; 3) finally, a LPV state feedback

controller capable of adaptively estimating system parameter variation is synthesized to guarantee the satisfactory mission performance in the absence/presence of sudden and dramatic changes in dynamics.

4.4.1 USV Linear Parameter Varying Steering Model

Assumption 7 *It is reasonable to neglect the sway velocity (this derives $u_v = 0$) since it is much smaller than the surge velocity in the case of underactuated USV.*

Based on *Assumption 7*, the following simplified USV model consisting of surge and steering dynamics can be achieved:

$$
\begin{aligned}
\dot{u}_u &= A_u u_u + B_u \tau_u \\
\dot{\psi} &= r \\
\dot{r} &= A_r r + B_r \theta,
\end{aligned}
\tag{178}
$$

where ψ, θ, and u_u denote the yaw angle, rudder deflection, and surge speed, respectively. $A_u = -d_{11}/m_{11}$, $A_r = -d_{33}/m_{33}$, $B_u = 1/m_{11}$, $B_r = N_\theta/m_{33}$.

In addition, the parameters $d_{33} = -N_r + (m\chi_g - \frac{1}{2}N_{\dot{v}} - \frac{1}{2}Y_{\dot{r}})u_u$ and $m_{11} = m - X_{\dot{u}}$ are functions of system overall mass m. When selecting m as a time-varying parameter, (178) is exactly a LPV model [138].

Without loss of generality, (178) can be written into the following state-space form:

$$
\begin{cases}
\dot{x}(t) = A(\delta)x(t) + B(\delta)u(t) \\
y(t) = C(\delta)x(t),
\end{cases}
\tag{179}
$$

where $u(t) = [\tau_u \ \theta]^T \in \Re^m$, $x(t) = [u_u \ \psi \ r]^T \in \Re^n$, and $y(t) \in \Re^p$ represent the system's control input, state, and output vector, respectively. $A(\delta) = \begin{bmatrix} A_u & 0 & 0 \\ 0 & 0 & 1 \\ 0 & 0 & A_r \end{bmatrix}$, $B(\delta) = \begin{bmatrix} B_u & 0 \\ 0 & 0 \\ 0 & B_r \end{bmatrix}$,

and $C(\delta) = \begin{bmatrix} 1 & 0 \\ 0 & 1 \end{bmatrix}$. δ is a time-varying vector that contains all possible trajectories of system.

The linearized USV model can then be expressed as:

$$(A(\delta), B(\delta), C(\delta)) = \sum_{i=1}^{N} \mu_i(A_i, B_i, C_i) \in Co\{(A_i, B_i, C_i) : i = 1, ..., N\}, \qquad (180)$$

with the convex coordinates $\mu_i > 0$ and $\sum_{i=1}^{N} \mu_i = 1$, $(A_i, B_i, C_i)(i = 1, ..., N)$ are a *priori* known constant matrices that denote USV models at all vertices, and $Co\{\cdot\}$ represents the convex hull.

$$\Omega = \{\mu_i \in \Re^N, \mu_i \geq 0, \sum_{i=1}^{N} \mu_i = 1\}, \qquad (181)$$

where Ω denotes a convex set, μ_i denotes the function of time-varying parameter δ, and its selection rule can use the *bounding box approach* presented in [139].

Therefore, a LPV system can be constructed if the parameter dependence is affine, that is matrices $A(\delta)$, $B(\delta)$, and $C(\delta)$ depend affinely on δ, while δ varies over a fixed polytope. In order to eliminate the steady-state error, the state feedback control is normally in augmentation with an integral action [140]. The augmented feedback system can then be described as follows:

$$\begin{cases} \dot{x}_a(t) = A_a(\delta)x_a(t) + B_a(\delta)u(t) + G_a(\delta)y_r(t) \\ y_a(t) = C_a(\delta)x_a(t), \end{cases} \qquad (182)$$

where $y_r(t)$ is the reference signal, $x_a(t) = [\int_0^t \varepsilon(\tau)d\tau, x(t)]^T$ and $y_a(t) = [\int_0^t \varepsilon(\tau)d\tau, y(t)]^T$, $\varepsilon(t) = y_r(t) - y(t)$.

$$A_a(\delta) = \begin{bmatrix} 0 & -SC(\delta) \\ 0 & A(\delta) \end{bmatrix} \in \Re^{(l+n)\times(l+n)}, B_a(\delta) = \begin{bmatrix} 0 \\ B(\delta) \end{bmatrix} \in \Re^{(l+n)\times m},$$

$$C_a(\delta) = \begin{bmatrix} I & 0 \\ 0 & C(\delta) \end{bmatrix} \in \Re^{(l+p)\times(l+n)}, G_a(\delta) = \begin{bmatrix} I \\ 0 \end{bmatrix} \in \Re^{(l+n)\times(l+r)}. \qquad (183)$$

Based on (180) and (183), system (182) can also be written in polytopic representation:

$$(A_a(\delta), B_a(\delta), C_a(\delta), G_a(\delta)) = \sum_{i=1}^{N} \mu_i (A_{ai}, B_{ai}, C_{ai}, G_{ai})$$

$$\in Co\{(A_{ai}, B_{ai}, C_{ai}, G_{ai}) : i = 1, ..., N\}. \tag{184}$$

4.4.2 Finite-Time Linear Parameter Varying Fault-Tolerant Control Design

The overall control design structure of the proposed scheme is outlined in Fig. 4.41. First, a LPV-based fault estimator is constructed to estimate the amplitude of actuator fault under different working conditions; then, a LPV scalar calculation law is developed for the determining the weight of control gains of each vertex; finally, a LPV-based feedback control method is chosen for the reconfigurable control design.
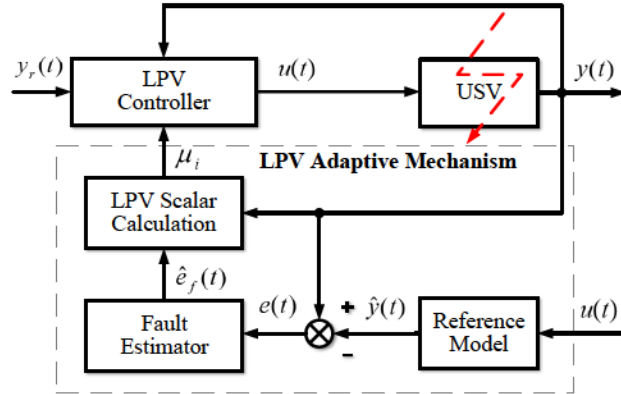
Figure 4.41: Schematic diagram of LPV-based fault-tolerant control method.

4.4.2.1 Linear Parameter Varying Fault-Tolerant Control Scheme

It is assumed that the states of the closed-loop system are measurable by the sensors at any time instant. Hence, the augmented system (182) with closed-loop state feedback and the integral tracking action can be represented by:

$$u(t) = K_{st}(\delta)x(t) = K_\varepsilon(\delta) \int_0^t \varepsilon(\tau)d\tau + K_x(\delta)x(t), \tag{185}$$

where $K_{st}(\delta) = [K_{\varepsilon}(\delta), K_x(\delta)] \in \Re^{m \times (l+n)}$. Choosing the output as $z_a(t) = C_z(\delta)x_a(t) + D_z(\delta)u(t) + G_z(\delta)\omega_a(t)$, the corresponding closed-loop augmented system in state feedback case can therein be represented by:

$$\begin{cases} \dot{x}_a(t) = A_{st}(\delta)x_a(t) + G_a(\delta)\omega_a(t) \\ z_a(t) = C_{st}(\delta)x_a(t) + G_z(\delta)\omega_a(t), \end{cases} \tag{186}$$

where $A_{st}(\delta) = A_a(\delta) + B_a(\delta)K_{st}(\delta)$, and $C_{st}(\delta) = C_z(\delta) + D_z(\delta)K_{st}(\delta)$. $z_a(t) \in \Re^p$, $C_z(\delta) \in \Re^{p \times n}$, $D_z(\delta) \in \Re^{p \times m}$, $G_z(\delta) \in \Re^{p \times r}$.

To ensure the existence of the linear parameter dependent state feedback control law (185) for the closed-loop system (186), the following *bounded real lemma* (BRL) [139] should be satisfied:

(1) $A_{st}(\delta)$ is quadratically stable [108];

(2) there exists a bound $\gamma > 0$ for any exogenous input $\omega_a(t) \in L_2[0.\infty)$, the performance criteria $||T(\delta)||_\infty < \gamma$, where $T(\delta)$ denotes the system transfer function.

If the aforementioned BRL is satisfied, and there exists a symmetric positive definite matrix $X(\delta)$ and a matrix $Y(\delta)$ such that LMI (187) holds [18]:

$$\Xi(\delta) = \begin{bmatrix} A_{lpv}(\delta) & G_a(\delta) & Y^T(\delta)R^{1/2} & X(\delta)Q^{1/2} \\ -\gamma I & * & 0 & 0 \\ * & * & -I & 0 \\ * & * & * & -I \end{bmatrix} < 0, \tag{187}$$

where $A_{lpv}(\delta) = A_a(\delta)X(\delta) + B_a(\delta)Y(\delta) + (A_a(\delta)X(\delta) + B_a(\delta)Y(\delta))^T$.

Remark 14 *For the sake of minimizing the conservative, the matrices $X(\delta)$ and $Y(\delta)$ are normally parameterized. However, the nonlinear uncertainties terms may yielded by the products between the uncertain matrices $A_a(\delta)$ and $X(\delta)$, or $B_a(\delta)$ and $Y(\delta)$. Therefore, the following procedure should be conducted to avoid the nonlinear uncertainties terms by eliminating the elements with the products of two uncertain terms.*

Theorem 9 *The closed-loop system ([186](#)) can be stabilized under the supervision of state feedback control law $u_t = K_{st}(\delta)x_a(t)$ with $K_{st}(\delta) = Y(\delta)X^{-1}(\delta)$, where the positive symmetric matrix $X(\delta) = \sum_{i=1}^{N} \mu_i X_i \in \Re^{(m+l)\times(m+l)}$ and matrices $Y(\delta) = \sum_{i=1}^{N} \mu_i Y_i \in \Re^{n\times(m+l)}$ and $Z(\delta) = \sum_{i=1}^{N} \mu_i Z_i \in \Re^{(m+l)\times(m+l)}$, if ([188](#)) and ([189](#)) hold ($*$ denotes the symmetric entry in the LMI).*

$$\Xi_{ij} + \Xi_{ji} < 0, \ \ (1 \le i \le j \le N), \tag{188}$$

$$\Xi_{ij} = \begin{bmatrix} A_{aj}X_i + B_{aj}Y_i + (A_{aj}X_i + B_{aj}Y_i)^T & G_{aj} & Y_i^T R^{1/2} & X_i Q^{1/2} \\ * & -\gamma I & 0 & 0 \\ * & * & -I & 0 \\ * & * & * & -I \end{bmatrix} < 0. \tag{189}$$

Proof: Expanding and parametrizing all terms in ([187](#)), then the following sufficient condition of ([187](#)) holds:

$$\Xi(\delta) = \sum_{i=1}^{N} \sum_{j=1}^{N} \mu_i \mu_j \Xi_{ij} < 0, \tag{190}$$

where Ξ_{ij} is the same as ([188](#)) and ([189](#)).

If ([188](#)) is true, the following inequalities can thereby be obtained

$$\begin{cases} \Xi_{ii} < 0, & (i = 1, ..., N) \\ \Xi_{ij} + \Xi_{ji} < 0, & (1 \le i < j \le N). \end{cases} \tag{191}$$

As $\sum_{i=1}^{N} \mu_i = 1$, $\mu_i \ge 0$, then

$$\Xi(\delta) = \sum_{i=1}^{N} \mu_i^2 \Xi_{ii} + \sum_{i=1}^{N-1} \sum_{j=i+1}^{N} \mu_i \mu_j \Xi_{ij} < 0, \tag{192}$$

which is equivalent to ([190](#)).

Consequently, if ([188](#)) holds, it can then derive that ([192](#)) is satisfied and ([189](#)) holds. Whilst the closed-loop system ([186](#)) can be stabilized with respect to all parameter variations δ.

4.4.2.2 Controller Synthesis

Employing the *bounding box* method proposed in [139], the LPV system matrices can be approximately described in an affine LPV form [141] as:

$$
\begin{cases}
A_a(\delta) = A_{a0} + \displaystyle\sum_{i=1}^{N} \mu_i(\delta) A_{ai} \\
B_a(\delta) = B_{a0} + \displaystyle\sum_{i=1}^{N} \mu_i(\delta) B_{ai},
\end{cases}
\tag{193}
$$

where N is the selected number of vertex.

According to the affine LPV assumption, infinite sets of LMI of (189) can then be reduced to finite evaluation in each vertex of convex set Ω. Thus, the controller for each vertex can be computed offline as $K_i = Y_i X_i^{-1}$ $(i = 1, 2, ..., N)$ [142].

Based on these vertex controllers, the LPV state feedback control law $K_{st}(\delta)$ can ultimately be obtained online as follow:

$$
K_{st}(\delta) = \sum_{i=1}^{N} \mu_i(\delta) K_i,
\tag{194}
$$

where δ can be measured or estimated in real time, then μ_i can be obtained through $\delta = \sum_{i=1}^{N} \mu_i \delta_i$, and δ_i denotes the value of each vertex.

4.4.2.3 Finite-Time Linear Parameter Varying Adaptive Fault Estimation Scheme

Suppose system without actuator fault can be formulated as:

$$
\begin{cases}
\dot{x}_a(t) = \displaystyle\sum_{i=1}^{N} \mu_i [A_i x_a(t) + B_i u(t)] \\
y_a(t) = C_a x_a(t).
\end{cases}
\tag{195}
$$

Then, system (195) with actuator fault (11) can be represented as:

$$
\begin{cases}
\dot{x}_a(t) = \displaystyle\sum_{i=1}^{N} \mu_i [A_i x_a(t) + B_a L_{fi}(t) u(t)] \\
y_a(t) = C_a x_a(t).
\end{cases}
\tag{196}
$$

To estimate the effectiveness of each faulty actuator, the following adaptive fault diagnosis observer is constructed:

$$
\begin{cases}
\dot{\hat{x}}_a(t) = \displaystyle\sum_{i=1}^{N} \mu_i [A_i \hat{x}_a(t) + B_a \hat{L}_{fi}(t) u(t) - K_{oi}(\hat{y}_a(t) - y_a(t))] \\
\hat{y}_a(t) = C_a \hat{x}_a(t),
\end{cases}
\tag{197}
$$

where the pair (A_i, C_a) is assumed to be observable, and the observer gain $K_o(\delta)$ is chosen to guarantee the stability of $(A_a(\delta) - K_o(\delta) C_a)$, which is given by:

$$
K_o(\delta) = \sum_{i=1}^{N} \mu_i(\delta) K_{oi} > 0, \ \mu_i(\delta) \geq 0, \ \sum_{i=1}^{N} \mu_i(\delta) = 1.
\tag{198}
$$

Thus, the dynamic error between (196) and (197) can be denoted as:

$$
\begin{cases}
\dot{e}_x(t) = \displaystyle\sum_{i=1}^{N} \mu_i (A_i - K_{oi} C_i) e_x(t) + B_a e_{fi}(t) u(t) = \sum_{i=1}^{N} \mu_i [A_{Ki} e_x(t) + B_a e_{fi}(t) u(t)] \\
e_y(t) = C_a e_x(t),
\end{cases}
\tag{199}
$$

where $e_x(t) = \hat{x}_a(t) - x_a(t)$, $e_y(t) = \hat{y}_a(t) - y_a(t)$, $e_f(t) = \sum_{i=1}^{N} \mu_i(e_{fi}(t))$, $e_{fi}(t) = \hat{L}_{fi}(t) - L_{fi}(t)$, $A_K(\delta) = \sum_{i=1}^{N} \mu_i(A_{Ki})$, and $A_{Ki} = A_i - K_{oi} C_a$.

The parameter-varying observer gain $K_o(\delta)$ can then be obtained by the stated LMI conditions in the following proposition.

Proposition 2 *If there exist matrices F_i and a symmetric matrix T making (199) asymptotically*

133

stable, the following LMI holds [143, 144]:

$$\begin{bmatrix} T & A_{Ki}^T T - C_a^T F_i^T \\ T A_{Ki} - F_i C_a & T \end{bmatrix} > 0. \tag{200}$$

Consequently, $K_o(\delta)$ is determined by $K_o(\delta) = \sum_{i=1}^{N} \mu_i(T^{-1}F_i)$.

For the convenience of constructing an adaptive law for the parameter (actuator efficiency factor) estimation, (199) can be rewritten as:

$$\begin{cases} \dot{e}_x(t) = \sum_{i=1}^{N} \mu_i[A_{Ki}e_x(t) + B_a\tilde{L}_f(t)u(t)] \\ e_y(t) = C_a e_x(t), \end{cases} \tag{201}$$

where $\tilde{L}_f(t) = \sum_{i=1}^{N} \mu_i[\hat{L}_{fi}(t) - L_{fi}(t)] = \hat{L}_f(t) - L_f(t)$.

4.4.2.4 Regressor Matrix and Vector

Defining a regressor matrix $M(t)$, and a vector $N(t)$ as:

$$\begin{cases} \dot{M}(t) = -k_{FF}M(t) + k_{FF}\phi^T(t)\phi(t), \ M(0) = 0 \\ \dot{N}(t) = -k_{FF}N(t) + k_{FF}\phi^T(t)\phi(t)L_f(t), \end{cases} \tag{202}$$

where $k_{FF} \in \Re^+$ denotes a forgetting factor, $\phi(t) = B_a u(t)$, whilst $N(0) = 0$ is the initial condition of $N(t)$.

The solution to (202) can then be obtained:

$$\begin{cases} M(t) = \int_0^t e^{-k_{FF}(t-\tau)} k_{FF}\phi^T(\tau)\phi(\tau)d\tau, \\ N(t) = \int_0^t e^{-k_{FF}(t-\tau)} k_{FF}\phi^T(\tau)\phi(\tau)L_f(t)d\tau = M(t)L_f(t). \end{cases} \tag{203}$$

Therefore, the following equations can be derived:

$$\begin{cases} \tilde{N}(t) = \hat{N}(t) - N(t) = M(t)L_f(t), \\ L_f(t) = M^{-1}(t)\tilde{N}(t). \end{cases} \tag{204}$$

4.4.2.5 Finite-Time Linear Parameter Varying Adaptive Parameter Estimation

Theorem 10 *The adaptive law can be formulated as:*

$$\dot{\hat{L}}_f(t) = -\Gamma \sum_{i=1}^{N} \mu_i [B_a^T P_i e_x(t) + R(t)], \tag{205}$$

where $R(t)$ is a sliding mode term, which is expected to guarantee the fast parameter convergence, can be written as:

$$\begin{aligned} R(t) =& M(t)\Omega_{f1} \frac{M(t)\hat{L}_f(t) - N(t)}{||M(t)\hat{L}_f(t) - N(t)||} + M(t)\Omega_{f2}[M(t)\hat{L}_f(t) - N(t)] \\ =& M(t)\Omega_{f1} \frac{\tilde{N}(t)}{||\tilde{N}(t)||} + M(t)\Omega_{f2}\tilde{N}(t), \end{aligned} \tag{206}$$

where $\Omega_{f1} = \omega_{f1}\Omega$ and $\Omega_{f2} = \omega_{f2}\Omega$. ω_{f1} and ω_{f2} are positive definite scalars. $\Omega = diag(\omega_1, \omega_2, ..., \omega_n)$ is a positive definite matrix, and $\Gamma = diag(\tau_1, \tau_2, ..., \tau_n)$ is a learning rate symmetric positive definite matrix.

Proof of Theorem 10: This proof procedure can be divided into two steps:

(1) Proving $e_x(t)$ can exponentially decay; and

(2) Proving the finite-time convergence property of control input.

Step 1): Choosing the following Lyapunov candidate:

$$\begin{aligned} V =& \frac{1}{2}e_x^T(t)P(\delta)e_x(t) + \frac{1}{2}\tilde{N}^T(t)M^{-1}(t)\Gamma^{-1}M^{-1}(t)\tilde{N}(t) \\ =& \frac{1}{2}\sum_{i=1}^{N} \mu_i[e_x^T(t)P_i e_x(t) + \frac{1}{2}\tilde{N}^T(t)M^{-1}(t)\Gamma^{-1}M^{-1}(t)\tilde{N}(t)] > 0, \end{aligned} \tag{207}$$

135

besides, setting:

$$V = V_1 + V_2,$$

$$V_1 = \frac{1}{2} \sum_{i=1}^{N} \mu_i [e_x^T(t) P_i e_x(t)], \tag{208}$$

$$V_2 = \frac{1}{2} \sum_{i=1}^{N} \mu_i [\tilde{N}^T(t) M^{-1}(t) \Gamma^{-1} M^{-1}(t) \tilde{N}(t)].$$

Differentiating (207) with respect to time and applying (201), one can then obtain that:

$$\dot{V} = \frac{1}{2} \sum_{i=1}^{N} \mu_i \{ [\dot{e}_x^T(t) P_i e_x(t) + e_x^T(t) P_i \dot{e}_x(t)] + \frac{d}{dt} [\frac{1}{2} \tilde{N}^T(t) M^{-1}(t) \Gamma^{-1} M^{-1}(t) \tilde{N}(t)] \}$$

$$= \frac{1}{2} \sum_{i=1}^{N} \mu_i \{ e_x^T [A_{Ki}^T P_i + P_i A_{Ki}] e_x + e_x^T P_i B_a \tilde{L}_f(t) + \tilde{N}^T(t) M^{-1}(t) \Gamma^{-1} \frac{d[M^{-1}(t) \tilde{N}(t)]}{dt} \}. \tag{209}$$

Since $A_K(\delta) = \sum_{i=1}^{N} \mu_i(A_{Ki})$ is a Hurwitz matrix, the following inequality should hold:

$$A_K(\delta)^T P(\delta) + P(\delta) A_K(\delta) = \sum_{i=1}^{N} \mu_i [A_{Ki}^T P_i + P_i A_{Ki}] \le -Q(\delta), \tag{210}$$

where $P(\delta) = P^T(\delta) = \sum_{i=1}^{N} \mu_i P_i \in \Re^{(l+n) \times (l+n)}$, $Q(\delta) = Q^T(\delta) = \sum_{i=1}^{N} \mu_i Q_i \in \Re^{(l+n) \times (l+n)}$.

Successively applying (204), (220), (206), and (210), then (209) can be rewritten as:

$$\dot{V} \le -\frac{1}{2} e_x^T Q(\delta) e_x - \tilde{N}^T(t) M^{-1}(t) R(t)$$

$$\le -\frac{1}{2} e_x^T Q(\delta) e_x - \tilde{N}^T(t) \Omega_{f1} \frac{\tilde{N}(t)}{||\tilde{N}(t)||} - \tilde{N}^T(t) \Omega_{f2} \tilde{N}(t). \tag{211}$$

For the convenience of plain demonstration, the analysis of each term in (211) is separately conducted as follows:

$$-\frac{1}{2} e_x^T Q(\delta) e_x \le -\frac{1}{2} \frac{\lambda_{min}(Q(\delta))}{\lambda_{max}(P(\delta))} V_1,$$

$$-\tilde{N}^T(t) \Omega_{f1} \frac{\tilde{N}(t)}{||\tilde{N}(t)||} \le -\frac{\lambda_{min}(\Omega_{f1})}{\lambda_{max}(\Gamma^{-1/2}) \lambda_{max}(M^{-1}(t))} V_2^{1/2}, \tag{212}$$

$$-\tilde{N}^T(t) \Omega_{f2} \tilde{N}(t) \le -\frac{\lambda_{min}(\Omega_{f2})}{\lambda_{max}(M^{-1}(t)) \lambda_{max}(\Gamma^{-1}) \lambda_{max}(M^{-1}(t))} V_2,$$

where $\lambda_{max}(\cdot)$ and $\lambda_{min}(\cdot)$ represent the maximum and minimum eigenvalues of a specific matrix.

Therefore, the derivative of the chosen Lyapunov candidate (207) is:

$$\dot{V} \leq -\alpha_1 V_1 - \alpha_2 V_2^{1/2} - \alpha_3 V_2, \tag{213}$$

and the $e_x(t)$ can exponentially decay with the existence of $\alpha_2 = \dfrac{\lambda_{min}(\Omega_{f1})}{\lambda_{max}(\Gamma^{-1/2})\lambda_{max}(M^{-1}(t))} > 0$,
$\alpha_1 = \dfrac{1}{2}\dfrac{\lambda_{min}(Q(\delta))}{\lambda_{max}(P(\delta))} > 0$, and $\alpha_3 = \dfrac{\lambda_{min}(\Omega_{f2})}{\lambda_{max}(M^{-1}(t))\lambda_{max}(\Gamma^{-1})\lambda_{max}(M^{-1}(t))} > 0$.

Step 2): Apply (205) and (206), the derivative of V_2 can then be achieved:

$$\begin{aligned}
\dot{V}_2 &= -\sum_{i=1}^{N} \mu_i [\tilde{N}^T(t)M^{-1}(t)\Gamma^{-1}\Gamma(B_a^T P_i e_x(t) + R(t))] \\
&= -\sum_{i=1}^{N} \mu_i [\tilde{L}_f^T(B_a^T P_i e_x(t)) + \tilde{L}_f^T(M(t)\Omega_{f1}\frac{M(t)\tilde{L}_f}{||M(t)\tilde{L}_f||} + M(t)\Omega_{f2}M(t)\tilde{L}_f)].
\end{aligned} \tag{214}$$

Furthermore, when (212) is applied, (214) can be further derived as:

$$\begin{aligned}
\dot{V}_2 \leq & \lambda_{max}(\sum_{i=1}^{N} \mu_i P_i)||B_a||||e_x||||\tilde{L}_f|| - \lambda_{min}(M)\lambda_{min}(\Omega_{f1})||\tilde{L}_f|| \\
& - \frac{\lambda_{min}(\Omega_{f2})\tilde{N}^2 M^{-1}\Gamma^{-1}M^{-1}}{\lambda_{max}(M^{-1})\lambda_{max}(\Gamma^{-1})\lambda_{max}(M^{-1})} \\
\leq & \frac{-2[\lambda_{min}(M)\lambda_{min}(\Omega_{f1}) - \lambda_{max}(\sum_{i=1}^{N} \mu_i P_i)||B_a||||e_x||]V_2^{1/2}}{\lambda_{max}(\Gamma^{-1/2})} - \alpha_3 V_2 \\
= & -\alpha_e V_2^{1/2} - \alpha_3 V_2,
\end{aligned} \tag{215}$$

where $\alpha_e = \frac{2}{\lambda_{max}(\Gamma^{-1/2})}[\lambda_{min}(M)\lambda_{min}(\Omega_{f1}) - \lambda_{max}(\sum_{i=1}^{N} \mu_i P_i)||B_a||||e_x||]$.

Since $||B_a||$ is bounded and $e_x(t) \to 0$, there exists a time interval T_1 so that the following inequality holds for $t > T_1$:

$$\lambda_{min}(M)\lambda_{min}(\Omega_{f1}) > \lambda_{max}(\sum_{i=1}^{N} \mu_i P_i)||B_a||||e_x||. \tag{216}$$

137

Consequently, there is a time threshold T_2 such that $\dot{V}_2 \leq -\alpha_e V_2^{1/2} - \alpha_3 V_2 \leq -\alpha_e V_2^{1/2}$.

Based on the finite-time stability theorem in [145], the finite-time convergence of $\lim_{t \to T_2} \tilde{L}_f = 0$ can thereby be achieved.

4.4.3 Adaptive Mass Variation Estimation Scheme

4.4.3.1 Mass Variation Estimation

In order to obtain mass variations online, an adaptive reference model is also established:

$$\dot{\hat{x}}_a(t) = (A_a(\delta) - A_s \hat{\rho}(\delta)) \hat{x}_a(t) + B_a(\delta) u(t) + G_a(\delta) y_r(t) \tag{217}$$

where $A_a(\delta) - A_s \hat{\rho}(\delta) = A_{a0}(\delta)$ is assumed to be observable, $A_{a0} \in \Re^{n \times n}$ denotes the invariant system dynamics, $A_s \in \Re^{n \times n}$ is to select the varying parameters, and $\hat{\rho}(\delta) = \sum_{i=1}^{N} \mu_i \hat{\rho}_i$ is the estimated value of mass variation [146].

Let the state error $e_x(t) = \hat{x}_a(t) - x_a(t)$, the derivative of state error can then be obtained:

$$\dot{e}_x(t) = A_a(\delta) e_x(t) - A_s \hat{\rho}(\delta) \hat{x}_a(t) = \sum_{i=1}^{N} \mu_i (A_{ai} e_x(t) - A_s \hat{\rho}_i \hat{x}_a(t)). \tag{218}$$

Theorem 11 *There exist positive definite matrices* $P(\delta) = P^T(\delta) = \sum_{i=1}^{N} \mu_i P_i \in \Re^{(l+n) \times (l+n)}$ *and* $Q(\delta) = Q^T(\delta) = \sum_{i=1}^{N} \mu_i Q_i \in \Re^{(l+n) \times (l+n)} > 0$ *making the following inequality holds:*

$$A_a(\delta)^T P(\delta) + P(\delta) A_a(\delta) = \sum_{i=1}^{N} \mu_i [A_{ai}^T P_i + P_i A_{ai}] \leq -Q(\delta), \tag{219}$$

and $\hat{\delta}(\rho)$ *is determined according to the following adaptive law:*

$$
\begin{aligned}
\dot{\hat{\rho}}(\delta) &= Proj_{[\underline{\rho}, \bar{\rho}]} \{\rho(\delta)\} \\
&= \begin{cases} 0 & \text{if } \hat{\rho} = \underline{\rho}, \Delta(\delta) \leqslant 0 \text{ or } \hat{\rho} = \bar{\rho}, \rho(\delta) \geqslant 0, \\ \Delta(\delta) & \text{otherwise}, \end{cases}
\end{aligned} \tag{220}
$$

where $\Delta(\delta) = \Gamma \sum_{i=1}^{N} \mu_i e_x^T P_i A_s \hat{x}(t)$. $\underline{\rho}$ and $\bar{\rho}$ denote the lower and upper bounds of $\hat{\rho}(\delta)$. Symmetric positive definite learning rate matrix $\Gamma = diag(\lambda_1, \lambda_2, ..., \lambda_n)$.

Proof of Theorem 11: Select the following Lyapunov candidate:

$$V_m = e_x^T(t)P(\delta)e_x(t) + \hat{\rho}^T(\delta)\Gamma^{-1}\hat{\rho}(\delta) > 0. \tag{221}$$

Differentiate (221) with respect to time and applying (218), (222) can then be obtained:

$$\begin{aligned}\dot{V}_m =& [\dot{e}_x^T(t)P(\delta)e_x(t) + e_x^T(t)P(\delta)\dot{e}_x(t)] + 2\hat{\rho}^T(\delta)\Gamma^{-1}\dot{\hat{\rho}}(\delta) \\ =& e_x^T[A_a(\delta)^T P(\delta) + P(\delta)A_a(\delta)]e_x - 2\hat{\rho}^T(\delta)e_x^T(t)P(\delta)A_s\hat{x}(t) + 2\hat{\rho}^T(\delta)\Gamma^{-1}\dot{\hat{\rho}}(\delta).\end{aligned} \tag{222}$$

If the LPV adaptive law is chosen as (220), the following inequality holds:

$$\hat{\rho}^T\Gamma^{-1}\dot{\hat{\rho}} - \hat{\rho}^T e_x^T(t)P(\delta)A_s\hat{x}(t) \leq 0, \tag{223}$$

therefore

$$\dot{V}_m \leq e_x^T[A_a(\delta)^T P(\delta) + P(\delta)A_a(\delta)]e_x \leq -e_x^T Q(\delta)e_x, \tag{224}$$

it follows that $A_a(\delta)^T P(\delta) + P(\delta)A_a(\delta) = \sum_{i=1}^{N} \mu_i[A_{ai}^T P_i + P_i A_{ai}] \leq -Q(\delta) < 0$.

4.4.3.2 Transient Reduction

The switching between two controllers may cause severe transients due to output mismatches of respective controllers. Instead of improving system performance, this phenomenon may seriously degrade system performance and even destabilize system. In order to reduce the negative effects of this phenomenon as much as possible, it is important to remarkably minimize the output mismatches at the instant of switching.

In this study, the following smooth switching function is adopted:

$$K_{st}(t) = K_f + [K_{st}(t_0) - K_f]e^{-\tau(t-t_0)}, \tag{225}$$

Table 4.3: Adopted system parameters

Parameter	Value
m_{11}	m+2 [kg]
m_{22}	m-10 [kg]
m_{33}	2.76 [kg]
m_{23}	0.046m [kg]
m_{32}	0.046m [kg]
d_{11}	0.7225
d_{22}	0.8897
d_{33}	1.9+0.046m
d_{23}	9.25+m
d_{32}	7.9687
N_θ	0.0284

where K_{st} is the ultimate control gain, $K_{st}(t_0)$ is the control gain when no actuator faults occur, K_f denotes the control gain of reconfigurable controller when actuators fail to operate as expected. τ is chosen according to the dynamics of closed-loop system. The design of this function is intended to guarantee a smooth transition from normal case $K_{st}(t_0)$ to fault-tolerant case K_f.

4.4.4 Simulation Results

In this study, numerical simulations are carried out to validate the effectiveness of the proposed control methodology on a nonlinear USV model [138].

The system parameters utilized for both controller design and nonlinear model are listed in Table 4.3. The overall mass m is denoted as the time-varying parameter ρ, and the vertex number is chosen as $N = 2$. Then, the LPV scalar μ_i is computed through $\mu_1 = (\rho - \underline{\rho})/(\bar{\rho} - \underline{\rho})$ and $\mu_2 = (\bar{\rho} - \rho)/(\bar{\rho} - \underline{\rho})$ according to the *bounding box approach* [139]. The initial value of mass is $m_0 = 23.8\ kg$. The upper and lower bounds of mass variation are defined as $\bar{\rho} = 80.0\ kg$ and

$\underline{\rho} = 23.8 \ kg$. Therefore, the corresponding LPV system matrices are given by:

$$
A_{a1} = \begin{bmatrix} 0 & 0 & -1 & 0 & 0 \\ 0 & 0 & 0 & -1 & 0 \\ 0 & 0 & -0.028 & 0 & 0 \\ 0 & 0 & 0 & 0 & 1 \\ 0 & 0 & 0 & 0 & -1.085 \end{bmatrix}, A_{a2} = \begin{bmatrix} 0 & 0 & -1 & 0 & 0 \\ 0 & 0 & 0 & -1 & 0 \\ 0 & 0 & -0.0088 & 0 & 0 \\ 0 & 0 & 0 & 0 & 1 \\ 0 & 0 & 0 & 0 & -2.0217 \end{bmatrix},
$$

$$
B_{a1} = \begin{bmatrix} 0 & 0 \\ 0 & 0 \\ 0.03876 & 0 \\ 0 & 0 \\ 0 & 0.01028 \end{bmatrix}, B_{a2} = \begin{bmatrix} 0 & 0 \\ 0 & 0 \\ 0.012195 & 0 \\ 0 & 0 \\ 0 & 0.01028 \end{bmatrix}.
$$

Employing the *bounding box approach* in [139], the weighting functions $\mu_i(\delta)$ are defined:

$$
\begin{aligned}
\mu_1(\delta) &= \frac{(\delta_i^A - \delta_{min}^A)}{(\delta_{max}^A - \delta_{min}^A)} \frac{(\delta_i^B - \delta_{min}^B)}{(\delta_{max}^B - \delta_{min}^B)} = \frac{(\delta_i^A - 0.5)(\delta_i^B - 0.1)}{9}, \\
\mu_2(\delta) &= \frac{(\delta_i^A - \delta_{min}^A)}{(\delta_{max}^A - \delta_{min}^A)} \frac{(\delta_{max}^B - \delta_i^B)}{(\delta_{max}^B - \delta_{min}^B)} = \frac{(\delta_i^A - 0.5)(1 - \delta_i^B)}{9}, \\
\mu_3(\delta) &= \frac{(\delta_{max}^A - \delta_i^A)}{(\delta_{max}^A - \delta_{min}^A)} \frac{(\delta_i^B - \delta_{min}^B)}{(\delta_{max}^B - \delta_{min}^B)} = \frac{(10.5 - \delta_i^A)(\delta_i^B - 0.1)}{9}, \\
\mu_4(\delta) &= \frac{(\delta_{max}^A - \delta_i^A)}{(\delta_{max}^A - \delta_{min}^A)} \frac{(\delta_{max}^B - \delta_i^B)}{(\delta_{max}^B - \delta_{min}^B)} = \frac{(10.5 - \delta_i^A)(1 - \delta_i^B)}{9},
\end{aligned}
\tag{226}
$$

where δ_i^A and δ_i^B are the time-varying parameters in matrices $A_a(\delta)$ and $B_a(\delta)$, while δ_{max}^A, δ_{max}^B, δ_{min}^A and δ_{min}^B denote the maximum and minimum values of the time-varying parameters in matrices $A_a(\delta)$ and $B_a(\delta)$, respectively.

In the simulation, the overall mass of USV is increased from $m = m_0 = 23.8 \ kg$ to $m = m_0 + \Delta m = 63.8 \ kg$, where Δm is the mass variation. Moreover, the output force of propulsion and deflection of rudder are respectively limited in $[-2 \ N, \ 2 \ N]$ and $[-30 \ deg, \ 30 \ deg]$. The state feedback control gains for each vertex is tuned as follows:

4.4.4.1 Example 1: Mass Variation Compensating Control and Transients Analysis

In this example, a conventional linear quadratic regulator (LQR) controller is selected to compare with the proposed controller in the presence of sudden USV overall mass variation (the dotted line in Fig. 4.44). LQR controller's gain $K_{lqr} = K_{st1}$, which is tuned with $m = 23.8 \ kg$.

(a)　　　　　　　　　　　　　　　　　(b)
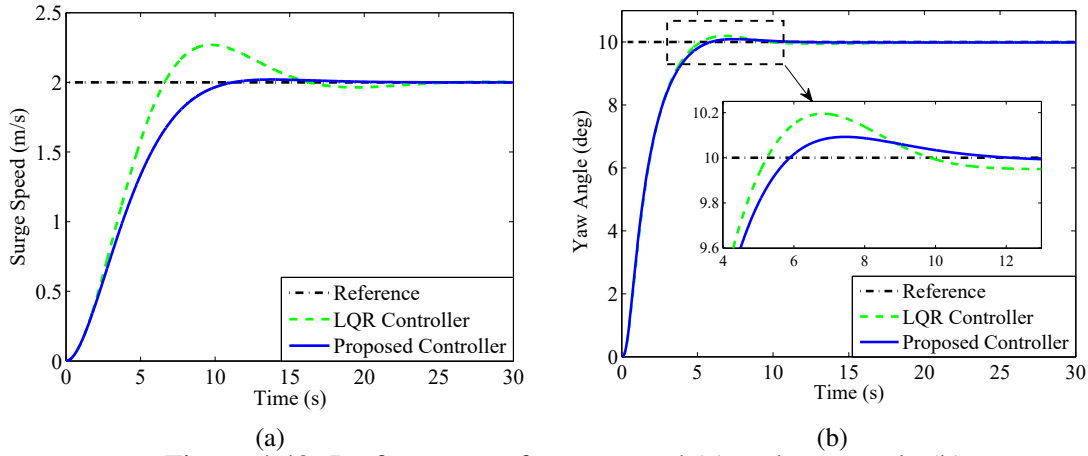
Figure 4.42: Performance of surge speed (a) and yaw angle (b).

(a)　　　　　　　　　　　　　　　　　(b)
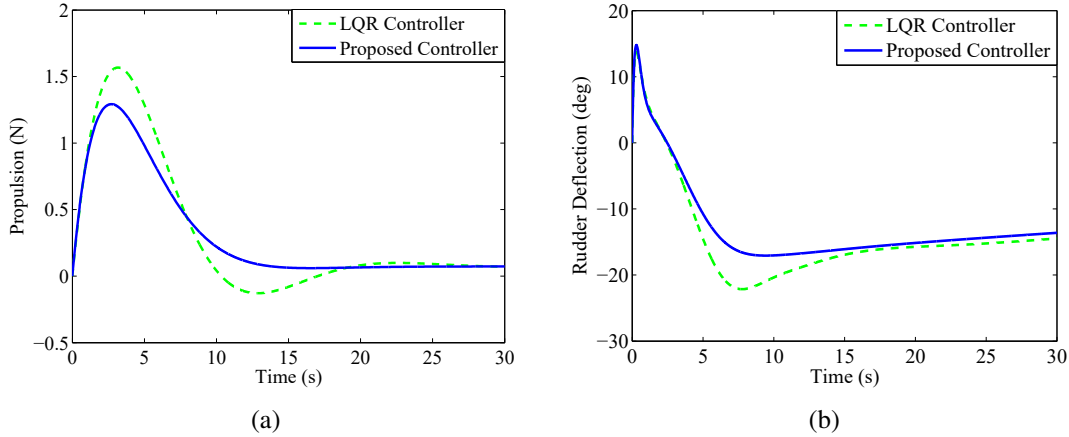
Figure 4.43: Output of propulsion force (a) and Performance of rudder deflection (b).

As shown in Fig. 4.42(a), the proposed controller remarkably outperforms LQR controller when mass changes. From Fig. 4.42(b), the proposed controller performs better than the compared controller, but performance improvement is not significant. This phenomenon is caused by the term $d_{33} = -N_r + (m\chi_g - \frac{1}{2}N_{\dot{v}} - \frac{1}{2}Y_{\dot{r}})u_u$ in $D(\nu)$ is not sensitive to mass variation. In addition, Fig. 4.43(a) and Fig. 4.43(b) show that the actuators are all under saturation.
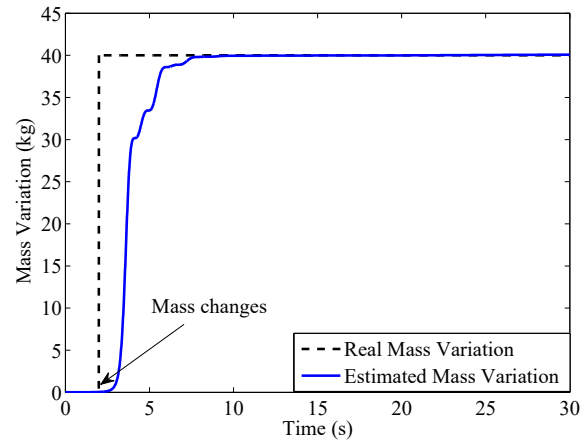
Figure 4.44: Mass variation estimation

Normally, it takes time to estimate and confirm the dynamic variation by adaptive estimator. Then, the reconfigurable controller is switched into closed-loop system based on the updated estimation information. However, the difference between the former and current control inputs can cause a certain amount of transient performance degradation. While longer time delay between the variation occurrence and reconfigurable action can cause more significant performance degradation. Thus, the selection of switching time is critical in reconfigurable control design. Based on the performance of adaptive parameter estimator, the switching time is chosen as $2\ s$ in this simulation.

4.4.4.2 Example 2: Mass Variation Estimation

As displayed in Fig. 4.44, the proposed parameter variation estimation method is effective in obtaining the online information of mass variation. More specifically, the variation (within 5% of error) can be estimated within $3.5\ s$.

4.4.4.3 Example 3: Fault-Tolerant Control

In this example, the performance of LQR controller and the proposed controller are compared in the event of actuator fault. The rudder is initially deployed at $0\ deg$, loss of 50% effectiveness is then imposed in rudder, which occurs at 4th second when the rudder is tracking the desired angle

143
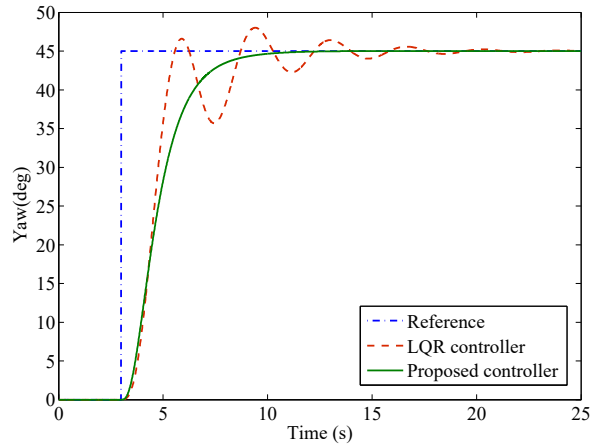
Figure 4.45: Yaw performance comparison.

($45\ deg$). The surge speed is consistently set at $0.5\ m/s$.

From Fig. 4.45, it shows that the proposed controller significantly outperforms the fixed-gain controller. This result is due to the smoother and more prompt action of rudder by the proposed controller (as observed in Fig. 4.46(b)). In addition, compared with the LQR controller, smaller heading (yaw) rate is caused by the proposed controller (as shown in Fig. 4.46(a)). This is of significance to the safety of USV steering control since the extremely abrupt turn of USV can result in undesirable motion, even capsizing.

Furthermore, as displayed in Fig. 4.46(b), rudder is operated without saturation by the proposed controller, while the compared controller violates the constraint of rudder deflection between 5th second and 6th second.
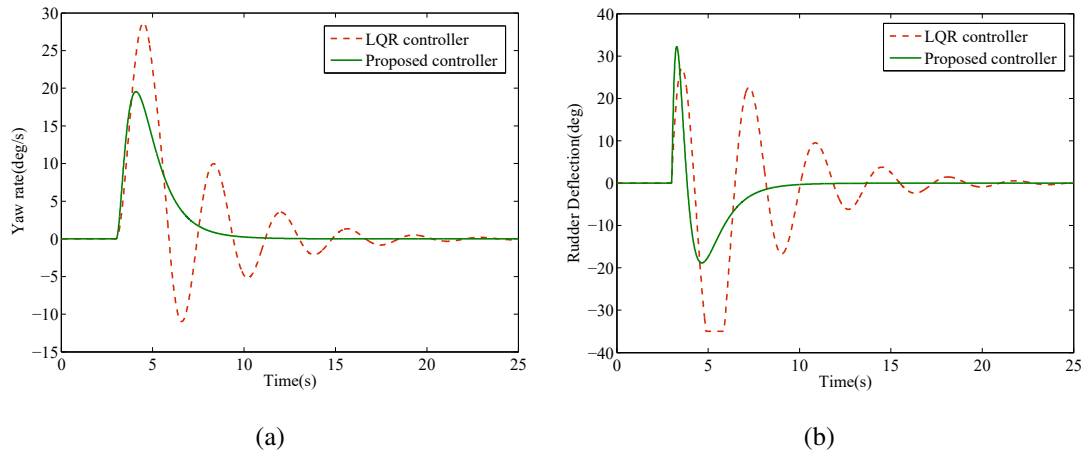
(a)   (b)
Figure 4.46: Performance comparison of yaw rate (a) and rudder deflection (b).

144
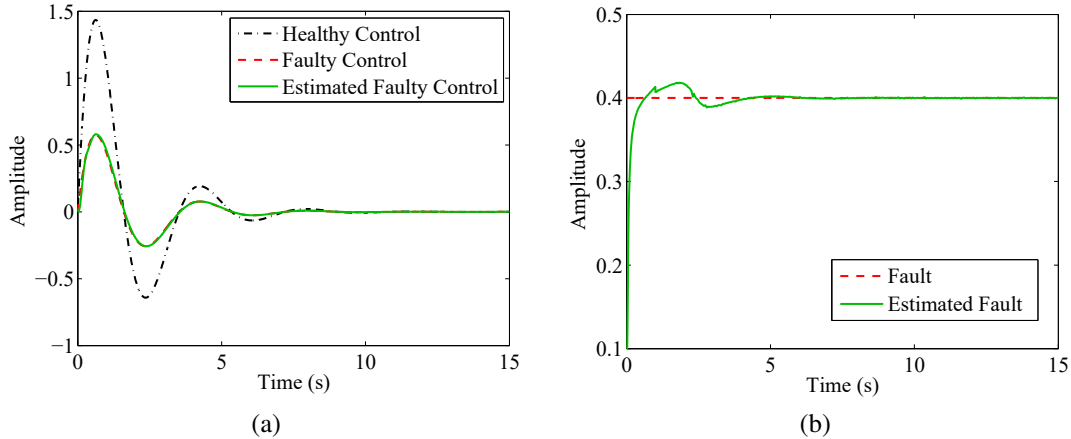
Figure 4.47: Control signal estimation (a) and Fault estimation result (b).

4.4.4.4 Example 4: Fault Estimation

As shown in Fig. 4.47(b), the imposed actuator fault is well estimated by the developed fault estimation scheme. Furthermore, the actual control input is tracked in an acceptable perspective level (see Fig. 4.47(a)).

4.4.5 Experimental Validation on An Unmanned Quadrotor Helicopter

The payload grasping, carrying, and dropping tasks are challenging which require UAVs remain balanced in flight when payload mass is added to or dropped off the vehicles. This phenomenon is mainly caused by two factors, the first one is the dynamic response of UAV system that can be significantly affected by the added or dropped payload mass; the other one is that the UAV may experience bias forces caused by the unevenly placed payload or improperly trimmed offset loads [147]. In recent years, numerous relevant research activities are conducted. In [148], both gain-scheduling PID and model predictive control (MPC) approaches are utilized for the application of payload dropping. The stability of UAV with added payload mass under classical PID control is studied in [147], but no additional payload compensating strategy is developed. In [149], a payload compensation scheme is integrated into the PID control structure rejecting the payload mass variation induced system performance deterioration. Moreover, the cooperative transportation of payloads using multiple UAVs is also investigated [11, 12].

145
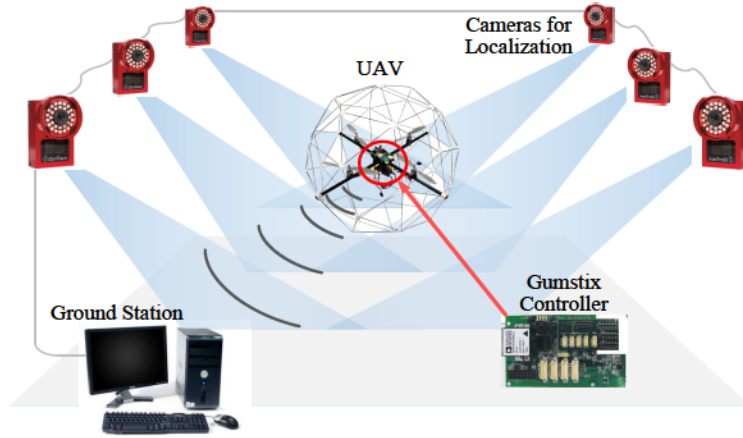
Figure 4.48: Layout of the experimental test environment.

In addition to mass variation issues, battery drainage is another unavoidable phenomenon during the flight of UAVs. Most UQHs are powered by batteries, but the battery voltage normally becomes lower over time. Accordingly, the combined performance of the motor-battery also changes, causing a partial loss of effectiveness of the thrust generated by propellers. The expected performance of UAV, as a result, cannot be guaranteed. This phenomenon can be treated as a kind of actuator fault. Despite this, only few relevant existing researches are carried out. In [149], a multiple subsystem control strategy is proposed, the PID control method is first selected for the design of the baseline controller, guaranteeing the system stability and desired performance. A battery drainage compensating subsystem is then designed to calculate the appropriate control command required to compensate the loss of control effectiveness induced by battery voltage reduction. The PID control input and the additional compensating control input, finally, are integrated to mitigate the negative impact of battery drainage. In [150, 151], a feedforward neural network structure is also utilized for mitigating the power loss in batteries.

In order to solve the above-mentioned challenging issues, as a possible solution, the proposed adaptive LPV control scheme is further validated on an UQH (see model (4)) in the experiment (the layout pf experimental environment is shown in Fig. 4.48), adapting to the system variation with a graceful system performance degradation [44]. In this research, the voltage variation in battery is seen as the loss of control effectiveness [152], this is reasonable and practical due to
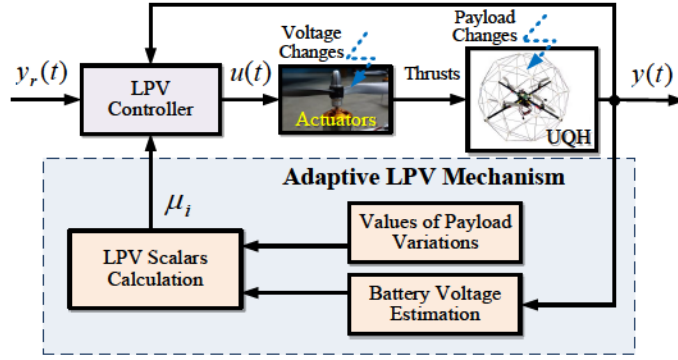
Figure 4.49: Schematic illustration of the proposed adaptive FDD and FTC methods.

the thrust of actuator is related to the voltage of battery. Under the same control command signal, lower voltage of battery means less thrust, while higher voltage of battery provides more thrust. Since the voltage of battery drops with time, it indicates that the control effectiveness also changed over time, which can then be treated as the time-varying states of actuators constrained in a specific bound. Besides, the variation of payload mass is chosen as the time-varying parameter as well. Selecting the boundary of these parameters as vertex, several group of control gains can be obtained offline for each vertex based on a robust state-feedback controller. The *bounding box approach* addressed in [139] is then adopted to calculate the ultimate control gain online based on the previously obtained control gains as well. The overall design philosophy of the proposed methodologies is outlined in Fig. 4.49.

The performance of the linear quadratic regulator (LQR) and proposed controllers are compared. Using the *bounding box approach*, the weighting functions $\mu_i(\delta)$ are then selected as:

$$
\begin{aligned}
\mu_1(\delta) &= \frac{(\delta_i^A - \delta_{min}^A)}{(\delta_{max}^A - \delta_{min}^A)} \frac{(\delta_i^B - \delta_{min}^B)}{(\delta_{max}^B - \delta_{min}^B)} \\
\mu_2(\delta) &= \frac{(\delta_i^A - \delta_{min}^A)}{(\delta_{max}^A - \delta_{min}^A)} \frac{(\delta_{max}^B - \delta_i^B)}{(\delta_{max}^B - \delta_{min}^B)} \\
\mu_3(\delta) &= \frac{(\delta_{max}^A - \delta_i^A)}{(\delta_{max}^A - \delta_{min}^A)} \frac{(\delta_i^B - \delta_{min}^B)}{(\delta_{max}^B - \delta_{min}^B)} \\
\mu_4(\delta) &= \frac{(\delta_{max}^A - \delta_i^A)}{(\delta_{max}^A - \delta_{min}^A)} \frac{(\delta_{max}^B - \delta_i^B)}{(\delta_{max}^B - \delta_{min}^B)},
\end{aligned}
\tag{227}
$$

147
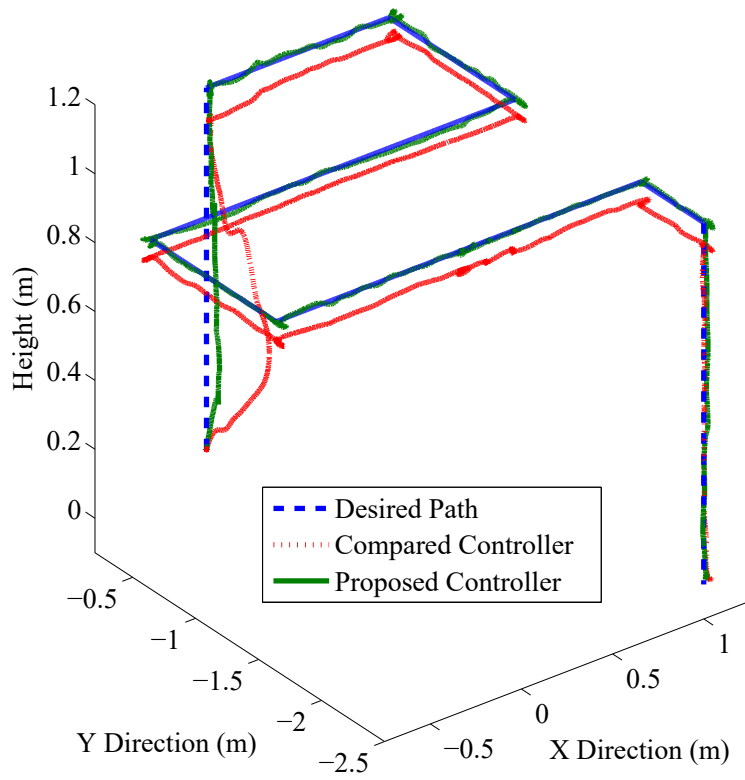
Figure 4.50: Trajectory tracking performance comparison.
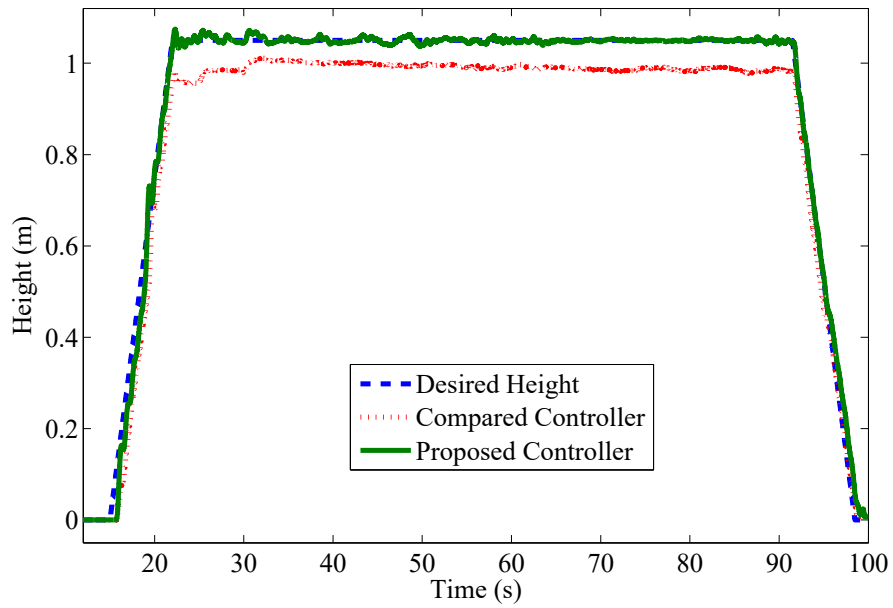
Figure 4.51: Performance comparison in vertical direction.
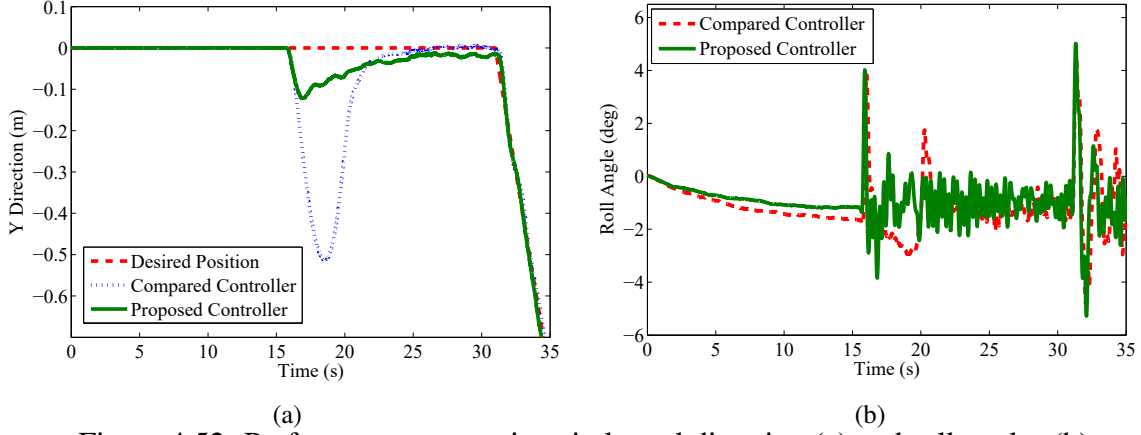
Figure 4.52: Performance comparison in lateral direction (a) and roll angles (b).
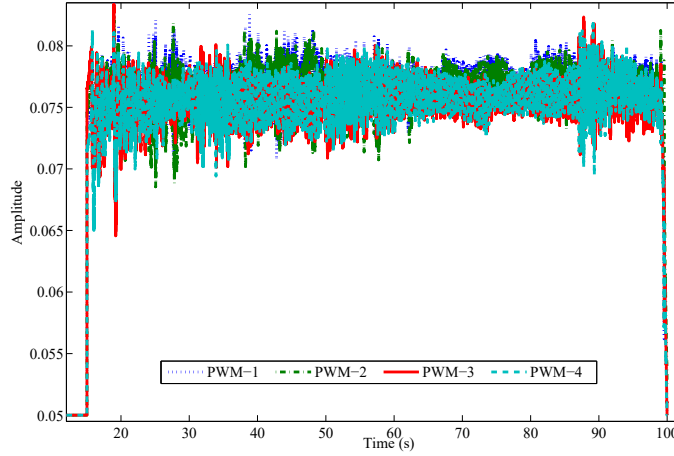
Figure 4.53: PWM signals of the compared controller.

where δ_i^A and δ_i^B denote the time-varying parameters of mass variations and control effectiveness, respectively, while $\delta_{max}^A = 1.6$, $\delta_{max}^B = 1$, $\delta_{min}^A = 1.4$ and $\delta_{min}^B = 0.7$ denote the maximum and minimum mass variations and control effectiveness values, respectively.

In the absence of battery drainage and mass variation, the compared (K_{lqr}) controller and gains of lower vertices ($K_{min}^A = K_{min}^B$) share the same state-feedback control gain $K_{lqr} = K_{min}^A = K_{min}^B$. A payload of $0.2\ Kg$ is attached at the bottom of UAV. The battery voltage drops from $12.5\ V$ to $11.7\ V$, which indicates the control effectiveness of actuator decreases from 100% to 80%. Both payload and battery voltage are changed at the start of experiment. Due to the compared and proposed controllers are both state feedback controller, but the state of UQH is partially measurable in practice, a classic Luenberger observer [101] and a low-pass filter (228) are then adopted for

149
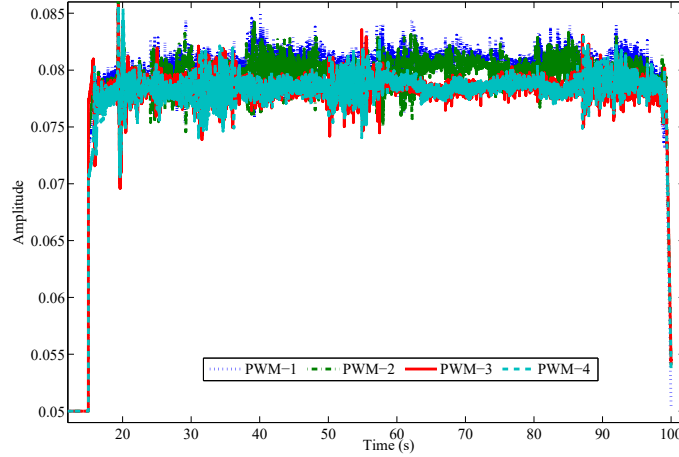
Figure 4.54: PWM signals of the proposed controller.

estimating the state of UQH and filtering the measurement noises.

$$\frac{x_{out}}{x_{in}} = \frac{30}{30+s},$$ (228)

where x_{out}, x_{in}, and s are the output, input, and Laplace transform variable, respectively.

As displayed in Fig. 4.50, a significant deviation (around $0.6\ m$ along the Y direction, also see Fig 4.52(a)) from the desired path is caused by the compared controller during the take-off period. Absence of mass variation counteracting mechanism results in its poor performance.

As shown in Figs. 4.50 and 4.51, there is a residual of $0.1\ m$ between the anticipated and real heights when the UQH is under the operation of the compared controller, this reduction in the height is due to the voltage loss in battery, while no corresponding compensation action is taken.

To be more specific, as the PWM performance of the two controllers demonstrated in Fig. 4.53 and Fig. 4.54, since the control gains of the compared controller is fixed, there is no significant PWM variation when the system dynamic changes, which exactly explains the deterioration in its performance. Alternatively, thanks to its reconfigurable properties, the proposed controller can correspondingly and effectively alter the PWM signal to compensate the negative effects induced by the system dynamics variation.

150

Chapter 5

Leader-Follower Fault-Tolerant Formation Control of Unmanned Aerial Vehicles

In the past decades, much attention has been dedicated to the cooperative control of multiple UAVs [153]. This phenomenon is caused by the possibility of deploying a group of UAVs in an organized topology for a variety of potentially practical applications [154], such as forest health/fire surveillance [4, 155], natural resources exploration [156], and search and rescue [157, 158]. Unfortunately, various challenging issues still seriously prevent these applications in practice. As the conjunction between the control command and physical action on UAVs, actuators are crucial for UAVs operation. But they may subject to a variety of failures, such as stuck (lock in place), float, partial or full loss of effectiveness, and outage [22, 33], due to various mechanical failures, including control surface malfunction, mechanical deformation, hydraulic failures, as well as wear and tear of the gear [28]. During the course of UAVs formation flight, the malfunctions of actuators can adversely degrade the overall system performance, affect the mission completion, and even result in catastrophic consequences (such as crash) to both UAVs and their surrounding environment. Furthermore, the remaining healthy actuators in UAV have to take a heavier load when some actuators fail to operate. This situation leads the healthy actuators to be more susceptible to the physical constraints. Actuator saturation can not only result in the potential damage to the

151

healthy actuators, but also seriously threaten the safety of UAVs and their surrounding objects. Therefore the capabilities of healthy actuators should also be explicitly considered in the controller design. In addition to these issues, the deployment of a group of UAVs presents the risk of collision with stationary and dynamical obstacles from both inter and outer formation. These issues severely threaten the safety of personnels, natural environment, infrastructures, and other manned/unmanned vehicles from both ground and air. It is therefore critical for developing a reliable and safe formation control strategy for UAVs, preventing them from disrupting or destroying each other and other environmental objects in their vicinity.

UAVs formation control has attracted significant attention over the past decades. Tremendous efforts have been devoted to solve a variety of challenging applications. These solutions include the design of a formulation and heuristic method to task allocation and routing of UAVs under limited communication conditions [159]; integrating task and motion planning for UAVs to improve performance in terms of the shortest path cost and search complexity [160]; developing a cooperative mission planning system for managing multiple UAVs of various capabilities to execute a series of missions, including classification, attack, verification, and search and rescue [161, 162]; designing a formal framework and architecture, that can be employed for the automated specification, generation and execution of high-level collaborative tasks involving multiple UAVs and human operators [163]; mobile ground target racking by a group of quadrotor UAVs [164]; the development of distributed task allocation approach which engages under-utilized UAVs to serve as communication relays, supporting the network missions [165]. Accordingly, various control methodologies have likewise been adopted, such as linear quadratic (LQ) control [166, 167], feedback linearization [168], proportional-integral (PI) control [169, 170], robust control [171, 172], sliding mode control (SMC) [173], hybrid supervisory control [174], and backstepping control [175].

Moreover, substantial efforts have also been devoted to the formation control of UAVs with explicit consideration of either collision avoidance or actuator/communication fault-tolerant control (FTC). Communication faults (such as delays, dropouts, and failures) accommodation has recently become an active topic since the superior performance of UAVs formation control heavily depends

on the reliable data exchange among UAVs [159, 165]. In [176–178], the FTC against the defects of UAVs communication is explicitly investigated by ensuring the expected manner of UAVs formation control or reconfiguring the topological structure of UAVs formation via the remaining healthy communication links. Although UAVs formation control considering communication faults has been extensively studied, little attention has been dedicated to the research of UAVs formation control with consideration of actuator faults. Some interesting investigations can be found in [179, 180], where actuator faults in a group of UAVs have been counteracted by applying the sliding mode control and robust control techniques. The research of UAVs formation control possessing collision avoidance capabilities is also extensively conducted in the past decade, partial existing work of this interesting topic can be referred in [181–185], and the references thereby. The existing UAVs formation control strategies are capable of effectively reducing the adverse influences of either actuator/communication faults or obstacles, and simultaneously maintaining the overall system stability. But the research combining both the actuator FTC and collision avoidance capabilities in UAVs formation control has not yet been extensively studied, while it is crucial for the practical UAVs applications.

The past decades have also seen a significant development of UAVs control system design with consideration of actuator constraints. The controller design considering actuator limits can be referred to [104, 186, 187]. The basic idea behind these investigations is to develop an anti-windup mechanism in terms of actuator status to compensate the side effects of actuator saturation. In [188, 189], the actuator saturation issues are also well investigated in adaptive control systems in the cases that all actuators in system are free of failures. A so-called positive μ-modification methodology is presented in [190, 191], where a virtual control input bound less than the physical constraints is established, combining the real control input signal and the virtual control input bounds. The stable adaptation within the actuator limitations can therefore be achieved by appropriately modifying both the adaptive reference model and the system tracking error dynamics.

Unfortunately, the following three fundamental issues still exist which are worth further investigation. First, in order to prevent the secondary damage of healthy actuators, it is always expected

that reference commands can be adaptive to a satisfactory and safe physical constraints and UAVs formation specifications, when one or more actuators fail to operate. In addition, although communication delays/faults are well investigated in the existing research, and the fault-tolerant formation control (FTFC) against loss of effectiveness in actuators is well treated as well, actuator outage and stuck failures have not yet been extensively studied in UAVs formation control. Another practical issue involves the potential collision caused by actuator faults. The time consumption and delay of fault compensating action may seriously threaten other objects from inter formation and surrounding environment. Thus, an effective FTC operation with collision avoidance capability is promising. Motivated by the aforementioned challenging issues, existing research, and remaining unsolved fundamental issues, this thesis presents a leader-follower kind of UAVs formation control approach with FTC, collision avoidance, and actuator saturation prevention capabilities. The proposed method is intended to guarantee all UAVs following their preplanned trajectories, while being free of collisions from both environment and inter-formation, along with stabilizing systems in the presence of actuator faults and constraints.

The proposed method is intended to guarantee all UAVs following their preplanned trajectories, while being free of collisions from both environment and inter-formation, along with stabilizing systems in the presence of actuator faults and constraints. The proposed approach consists of an active FTC (AFTC) mechanism and a collision avoidance mechanism for multiple UAVs, which operates as follows: 1) once any of follower UAVs encounters actuator faults, a direct adaptive FTC mechanism is activated to compensate the adverse effects of faulty actuators; 2) when the potential obstacles are detected by the collision avoidance function in the threatened UAVs, a collision avoidance action is then conducted; 3) after all obstacles being avoided, UAVs all return to track their respective trajectory and keep the desired formation. During the entire operation period, actuators of each UAVs can be guaranteed under saturation.
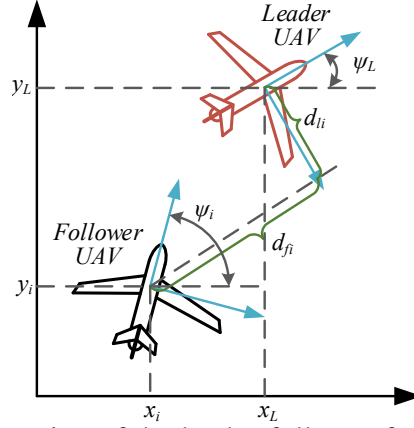
Figure 5.1: Illustration of the leader-follower formation geometry.

5.1 Premilinaries

5.1.1 UAVs Outer-Loop Kinematics

In this study, the kinematics and dynamics of UAVs are separately adopted for the outer- and inner-loop control strategies design. The outer-loop formation control law mainly relies on UAVs' kinematics, while the inner-loop control scheme for each individual UAV depends on its dynamics. More specifically, issues related to formation keeping and collision avoidance are managed in outer-loop controller based on kinematics of UAV. In terms of problems involving attitude control and fault-tolerant control, they are disposed by inner-loop controller employing UAV's dynamics.

The leader-follower formation structure is considered here, which constitutes i $(i \geq 2)$ UAVs. The kinematic model of each individual UAV is:

$$
\begin{cases}
\dot{x}_i = v_i cos\psi_i \\
\dot{y}_i = v_i sin\psi_i \\
\dot{\psi}_i = \omega_i,
\end{cases}
\tag{229}
$$

where detailed explanation of all symbols are illustrated in Table 5.1.1.

Table 5.1: Nomenclature

Symbols	Explanation
x_i	The position along the X coordinate of earth reference frame (m)
y_i	The position along the Y coordinate of earth reference frame (m)
v_i	The forward velocity (m/s)
ψ_i	The heading angle between the forward velocity and X coordinate (deg)
ω_i	The angular velocity of heading angle deg/s
d_{fi}^d	The desired distance with respect to forward direction (m)
d_{li}^d	The desired distance with respect to lateral direction (m)
e_{fi}	The forward distance error between the actual and desired values (m)
e_{li}	The lateral distance error between the actual and desired values (m)
α_i	The angle of attack (deg)
β_i	The sideslip angle (deg)
θ_i	The pitch angle (deg)
p_i	The roll rate (deg/s)
q_i	The pitch rate (deg/s)
r_i	The yaw rate (deg/s)
δ_{ei}	The elevator deflection (deg)
δ_{ti}	The throttle deflection (deg)
δ_{ai}	The aileron deflection (deg)
δ_{ri}	The rudder deflection (deg)

Note: this table includes the information of the ith UAV.

It is worth mentioning that only the planar kinematic model of UAV is considered while the altitude is assumed to be constant during the entire flight mission. This model simplification is reasonable since the primary concern of this research is to develop a formation control mechanism for keeping a desired mutual distance between the leader UAV and each follower UAV in the horizontal plane. The assigned altitude can also be maintained by designing a separate controller which is independent of the formation control system.

As shown in Fig. 5.1, assuming the communication links are healthy and the information of all UAVs are available. The actual distance errors between the leader and the ith follower UAV along their forward and lateral directions can be described as:

$$
\begin{cases}
d_{fi} = (x_i - x_L)cos\psi_i + (y_i - y_L)sin\psi_i + Dcos(\psi_i - \psi_L) \\
d_{li} = (x_i - x_L)sin\psi_i + (y_i - y_L)cos\psi_i - Dsin(\psi_i - \psi_L),
\end{cases}
\tag{230}
$$

where (x_L, y_L) and ψ_L are the actual position and heading angle of leader UAV, respectively, and D denotes the distance between the centre of mass and the control point [192].

The separation distance errors between the desired and actual distances in forward and lateral directions can be defined as $e_{fi} = d_{fi} - d_{fi}^d$ and $e_{li} = d_{li} - d_{li}^d$. The derivation of e_{fi} and e_{li} with respect to time can then be obtained:

$$\begin{bmatrix} \dot{e}_{fi} \\ \dot{e}_{li} \end{bmatrix} = \begin{bmatrix} -v_L - d_{li}\omega_L \\ d_{fi}\omega_L \end{bmatrix} + \begin{bmatrix} cos(\psi_i - \psi_L) & -Dsin(\psi_i - \psi_L) \\ -sin(\psi_i - \psi_L) & -Dcos(\psi_i - \psi_L) \end{bmatrix} \begin{bmatrix} v_i \\ \omega_i \end{bmatrix}, \tag{231}$$

where v_L and ω_L represent the forward velocity and angular velocity of leader UAV, respectively.

The objectives of the outer-loop control design, introduced here, are to develop an effective control scheme so that:

(1) The desired leader-follower formation pattern is guaranteed within an acceptable time span;

(2) The tracking errors can be significantly eliminated;

(3) The UAVs are required to avoid collisions when there are obstacles in the path or there is a chance of collision in their vicinity.

5.1.2 Inner-Loop UAV Model under Actuator Faults and Saturation

In terms of a specified trimming point, a linear time-invariant dynamic model of the investigated UAV can be formulated as:

$$\begin{cases} \dot{x}(t) = Ax(t) + Bu(t) \\ y(t) = Cx(t), \end{cases} \tag{232}$$

where $x(t) = [v_i, \alpha_i, q_i, \theta_i, \beta_i, p_i, r_i, \psi_i]^T \in \Re^n$, $u(t) = [\delta_{ei}, \delta_{ti}, \delta_{ai}, \delta_{ri}]^T \in \Re^m$, and $y(t) = [v_i, \psi_i - \beta_i]^T \in \Re^p$ denote the system states, control inputs, and system outputs of the ith UAV, respectively, whose details are all introduced in Table 3.2. $A \in \Re^{n \times n}$, $B \in \Re^{n \times m}$, and $C \in \Re^{n \times n}$

are the known matrices with appropriate dimensions.

In order to eliminate the steady-state error, the integral of tracking error is introduced into the system states [105, 140], the corresponding augmented system can then be represented by:

$$
\begin{cases}
\dot{x}_a(t) = A_a x_a(t) + B_a u(t) + G_a r(t) \\
y_a(t) = C_a x_a(t),
\end{cases}
\tag{233}
$$

where $r(t)$ $(\|r(t)\| \leq r_{max})$ is a uniformly bounded reference input, and $\epsilon(t) = r(t) - y(t)$ is the error between the reference signal and system output, $x_a(t) = \left[(\int_0^t \epsilon(t)dt)^T, \quad x^T(t) \right]^T$ and

$y_a(t) = \left[(\int_0^t \epsilon(t)dt)^T, \quad y^T(t) \right]^T$, $A_a = \begin{bmatrix} 0 & -C \\ 0 & A \end{bmatrix} \in \Re^{(n+q)\times(n+q)}$, $B_a = [0 \; B]^T \in \Re^{(n+q)\times m}$,

$G_a = [I \; 0]^T \in \Re^{(n+q)\times q}$.

In practice, UAVs' control surfaces may be stuck at a stochastic position owing to the hydraulics failure, whose value can be modeled as $\bar{u} = [\bar{u}_1, \bar{u}_2, ..., \bar{u}_m]^T$. $\bar{u}_j$ $(j = 1, 2, ..., m)$ represents the jth actuator is stuck with the value of $\bar{u}_j$. Considering $v(t) = [v_1, v_2, ..., v_m]^T \in \Re^m$ to be the commanded control input signal. The actual control input $u(t)$ with consideration of actuator faults can then be written into:

$$
u(t) = v(t) + \sigma[\bar{u} - v(t)] = (I - \sigma)v(t) + \sigma\bar{u},
\tag{234}
$$

where $\sigma = diag\{\sigma_1, \sigma_2, ..., \sigma_m\}$ denotes the failure pattern matrix. $\sigma_i = 1$ when the ith actuator fails to work properly, while $\sigma_i = 0$ indicates the ith actuator is healthy.

System (233) with consideration of actuator faults can thereby be rewritten as:

$$
\begin{cases}
\dot{x}_a(t) = A_a x_a(t) + B_a(I - \sigma)v(t) + B_a \sigma\bar{u} + G_a r(t) \\
y_a(t) = C_a x_a(t).
\end{cases}
\tag{235}
$$

158

The so-called ideal reference model of UAVs, in this work, is considered as follows:

$$\dot{x}_m(t) = A_m x_m(t) + B_m r(t), \tag{236}$$

where $x_m(t) \in \Re^{n+q}$ is the state of the reference model, $A_m \in \Re^{(n+q)\times(n+q)}$ is a Hurwitz matrix and $B_m \in \Re^{(n+q)\times m}$, and the pair (A_m, B_m) is controllable.

The state feedback for state tracking (SFST) matching condition owns advantages of simplicity and suitability for aircraft flight control applications [146]. According to this condition, the nominal system (A, B) is assumed to match the reference model (236) (with the control law $v(t) = K_s^T x + K_{ad1} r + K_{ad2}$) such that:

$$\begin{cases} A + B(I - \sigma)K_s^T = A_m, \\ B(I - \sigma)K_{ad1} + G_a = B_m, \\ B(I - \sigma)K_{ad2} = -B\sigma\bar{u}. \end{cases} \tag{237}$$

Furthermore, considering the control input u is amplitude limited (233), which is calculated using the following static actuator model:

$$\begin{aligned} u(t) &= u_{max} sat\left(\frac{u_r}{u_{max}}\right) \\ &= \begin{cases} u_r(t), & |u_r(t)| \le u_{max}, \\ u_{max} sgn(u_r(t)), & |u_r(t)| > u_{max}, \end{cases} \end{aligned} \tag{238}$$

where $u_r(t)$ is the reference control input, while $u_{max} > 0$ denotes the amplitude limitation level of the actuator.

The objectives of inner-loop control design can be stated as follows:

(1) Designing an adaptive state feedback control methodology so that the unfavorable effect of actuator stuck failures can be counteracted by means of the configured redundancy of actuators, and the state of the reference model given above can be tracked by UAV's states;

159

(2) The reference model is modified in response to the output deficiencies between the proposed FTC and actuator, adopting a virtual bound for actuator. Therefore, all actuators operate under saturation, preventing a secondary damage to the faulty UAVs.

5.2 Formation Controller Design Procedure

5.2.1 Outer-Loop Controller Design

5.2.1.1 Rigid Formation Control Strategy

From (231), the following relationship can be defined:

$$
\begin{aligned}
\begin{bmatrix} \dot{e}_{fi} \\ \dot{e}_{li} \end{bmatrix} &= \begin{bmatrix} -v_L - d_{li}\omega_L \\ d_{fi}\omega_L \end{bmatrix} + \begin{bmatrix} cos(\psi_i - \psi_L) & -Dsin(\psi_i - \psi_L) \\ -sin(\psi_i - \psi_L) & -Dcos(\psi_i - \psi_L) \end{bmatrix} \begin{bmatrix} v_i^* \\ \omega_i^* \end{bmatrix} \\
&+ \begin{bmatrix} cos(\psi_i - \psi_L) & -Dsin(\psi_i - \psi_L) \\ -sin(\psi_i - \psi_L) & -Dcos(\psi_i - \psi_L) \end{bmatrix} \begin{bmatrix} v_i - v_i^* \\ \omega_i - \omega_i^* \end{bmatrix} \\
&= \begin{bmatrix} -v_L - d_{li}\omega_L \\ d_{fi}\omega_L \end{bmatrix} + \begin{bmatrix} cos(\psi_i - \psi_L) & -Dsin(\psi_i - \psi_L) \\ -sin(\psi_i - \psi_L) & -Dcos(\psi_i - \psi_L) \end{bmatrix} \begin{bmatrix} v_i^* \\ \omega_i^* \end{bmatrix},
\end{aligned}
\tag{239}
$$

where v_i^* and ω_i^* denote the expected control laws, distributing to the inner-loop controller of each follower, so that the overall formation system can be stabilized.

In order to effectively track the desired trajectory, while eliminate the steady-state trajectory tracking error, a PI type of control method is adopted for the outer-loop controller design, which can be formulated as:

$$
\begin{bmatrix} v_i^* \\ \omega_i^* \end{bmatrix} = \begin{bmatrix} cose_\psi & -sine_\psi \\ -\frac{1}{D}sine_\psi & -\frac{1}{D}cose_\psi \end{bmatrix} \times \begin{bmatrix} -(k_{1P}e_{fi} + k_{1I}\int e_{fi}dt) + v_L + d_{li}\omega_L \\ -(k_{2P}e_{li} + k_{2I}\int e_{li}dt) - d_{fi}\omega_L \end{bmatrix},
\tag{240}
$$

where $e_\psi = \psi_i - \psi_L$, and the feedback gains $k_{1P}, k_{1I}, k_{2P}, k_{2I} > 0$ are chosen for the longitudinal

and lateral directions control, respectively.

5.2.1.2 Semi-Rigid Formation Strategy

For the purpose of developing a safer and more flexible formation control strategy, this work employs a collision avoidance mechanism. This mechanism is incorporated into the outer-loop of formation control design, preventing UAVs from threatening their surrounding objects (other vehicles, personnels, and infrastructures) from either air or ground.

A semi-rigid type of formation strategy is chosen here for the collision avoidance design, which is capable of ensuring all UAVs following the expected formation, while avoiding the potential obstacles from both inter-formation and surrounding environment. As depicted in Fig. 5.2, the main idea of the proposed semi-rigid formation control scheme is to modify the forward and angular velocities, such that keeping the desired separation distances (both longitudinal and lateral directions) between the UAVs. The concept of this formation control strategy can also be mathematically written as follows:

$$
\begin{cases}
v_i = v_i^* + v_{vi} \\
\omega_i = \omega_i^* + \omega_{vi},
\end{cases}
\tag{241}
$$

where v_i and ω_i represent the modified forward and angular velocities, respectively. v_{vi} and ω_{vi} denote the reactive obstacle avoidance terms for modifying forward and angular velocities of each UAV to avoid the potential collisions.

Assumption 8 *It is assumed that each UAV capable of detecting any approaching obstacles and measuring their distances has equipped the onboard sensing systems. Moreover, communication links among UAVs are assumed to be healthy enough.*

As illustrated in Fig. 5.3, adopting the so-called *mechanical impedance principle* approach in [193], each UAV in formation is allocated with a virtual repulsive force which is intended to characterize the interaction of individual UAV and its surrounding environment. Accordingly, this
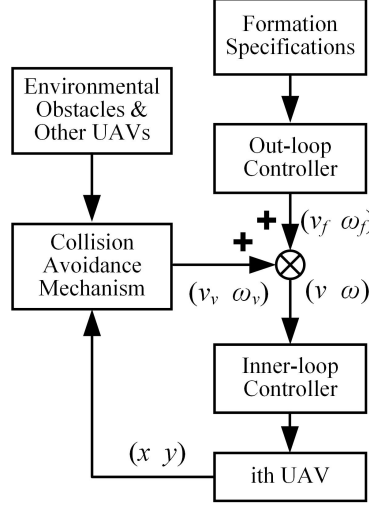
Figure 5.2: Schematic diagram of the presented semi-rigid formation control strategy.

force changes forward and angular velocities of each UAV using the following scheme:

$$
F_f = \begin{cases} c(d_{max} - d_o)^\alpha & \text{if } d_o < d_{max}, \\ 0 & \text{if } d_o \geq d_{max}, \end{cases} \tag{242}
$$

where d_o is the distance away from the closest obstacle, α denotes a predefined positive value, while d_{max} represents the safe distance between the UAV and potential obstacles, causing no fictitious forces ($F_f = 0$ if $d_o \geq d_{max}$), and c is a constant determined by the following system calibration:

$$
F_{fmax} = c(d_{max} - d_{min})^\alpha, \tag{243}
$$

where F_{fmax} and d_{min} denote the maximum virtual repulsive force and the minimum acceptable collision avoidance distance, respectively.

Then the heading angle changed to avoid an approaching obstacle can be achieved by:

$$
\begin{cases} \psi_{cL} = \Phi^{-1} F_{fL} \\ \psi_{cR} = \Phi^{-1} F_{fR}, \end{cases} \tag{244}
$$
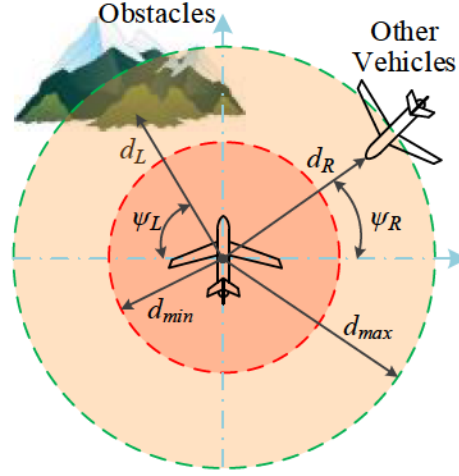
Figure 5.3: Illustration of the collision avoidance mechanism.

where ψ_{cL} and ψ_{cR} represent the regulation angle for obstacles coming from UAV's left and right sides, respectively; $\Phi = K_I s^2 + K_D s + K_E$, which denotes the mechanical impedance, characterizes the interaction of UAV and obstacles; $K_I, K_D, K_E \geq 0$ are the inertia, damping, and elastic constants, respectively; while F_{fL} and F_{fR} denote the fictitious forces in terms of the closest obstacles to the UAV, approaching from its left and right sides, respectively; the use of these two fictitious forces intended to guarantee the effective formation control system is effective for the operation in more cluttered environment.

The ultimate corrections to the forward and angular velocities can therefore be obtained:

$$
\begin{cases}
v_{vi} = \Phi^{-1}(F_{fL} sin\psi_{cL} + F_{lR} sin\psi_{cR}) \\
\omega_{vi} = \Phi^{-1}(F_{fR} - F_{fL}).
\end{cases}
\tag{245}
$$

5.2.2 Inner-Loop Controller Design

In order to effectively track guidance commands from the outer-loop controller, a direct adaptive FTC approach introduced in [194] is employed and modified to counteract actuator failures
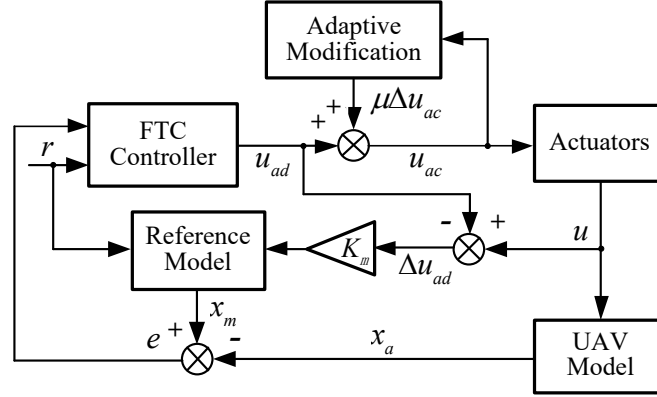
Figure 5.4: Illustration of the proposed adaptive FTC scheme.

under actuator saturation. The overall control design structure of the proposed controller is depicted in Fig. 5.4.

Due to the static actuator model (238), a control deficiency $\Delta u(t) = u(t) - u_{ac}(t)$ can be yielded. Adopting the μ-modification method in [190], a virtual amplitude bound of the actuator is first chosen as:

$$v_{max} = u_{max} - \Delta v, \tag{246}$$

where v_{max} and $0 < \Delta v < u_{max}$ denote the virtual bound and performance specification constant, respectively.

A modified direct adaptive model reference control is then defined as follows:

$$u_{ac}(t) = u_{ad}(t) + \mu \Delta u_{ac}(t), \tag{247}$$

where $\Delta u_{ac}(t) = v_{max} sat\left(\frac{u_{ac}(t)}{v_{max}} - u_{ac}(t)\right)$ represents the control deficiency signal due to v_{max}, μ denotes the design constant, while $u_{ad}(t) = K_s^T x_a(t) + K_{ad1}r(t) + K_{ad2}$ is the control input produced from the adaptive FTC.

To provide a more explicit definition of $u_{ac}(t)$, the following solution to (247) is further given

by the convex combination of $u_{ad}(t)$ and $v_{max}sat\left(u_{ad}(t)/v_{max}\right)$, $\forall t > 0$:

$$
\begin{aligned}
u_{ac}(t) &= \frac{1}{1+\mu}\left(u_{ad}(t) + \mu v_{max}sat\left(\frac{u_{ad}(t)}{v_{max}}\right)\right) \\
&= \begin{cases}
u_{ad}(t), & |u_{ad}(t)| \leq v_{max}, \\
\frac{1}{1+\mu}(u_{ad}(t) + \mu v_{max}), & u_{ad}(t) > v_{max}, \\
\frac{1}{1+\mu}(u_{ad}(t) - \mu v_{max}), & u_{ad}(t) < -v_{max},
\end{cases}
\end{aligned}
\tag{248}
$$

where $\mu \geq 0$. For the case of setting $\Delta v = 0$ and $\mu = \infty$, it is noteworthy that the final control input $u_{ac}(t) = u_{max}sat\left(u_{ad}(t)/u_{max}\right)$, which recovers the general adaptive FTC architecture with amplitude limiter.

To associate the adaptive control $u_{ad}(t)$ with the ultimate actuator output $u(t)$, defining the deficiency of the adaptive control signal as follows:

$$
\Delta u_{ad}(t) = u(t) - u_{ad}(t).
\tag{249}
$$

Substituting (249) and $u_{ad}(t) = K_s^T x_a(t) + K_{ad1}r(t) + K_{ad2}$ into (235), the following closed-loop system dynamics can be obtained:

$$
\dot{x}_a(t) = \left[A_a + B_a(I-\sigma)K_s^T\right]x_a(t) + B_a(I-\sigma)\left[K_{ad1}r(t) + K_{ad2} + \Delta u_{ad}(t)\right] + G_a r(t) + B_a \sigma \bar{u}.
\tag{250}
$$

Due to the system dynamics changing from (235) to (250), the following variation to the adaptive reference model dynamics (236) is considered:

$$
\dot{x}_m(t) = A_m x_m(t) + B_m\left[r(t) + K_m \Delta u_{ad}(t)\right],
\tag{251}
$$

where K_m is a *priori* determined adaptive gain, achieving from stability proof.

Remark 15 K_s *is the linear quadratic regulator (LQR) gain designed for the minimization of a quadratic performance function, K_s along with the adaptive FTC gain K_{ad1} aim at stabilizing the*

closed-loop system, K_{ad2} is designed to counteract the adverse effect of actuator faults, while K_m

is incorporated into the adaptive reference model for preventing actuators from saturation.

In order to match (250) to (251), the previously defined matching condition (237) can be rewritten as follows:

$$
\begin{cases}
A_a + B_a(I - \sigma)K_s^T = A_m, \\[2mm]
B_a(I - \sigma)K_{ad1} + G_a = B_m, \\[2mm]
\qquad B_a(I - \sigma)K_{ad2} = -B_a\sigma\bar{u}, \\[2mm]
\qquad\quad B_a(I - \sigma) = B_m K_m.
\end{cases}
\tag{252}
$$

Defining $e(t) = x_a(t) - x_m(t)$ to be the tracking error signal, with the matching condition in (252), the following tracking error dynamics can then be obtained:

$$
\dot{e}(t) = A_m e(t) + B_a(I - \sigma)\Big[\tilde{K}_s x_a(t) + \tilde{K}_{ad1} r + \tilde{K}_{ad2}\Big] + B_m \tilde{K}_m \Delta u_{ad}(t),
\tag{253}
$$

where $\tilde{K}_{ad1} = K_{ad1} - \hat{K}_{ad1}$, $\tilde{K}_{ad2} = K_{ad2} - \hat{K}_{ad2}$, and $\tilde{K}_m = K_m - \hat{K}_m$ represent the parameter errors between the actual and estimated values. $\hat{K}_{ad1}$, $\hat{K}_{ad2}$, and $\hat{K}_m$ denote the estimated values of the FTC gains K_{ad1}, K_{ad2}, K_m, respectively.

Theorem 12 *Consider the systems given by (250) and (251), the control gains in adaptive FTC control law $u_{ad}(t) = K_s^T x_a(t) + K_{ad1} r(t) + K_{ad2}$ and adaptive gain K_m in the adaptive reference model can be determined by the following adaptive FTC gain adaptation law:*

$$
\begin{aligned}
\dot{\hat{K}}_s &= -\Gamma_s B_a^T P e(t) x^T(t), \\[2mm]
\dot{\hat{K}}_{ad1} &= -\gamma_1 B_a^T P e(t) r^T(t), \\[2mm]
\dot{\hat{K}}_{ad2} &= -\gamma_2 B_a^T P e(t), \\[2mm]
\dot{\hat{K}}_m &= -\gamma_3 \Delta u_{ad}(t) e^T(t) P B_m,
\end{aligned}
\tag{254}
$$

where $\Gamma_s \in \Re^{n \times n}$ is a positive definite and symmetric matrix, γ_1 and γ_2 are positive scalars, ensuring that $\lim_{t \to \infty} e(t) = 0$ as well as all closed-loop system signals and adaptive gains are

bounded. Meanwhile, there exist positive definite matrices $P = P^T \in \Re^{n \times n}$ and $Q = Q^T \in \Re^{n \times n}$, so that the following inequality holds:

$$A_m^T P + P A_m \leq -Q. \tag{255}$$

Proof of Theorem 12: The tracking error dynamics (253) can be rewritten as:

$$\dot{e}(t) = A_m e(t) + \sum_{i \notin F_p}^{m} b_i \Big[\tilde{K}_{si} x_a(t) + \tilde{K}_{ad1i} r + \tilde{K}_{ad2i} \Big] + \sum_{i \notin F_p}^{m} b_{mi} \tilde{K}_{mi} \Delta u_{ad}(t), \tag{256}$$

where $F_p = f_1, f_2, ..., f_p$ indicates the set of failed actuators.

In order to assess the closed-loop system stability, select Lyapunov candidate function as:

$$V_{lf} = e^T P e + \sum_{i \notin F_p}^{m} b_i \Big[\tilde{K}_{si}^T \Gamma_{si}^{-1} \tilde{K}_{si} + \tilde{K}_{ad1i}^T \gamma_1^{-1} \tilde{K}_{ad1i} + \tilde{K}_{ad2i}^T \gamma_2^{-1} \tilde{K}_{ad2i} \Big] + \sum_{i \notin F_p}^{m} b_{mi} \tilde{K}_{mi}^T \gamma_3^{-1} \tilde{K}_{mi}. \tag{257}$$

The time derivative of the Lyapunov candidate function (257) along the system trajectories of (253) and (254) can then be obtained:

$$
\begin{aligned}
\dot{V}_{lf} = & e^T (P A_m + A_m P) e + 2 e^T P \Bigg\{ A_m e + \sum_{i \notin F_p}^{m} b_i \Big[\tilde{K}_{si} x_a + \tilde{K}_{ad1i} r + \tilde{K}_{ad2i} \Big] \\
& + \sum_{i \notin F_p}^{m} b_{mi} \tilde{K}_{mi} \Delta u_{ad} \Bigg\} + 2 \sum_{i \notin F_p}^{m} b_i \Big(\tilde{K}_{si} \Gamma_{si}^{-1} \dot{\tilde{K}}_{si} + \tilde{K}_{ad1i} \gamma_{1i}^{-1} \dot{\tilde{K}}_{ad1i} \\
& + \tilde{K}_{ad2i} \gamma_{2i}^{-1} \dot{\tilde{K}}_{ad2i} \Big) + 2 \sum_{i \notin F_p}^{m} b_{mi} \tilde{K}_{mi} \gamma_{3i}^{-1} \dot{\tilde{K}}_{mi}.
\end{aligned}
\tag{258}
$$

Applying the adaptive FTC parameter adaptation laws (254) and inequality (255) in Theorem 12, (258) can in turn be derived as:

$$\dot{V}_{lf} \leq -e^T Q e. \tag{259}$$

That is, $e(t)$, $\tilde{K}_s$, $\tilde{K}_{ad1}$, $\tilde{K}_{ad2}$, and $\tilde{K}_m$ are all bounded, and the equilibrium of (254) and (256) is Lyapunov stable.

However, the bound of the reference model state cannot be guaranteed due to the adaptive modification of the reference system. Accordingly, the Barbalat's lemma cannot be applied to prove the asymptotic properties of $\lim_{t\to\infty} e(t) = 0$ and the stability of the closed-loop system in this case. In order to make such a asymptotic stability proof, the state $x_a(t)$ needs to remain bounded under the adaptive modification. Therefore, two further proof steps are provided in the following.

Step 1 (no actuators are saturated): If $\Delta u_{ad}(t) = 0$ which means no actuators are saturated, the tracking error dynamics (253) can then be rewritten as follows:

$$\dot{e}(t) = A_m e(t) + B_a(I - \sigma)\left[\tilde{K}_s x_a(t) + \tilde{K}_{ad1} r + \tilde{K}_{ad2}\right]. \tag{260}$$

Therefore, the closed-loop system under actuator failures can be stabilized applying *Barbalat's Lemma*.

Step 2 (actuator saturation occurs): If $\Delta u_{ad}(t) \neq 0$, which indicates that some actuators encounter saturation, then applying the matching conditions in (254), $u_{ad}(t) = K_s^T x_a(t) + K_{ad1} r(t) + K_{ad2}$, and the faulty system (250), the system dynamics can be written in the following form:

$$\dot{x}_a(t) = A_m x_a(t) + B_a(I - \sigma)u(t) + G_a r(t) - B_a(I - \sigma)(K_s^T x_a(t) + K_{ad2}). \tag{261}$$

Since $\Delta u(t) \neq 0$, then $|u_{ac}(t)| > u_{max}$, $u(t) = u_{max} sgn(u_{ac}(t))$, therefore (261) becomes:

$$\dot{x}_a(t) = A_m x_a(t) + B_a(I-\sigma)u_{max}(t)sgn(u_{ac}(t)) + G_a r(t) - B_a(I-\sigma)(K_s^T x_a(t) + K_{ad2}). \tag{262}$$

Considering the following Lyapunov function candidate which is with respect to $x_a(t)$:

$$V_{x_a} = x_a^T(t) P x_a(t), \tag{263}$$

where $P = P^T > 0$. Deriving (263) with respect to time, one can then obtain:

$$\dot{V}_{x_a} = x_a^T(t)(PA_m + A_m P)x_a(t) + 2x_a^T(t)PB_a(I - \sigma)[u(t) - K_s^T x_a(t) - K_{ad2}] + 2x_a^T(t)PG_a r(t). \tag{264}$$

Consider the condition $u_{min} \leq ||u(t)|| \leq \sqrt{m}u_{max}$, where $u_{min} = min\{u_{max_1}, ..., u_{max_m}\}$, the following two possibilities are then taken into consideration:

(1) Possibility 1: $x_a^T(t)PB_a(I - \sigma)u(t) < -||x_a(t)|| \, ||PB_a(I - \sigma)||u_{min}$;

(2) Possibility 2: $x_a^T(t)PB_a(I - \sigma)u(t) \geq -||x_a(t)|| \, ||PB_a(I - \sigma)||u_{min}$.

If the *Possibility 1* is true, then (264) becomes:

$$\begin{aligned}\dot{V}_{x_a} \leq & -Q_m||x_a(t)||^2 - 2||x_a(t)||^2 \, ||PB_a(I - \sigma)||||K_s|| + 2r_{max}||x_a(t)|| \, ||PG_a|| \\ & - 2||x_a(t)||||PB_a(I - \sigma)||(u_{min} + ||K_{ad2}||).\end{aligned} \tag{265}$$

Thus, it follows that $\dot{V}_{x_a} < 0$ if

$$x_a \in \Omega_1 \triangleq \left\{ x_a \Big| \, ||x_a|| < \Big[||PB_a(I - \sigma)||(u_{min} + ||K_{ad2}||) - r_{max}||PG_a||\Big]\Big/\xi = x_{a_{max}} \right\}, \tag{266}$$

and

$$u_{max} \geq \Big[||PB_a(I - \sigma)||(u_{min} + ||K_{ad2}||) - r_{max}||PG_a||\Big]\Big/||PB_a(I - \sigma)||, \tag{267}$$

where $\xi = \Big|Q_m - 2||PB_a(I - \sigma)|| \, ||K_s||\Big|$.

Consider a largest set Θ_1. This set is enclosed in Ω_1, which limits system state $x_a(t)$ in boundary

$$\Theta_1 = \{x_a(t)| \, V_{x_a} \leq P_{min}x_{a_{max}}^2\}, \tag{268}$$

where P_{min} denote the minimum eigenvalue of P.

169

If the *Possibility 2* is true, applying the *Lemma 2* in [190], then one can have

$$x_a^T(t)PB_a(I-\sigma)\left[\frac{K_s^T x_a(t) + K_{ad1}^T r(t) + K_{ad2}^T}{||U_{max}^{-1} u_{ac}(t)||_\infty} + \bar{u}(t)\right] + ||x_a(t)||\,||PB_a(I-\sigma)||u_{min}(t) \geq 0. \tag{269}$$

Since $u_0 = u_{min} + \sqrt{m}u_{max}$, therefore the derivative of the Lyapunov function candidate Eq. (264) can be further derived as:

$$\begin{aligned}
\dot{V}_{x_a} =& x_a^T(t)(PA_m + A_mP)x_a(t) + 2x_a^T(t)PB_a(I-\sigma)[u(t) - K_s^T x_a(t) - K_{ad2}] \\
& + 2x_a^T(t)PG_a r(t) \\
\leq& -Q_m||x_a(t)||^2 + 2r_{max}||x_a(t)||\,||PG_a|| + 2||x_a(t)||\,||PB_a(I-\sigma)|| \\
& \left[\tilde{K}_s^{max}\,||x_a(t)|| + (\tilde{K}_{ad1}^{max} + ||\hat{K}_{ad1}||)r_{max} + \tilde{K}_{ad2}^{max} + ||\hat{K}_{ad2}||\right] \\
& + 2||U_{max}^{-1}||_\infty||u_{ac}(t||\,||x_a(t)||\,||PB_a(I-\sigma)||u_0.
\end{aligned} \tag{270}$$

In addition, $||u_{ac}(t)||_\infty \leq ||u_{ac}(t)||$, and applying the adaptive modification law (248) with setting $\mu = 0$, (270) can be rewritten as:

$$\begin{aligned}
\dot{V}_{x_a} \leq& -Q_m||x_a(t)||^2 + 2r_{max}||x_a(t)||\,||PG_a|| + 2||x_a(t)||\,||PB_a(I-\sigma)||\left[\tilde{K}_s^{max}\,||x_a(t)|| \right. \\
& + (\tilde{K}_{ad1}^{max} + ||\hat{K}_{ad1}||)r_{max} + \tilde{K}_{ad2}^{max} + ||\hat{K}_{ad2}||\left. \right] + 2||U_{max}^{-1}||_\infty\,||x_a(t)||\,||PB_a(I \\
& - \sigma)||u_0\left[(\tilde{K}_s^{max} + ||\hat{K}_s||)||x_a(t)|| + (\tilde{K}_{ad1}^{max} + ||\hat{K}_{ad1}||)r_{max} + (\tilde{K}_{ad2}^{max} + ||\hat{K}_{ad2}||)\right] \\
\leq& -||x_a(t)||^2\left[Q_m - 2||PB_a(I-\sigma)||\tilde{K}_s^{max} - 2u_0||U_{max}^{-1}||_\infty||PB_a(I-\sigma)||(\tilde{K}_s^{max} \right. \\
& + ||\hat{K}_s||)\left. \right] + 2||x_a(t)||\,||PB_a(I-\sigma)||(1 + u_0||U_{max}^{-1}||_\infty)\left[(\tilde{K}_{ad1}^{max} + ||\hat{K}_{ad1}||)r_{max} \right. \\
& + (\tilde{K}_{ad2}^{max} + ||\hat{K}_{ad2}||)\left. \right] + 2r_{max}||x_a(t)||\,||PG_a||.
\end{aligned} \tag{271}$$

Thus, $\dot{V}_{x_a} < 0$ if the following inequalities hold:

$$x_a \in \Omega_2 \triangleq \left\{ x_a \middle| \; ||x_a|| \geq \kappa/\xi_2 = x_{a_{min}} \right\}, \tag{272}$$

where $\xi_2 = Q_m - 2||PB_a(I - \sigma)||\tilde{K}_s^{max} - 2u_0 \, ||U_{max}^{-1}||_\infty \, ||PB_a(I - \sigma)|| \, (\tilde{K}_s^{max} + ||\hat{K}_s||)$, and $\kappa = ||PB_a(I-\sigma)||(1+u_0||U_{max}^{-1}||_\infty)\left[(\tilde{K}_{ad1}^{max}+||\hat{K}_{ad1}||)r_{max}+(\tilde{K}_{ad2}^{max}+||\hat{K}_{ad2}||) \right]+2r_{max}||PG_a||$.

Furthermore, defining the smallest set $\Theta_2 = \{x_a(t)| \; ||x_a(t) \leq x_a^{min}(t)||\}$ enclosing Ω_2 as:

$$\Theta_1 = \{x_a(t)| \; V_{x_a} \leq P_M x_{a_{max}}^2\}. \tag{273}$$

where P_{max} denotes the maximum eigenvalue of P.

Consequently, it can be obtained that $\Omega_2 \subset \Omega_1$, which implies that $\dot{V}_{x_a} < 0$ holds $\forall \; x_a^{min}(t) < x_a(t) < x_a^{max}(t)$ when $\Delta u_{ad}(t) \neq 0$.

Remark 16 *The reference model (236) is time-varying and updated when the control input $u_{ac}(t)$ approaches the amplitude boundaries of actuators. This action is made by adopting the parameter projection, which can guarantee the satisfactory stability and performance characteristics of the reference model.*

Remark 17 *(updating the reference model): when $u_{ac}(t)$ exceeds a predetermined threshold v_{max}, the reference model can then be updated as follows (see also Fig. 5.4):*

(1) Design a reference model (236), satisfying the matching conditions (252);

(2) Once the adaptive FTC input signal $u_{ac}(t)$ violates the virtual bound of actuators, such that $u_{ac}(t) > v_{max}$ and $\Delta u_{ad}(t) \neq 0$, based on the adaptive control scheme in (254), the reference command $r(t)$ is then replaced by $r(t) + K_m \Delta u_{ad}(t)$ in reference model (236), resulting in the modified reference model (251);

(3) Update the reference model and go to step (2).

Table 5.2: Adopted parameter values

Parameter	α	d_{max}	d_{min}	F_{max}	K_I	K_B	K_K
Value	2	100	50	2.5	0.1	0.2	1

Note: this table includes the information of the ith UAV.

5.3 Simulation Results

In order to verify the effectiveness of the proposed strategy in a more practical manner, the vehicle dynamics from a real UAV are applied in the simulation validation. This work is different from others that only utilized single- or double-integrator dynamics to validate their proposed formation control methodologies. Three UAVs (the proposed method is also applicable for the formation with more than three agents) are employed in the simulation, one is chosen as the leader, others are set as followers. System matrices of the selected UAV [180] are given as:

$$
A = \begin{bmatrix} A_f & 0 \\ 0 & A_l \end{bmatrix}, B = \begin{bmatrix} B_f & 0 \\ 0 & B_l \end{bmatrix}, A_f = \begin{bmatrix} -0.0334 & -2.977 & 0 & -9.81 \\ -0.0016 & -4.133 & 0.98 & 0 \\ 0.0077 & -140.2 & -4.435 & 0 \\ 0 & 0 & 1 & 0 \end{bmatrix},
$$

$$
A_l = \begin{bmatrix} -0.732 & -0.0143 & -0.996 & 0.0706 \\ -893 & -9.059 & 2.044 & 0 \\ 101.673 & 0.0186 & -1.283 & 0 \\ 0 & 0 & 1 & 0 \end{bmatrix}, B_f = \begin{bmatrix} -1.075 & -0.2453 \\ 0.347 & -4.133 \\ -140.22 & 0 \\ 0 & 0 \end{bmatrix},
$$

$$
B_l = \begin{bmatrix} 0 & 0.244 \\ 328.653 & 308.498 \\ 47.528 & 102.891 \\ 0 & 0 \end{bmatrix}, C = \begin{bmatrix} 1 & 0 & 0 & 0 & 0 & 0 & 0 & 0 \\ 0 & 0 & 0 & 0 & -1 & 0 & 0 & 1 \end{bmatrix},
$$

172
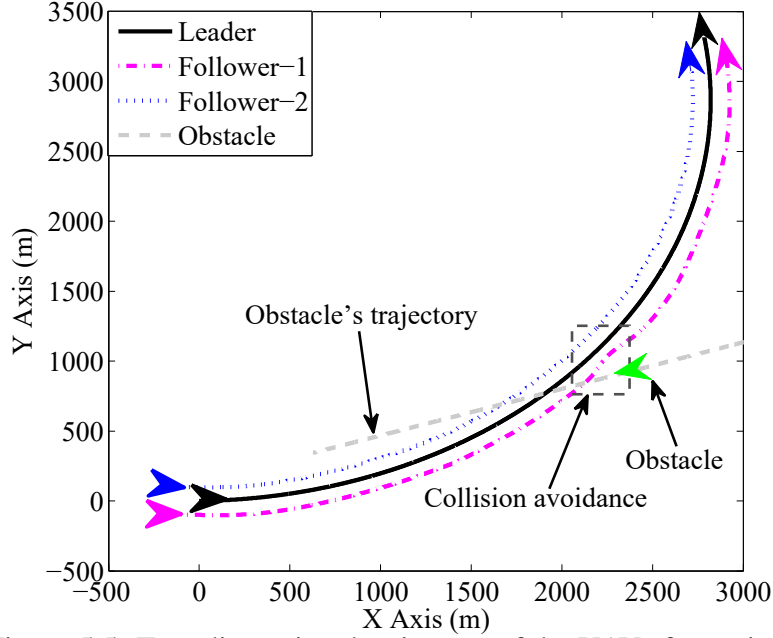
Figure 5.5: Two-dimensional trajectory of the UAVs formation.

where A_f and B_f are the dynamics along the longitudinal direction, while A_l and B_l are the dynamics along the lateral direction. Control surfaces for the longitudinal direction operation are elevator δ_e and throttle δ_t, while control surfaces for lateral direction operation are rudder δ_r and aileron δ_a.

5.3.1 Scenarios Description

The expected forward and angular velocities of the leader UAV are chosen as $v_L^* = 10m/s$ and $\omega_L^* = 0.5deg/s$, respectively. In terms of the expected distances between the leader UAV and follower UAVs in forward and lateral directions, $d_{f1}^d = -100m$ and $d_{l1}^d = -100m$ are selected for the distances between the leader UAV and Follower-1 UAV, while $d_{f2}^d = -100m$ and $d_{l2}^d = 100m$ are chosen for the distances between the leader UAV and Follower-2 UAV. The Leader, Follower-1, and Follower-2 UAVs start at $(0m, 0m)$, $(-100m, -100m)$, and $(-100m, 100m)$, respectively. Table 5.2.2 summarizes the adopted parameters values for the controller design.

Three scenarios are involved in the simulation to demonstrate the effectiveness of the proposed approach:
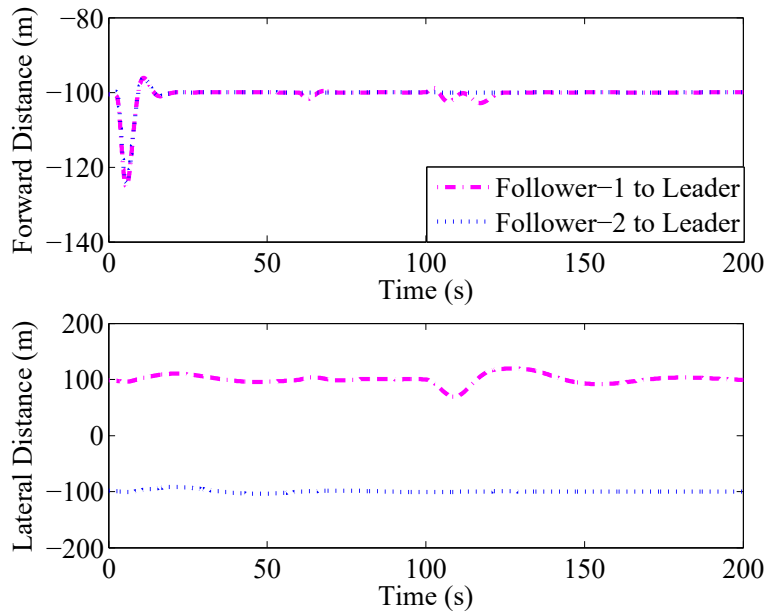
Figure 5.6: Distances between the leader and follower UAVs.
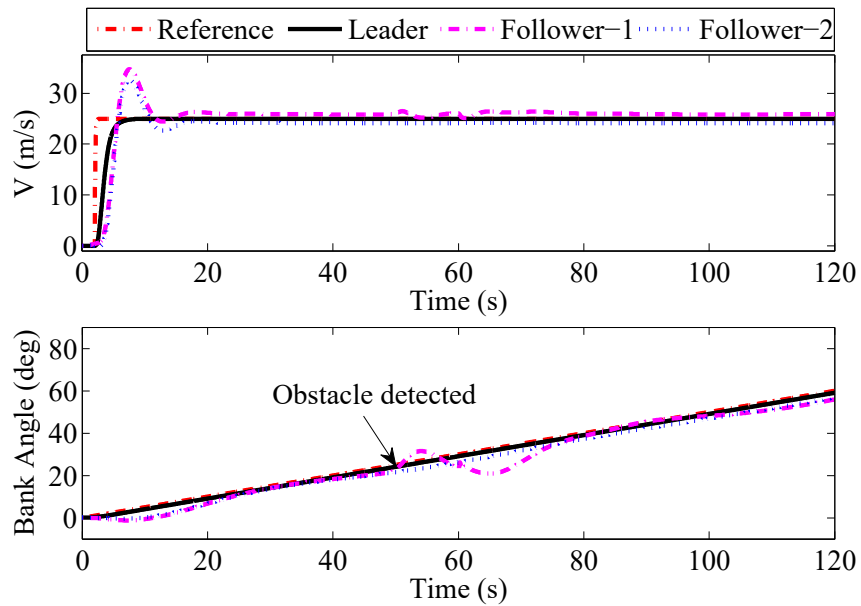
Figure 5.7: Forward velocity and bank angle performance of each UAV in formation.

174
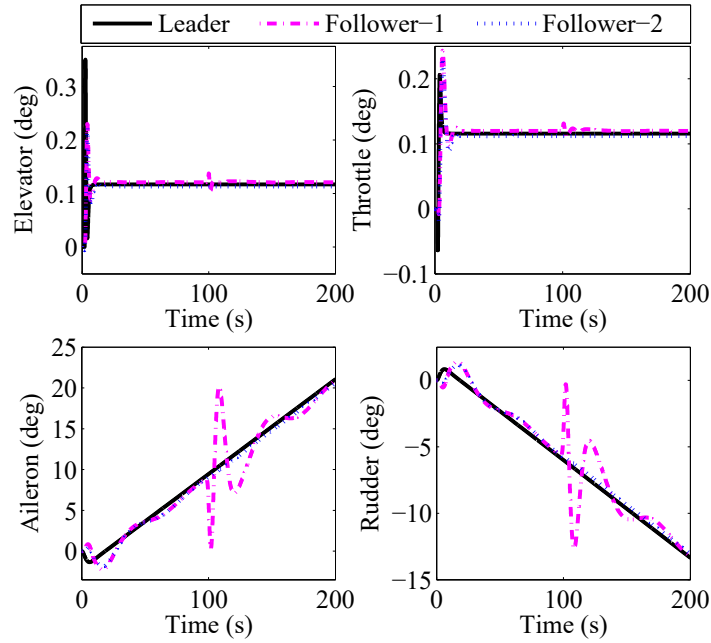
Figure 5.8: Actuator performance of the UAVs in formation.

(1) In *Scenario 1*, it assumes that a dynamic obstacle moves toward the formation with the specific heading angle and forward velocity. Its position (x_{obs}, y_{obs}) can be obtained by the following formula:

$$\begin{cases} x_{obs} = 2070 - 20t \\ y_{obs} = 368 - 5t. \end{cases} \tag{274}$$

This obstacle may collide with the Follower-1 UAV if no collision avoidance actions are conducted.

(2) In *Scenario 2*, the aileron of the Follower-2 UAV is suddenly stuck at $20\ deg$ (at 60th second), which directly leads to the faulty UAV rapidly deviate from the desired trajectory, and may also result in collision among the Follower-2 UAV and other healthy UAVs.

(3) In *Scenario 3*, it is supposed that sensors onboard UAVs are all polluted by Gaussian white noise for the purpose of making the simulation to be more realistic and further verifying

175

the effectiveness of the proposed approach. These random signals' sampling time and co-variance are chosen as 0.01 and 0.0001, respectively [119], while the amplitudes of these injected signals are selected as $5\ m/s$ for the velocity measurement and $5\ deg$ for the measure of bank angle. Moreover, since the traditional linear quadratic regulator (LQR) control method is adopted for the baseline controller design in the proposed controller, a LQR controller is thereby selected for performance comparison. Both controllers are simulated with the same faulty case; the aileron is stuck at $-10\ deg$ at 60th second. The LQR feedback control gains for both controllers are the same as well.

In both cases, the deflections of actuators are all constrained in the limitation $[-25deg,\ 25deg]$.
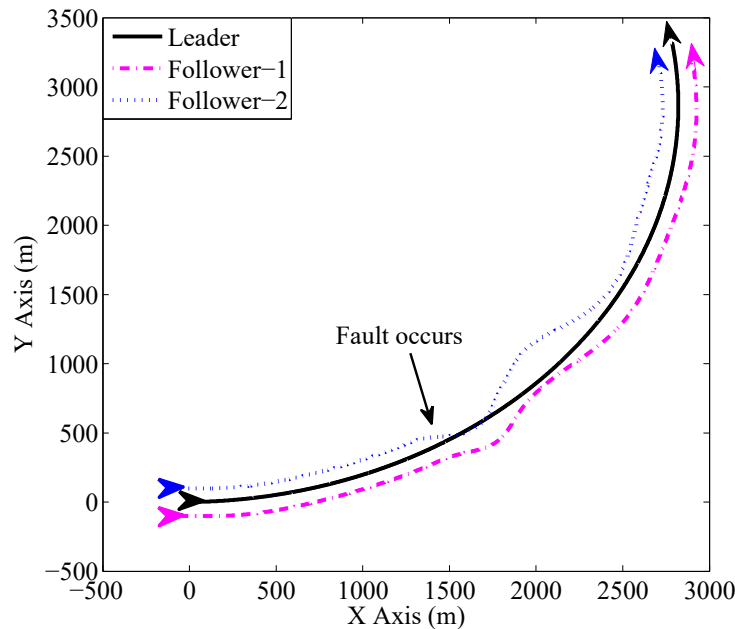
Figure 5.9: Two-dimensional trajectory of the UAVs formation.

5.3.2 Results of Scenario 1 and Evaluation

As shown in Fig. 5.5, there is an obstacle moving toward the formation, which is successfully detected and an effective collision avoidance operation with graceful performance degradation is
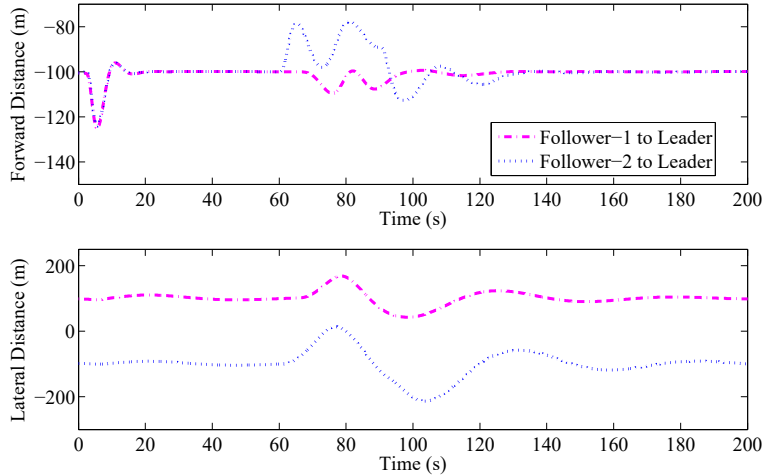
Figure 5.10: Distances between the leader and follower UAVs.

then made by the Follower-1 UAV. To be more specifically illustrated in Fig. 5.6, during the collision avoidance maneuver, around $2m$ and $25m$ maximum tracking errors are yielded in forward and lateral directions, respectively. From Fig. 5.7 and 5.8, the collision avoidance action occurs at 100th second, this safety behaviour indeed attributes to the effective operation of the Follower-1 UAV's bank angle.

As revealed in Fig. 5.4, although there are large deflections in both the aileron and rudder of the Follower-1 UAV when the Follower-1 UAV is performing collision avoidance action, all actuators still work under saturation.

5.3.3 Results of Scenario 2 and Evaluation

Fig. 5.9 displays a satisfactory and safety performance of UAVs formation control after FTC and obstacle avoidance operations. A rigid formation is finally maintained, though experienced a certain period of regulation.

As displayed in Fig. 5.10, the distances between the Follower-2 UAV and the Leader UAV in both forward and lateral directions are rapidly and significantly altered after the aileron of Follower-2 UAV is stuck at $20deg$ at 60th second. Meanwhile, the Follower-2 UAV is gradually approaching to the Follower-1 UAV due to the aileron of Follower-2 UAV has failed. By virtue

177
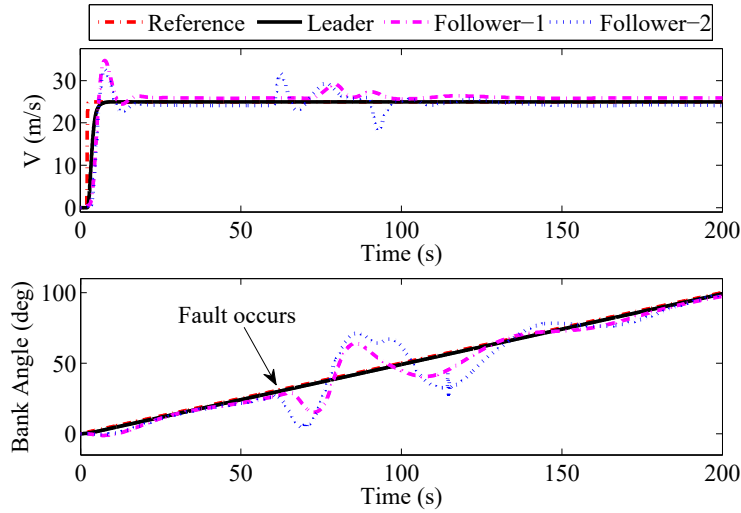
Figure 5.11: Forward velocity and bank angle performance of each UAV in formation.

of the collision avoidance mechanism, the approaching Follower-1 UAV can be promptly detected by the Follower-2 UAV, while a safe distance away from the Follower-1 UAV is correspondingly kept. Moreover, the actuator fault in Follower-1 UAV can also be properly accommodated, and the desired formation can be ultimately maintained. The corresponding performance of forward velocities and bank angles of each UAV in formation are all shown in Fig. 5.11, and their actuators performance are displayed in Fig. 5.12. In order to demonstrate the effectiveness of the proposed actuator saturation mechanism in a clearer way, a more serious actuator fault (the rudder is stuck at $-10 deg$ at 10th second) is imposed in the rudder of a single UAV, while the proposed control method is compared with a classic direct adaptive FTC approach designed in [194].

The performance of actuators in Fig. 5.13 shows that the aileron controlled by the proposed controller is still under saturation, while the aileron, which is under supervision of the compared controller, has violated the constraint. Furthermore, as displayed in Fig. 5.13, the control action produced by the proposed controller is less aggressive to avoid actuator saturation, comparing with the classic adaptive FTC controller. This good performance is mainly because of the introduction of the so-called $\mu-$modification mechanism in the proposed controller design. The modification parameter μ and virtual amplitude bound v_{max} play a crucial role in preventing the saturation of
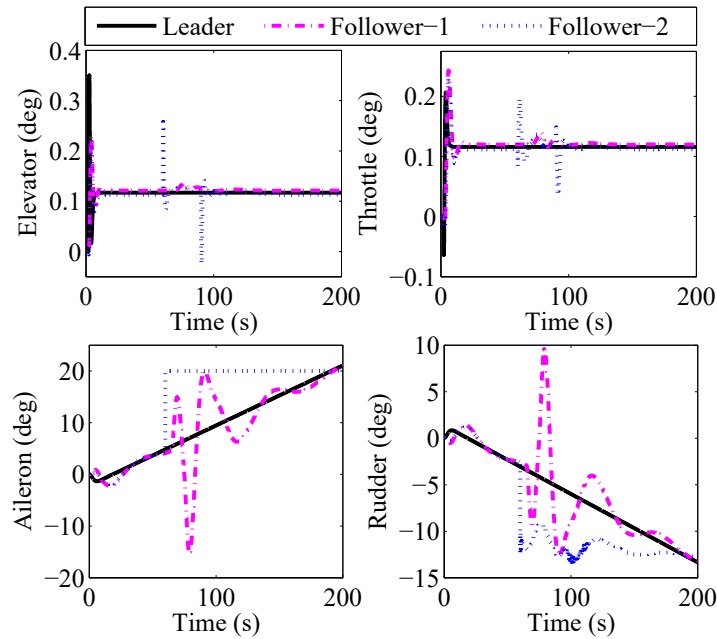
Figure 5.12: Actuator performance of the UAVs in formation.

healthy actuators. According to the control design law and authors' experience, v_{max} is normally chosen as slightly smaller than the actuator's practical amplitude constraint u_{max}. On the one hand, the decrease of μ can lead the healthy actuators to be susceptible to saturation. On the other hand, the healthy actuators operate in a slower manner due to the increase of μ.

5.3.4   Results of Scenario 3 and Evaluation

From Fig. 5.14, the simulation results reveal that the proposed controller can stabilize the system in the presence of both actuator faults and measurement noises with acceptable performance degradation. Whereas the compared controller cannot tolerate the imposed fault and ultimately fails to maneuver the UAV. As displayed in Fig. 5.15, the better performance of the proposed controller is due to the prompt and effective actuator action, comparing with the poor actuator performance of the compared controller.
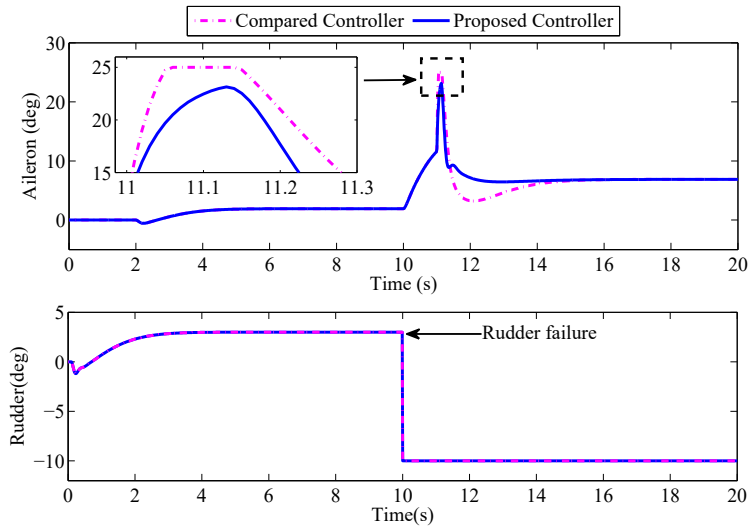
Figure 5.13: Actuator performance comparison.
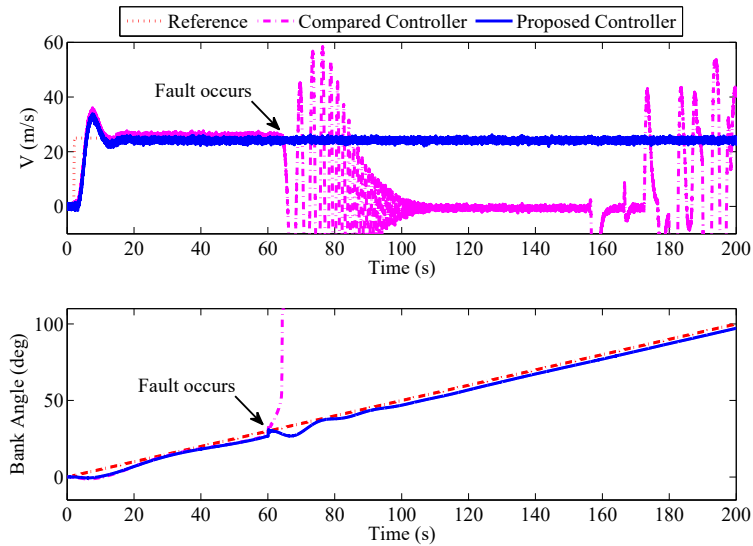
Figure 5.14: Forward velocity and bank angle performance comparison.

180
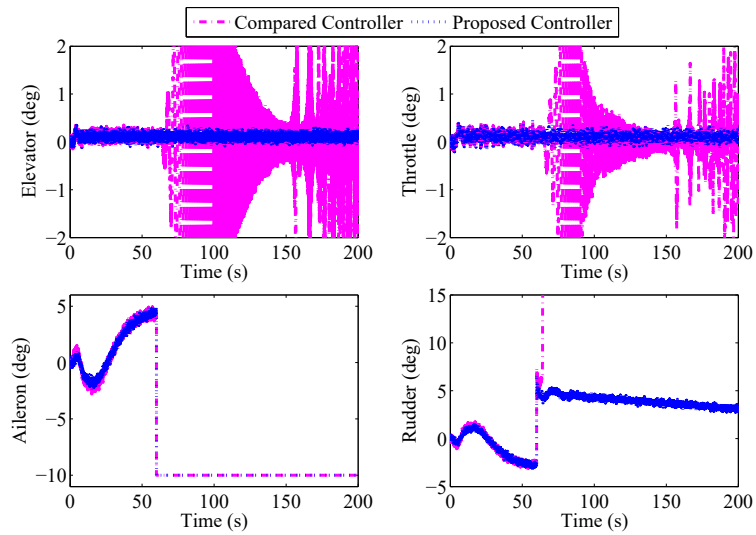
Figure 5.15: Actuator performance comparison.

Chapter 6

Conclusions and Future Works

6.1 Conclusions

In this thesis, several unmanned vehicles related critical issues on reliable and safe motion control are well studied, these issues include:

- A comprehensive literature review on unmanned vehicles as well as their guidance, navigation and control systems is provided.

- Two types of path following laws are designed, namely the Serret-Frenet frame based path following scheme and line-of-sight path following scheme. Regarding the first scheme, the path following and control schemes are integrated. Simulation results have demonstrated that the developed scheme is capable of facilitating control system design and effectively compensating environmental disturbances without violating actuator constraints. Regarding the second scheme, path following and control schemes are separately designed. The philosophy of this design is to deal with environmental disturbances and inertia motion caused sideslip angle in the path following phase without introducing it to the control system. This is of significant importance due to the fact that the unacceptable control performance sometimes is not caused by the poor control system design, but the disturbances existing in the

control reference distributed from the path following system. Both simulation and experimental results have validated that dramatical performance improvement to path following has been made.

- A new nonlinear adaptive observer is developed to estimate the sideslip angle which has been precisely estimated for correcting the reference signal to be allocated to the control system.

- Next, several reliable and safe control methodologies are devised for the operation of unmanned vehicles. First, a learning-based fault-tolerant tracking control method, which is expected to mitigate the adverse effects of actuator faults, disturbances, and uncertainties, has been successfully developed for the unmanned quadrotor helicopter without accurate system model to automatically regulate its gain online according to the errors between the reference signals and states measurements. Then, two types of adaptive fault estimation and fault-tolerant tracking control approaches are developed for an unmanned quadrotor helicopter and an unmanned surface vehicle, respectively. Both controllers are proved to be effective for improving systems' reliability and safety in simulation, and the amplitudes of the imposed faults are also well estimated. Finally, a linear parameter varying based control scheme along with a linear parameter varying based parameter estimation scheme are developed for the operation of USV under different working conditions. Simulation results have verified the effectiveness of the proposed control and parameter estimation schemes. Either actuator fault or mass variation is well detected and their magnitudes are accurately obtained. Experimental test on an unmanned quadrotor helicopter also demonstrates the efficacy of the designed algorithm.

- In addition to the control of individual unmanned vehicle, the problem of operating a group of unmanned aerial vehicles is also studied. The effectiveness of the proposed leader-follower formation control methodology is verified. The desired and safe formation is guaranteed with an acceptable performance degradation in the event of both actuator faults and obstacles.

183

6.2 Future Works

Following the current research in this thesis, the following future directions are outlined:

- The faults/failures considered in this thesis only occur in actuators, while the sensor and communication faults/failures are not included, though they are of significance for safety-critical control system design as well. Therefore, the future work can be extended to the studies of more sorts of faults/failures in the sensors and communications.

- Although most of the developed control schemes are validated in simulations, more field tests are still needed.

- Only loss of control effectiveness and stuck faults are studied in this thesis, more categories of faults should be simultaneously considered in the future research to further increase the robustness and effectiveness of the proposed control approaches.

- The studied Serret-Frenet frame based path following scheme can be incorporated with a predictive term (based on system dynamics) for the cross-track error to enhance its robustness to environmental disturbances and improve its path following performance.

- The presented adaptive line-of-sight path following method is proved to be effective in two-dimensional space and can be extended to the three-dimensional space in the future.

- The leader-follower formation control problem is well investigated, while more complicated and challenging issues, such as distributed control, are expected to be included as well.

- Obstacles avoidance is critical for unmanned vehicles. While a relatively simple case has been studied in this thesis, which may be difficult to be effective in the event of local and global minima problems, more powerful hybrid collision avoidance methods consisting of both global and local collision avoidance as well as considering the specific traffic rules are desirable.

Bibliography

[1] Z. X. Liu, Y. M. Zhang, X. Yu, and C. Yuan, "Unmanned surface vehicles: An overview of developments and challenges," *Annual Reviews in Control*, vol. 41, pp. 71–93, 2016.

[2] K. R. Muske, H. Ashrafiuon, G. Haas, R. McCloskey, and T. Flynn, "Identification of a control oriented nonlinear dynamic USV model," in *American Control Conference*, pp. 562–567, 2008.

[3] Y. M. Zhang, A. Chamseddine, C. A. Rabbath, B. W. Gordon, C.-Y. Su, S. Rakheja, C. Fulford, J. Apkarian, and P. Gosselin, "Development of advanced FDD and FTC techniques with application to an unmanned quadrotor helicopter testbed," *Journal of the Franklin Institute*, vol. 350, no. 9, pp. 2396–2422, 2013.

[4] C. Yuan, Y. M. Zhang, and Z. X. Liu, "A survey on technologies for automatic forest fire monitoring, detection, and fighting using unmanned aerial vehicles and remote sensing techniques," *Canadian Journal of Forest Research*, vol. 45, no. 7, pp. 783–792, 2015.

[5] N. Metni and T. Hamel, "A UAV for bridge inspection: Visual servoing control law with orientation limits," *Automation in Construction*, vol. 17, no. 1, pp. 3–10, 2007.

[6] G. M. Hoffmann, H. M. Huang, S. L. Waslander, and C. J. Tomlin, "Precision flight control for a multi-vehicle quadrotor helicopter testbed," *Control Engineering Practice*, vol. 19, no. 9, pp. 1023–1036, 2011.

[7] D. Mellinger, N. Michael, and V. Kumar, "Trajectory generation and control for precise aggressive maneuvers with quadrotors," *The International Journal of Robotics Research*, vol. 31, no. 5, pp. 664–674, 2012.

[8] M. Bernard, K. Kondak, I. Maza, and A. Ollero, "Autonomous transportation and deployment with aerial robots for search and rescue missions," *Journal of Field Robotics*, vol. 28, no. 6, pp. 914–931, 2011.

[9] F. Rinaldi, S. Chiesa, and F. Quagliotti, "Linear quadratic control for quadrotors UAVs dynamics and formation flight," *Journal of Intelligent & Robotic Systems*, vol. 70, no. 1, pp. 203–220, 2013.

[10] M. Saska, T. Krajník, V. Vonásek, Z. Kasl, V. Spurnỳ, and L. Přeučil, "Fault-tolerant formation driving mechanism designed for heterogeneous MAVs-UGVs groups," *Journal of Intelligent & Robotic Systems*, vol. 73, no. 1-4, pp. 603–622, 2014.

[11] N. Michael, J. Fink, and V. Kumar, "Cooperative manipulation and transportation with aerial robots," *Autonomous Robots*, vol. 30, no. 1, pp. 73–86, 2011.

[12] I. Maza, K. Kondak, M. Bernard, and A. Ollero, "Multi-UAV cooperation and control for load transportation and deployment," *Journal of Intelligent & Robotic Systems*, vol. 57, no. 1-4, pp. 417–449, 2010.

[13] M. Mammarella, G. Campa, M. R. Napolitano, M. L. Fravolini, Y. Gu, and M. G. Perhinschi, "Machine vision/GPS integration using EKF for the UAV aerial refueling problem," *IEEE Transactions on Systems, Man, and Cybernetics, Part C: Applications and Reviews*, vol. 38, no. 6, pp. 791–801, 2008.

[14] J. Escareño, S. Salazar, H. Romero, and R. Lozano, "Trajectory control of a quadrotor subject to 2D wind disturbances," *Journal of Intelligent & Robotic Systems*, vol. 70, no. 1-4, pp. 51–63, 2013.

[15] G. N. Roberts and R. Sutton, *Advances in unmanned marine vehicles*, vol. 69. IET, 2006.

[16] M. A. Djeziri, R. Merzouki, B. O. Bouamama, and M. Ouladsine, "Fault diagnosis and fault-tolerant control of an electric vehicle overactuated," *IEEE Transactions on Vehicular Technology*, vol. 62, no. 3, pp. 986–994, 2013.

[17] X. Qi, C. Zhang, and J. Gu, "Output feedback fault tolerant control for networked control systems with random access," *Control and Intelligent Systems*, vol. 40, no. 4, p. 226, 2012.

[18] X. Yu and J. Jiang, "Hybrid fault-tolerant flight control system design against partial actuator failures," *IEEE Transactions on Control Systems Technology*, vol. 20, no. 4, pp. 871–886, 2012.

[19] Y. Xu, H. Chen, and J. Gu, "Power loss analysis for switched reluctance motor converter by using electrothermal model," *IET Power Electronics*, vol. 8, no. 1, pp. 130–141, 2015.

[20] R. Isermann, *Fault-diagnosis applications: Model-based condition monitoring: actuators, drives, machinery, plants, sensors, and fault-tolerant systems*. Springer Science & Business Media, 2011.

[21] "Washington Post: When drones fall from the sky." http://www.washingtonpost.com/sf/investigative/2014/06/20/when-drones-fall-from-the-sky/. Accessed on: 2016-09-18.

[22] Y. M. Zhang and J. Jiang, "Bibliographical review on reconfigurable fault-tolerant control systems," *Annual Reviews in Control*, vol. 32, no. 2, pp. 229–252, 2008.

[23] M. Blanke, M. Kinnaert, J. Lunze, M. Staroswiecki, and J. Schröder, *Diagnosis and fault-tolerant control*. 2nd Ed., Springer, 2006.

[24] H. Noura, D. Theilliol, J.-C. Ponsart, and A. Chamseddine, *Fault-tolerant control systems: Design and practical applications*. Springer Science & Business Media, 2009.

[25] G. J. Ducard, *Fault-tolerant flight control and guidance systems: Practical methods for small unmanned aerial vehicles.* Springer Science & Business Media, 2009.

[26] C. Edwards, T. Lombaerts, and H. Smaili, "Fault tolerant flight control," *Lecture Notes in Control and Information Sciences*, vol. 399, 2010.

[27] H. Yang, B. Jiang, and V. Cocquempot, "Fault tolerant control and hybrid systems," in *Fault Tolerant Control Design for Hybrid Systems*, pp. 1–9, Springer, 2010.

[28] H. Alwi, C. Edwards, and C. P. Tan, *Fault detection and fault-tolerant control using sliding modes.* Springer Science & Business Media, 2011.

[29] R. J. Patton, "Fault-tolerant control," *Encyclopedia of Systems and Control*, pp. 422–428, 2015.

[30] J. Jiang and X. Yu, "Fault-tolerant control systems: A comparative study between active and passive approaches," *Annual Reviews in Control*, vol. 36, no. 1, pp. 60–72, 2012.

[31] M. H. Amoozgar, A. Chamseddine, and Y. M. Zhang, "Fault-tolerant fuzzy gain-scheduled PID for a quadrotor helicopter testbed in the presence of actuator faults," in *IFAC Conference on Advances in PID Control, Brescia, Italy*, 2012.

[32] T. Li, Y. M. Zhang, and B. W. Gordon, "Passive and active nonlinear fault-tolerant control of a quadrotor unmanned aerial vehicle based on the sliding mode control technique," *Proceedings of the Institution of Mechanical Engineers, Part I: Journal of Systems and Control Engineering*, vol. 227, no. 1, pp. 12–23, 2013.

[33] Z. X. Liu, C. Yuan, Y. M. Zhang, and J. Luo, "A learning-based fault tolerant tracking control of an unmanned quadrotor helicopter," *Journal of Intelligent & Robotic Systems*, pp. 1–18, 2015.

[34] I. Sadeghzadeh, A. Mehta, and Y. M. Zhang, "Fault-tolerant control of quadrotor helicopter using gain-scheduled PID and model reference adaptive control," *Journal of Unmanned System Technology*, vol. 3, no. 3, pp. 108–118, 2016.

[35] A. Lanzon, A. Freddi, and S. Longhi, "Flight control of a quadrotor vehicle subsequent to a rotor failure," *Journal of Guidance, Control, and Dynamics*, vol. 37, no. 2, pp. 580–591, 2014.

[36] A. Freddi, A. Lanzon, and S. Longhi, "A feedback linearization approach to fault tolerance in quadrotor vehicles," in *IFAC World Congress*, pp. 5413–5418, 2011.

[37] M. Ranjbaran and K. Khorasani, "Fault recovery of an under-actuated quadrotor aerial vehicle," in *IEEE Conference on Decision and Control (CDC)*, pp. 4385–4392, IEEE, 2010.

[38] A. B. Milhim, Y. M. Zhang, and C. A. Rabbath, "Gain scheduling based PID controller for fault tolerant control of a quad-rotor UAV," *AIAA Infotech Aerospace*, pp. 20–22, 2010.

[39] Q.-L. Zhou, Y. M. Zhang, C.-A. Rabbath, and D. Theilliol, "Design of feedback linearization control and reconfigurable control allocation with application to a quadrotor UAV," in *International Conference on Control and Fault-Tolerant Systems (SysTol)*, pp. 371–376, IEEE, 2010.

[40] D. Rotondo, F. Nejjari, and V. Puig, "Robust quasi-LPV model reference FTC of a quadrotor UAV subject to actuator faults," *International Journal of Applied Mathematics and Computer Science*, vol. 25, no. 1, pp. 7–22, 2015.

[41] H. A. Izadi, Y. M. Zhang, and B. W. Gordon, "Fault tolerant model predictive control of quad-rotor helicopters with actuator fault estimation," in *Proceedings of the 18th IFAC World Congress*, pp. 6343–6348, 2011.

[42] J. D. Schierman, D. G. Ward, J. R. Hull, N. Gandhi, M. Oppenheimer, and D. B. Doman, "Integrated adaptive guidance and control for re-entry vehicles with flight test results," *Journal of Guidance, Control, and Dynamics*, vol. 27, no. 6, pp. 975–988, 2004.

[43] M. Benosman and K.-Y. Lum, "Online references reshaping and control reallocation for nonlinear fault tolerant control," *IEEE Transactions on Control Systems Technology*, vol. 17, no. 2, pp. 366–379, 2009.

[44] Y. M. Zhang and J. Jiang, "Fault tolerant control system design with explicit consideration of performance degradation," *IEEE Transactions on Aerospace and Electronic Systems*, vol. 39, no. 3, pp. 838–848, 2003.

[45] F. Bateman, H. Noura, and M. Ouladsine, "Fault diagnosis and fault-tolerant control strategy for the aerosonde UAV," *IEEE Transactions on Aerospace and Electronic Systems*, vol. 47, no. 3, pp. 2119–2137, 2011.

[46] B. Xiao, Q. L. Hu, and Y. M. Zhang, "Adaptive sliding mode fault tolerant attitude tracking control for flexible spacecraft under actuator saturation," *IEEE Transactions on Control Systems Technology*, vol. 20, no. 6, pp. 1605–1612, 2012.

[47] B. Xiao, Q. L. Hu, and P. Shi, "Attitude stabilization of spacecrafts under actuator saturation and partial loss of control effectiveness," *IEEE Transactions on Control Systems Technology*, vol. 21, no. 6, pp. 2251–2263, 2013.

[48] M. Burger, A. Pavlov, E. Børhaug, and K. Y. Pettersen, "Straight line path following for formations of underactuated surface vessels under influence of constant ocean currents," in *American Control Conference*, pp. 3065–3070, IEEE, 2009.

[49] K. D. Do and J. Pan, "Robust path-following of underactuated ships: Theory and experiments on a model ship," *Ocean Engineering*, vol. 33, no. 10, pp. 1354–1372, 2006.

[50] K. D. Do, Z.-P. Jiang, and J. Pan, "Robust adaptive path following of underactuated ships," *Automatica*, vol. 40, no. 6, pp. 929–944, 2004.

[51] L. Moreira, T. I. Fossen, and C. G. Soares, "Path following control system for a tanker ship model," *Ocean Engineering*, vol. 34, no. 14, pp. 2074–2085, 2007.

[52] Y. Yang, J. L. Du, H. B. Liu, C. Guo, and A. Abraham, "A trajectory tracking robust controller of surface vessels with disturbance uncertainties," *IEEE Transactions on Control Systems Technology*, vol. 22, no. 4, pp. 1511–1518, 2014.

[53] K. P. Tee and S. Z. S. Ge, "Control of fully actuated ocean surface vessels using a class of feedforward approximators," *IEEE Transactions on Control Systems Technology*, vol. 14, no. 4, pp. 750–756, 2006.

[54] M. E. Serrano, G. J. Scaglia, S. A. Godoy, V. Mut, and O. A. Ortiz, "Trajectory tracking of underactuated surface vessels: A linear algebra approach," *IEEE Transactions on Control Systems Technology*, vol. 22, no. 3, pp. 1103–1111, 2014.

[55] Z. Li and J. Sun, "Disturbance compensating model predictive control with application to ship heading control," *IEEE Transactions on Control Systems Technology*, vol. 20, no. 1, pp. 257–265, 2012.

[56] M. Breivik and T. I. Fossen, "Path following for marine surface vessels," in *MTTS/IEEE Conference on OCEAN*, vol. 4, pp. 2282–2289, IEEE, 2004.

[57] A. P. P. Encarnacao and M. Arcak, "Path following for autonomous marine craft," in *IFAC Conference on Manoeuvring and Control of Marine Craft*, pp. 117–122, IFAC, 2000.

[58] Z. Li, J. Sun, and S. Oh, "Design, analysis and experimental validation of a robust nonlinear path following controller for marine surface vessels," *Automatica*, vol. 45, no. 7, pp. 1649–1658, 2009.

[59] K. D. Do and J. Pan, "State- and output-feedback robust path-following controllers for underactuated ships using Serret–Frenet frame," *Ocean Engineering*, vol. 31, no. 5, pp. 587–613, 2004.

[60] M. Bibuli, G. Bruzzone, M. Caccia, and L. Lapierre, "Path-following algorithms and experiments for an unmanned surface vehicle," *Journal of Field Robotics*, vol. 26, pp. 669–688, 2009.

[61] M. Bibuli, M. Caccia, L. Lapierre, and G. Bruzzone, "Guidance of unmanned surface vehicles: Experiments in vehicle following," *IEEE Robotics & Automation Magazine*, vol. 19, no. 3, pp. 92–102, 2012.

[62] Y.-L. Liao, M.-J. Zhang, and L. Wan, "Serret-Frenet frame based on path following control for underactuated unmanned surface vehicles with dynamic uncertainties," *Journal of Central South University*, vol. 22, pp. 214–223, 2015.

[63] X.-F. Wang, Z.-J. Zou, T.-S. Li, and W.-L. Luo, "Adaptive path following controller of underactuated ships using Serret-Frenet frame," *Journal of Shanghai Jiaotong University (Science)*, vol. 15, pp. 334–339, 2010.

[64] S. A. Arogeti and N. Berman, "Path following of autonomous vehicles in the presence of sliding effects," *IEEE Transactions on Vehicular Technology*, vol. 61, no. 4, pp. 1481–1492, 2012.

[65] T. I. Fossen, *Handbook of marine craft hydrodynamics and motion control*. John Wiley & Sons, 2011.

[66] F. A. Papoulias, "Bifurcation analysis of line of sight vehicle guidance using sliding modes," *International Journal of Bifurcation and Chaos*, vol. 1, no. 4, pp. 849–865, 1991.

[67] T. I. Fossen, M. Breivik, and R. Skjetne, "Line-of-sight path following of underactuated marine craft," in *IFAC Conference on Manoeuvring and Control of Marine Craft (MCMC)*, pp. 244–249, 2003.

[68] E. Fredriksen and K. Y. Pettersen, "Global κ-exponential way-point maneuvering of ships: Theory and experiments," *Automatica*, vol. 42, no. 4, pp. 677–687, 2006.

[69] T. I. Fossen and K. Y. Pettersen, "On uniform semiglobal exponential stability (USGES) of proportional line-of-sight guidance laws," *Automatica*, vol. 50, no. 11, pp. 2912–2917, 2014.

[70] T. I. Fossen and A. M. Lekkas, "Direct and indirect adaptive integral line-of-sight path-following controllers for marine craft exposed to ocean currents," *International Journal of Adaptive Control and Signal Processing*, 2015.

[71] E. Børhaug, A. Pavlov, and K. Y. Pettersen, "Integral LOS control for path following of underactuated marine surface vessels in the presence of constant ocean currents," in *IEEE Conference on Decision and Control (CDC)*, pp. 4984–4991, 2008.

[72] W. Caharija, M. Candeloro, K. Y. Pettersen, and A. J. Sørensen, "Relative velocity control and integral LOS for path following of underactuated surface vessels," in *IFAC Conference on Manoeuvring and Control of Marine Craft (MCMC)*, 2012.

[73] A. M. Lekkas and T. I. Fossen, "Line-of-sight guidance for path following of marine vehicles," *Advanced in Marine Robotics*, pp. 63–92, 2013.

[74] A. M. Lekkas and T. I. Fossen, "Integral LOS path following for curved paths based on a monotone cubic hermite spline parametrization," *IEEE Transactions on Control Systems Technology*, vol. 22, no. 6, pp. 2287–2301, 2014.

[75] T. I. Fossen, K. Y. Pettersen, and R. Galeazzi, "Line-of-sight path following for dubins paths with adaptive sideslip compensation of drift forces," *IEEE Transactions on Control Systems Technology*, vol. 23, no. 2, pp. 820–827, 2015.

[76] J. Candela, R. C. Beardsley, and R. Limeburner, "Separation of tidal and subtidal currents in ship-mounted acoustic Doppler current profiler observations," *Journal of Geophysical Research*, vol. 97, no. C1, pp. 769–788, 1992.

[77] F. Prieur and R. E. Hansen, "Theoretical improvements when using the second harmonic signal in acoustic Doppler current profilers," *IEEE Journal of Oceanic Engineering*, vol. 38, no. 2, pp. 275–284, 2013.

[78] J. Stephant, A. Charara, and D. Meizel, "Virtual sensor: Application to vehicle sideslip angle and transversal forces," *IEEE Transactions on Industrial Electronics*, vol. 51, no. 2, pp. 278–289, 2004.

[79] H. F. Grip, L. Imsland, T. A. Johansen, J. C. Kalkkuhl, and A. Suissa, "Vehicle sideslip estimation," *IEEE Control Systems Magzine*, vol. 29, no. 5, pp. 36–52, 2009.

[80] A. M. Lekkas and T. I. Fossen, "Trajectory tracking and ocean current estimation for marine underactuated vehicles," in *IEEE Conference on Control Applications (CCA)*, pp. 905–910, 2014.

[81] S. Campbell, W. Naeem, and G. W. Irwin, "A review on improving the autonomy of unmanned surface vehicles through intelligent collision avoidance manoeuvres," *Annual Reviews in Control*, vol. 36, no. 2, pp. 267–283, 2012.

[82] M. Breivik, *Topics in guided motion control of marine vehicles*. PhD thesis, 2010.

[83] C. A. Goudey, T. Consi, J. Manley, M. Graham, *et al.*, "A robotic boat for autonomous fish tracking," *Marine Technology Society Journal*, vol. 32, no. 1, p. 47, 1998.

[84] R.-j. Yan, S. Pang, H.-b. Sun, and Y.-j. Pang, "Development and missions of unmanned surface vehicle," *Journal of Marine Science and Application*, vol. 9, no. 4, pp. 451–457, 2010.

[85] J. Majohr and T. Buch, "Modelling, simulation and control of an autonomous surface marine vehicle for surveying applications measuring Dolphin MESSIN," *IEE Control Engineering Series*, vol. 69, p. 329, 2006.

[86] W. Naeem, T. Xu, R. Sutton, and A. Tiano, "The design of a navigation, guidance, and control system for an unmanned surface vehicle for environmental monitoring," *Proceedings of the Institution of Mechanical Engineers, Part M: Journal of Engineering for the Maritime Environment*, vol. 222, no. 2, pp. 67–79, 2008.

[87] R. R. Murphy, E. Steimle, C. Griffin, C. Cullins, M. Hall, and K. Pratt, "Cooperative use of unmanned sea surface and micro aerial vehicles at Hurricane Wilma," *Journal of Field Robotics*, vol. 25, no. 3, pp. 164–180, 2008.

[88] M. Breivik, V. E. Hovstein, and T. I. Fossen, "Straight-line target tracking for unmanned surface vehicles," *Modeling, Identification and Control*, vol. 29, no. 4, pp. 131–149, 2008.

[89] M. Caccia, M. Bibuli, R. Bono, G. Bruzzone, G. Bruzzone, and E. Spirandelli, "Unmanned surface vehicle for coastal and protected waters applications: The Charlie project," *Marine Technology Society Journal*, vol. 41, no. 2, pp. 62–71, 2007.

[90] T. Pastore and V. Djapic, "Improving autonomy and control of autonomous surface vehicles in port protection and mine countermeasure scenarios," *Journal of Field Robotics*, vol. 27, no. 6, pp. 903–914, 2010.

[91] P. Svec and S. K. Gupta, "Automated synthesis of action selection policies for unmanned vehicles operating in adverse environments," *Autonomous Robots*, vol. 32, no. 2, pp. 149–164, 2012.

[92] V. Bertram, "Unmanned surface vehicles–A survey," *Skibsteknisk Selskab, Copenhagen, Denmark*, pp. 1–14, 2008.

[93] U. Kiencke, L. Nielsen, R. Sutton, K. Schilling, M. Papageorgiou, and H. Asama, "The impact of automatic control on recent developments in transportation and vehicle systems," *Annual Reviews in Control*, vol. 30, no. 1, pp. 81–89, 2006.

[94] M. Caccia, M. Bibuli, R. Bono, and G. Bruzzone, "Basic navigation, guidance and control of an unmanned surface vehicle," *Autonomous Robots*, vol. 25, no. 4, pp. 349–365, 2008.

[95] S. Savitz, I. Blickstein, P. Buryk, and Button, "US navy employment options for unmanned surface vehicles (USVs)," DTIC Document, 2013.

[96] T. I. Fossen, *Marine control systems: Guidance, navigation and control of ships, rigs and underwater vehicles*. Marine Cybernetics, 2002.

[97] K. D. Do and J. Pan, *Control of ships and underwater vehicles: Design for underactuated and nonlinear marine systems*. Springer Science & Business Media, 2009.

[98] T. I. Fossen, *Guidance and control of ocean vehicles*. John Wiley & Sons Inc, 1994.

[99] J. Velagic, Z. Vukic, and E. Omerdic, "Adaptive fuzzy ship autopilot for track-keeping," *Control Engineering Practice*, vol. 11, no. 4, pp. 433–443, 2003.

[100] P. A. Ioannou and J. Sun, *Robust adaptive control*. Courier Corporation, 2012.

[101] H. K. Khalil and J. Grizzle, *Nonlinear systems*, vol. 3. Prentice Hall New Jersey, 1996.

[102] S. F. Shiffman, Daniel and Z. Marsh, *The nature of code: Simulating natural systems with processing*. The Nature of Code, 2012.

[103] D. Henrion and S. Tarbouriech, "LMI relaxations for robust stability of linear systems with saturating controls," *Automatica*, vol. 35, no. 9, pp. 1599–1604, 1999.

[104] T. S. Hu and Z. L. Lin, *Control systems with actuator saturation: Analysis and design.* Springer Science & Business Media, 2001.

[105] F. Liao, J. L. Wang, and G.-H. Yang, "Reliable robust flight tracking control: An LMI approach," *IEEE Transactions on Control Systems Technology*, vol. 10, no. 1, pp. 76–89, 2002.

[106] D. k. Chwa, J. Y. Choi, and J. H. Seo, "Compensation of actuator dynamics in nonlinear missile control," *IEEE Transactions on Control Systems Technology*, vol. 12, no. 4, pp. 620–626, 2004.

[107] P. Apkarian, H. D. Tuan, and J. Bernussou, "Continuous-time analysis, eigenstructure assignment, and H_2 synthesis with enhanced linear matrix inequalities (LMI) characterizations," *IEEE Transactions on Automatic Control*, vol. 46, no. 12, pp. 1941–1946, 2001.

[108] S. P. Boyd, L. El Ghaoui, E. Feron, and V. Balakrishnan, *Linear matrix inequalities in system and control theory*, vol. 15. SIAM, 1994.

[109] C.-S. Liu and H. Peng, "Disturbance observer based tracking control," *Journal of Dynamic Systems, Measurement, and Control*, vol. 122, no. 2, pp. 332–335, 2000.

[110] Y. Nesterov, A. Nemirovskii, and Y. Y. Ye, *Interior-point polynomial algorithms in convex programming*, vol. 13. SIAM, 1994.

[111] K. D. Do and J. Pan, "Underactuated ships follow smooth paths with integral actions and without velocity measurements for feedback: Theory and experiments," *IEEE Transactions on Control Systems Technology*, vol. 14, no. 2, pp. 308–322, 2006.

[112] D. Simon, "Sum normal optimization of fuzzy membership functions," *International Journal of Uncertainty, Fuzziness and Knowledge-Based Systems*, vol. 10, no. 04, pp. 363–384, 2002.

[113] A. Jiménez, B. M. Al-Hadithi, and F. Matía, *Extended Kalman filter for the estimation and fuzzy optimal control of Takagi-Sugeno model*. INTECH Open Access Publisher, 2011.

[114] R. G. Berstecher, R. Palm, and H. D. Unbehauen, "An adaptive fuzzy sliding-mode controller," *IEEE Transactions on Industrial Electronics*, vol. 48, no. 1, pp. 18–31, 2001.

[115] C.-W. Tao, J.-S. Taur, and Y. Chen, "Design of a parallel distributed fuzzy LQR controller for the twin rotor multi-input multi-output system," *Fuzzy Sets and Systems*, vol. 161, no. 15, pp. 2081–2103, 2010.

[116] H. S. Sii, T. Ruxton, and J. Wang, "A fuzzy-logic-based approach to qualitative safety modelling for marine systems," *Reliability Engineering & System Safety*, vol. 73, no. 1, pp. 19–34, 2001.

[117] K. K. Ahn and D. Q. Truong, "Online tuning fuzzy PID controller using robust extended Kalman filter," *Journal of Process Control*, vol. 19, no. 6, pp. 1011–1023, 2009.

[118] M. S. Grewal and A. P. Andrews, "Kalman filtering: Theory and practice using MATLAB," *Theory and Practice*, vol. 5, no. 5, pp. 705–708, 2001.

[119] J. H. Fan, Y. M. Zhang, and Z. Q. Zheng, "Robust fault-tolerant control against time-varying actuator faults and saturation," *IET Control Theory & Applications*, vol. 6, no. 14, pp. 2198–2208, 2012.

[120] H. Ashrafiuon, K. R. Muske, L. C. McNinch, and R. A. Soltan, "Sliding-mode tracking control of surface vessels," *IEEE Transactions on Industrial Electronics*, vol. 55, no. 11, pp. 4004–4012, 2008.

[121] D. Ye and G.-H. Yang, "Adaptive fault-tolerant tracking control against actuator faults with application to flight control," *IEEE Transactions on Control Systems Technology*, vol. 14, no. 6, pp. 1088–1096, 2006.

[122] T. Xu, J. Chudley, and R. Sutton, "A fault tolerant multi-sensor navigation system for an un-manned surface vehicle," in *Fault Detection, Supervision and Safety of Technical Processes*, vol. 6, pp. 1503–1508, 2006.

[123] M. Blanke, R. Izadi-Zamanabadi, and T. F. Lootsma, "Fault monitoring and re-configurable control for a ship propulsion plant," *International Journal of Adaptive Control and Signal Processing*, vol. 12, no. 8, pp. 671–688, 1998.

[124] R. Sutton, S. Sharma, and T. Xao, "Adaptive navigation systems for an unmanned surface vehicle," *Journal of Marine Engineering & Technology*, vol. 10, no. 3, pp. 3–20, 2011.

[125] T. Xu, R. Sutton, and S. Sharma, "A multi-sensor data fusion navigation system for an unmanned surface vehicle," *The Institution of Mechanical Engineers, Part M: Journal of Engineering for the Maritime Environment*, vol. 221, no. 4, pp. 167–182, 2007.

[126] C. Bonivento, A. Paoli, and L. Marconi, "Fault-tolerant control of the ship propulsion system benchmark," *Control Engineering Practice*, vol. 11, no. 5, pp. 483–492, 2003.

[127] A. Cristofaro and T. A. Johansen, "Fault tolerant control allocation using unknown input observers," *Automatica*, vol. 50, no. 7, pp. 1891–1897, 2014.

[128] Z. X. Liu, Y. M. Zhang, C. Yuan, and J. Luo, "An adaptive linear parameter varying fault tolerant control scheme for unmanned surface vehicle steering control," in *Chinese Control Conference (CCC)*, pp. 6197–6202, 2015.

[129] M. Rodrigues, H. Hamdi, D. Theilliol, C. Mechmeche, and N. BenHadj Braiek, "Actuator fault estimation based adaptive polytopic observer for a class of LPV descriptor systems," *International Journal of Robust and Nonlinear Control*, vol. 25, no. 5, pp. 673–688, 2015.

[130] A. Annamalai, R. Sutton, C. Yang, P. Culverhouse, and S. Sharma, "Robust adaptive control of an uninhabited surface vehicle," *Journal of Intelligent & Robotic Systems*, vol. 78, no. 2, pp. 319–338, 2015.

[131] J. S. Shamma, "An overview of LPV systems," in *Control of Linear Parameter Varying Systems with Applications*, pp. 3–26, Springer, 2012.

[132] C. Hoffmann and H. Werner, "A survey of linear parameter-varying control applications validated by experiments or high-fidelity simulations," *IEEE Transactions on Control Systems Technology*, vol. 23, no. 2, pp. 416–433, 2015.

[133] F. Wu and K. Dong, "Gain-scheduling control of LFT systems using parameter-dependent Lyapunov functions," *Automatica*, vol. 42, no. 1, pp. 39–50, 2006.

[134] J. S. Shamma, *Analysis and design of gain scheduled control systems*. PhD thesis, Massachusetts Institute of Technology, 1988.

[135] F. Wu, "A generalized LPV system analysis and control synthesis framework," *International Journal of Control*, vol. 74, no. 7, pp. 745–759, 2001.

[136] F. Blanchini, D. Casagrande, S. Miani, and U. Viaro, "Stable LPV realization of parametric transfer functions and its application to gain-scheduling control design," *IEEE Transactions on Automatic Control*, vol. 55, no. 10, pp. 2271–2281, 2010.

[137] F. Blanchini and S. Miani, *Set-theoretic methods in control*. Springer, 2008.

[138] R. Skjetne, Ø. N. Smogeli, and T. I. Fossen, "A nonlinear ship manoeuvering model: Identification and adaptive control with experiments for a model ship," *Modeling, Identification and Control*, vol. 25, no. 1, pp. 3–27, 2004.

[139] P. Apkarian, J.-M. Biannic, and P. Gahinet, "Self-scheduled H_∞ control of missile via linear matrix inequalities," *Journal of Guidance, Control, and Dynamics*, vol. 18, no. 3, pp. 532–538, 1995.

[140] Y. M. Zhang and J. Jiang, "Integrated design of reconfigurable fault-tolerant control systems," *Journal of Guidance, control, and Dynamics*, vol. 24, no. 1, pp. 133–136, 2001.

[141] P. Apkarian and R. J. Adams, "Advanced gain-scheduling techniques for uncertain systems," *IEEE Transactions on Control Systems Technology*, vol. 6, no. 1, pp. 21–32, 1998.

[142] S. Montes de Oca, S. Tornil-Sin, V. Puig, and D. Theilliol, "Fault-tolerant control design using the linear parameter varying approach," *International Journal of Robust and Nonlinear Control*, vol. 24, no. 14, pp. 1969–1988, 2014.

[143] W. M. H. Heemels, J. Daafouz, and G. Millerioux, "Observer-based control of discrete-time LPV systems with uncertain parameters," *IEEE Transactions on Automatic Control*, vol. 55, no. 9, pp. 2130–2135, 2010.

[144] D. J. Stilwell and W. J. Rugh, "Interpolation of observer state feedback controllers for gain scheduling," *IEEE Transactions on Automatic Control*, vol. 44, no. 6, pp. 1225–1229, 1999.

[145] S. P. Bhat, D. S. Bernstein, *et al.*, "Continuous finite-time stabilization of the translational and rotational double integrators," *IEEE Transactions on Automatic Control*, vol. 43, no. 5, pp. 678–682, 1998.

[146] S. M. Joshi, P. Patre, and G. Tao, "Adaptive control of systems with actuator failures using an adaptive reference model," *Journal of Guidance, Control, and Dynamics*, vol. 35, no. 3, pp. 938–949, 2012.

[147] P. E. Pounds, D. R. Bersak, and A. M. Dollar, "Stability of small-scale UAV helicopters and quadrotors with added payload mass under PID control," *Autonomous Robots*, vol. 33, no. 1-2, pp. 129–142, 2012.

[148] I. Sadeghzadeh, M. Abdolhosseini, and Y. M. Zhang, "Payload drop application using an unmanned quadrotor helicopter based on gain-scheduled PID and model predictive control," *Unmanned Systems*, vol. 2, no. 1, pp. 39–52, 2014.

[149] C. Wang, M. Nahon, and M. Trentini, "Controller development and validation for a small quadrotor with compensation for model variation," in *International Conference on Unmanned Aircraft Systems (ICUAS)*, pp. 902–909, IEEE, 2014.

[150] M. Ö. Efe, "Battery power loss compensated fractional order sliding mode control of a quadrotor UAV," *Asian Journal of Control*, vol. 14, no. 2, pp. 413–425, 2012.

[151] M. Ö. Efe, "Neural network assisted computationally simple PID control of a quadrotor UAV," *IEEE Transactions on Industrial Informatics*, vol. 7, no. 2, pp. 354–361, 2011.

[152] Y. M. Zhang and J. Jiang, "Active fault-tolerant control system against partial actuator failures," *IEE Control Theory and Applications*, vol. 149, no. 1, pp. 95–104, 2002.

[153] G. W. Cai, J. Dias, and L. Seneviratne, "A survey of small-scale unmanned aerial vehicles: Recent advances and future development trends," *Unmanned Systems*, vol. 2, no. 2, pp. 175–199, 2014.

[154] X. Yu and Y. M. Zhang, "Sense and avoid technologies with applications to unmanned aircraft systems: Review and prospects," *Progress in Aerospace Sciences*, vol. 74, pp. 152–166, 2015.

[155] D. W. Casbeer, D. B. Kingston, R. W. Beard, and T. W. McLain, "Cooperative forest fire surveillance using a team of small unmanned air vehicles," *International Journal of Systems Science*, vol. 37, no. 6, pp. 351–360, 2006.

[156] A. Rango, A. Laliberte, J. E. Herrick, C. Winters, K. Havstad, C. Steele, and D. Browning, "Unmanned aerial vehicle-based remote sensing for rangeland assessment, monitoring, and management," *Journal of Applied Remote Sensing*, vol. 3, no. 1, pp. 1–15, 2009.

[157] D. Kingston, R. W. Beard, and R. S. Holt, "Decentralized perimeter surveillance using a team of UAVs," *IEEE Transactions on Robotics*, vol. 24, no. 6, pp. 1394–1404, 2008.

[158] M. A. Goodrich, B. S. Morse, D. Gerhardt, J. L. Cooper, M. Quigley, J. A. Adams, and C. Humphrey, "Supporting wilderness search and rescue using a camera-equipped mini UAV," *Journal of Field Robotics*, vol. 25, no. 1-2, pp. 89–110, 2008.

[159] C. Sabo, D. Kingston, and K. Cohen, "A formulation and heuristic approach to task allocation and routing of UAVs under limited communication," *Unmanned Systems*, vol. 2, no. 1, pp. 1–17, 2014.

[160] M. S. Cons, T. Shima, and C. Domshlak, "Integrating task and motion planning for unmanned aerial vehicles," *Unmanned Systems*, vol. 2, no. 1, pp. 19–38, 2014.

[161] J. W. Hu, J. Xu, and L. H. Xie, "Cooperative search and exploration in robotic networks," *Unmanned Systems*, vol. 1, no. 1, pp. 121–142, 2013.

[162] L. Geng, Y. F. Zhang, J. J. Wang, J. Y. H. Fuh, and S. H. Teo, "Cooperative mission planning with multiple UAVs in realistic environments," *Unmanned Systems*, vol. 2, no. 1, pp. 73–86, 2014.

[163] P. Doherty, F. Heintz, and J. Kvarnström, "High-level mission specification and planning for collaborative unmanned aircraft systems using delegation," *Unmanned Systems*, vol. 1, no. 1, pp. 75–119, 2013.

[164] R. Y. Tan and M. Kumar, "Tracking of ground mobile targets by quadrotor unmanned aerial vehicles," *Unmanned Systems*, vol. 2, no. 2, pp. 157–173, 2014.

[165] A. N. Kopeikin, S. S. Ponda, L. B. Johnson, and J. P. How, "Dynamic mission planning for communication control in multiple unmanned aircraft teams," *Unmanned Systems*, vol. 1, no. 1, pp. 41–58, 2013.

[166] F. Giulietti, M. Innocenti, M. Napolitano, and L. Pollini, "Dynamic and control issues of formation flight," *Aerospace Science and Technology*, vol. 9, no. 1, pp. 65–71, 2005.

[167] F. Giulietti, L. Pollini, and M. Innocenti, "Autonomous formation flight," *IEEE Control Systems Magazine*, vol. 20, no. 6, pp. 34–44, 2000.

[168] G. Campa, Y. Gu, B. Seanor, M. R. Napolitano, L. Pollini, and M. L. Fravolini, "Design and flight-testing of non-linear formation control laws," *Control Engineering Practice*, vol. 15, no. 9, pp. 1077–1092, 2007.

[169] M. Pachter, J. J. D', Azzo, and A. W. Proud, "Tight formation flight control," *Journal of Guidance, Control, and Dynamics*, vol. 24, no. 2, pp. 246–254, 2001.

[170] Y. Gu, B. Seanor, G. Campa, M. R. Napolitano, L. Rowe, S. Gururajan, and S. Wan, "Design and flight testing evaluation of formation control laws," *IEEE Transactions on Control Systems Technology*, vol. 14, no. 6, pp. 1105–1112, 2006.

[171] D. M. Stipanović, G. Inalhan, R. Teo, and C. J. Tomlin, "Decentralized overlapping control of a formation of unmanned aerial vehicles," *Automatica*, vol. 40, no. 8, pp. 1285–1296, 2004.

[172] S. N. Singh, R. Zhang, P. Chandler, and S. Banda, "Decentralized nonlinear robust control of UAVs in close formation," *International Journal of Robust and Nonlinear Control*, vol. 13, no. 11, pp. 1057–1078, 2003.

[173] S. N. Singh, M. Pachter, P. Chandler, S. Banda, S. Rasmussen, and C. Schumacher, "Input–output invertibility and sliding mode control for close formation flying of multiple UAVs," *International Journal of Robust and Nonlinear Control*, vol. 10, no. 10, pp. 779–797, 2000.

[174] A. Karimoddini, H. Lin, B. M. Chen, and T. H. Lee, "Hybrid three-dimensional formation control for unmanned helicopters," *Automatica*, vol. 49, no. 2, pp. 424–433, 2013.

[175] J. H. Shin and H. J. Kim, "Nonlinear model predictive formation flight," *IEEE Transactions on Systems, Man and Cybernetics, Part A: Systems and Humans*, vol. 39, no. 5, pp. 1116–1125, 2009.

[176] M. M. Tousi and K. Khorasani, "Optimal hybrid fault recovery in a team of unmanned aerial vehicles," *Automatica*, vol. 48, no. 2, pp. 410–418, 2012.

[177] S. Waydo, J. Hauser, R. Bailey, E. Klavins, and R. M. Murray, "UAV as a reliable wingman: A flight demonstration," *IEEE Transactions on Control Systems Technology*, vol. 15, no. 4, pp. 680–688, 2007.

[178] A. Abdessameud and A. Tayebi, "Formation control of VTOL unmanned aerial vehicles with communication delays," *Automatica*, vol. 47, no. 11, pp. 2383–2394, 2011.

[179] M. S. Qian, B. Jiang, and D. Z. Xu, "Fault tolerant control scheme design for the formation control system of unmanned aerial vehicle," *Proceedings of the Institution of Mechanical Engineers, Part I: Journal of Systems and Control Engineering*, vol. 227, no. 8, pp. 626–634, 2013.

[180] Q. Xu, H. Yang, B. Jiang, D. H. Zhou, and Y. M. Zhang, "Fault tolerant formations control of UAVs subject to permanent and intermittent faults," *Journal of Intelligent & Robotic Systems*, vol. 73, no. 1-4, pp. 589–602, 2014.

[181] X. H. Wang, V. Yadav, and S. N. Balakrishnan, "Cooperative UAV formation flying with obstacle/collision avoidance," *IEEE Transactions on Control Systems Technology*, vol. 15, no. 4, pp. 672–679, 2007.

[182] E. W. Justh and P. S. Krishnaprasad, "Equilibria and steering laws for planar formations," *Systems & Control Letters*, vol. 52, no. 1, pp. 25–38, 2004.

[183] T. Keviczky, F. Borrelli, K. Fregene, D. Godbole, and G. J. Balas, "Decentralized receding horizon control and coordination of autonomous vehicle formations," *IEEE Transactions on Control Systems Technology*, vol. 16, no. 1, pp. 19–33, 2008.

[184] T. Paul, T. R. Krogstad, and J. T. Gravdahl, "Modelling of UAV formation flight using 3D potential field," *Simulation Modelling Practice and Theory*, vol. 16, no. 9, pp. 1453–1462, 2008.

[185] F. Borrelli, T. Keviczky, and G. J. Balas, "Collision-free UAV formation flight using decentralized optimization and invariant sets," in *IEEE Conference on Decision and Control*, vol. 1, pp. 1099–1104, 2004.

[186] S. Tarbouriech, G. Garcia, J. M. G. da Silva Jr, and I. Queinnec, *Stability and stabilization of linear systems with saturating actuators*. Springer Science & Business Media, 2011.

[187] A. R. Teel, *Modern Antiwindup Synthesis*. Princeton University Press, 2011.

[188] S. P. Karason and A. M. Annaswamy, "Adaptive control in the presence of input constraints," *IEEE Transactions on Automatic Control*, vol. 39, no. 11, pp. 2325–2330, 1994.

[189] M. Chen, S. Z. S. Ge, and B. B. Ren, "Adaptive tracking control of uncertain MIMO nonlinear systems with input constraints," *Automatica*, vol. 47, no. 3, pp. 452–465, 2011.

[190] E. Lavretsky and N. Hovakimyan, "Stable adaptation in the presence of input constraints," *Systems & Control Letters*, vol. 56, no. 11, pp. 722–729, 2007.

[191] E. Lavretsky and N. Hovakimyan, "Stable adaptation in the presence of actuator constraints with flight control applications," *Journal of Guidance, Control, and Dynamics*, vol. 30, no. 2, pp. 337–345, 2007.

[192] F. Fahimi, "Non-linear model predictive formation control for groups of autonomous surface vessels," *International Journal of Control*, vol. 80, no. 8, pp. 1248–1259, 2007.

[193] C. De La Cruz and R. Carelli, "Dynamic model based formation control and obstacle avoidance of multi-robot systems," *Robotica*, vol. 26, no. 3, pp. 345–356, 2008.

[194] G. Tao, S. H. Chen, X. D. Tang, and S. M. Joshi, *Adaptive control of systems with actuator failures*. Springer Science & Business Media, 2013.